Mount
Sinai

TMII

Translational and Molecular Imaging Institute

July 2013

Table of Content

Biographies from invited speakers ....

Translational and Molecular Imaging Institute..

Abstracts selected for oral presentation...

Message from the Translational and Molecular Imaging Institute Director

It is with great enthusiasm and pride that we introduce the 3rd Annual Translational and Molecular Imaging Institute (TMII) Symposium.

The TMII symposium is intended to offer some snapshots of most current translational imaging research at Mount Sinai and other institutions in and outside the New York metropolitan area.

The TMII team and the Icahn School of Medicine at Mount Sinai have carefully worked to organize this symposium, and we look forward to familiarizing you with our Institute and its research endeavors. We encourage you to review the Program Book, which provides abstracts and the program summary. In addition, it includes information about the speakers, activities, facilities and faculty members at our Institute and Mount Sinai's efforts in translational research.

Welcome to New York and Mount Sinai.

Zahi A. Fayad, Ph.D.

Fayad

TMII Director
Professor of Radiology
Professor of Medicine (Cardiology)

Mount Sinai TMII
Translational and Molecular Imaging Institute

The 3rd Annual TMII Symposium – 2013
Icahn School of Medicine at Mount Sinai
Leon and Norma Hess Center for Science and Medicine
1470 Madison Avenue, between 101 and 102 St.; New York, NY 10029

	Title	**Speaker**	**Affiliation**
7:00-8:00	**Registration/Breakfast**		
8:00-8:15	Opening remarks	Zahi A. Fayad, PhD	Director, Translational and Molecular Imaging Institute
8:15-8:30	Opening remarks	Dennis Charney, MD	Dean, Icahn School of Medicine at Mount Sinai
8:30-8:45	Opening remarks	A. Gregory Sorensen, MD	CEO, Siemens Healthcare North America
Neuroimaging Session (I) - Moderator: Junqian Gordon Xu, PhD			
8:50-9:50	The Human Connectome Project	David Van Essen, PhD	Washington University, St. Louis
9:50-10:05	*DREAMM: In vivo cell type-specific functional whole-brain circuit mapping of limbic networks in freely-moving animals*	*Michael Michaelides*	*Icahn School of Medicine at Mount Sinai*
10:05 -10:30	Break		
Cancer Imaging Session (II) - Moderator: Bachir Taouli, MD			
10:30-11:15	Multiparametric whole body MRI of bone marrow in health and disease	Anwar R. Padhani, MD, PhD	Mount Vernon Cancer Centre, London
11:15-11:30	*Quantitative Susceptibility Mapping of Contrast Agent in a Mouse Prostate Cancer Model*	*Tian Liu*	*Weill Cornell Medical College; MedImageMetric LLC*
Poster Session (III) - Facilitators: Priti Balchandani, PhD; Venkatesh Mani, PhD; Cheuk Tang, PhD			
11:30-1:30	*Poster viewing*		
12:00-1:30	Lunch		
Nanomedicine Session (IV) - Moderator: Willem Mulder, PhD			
1:30-2:15	Co-opting Moore's Law: Design of Shape-specific Particulate-based Vaccines and Therapeutics	Joseph M. DeSimone, PhD	The University of North Carolina at Chapel Hill
2:15-2:30	*A Multi-Functional Nanoplatform for Imaging, Radiotherapy, and the Prediction of Therapeutic Response*	*Ajlan Al Zaki*	*University of Pennsylvania*
2:30-3:00	Break		
Cardiovascular Imaging Session (V) - Moderator: Zahi A. Fayad, PhD			
3:00-3:45	Emerging Applications of Cardiovascular MR at 7T - Hype or Hope?	Jeanette Schulz-Menger, MD	Charité, Humboldt-University and HELIOS-Klinikum, Berlin
3:45-4:00	*Role of chronic stress on experimental atherosclerosis*	*Chiara Giannarelli*	*Icahn School of Medicine at Mount Sinai*
4:00-4:15	Closing remarks	Burton P. Drayer, MD	Chairman, Department of Radiology
4:15	Adjournment	Zahi A. Fayad, PhD	

Biographies of invited speakers

Zahi A. Fayad, PhD, FAHA, FACC
Professor of Radiology and Medicine (Cardiology)
Director, Translational and Molecular Institute
Vice chair for Research, Department of Radiology
Mount Sinai School of Medicine, New York, NY
Zahi.Fayad@mssm.edu

Biography

Dr. Fayad serves as professor of Radiology and Medicine (Cardiology) at the Mount Sinai School of Medicine. He is the Director of the Translational and Molecular Imaging Institute; Vice chair for Research, Department of Radiology and Director of Cardiovascular Imaging Research at the Mount Sinai School of Medicine and Mount Sinai Medical Center. Dr. Fayad's interdisciplinary and discipline bridging research - from engineering to biology and from pre-clinical to clinical investigations - has been dedicated to the detection and prevention of cardiovascular disease with many seminal contributions in the field of biomedical imaging and nanomedicine. Dr. Fayad's is one of the world's leader in the innovative development and use of multimodality cardiovascular imaging including, Magnetic Resonance imaging (MRI), computed tomography (CT), and positron emission tomography (PET), as well as molecular imaging and nanomedicine to study, prevent and treat cardiovascular disease. His focus in the past 15 years at Mount Sinai has been on the noninvasive assessment and understanding of atherosclerosis (Nature 2008; 451:953-957; Nat Rev Drug Discov. 2011;10:835-52). He holds 12 US and Worldwide patents and/or patent applications. He has authored more than 300 peer-reviewed publications (h-index of 56 accessed 1/1/2013 on Thomson Reuters Web of Science), 50 book chapters, and over 400 meeting presentations. Recently, he published in the Lancet (2011;378:1547-59) the results of the dal-PLAQUE multicenter clinical trial evaluating atherosclerosis with MRI and FDG-PET demonstrating the efficacy and safety of Dalcetrapib, a first-in-class CETP modulator. He is currently the Principal Investigator of four federal grants/contracts funded by the National Institutes of Health's National Heart, Lung and Blood Institute and National institute of Biomedical Imaging and Bioengineering with a recent large award from NHLBI to support the Program of Excellence in Nanotechnology. In addition, he serves as Principal Investigator of the Imaging Core of the Mount Sinai National Institute of Health (NIH)/Clinical and Translational Science Awards (CTSA). Dr. Fayad had his trainings at the Johns Hopkins University and at the University of Pennsylvania. From 1996 to 1997 he was junior faculty in the Department of Radiology at the University of Pennsylvania. In 1997 he joined the faculty at Mount Sinai School of Medicine. Dr. Fayad is past-deputy Editor of Magnetic Resonance in Medicine (MRM), past-president of the Society of Atherosclerosis and Prevention (SAIP), fellow of the American Heart Association (AHA) where he served on the National Research Committee and on the Council on Cardiovascular Radiology and Intervention (CVRI). He is also a fellow of the American College of Cardiology (ACC), where he served on the Cardiovascular Collaborative Imaging (CCI) Committee. He is member of the NIH's National Lung, and Blood Institute (NHLBI) Cardiovascular Strategic Planning Working Group on Vascular Disease and Hypertension. He is a member of the Foundation of the NIH (FNIH)

Biomarkers Consortium. Dr. Fayad is Associate Editor for the Journal of the American College of Cardiology Imaging (JACC Imaging) and Consulting Editor for Arteriosclerosis Thrombosis and Vascular Biology (ATVB). Dr. Fayad is on the editorial boards of Journal of Cardiovascular Magnetic Resonance (JCMR), Nature Reviews Cardiology, Atherosclerosis, and Cancer Nanotechnology. He often serves as guest editor for several prestigious journals in the fields of imaging, vascular biology, cardiology and radiology. He participates regularly to the AHA/ACC writing groups. In 2013, he became a Charter Member, NIH Center of Scientific Review, Clinical Molecular Imaging and Probe Development Study Section and a Member, NIH Center of Scientific Review, Recurring Special Emphasis Panel ZRG1 SBIB-W (56) - Early Phase Clinical Trials in Imaging and Image-Guided Interventions Special Emphasis Panel. He is past member of the Medical Imaging (MEDI) study section and ad-hoc member on numerous other study sections including those from NIH and the National Academy of Science. He is a member of the New York University Program in Computational Biology. He is a past member of the board of trustees of the Society of Cardiovascular Magnetic Resonance (SCMR) and he is also a past member of the Scientific Program Committee of the International Society of Magnetic Resonance in Medicine (ISMRM). He also serves on the boards of several national and international scientific boards, committees and foundations.

Dr. Fayad is the recipient of multiple prestigious awards. In 2007 he was given the John Paul II Medal from Krakow, Poland in recognition for the potential of his work on humankind. As a teacher and mentor, Dr. Fayad has been also extremely successful. He has trained over 40 postdoctoral fellows, clinical fellows and students. His trainees have received major awards, fellowships, and positions in academia and industry. In 2008, he received the Outstanding Teacher Award from the International Society of Magnetic Resonance in Medicine (ISMRM) for his teaching on cardiovascular imaging and molecular imaging. In 2009 he was awarded the title of Honorary Professor in Nanomedicine at Aarhus University in Denmark. Recently, he was one of opening speakers at the 2011 97th Scientific Assembly and Scientific meeting of the Radiological Society of North America (RSNA). In 2012, he was invited to give the Henry I Russek Lecture at the 45th Anniversary of the ACCF New York Cardiovascular Symposium. In 2013, he was elected Fellow of the International Society of Magnetic Resonance In Medicine, Magnetic Resonance Imaging, received a Distinguished Reviewer from Magnetic Resonance in Medicine and was selected as an Academy of Radiology Research, Distinguished Investigator. He is married to Monique P. Fayad, MBA and is the proud father of Chloé (11 year old) and Christophe (7 year old) and after spending seven years in Manhattan now lives, runs in Central Park and participates regularly in New York Road Runners races. He also enjoys regular sailing in Larchmont, NY and beyond.

Dennis S. Charney, MD
Anne and Joel Ehrenkranz Dean
Icahn School of Medicine at Mount Sinai
Executive Vice President for Academic Affairs
The Mount Sinai Medical Center

Biography

Dr. Charney is a world expert in the neurobiology and treatment of mood and anxiety disorders. He has made fundamental contributions to the understanding of the causes of human anxiety, fear and depression and the discovery of new treatment for mood and anxiety disorders. More recently, his pioneering research has expanded to include the psychobiological mechanisms of human resilience to stress.

Dr. Charney's work in depression has led to new hypotheses regarding the mechanisms of antidepressant drugs and discovery of new and novel therapies for treatment resistant depression including Lithium and Ketamine. The work demonstrating that Ketamine is a rapidly acting antidepressant has been hailed as one of the most exciting developments in antidepressant therapy in more than half a century.

Dr. Charney's studies on human resilience have culminated in the identification of ten key resilience factors for building the strength to weather and bounce back from stress and trauma. This work is summarized in an inspiring new book "*Resilience: The Science of Mastering Life's Greatest Challenges*" co-authored by Steven Southwick and published by Cambridge University Press in 2012.

As Dean of the Icahn School of Medicine at Mount Sinai, Dr. Charney unveiled Mount Sinai's $2.25 billion strategic plan, laying the foundation for the robust 15-institute structure that Icahn School of Medicine at Mount Sinai is known for today. Today these institutes are hubs of scientific and clinical enterprise, working together to challenge the limits of science and medicine. Within—and across—them, scientists and physicians, who themselves are members of the teaching faculty, can facilitate the development of effective treatments for the most serious medical conditions. Icahn School of Medicine at Mount Sinai now stands among the most innovative of the top medical schools in the United States and is a beacon for advances in education, transformative biomedical research, and personalized, compassionate, world-class clinical care.

During Dr. Charney's tenure, Icahn School of Medicine at Mount Sinai rose to and has maintained its strength among the top 20 institutions in National Institutes of Health (NIH) funding, and it currently ranks third in funding per faculty member from the NIH. The institution is also listed consistently among the top 20 medical schools in the country according to *U.S. News & World Report*, and in 2009, it received the Spencer Foreman Award for Outstanding Community Service from the Association of American Medical Colleges.

Even within the confines of tight city streets, the campus itself has grown—and continues to grow. The Hess Center for Science and Medicine, opened in the fall 2012, provides over a half-million square-feet of state-of-the-art research and clinical space. This allows Mount Sinai to expand its capabilities as a center for innovation and discovery.

Dr. Charney's career began in 1981 at Yale, where, within nine years, he rose from Assistant Professor to Professor of Psychiatry, a position he held from 1990 to 2000. While there, he chaired the NIMH Board of Scientific Counselors, which advises the institute's director on intramural research programs. In 2000, NIMH recruited Dr. Charney to lead the Mood and Anxiety Disorder Research Program — one of the largest programs of its kind in the world — and the Experimental Therapeutics and Pathophysiology Branch. That year he was also elected to the Institute of Medicine of the National Academy of Sciences. His scientific research has been honored by every major award in his field.

In 2004, Icahn School of Medicine at Mount Sinai recruited Dr. Charney as Dean of Research. In 2007, he became the Dean of the School and Executive Vice President for Academic Affairs of the Medical Center.

A prolific author, Dr. Charney has written more than 700 publications, including groundbreaking scientific papers, chapters, and books. He has authored many books, including *Neurobiology of Mental Illness* (Oxford University Press, USA, Third Edition, 2009); *The Peace of Mind Prescription: An Authoritative Guide to Finding the Most Effective Treatment for Anxiety and Depression* (Houghton Mifflin Harcourt, 2004); *The Physicians Guide to Depression and Bipolar Disorders* (McGraw-Hill Professional, 2006), *Resilience and Mental Health: Challenges Across the Lifespan* (Cambridge University Press, 2011), and, as mentioned, *Resilience: The Science of Mastering Life's Greatest Challenges*, for lay audiences (Cambridge University Press, 2012).

Gregory Sorensen, MD

President and Chief Executive Officer
Siemens Healthcare North America

Biography

Gregory Sorensen, MD, is the President and Chief Executive Officer of Siemens Healthcare in North America, charged with leading the USA organization and providing additional oversight for Canada and Latin America.

As a trendsetter in medical imaging, therapy systems, laboratory diagnostics, and healthcare information technology, Siemens Healthcare offers optimized clinical solutions across the entire care continuum – from prevention and early detection to diagnosis, treatment and follow-up. By offering novel tools for improved diagnosis, as well as optimizing clinical workflows for the most common conditions, Siemens helps make healthcare faster, better and more cost-effective. As head of the business in the largest global market, Sorensen brings to his leadership position a deep understanding of technology, the biological basis of disease, the importance of measurable outcomes, and the environment of clinical practice. Sorensen was appointed to his current role in June 2011.

Previously, Sorensen served as Professor of Radiology and Health Sciences & Technology at Harvard Medical School; faculty member of the Harvard-MIT Division of Health Sciences and Technology; and Co-Director of the A.A. Martinos Center for Biomedical Imaging at Massachusetts General Hospital, as well as a visiting professor of neuroradiology at Oxford University.

Leading up to his appointment with Siemens, Sorensen was a practicing neuroradiologist and active researcher with significant experience in clinical care, clinical trials, and translational research. His research and techniques are utilized by scores of centers throughout the world in phase II and III trials in cancer, stroke, and other illnesses.

Dr. Sorensen holds a B.S. in Biology from California Institute of Technology, a M.S. in Computer Science from Brigham Young University, and a Medical Degree from Harvard Medical School. He is married with three children.

David Van Essen, PhD
Edison Professor of Neurobiology
Chair, Department of Anatomy and Neurobiology
Washington University School of Medicine
St. Louis, MO

Biography

David C. Van Essen is Alumni Endowed Professor in the Anatomy & Neurobiology Department at Washington University in St. Louis. Along with Kamil Ugurbil, he is Principal Investigator of the Human Connectome Project, a $30 million NIH grant to map brain circuitry in a large population of healthy adults using cutting-edge neuroimaging methods. Van Essen's physiological and anatomical studies of macaque visual cortex provide many insights into functional specialization within this distributed hierarchical system. He has pioneered the use of surface-based atlases for visualizing and analyzing cortical structure, function, development, and connectivity and for making comparisons across studies and across species. His tension-based theory of morphogenesis accounts for how and why the cortex gets its folds. His studies of human cerebral cortex provide insights regarding normal variability, abnormalities in specific diseases, and patterns of cortical development. He has served as Editor-in-Chief of the Journal of Neuroscience, founding chair of the OHBM, and President of the Society for Neuroscience. He is a fellow of the AAAS and has received the Raven Lifetime Achievement Award from the St. Louis Academy of Sciences and the Krieg Cortical Discoverer Award from the Cajal Club.

Abstract: "The Human Connectome Project"

Recent advances in noninvasive neuroimaging have set the stage for the systematic exploration of human brain circuits in health and disease. The Human Connectome Project (HCP) is one such effort that will characterize brain circuitry and its variability in a large population of healthy adults. This talk will review progress by a consortium of HCP investigators at Washington University, University of Minnesota, University of Oxford, and 7 other institutions, who are engaged in a 5-year project to characterize the human connectome in 1,200 individuals (twins and their non-twin siblings). Information about structural and functional connectivity is being acquired using diffusion MRI and resting-state fMRI, respectively. Additional modalities include task-evoked fMRI and MEG/EEG, plus extensive behavioral testing and genotyping. Each of these methods is powerful, yet faces significant technical limitations that are important to characterize and be mindful of when interpreting neuroimaging data.

Advanced visualization and analysis methods developed by the HCP enable characterization of brain circuits in individuals and group averages at high spatial resolution and at the level of functionally distinct brain parcels.

Comparisons across subjects will reveal aspects of brain circuitry which are related to particular behavioral capacities and which are heritable or related to specific genetic variants. Data from the HCP is being made freely available to the neuroscience community via a user-friendly informatics platform. Altogether, the HCP will provide invaluable information about the healthy human brain and its variability. It will set the stage for characterizing brain circuits during healthy development as well as abnormal brain connectivity in a variety of brain disorders and diseases.

Anwar Padhani, MBBS FRCP FRCR

Consultant Radiologist and Professor of Cancer Imaging
Paul Strickland Scanner Centre
Mount Vernon Cancer Centre
Northwood, Middlesex, United Kingdom

Biography

Prof. Anwar R. Padhani is an internationally recognized Oncological MRI radiologist and currently, the clinical lead in MRI and head of imaging research at the Paul Strickland Scanner Centre, Mount Vernon Cancer Centre, London. He is Professor of Cancer Imaging at the Institute of Cancer Research, London.

He is involved in the development of innovative research programs investigating the use of functional imaging on the microenvironment of human tumours, and has performed numerous clinical research studies evaluating tumour perfusion, permeability, oxygenation and water diffusion imaging of breast, brain, rectal and prostate cancers as well as studies of antiangiogenic and antivascular treatments. This work which involves CT scanning, MRI and PET-CT is of international renown. He is a co-applicant in a number of successful grant proposals in support of this research.

He has helped establish MRI perfusion and diffusion as biomarkers of tumour response. In this regard, he has advised the National Cancer Institute of the USA and Cancer Research UK (CR-UK) on clinical trials imaging methodology; this work has attracted clinical research organisation and pharmaceutical interest.

He is also expert in prostate MRI looking after patients on a weekly basis and is also a specialist in a number of emerging clinical MRI applications including dynamic MRI, diffusion weighted MRI, MR spectroscopy, whole body MRI and multiparametric MRI of the prostate for primary and metastatic disease.

Dr. Padhani has a passion for teaching and has published chapters in 31 textbooks, 64 educational and scientific journal reviews in peer reviewed journals, and published over 103 full scientific articles in peer reviewed journals. He co-edited the book “Advances in Oncologic Imaging Techniques” (Taylor & Francis, New York) published in 2006.

Dr Padhani has given over 250 invited lectures at national and international scientific and educational meetings including several plenary talks on multifunctional imaging, imaging of angiogenesis, advanced prostate MRI, whole body diffusion imaging and the imaging of metastatic bone disease. He has to his credit several education related awards including outstanding teacher award from the ISMRM in 2011 & 2012 and honoured educator award from the RSNA 2011. He was the organised of weekend educational course on “clinical MRI of cancer” at the annual meeting of the International Society of Magnetic Resonance in Medicine (ISMRM) for 2006-2009, 2010-2012. He was the 2012 president of the International Cancer Imaging Society.

Abstract: “Multiparametric whole body MRI of bone marrow in health and disease”

There are increasing therapy options against a diverse array of targets for metastatic bone disease. However limited rates and durations of response mean that survival remains poor for some groups. The inability to accurately determine bone metastasis status results in the poor performance of conventional trial endpoints such as progression free survival; the latter cannot be used as a surrogate of overall survival. Current methods of assessing tumor response at skeletal sites do not always enable the positive assessment of therapeutic benefit to be made but instead provide an evaluation of progression, which then guides therapy decisions in the clinic. Whole body diffusion weighted imaging is emerging as a promising bone marrow assessment tool for detection and therapy monitoring of bone metastases. Whole body MRI is also evolving to a multiparametric/multimodal approach (within MRI (marrow fat, trabecullar bone, vascularity), with PET (various tracers) and CT (bone density & iodine maps). These imaging approaches when combined with wet biomarkers will more accurately predict who will benefit from novel bone direct therapies. Future challenges include (1) integration of multiple individual tests all of which can be done at a single patient visit (new bioinformatics challenge), (2) dealing with heterogeneity that exists between patients, between lesions (in the same patients) and within lesions (at baseline and in response to therapy), (3) developing methods for understanding correlations between imaging findings with underlying biologic properties & other therapeutic efficacy measures, (4) the need to develop common measurements and analysis methods, uniform data displays, standardization, reproducibility, multicentre methodologies and (5) developing roadmaps for BM qualification fit for drug development and personalized medicine

Joseph M. DeSimone, PhD

Director, Frank Hawkins Kenan Institute of Private Enterprise
Chancellor's Eminent Professor of Chemistry
University of North Carolina at Chapel Hill
William R. Kenan, Jr. Distinguished Professor of Chemical Engineering
North Carolina State University

Biography

Joseph DeSimone is the Chancellor's Eminent Professor of Chemistry at the University of North Carolina at Chapel Hill, and William R. Kenan, Jr. Distinguished Professor of Chemical Engineering at North Carolina State University and of Chemistry at UNC. In 2012 he was named director of the Frank Hawkins Kenan Institute of Private Enterprise at UNC—the Institute is the equivalent of a $50 million endowment focused on facilitating entrepreneurship at UNC and in North Carolina more broadly. DeSimone is an adjunct member at Memorial Sloan-Kettering Cancer Center. DeSimone has published over 300 scientific articles and has 140 issued patents in his name with over 80 patents pending.

DeSimone is a member of both the National Academy of Sciences (2012) and the National Academy of Engineering (2005). He is also a member of the American Academy of Arts and Sciences (2005). DeSimone has received over 50 major awards and recognitions including the 2012 Walston Chubb Award for Innovation by Sigma Xi; the 2010 AAAS Mentor Award in recognition of his efforts to advance diversity in the chemistry PhD workforce; the 2009 NIH Director's Pioneer Award*;* the 2009 North Carolina Award; the 2008 $500,000 Lemelson-MIT Prize for Invention and Innovation; the 2007 Collaboration Success Award from the Council for Chemical Research; the 2005 ACS Award for Creative Invention*;* the 2002 John Scott Award presented by the City Trusts, Philadelphia, given to "the most deserving" men and women whose inventions have contributed in some outstanding way to the "comfort, welfare and happiness" of mankind; the 2002 Engineering Excellence Award by DuPont; and the 2002 Wallace H. Carothers Award from the Delaware Section of the ACS.

DeSimone, an innovative polymer chemist, has made breakthrough contributions in green chemistry, fluoropolymer synthesis, colloid science, and nano-biomaterials. He pioneered supercritical CO_2-based polymerization reactions and the self-assembly of molecules in compressible media. He has shown the benefit of novel fluoro-elastomers for soft lithographic applications, including the synthesis of shape-controlled nano-biomaterials. DeSimone received his BS in Chemistry in 1986 from Ursinus College in Collegeville, PA and his Ph.D. in Chemistry in 1990 from Virginia Tech.

Abstract: “Co-opting Moore’s Law: Design of Shape-specific Particulate-based Vaccines and Therapeutics”

In 1965, Gordon Moore, co-founder of Intel, described the trend that the number of components in integrated circuits had doubled every year since 1958. This trend has continued to today, enabled by advances in photolithography which has taken the minimum feature size of transistors down from about 10 microns in 1970 to 0.045 microns (45 nm) today. In biological terms, this corresponds to going from the size of a red blood cell to the size of a single virus particle! As such, this top-down nano-fabrication technology from the semiconductor industry is, for the first time, in the size range to be relevant for the design of medicines, vaccines and interfacially active Janus particles. This lecture will describe the design, synthesis and efficacy of organic nano- and micro-particles using a top-down nano-fabrication technique we developed called PRINT (Particle Replication in Non-wetting Templates). PRINT is a continuous, roll-to-roll, high resolution molding technique that allows the fabrication of precisely defined micro- and nano-particles in a continuous manner with control over chemical composition, size, shape, deformability and surface chemistry. With these ‘nanotools’, we are establishing definitive biodistribution maps to elucidate the interdependent roles that size, shape, deformability and surface chemistry play on particle distribution as a function of different dosage forms (IV, IP, inhaled, subcutaneous, intramuscular, etc). This information is setting the stage for the design of highly effective chemo-therapeutics, respiratory therapeutics and vaccines which will be described.

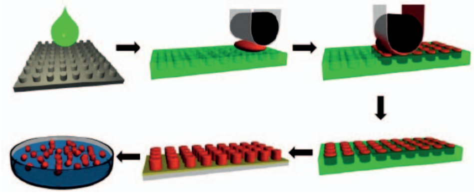

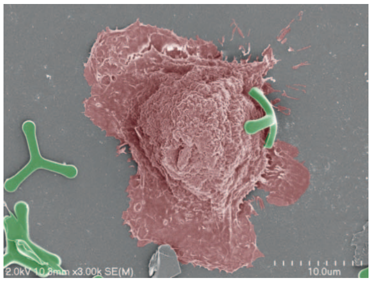

Jeanette Schulz-Menger, MD
Noninvasive Cardiac Imaging
University Medicine Berlin, Charité Campus Buch
Experimental Clinical Research Center, a joint institution between Charité and MDC
HELIOS Clinics Berlin Buch, Department Cardiology and Nephrology

Biography

Dr. Schulz-Menger is originally from Berlin. She is married and has an 18y old son. He left home and is studying medicine.

J. Schulz-Menger is a cardiologist by training and active in CMR since 1996. She has a significant interest in imaging inflammatory disease and cardiomyopathies applying CMR. She has a board certification in internal medicine and cardiology followed by board certification dedicated on CMR. Since 2004 she is heading the Working Group Cardiac Magnetic Resonance at Charité Campus Buch. Furthermore, she established the department Non-Invasive Cardiac Imaging in the clinical environment.

In 2008 her application for a University-Professorship in Cardiology “Noninvasive Imaging focused on Cardiovascular Magnetic Resonance” was successful. The research of the group is focused on clinical topics including growing interests in MR-physics. That is based on collaboration with MR physicists world wide and strong interaction with the group of Prof. Thoralf Niendorf “Experimental MR”, which is located nearby. As she was the contact and “driving” person for an inter-disciplinary Berlin consortium which successfully obtained funding to buy a 7 tesla whole body MR scanner in 2006, she had also to take the interim responsibility for the Ultra-Highfield Unit until Thoralf Niendorf´s appointment was successful.

Dr. Schulz-Menger has a high interest in CMR-teaching and was one of the founding members the UTC (University Teaching Courses for Cardiovascular Magnetic Resonance) in Berlin in 2001. During a long time period she was the director and scientific head. Three years ago she founded a CMR-Teaching network within the HELIOS-Clinics. There are 15 sites characterized by an effective interaction between radiologists and cardiologists. She is an Elected Member of the University Council of the Charité since 2011.

Dr. Schulz-Menger authored and co-authored more than 100 publications focused on CMR. The group established an active clinical CMR-service for in- and outpatients covering all clinical indications with a focus on ischemic and inflammatory disease.

Abstract: “Emerging Applications of Cardiovascular MR at 7T: Hype or Hope?”

Cardiovascular MR (CMR) is of growing impact in the clinical setting; nevertheless there are a lot of not well-defined areas. The distribution of clinical guidelines including CMR and well-defined teaching criteria will help to overcome this. Whereas it is necessary to get robust protocols working in a clinical scenario, innovative developments are required.

Increasing the field strength comes along with increases in signal- and contrast-to-noise ratio. This benefit is expected to be translated into higher spatial and temporal resolution and faster imaging techniques. However, increasing the field strength also means to increase the technological challenges, e.g. to achieve sufficient homogeneity of the magnetic field within the scanner, requiring many innovation by experienced physicists and engineers. Meanwhile, a growing number of centers are stepping into the field.

Hence, the technique itself is only a part of the challenge. The clinical challenge is to define the place or the chance of 7T. The bar of each diagnostic tool is the diagnostic accuracy compared to different gold standards and its impact on patient outcome. Thus, to lead CMR at 7T to reasonable success requires close cooperation between physicists and physician scientists.

First steps of human cardiac imaging at 7T have been gone successfully. Until now the published experience is based on healthy volunteer studies. Experiences in patients are needed to enhance our knowledge.

All further steps are based on careful technical developments of soft- and hardware. Dedicated coils have to be developed. Several models are introduced and have to survive a more “routine “ use. That opens the door to focus on new steps into the myocardium. There is first evidence that CINE-myocardial T2* mapping using susceptibility weighted gradient-echo imaging is feasible at 7.0T. Meanwhile next generation sequences are in development.

Nevertheless, before CMR at 7.0T can be applied in the wide range of diseases, safety basic homework have to be done.

The talk will give an overview on current state of the art based on ongoing research of different centers. The intention is to share thoughts and to learn lessons from different centers around the world.

Burton Drayer, MD, FACR
Professor of Radiology
Chair of the Department of Radiology
Icahn School of Medicine at Mount Sinai

Biography

Burton Paul Drayer, MD is currently the Dr. Charles M. and Marilyn Newman Professor and Chairman of the Department of Radiology (1995-present) Mount Sinai School of Medicine and the Executive Vice President for Risk at The Mount Sinai Medical Center. Additionally, from 2003 to 2008, Dr. Drayer served as President of The Mount Sinai Hospital. He completed his internship and Neurology residency at the University of Vermont and then a Radiology residency and Neuroradiology fellowship at the University of Pittsburgh Health Center. He is Board certified in both Neurology and Radiology and a fellow of both the American College of Radiology and the American Academy of Neurology.

Dr. Drayer served as Associate Professor and Professor of Radiology at Duke University from 1979 to 1986 where he was also Director of Neuroradiology. In 1986, he joined the Barrow Neurological Institute as Director of Magnetic Resonance Imaging and Research. Internationally known for his CT and MRI research on the aging brain and neurodegenerative disorders, brain infarction, multiple sclerosis, and physiological and functional brain imaging, Dr. Drayer has written over 200 publications as well as multiple book chapters. He was the first to describe metrizamide encephalopathy, nonradioactive xenon enhanced CT for measuring rCBF (ASNR Cornelius G. Dyke Award 1977) and the normal and abnormal distribution of brain iron using MRI. He also popularized carotid and intracranial MRA and educated a generation of physicians in the efficient clinical use of brain and spine MRI. He has been on numerous editorial boards and was the editor of Neuroimaging Clinics of North America from 1990 to 2005.

Dr. Drayer was elected President of the ASNR in 1996, was the inaugural Chairman of its Research Foundation, and was awarded the ASNR Gold Medal in 2011. In 2003, Dr. Drayer was elected to the Board of Directors of the RSNA and in 2009 ascended to Chairman of the Board, 2010 President elect, and 2011 RSNA President. He also presently serves on the Board of Chancellors of the ACR and the Board of Trustees of the RSNA Research and Education Foundation, is a past-President of the New York Roentgen Ray Society, and has served on numerous national advisory boards for multiple sclerosis, stroke, and Alzheimer’s disease.

Translational and Molecular Imaging Institute

About The Hess Center

Bringing nearly a half-million square-feet of newly constructed medical research and clinical facilities to the area, the Leon and Norma Hess Center for Science and Medicine meets the expansion needs of Mount Sinai's world-class research and clinical programs.

Featuring a layout including six full floors of laboratory space and two floors of outpatient clinical space, the new building increases Mount Sinai's research space by fifty percent. A full floor is devoted for advanced imaging technologies. The new space augments existing capabilities in cancer patient care and enables patients to receive multidisciplinary care by a team of doctors and other specialists. Translational research relating to cancer, cardiovascular disease, child health, genetics, and the brain are also expanding into this building. Hess Center will bring experts across disciplines together in one state-of-the-art facility—a union of talent and technology designed to advance Mount Sinai's fight against the world's most challenging diseases.

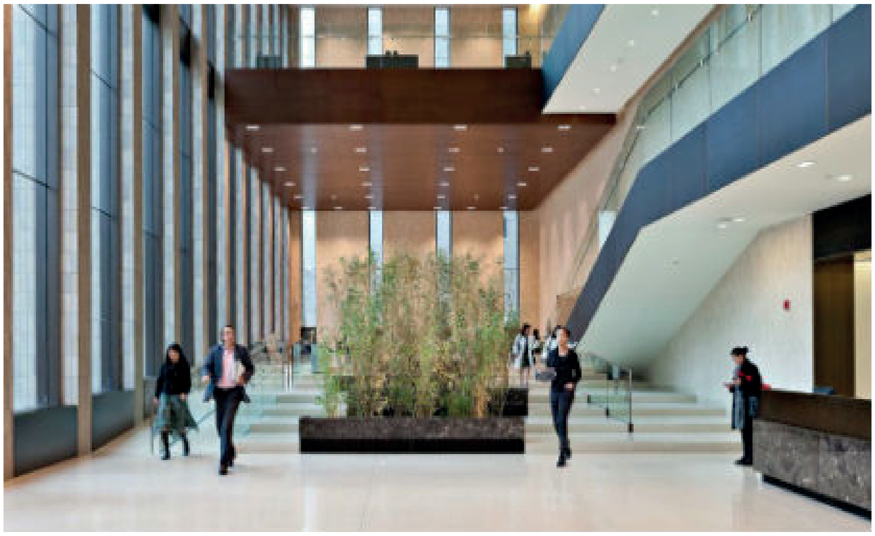

Hess Center Statistics:

- The building stands at 187 feet tall and has a gross square footage of approximately 500,000 square feet.
- More than 650 permanent new employment opportunities with an annual payroll of nearly $40 million. These new jobs will include 100 new faculty members, 100 graduate students, 125 postdoctoral fellows, 200 technicians, 35 administrators, 21 engineering jobs and at least 50 building operations jobs.
- More than 200 physicians, nurses, social workers, nutritionists, medical assistants, registration and financial personnel, and other administrative staff will support the operations of the outpatient facilities located in the building.
- 400 new patient visits per day are projected.

About the Translational and Molecular Imaging Institute

The Translational and Molecular Imaging Institute (TMII) is a comprehensive, multi-disciplinary, and integrated imaging research institute, which focuses on the use of multimodality imaging for brain, heart, and cancer research, along with research in nanomedicine for precision imaging and drug delivery. TMII is composed of research groups in all aspects of imaging research, including engineering, physics, chemistry, analysis, basic science, and medicine.

Our mission is centered around development, validation, translation and education of innovative technology in biomedical imaging to address both basic and clinical research problems and therefore improve human health.

Since 2013, the Translational and Molecular Imaging Institute occupies approximately 20,000 square feet at The Mount Sinai Medical Center. Housed on four partial floors (CSM-SC2, CSM-SC1, CSM-1, and CSM-7) of Mount Sinai's new signature building, the Leon and Norma Hess Center for Science and Medicine, TMII is located in close proximity to both research and clinical activities in The Mount Sinai Medical Center. Space within the new facility was strategically designed to be flexible; it was built for today's leading-edge research equipment, but it will also accommodate the evolution of research platforms as new technologies emerge in the future.

To fulfill our mission, TMII combines state-of-the-art facilities with outstanding faculty, technical staff scientists, and administrative support staff.

The Translational and Molecular Imaging Institute serves as a research catalyst for a new generation of translational and molecular imaging methodologies. TMII applies and validates imaging modalities, in both preclinical basic science and clinical research settings, to:

- Improve diagnostic accuracy
- Increase the understanding of disease mechanisms
- Measure therapeutic efficacy
- Provide education and training opportunities for students and postdoctoral research and clinical fellows
- Provide a comprehensive in vivo imaging research service to the Mount Sinai and New York area communities

You can read more about TMII Faculty and Team Members here.

TMII Research Laboratories

Fayad Lab (Cardiovascular Imaging)

Dr. Fayad's laboratory is dedicated to the detection and prevention of cardiovascular disease and conducts interdisciplinary and discipline bridging research, from engineering to biology, which includes pre-clinical and clinical investigations. The focus of this lab is to develop and use innovative multimodality cardiovascular imaging including to study, prevent and treat cardiovascular disease, including: Magnetic Resonance imaging (MRI), computed tomography (CT), and positron emission tomography (PET), as well as molecular imaging and nanomedicine. Dr. Fayad's focus at Mount Sinai is on the noninvasive assessment and understanding of atherosclerosis (Nature 2008; 451:953-957; Nat Rev Drug Discov. 2011;10:835-52; Lancet 2012; 378:1547-1559). View the complete list of publications

Current projects include:

- Imaging Acquisition and Analysis Methods - Development of novel multimodality cardiovascular imaging and analysis techniques using MRI, PET/MR and CT (NIH/NHLBI R01 HL071021)
- Early Detection and Outcomes Prediction - Use of in vivo noninvasive multimodality imaging methods for the early detection of atherosclerosis and other inflammatory diseases in humans and for cardiovascular events and outcomes prediction (NIH/NHLBI R01 LHL078667)
- Molecular Imaging - Development and use of novel multimodality imaging nanoparticulate systems to monitor fundamental cellular/molecular events in living subjects including patients (NIH/NIBIB R01 EB009638)
- Nanomedicine - Development and use of novel targeted drug delivery nanoparticulate systems to improve the imaging and treatment of atherosclerosis (NIH/NHLBI Program of Excellence in Nanotechnology (PEN) Award, Contract #HHSN268201000045C)
- Preclinical and clinical trials and drug development - Use in vivo noninvasive multimodality imaging methods (MR, PET, CT etc.) in preclinical and clinical trials for the development and testing of novel therapies to treat atherothrombosis (Industry funded)

Balchandani Lab (MRI technical development, High Field MRI)

Dr. Balchandani's research is focused on the design of innovative radio frequency (RF) pulses and pulse sequences that harness the power of high-field magnets and exploit new contrast mechanisms in order to enable novel applications of magnetic resonance imaging (MRI). Her lab explores engineering solutions for MR imaging and spectroscopy at high magnetic fields such as 7 Tesla (7T). Beyond higher resolution images that elucidate finer anatomical features, high-field MR offers greater spectral resolution for spectroscopic imaging, new and enhanced contrast mechanisms and improved detection of nuclei other than protons that are essential to cell processes. A main goal of Dr. Balchandani's lab is to develop techniques that exploit the benefits offered by 7T magnets for neuroimaging applications by overcoming the limitations associated with their operation. Dr. Balchandani's additional research interests include creative pulse and pulse sequence designs for nontraditional MR applications such as multinuclear imaging and stem cell tracking.

Mani Lab (Cardiovascular Imaging)
As a faculty member at TMII and Director of the Cardiovascular Imaging Clinical trials Units (CICTU), Dr. Mani works to translate novel multi-modality imaging techniques for use in multicenter clinical trials. His main interests are in imaging of cardiovascular diseases, specifically focusing on atherosclerosis, thrombosis and their complications using FDG-PET, CT and MRI. The CICTU is composed of clinicians, image processing and programming experts, image analysts, data managers, IT personnel and research coordinators. CICTU is a modern hybrid between a contract research organization (CRO) and an imaging core lab. They undertake and manage all aspects of clinical trials, ranging from scientific conduct to administrative management, with imaging endpoints led by TMII. CICTU's tasks span from industry or federally sponsored multicenter clinical trials to the support of individual investigators interested in using imaging endpoints for their work. Typical services offered include but are not limited to trial design and consultation, imaging protocol development, site training and qualification, data repository and database management, data quality control and analysis, and publication support.

Mulder Lab (Nanomedicine)
The Nanomedicine Laboratory is part of the Translational and Molecular Imaging Institute (Nano-TMII) at the Icahn School of Medicine. Nano-TMII's mission is to develop and advance nanomedical approaches to allow a better understanding, identification and treatment of the most detrimental pathologies today: cardiovascular disease and cancer. Nano-TMII is directed by Dr. Willem Mulder and is funded by the National Heart Lung and Blood Institute, the National Cancer Institute and NHLBI's Program of Excellence in Nanotechnology.
Publications
PubMed

Tang Lab (Neuroimaging Core and Preclinical Imaging)
Dr. Tang's lab is involved with the research and development of novel imaging strategies for the study of neuro-psychiatric diseases. The work consists of both hardware and software development. The lab develops novel image analysis software approaches to integrate functional and structural connectivity using DTI, DSI and fMRI. The lab has also developed novel technologies (e.g. olfactory meter, real time fMRI) in use for the study of memory, OCD and mood-disorders. The research is performed on both human and preclinical systems.

Taouli Lab (Body Imaging)
The Quantitative Body Imaging Group develops, tests and validates quantitative MR imaging techniques applied to body imaging. Our current research includes the optimization and validation of novel functional MRI techniques applied to diffuse and focal liver diseases, including diffusion-weighted MRI, dynamic contrast enhanced MRI, MR Elastography, flow quantification, spectroscopy and multi echo Dixon methods. We believe that these imaging modalities will provide non-invasive information for:

- Detection of liver fibrosis and cirrhosis
- Assessment of portal hypertension
- Hepatocellular carcinoma characterization
- Tumor response to novel therapies

These techniques can be transposed to other organs, such as the kidneys, prostate and pancreas.

Xu Lab (Neuroimaging)
Dr. Xu's lab develops quantitative and functional magnetic resonance (MR) techniques and applies them to study neurometablism and neuropathophysiology. Our current projects are to develop: (1) fast MR imaging and spectroscopy methods for quantitative neuroimaging, (2) reliable MR techniques for functional assessment of spinal cord, and (3) a "Connectomic" imaging approach for tissue recovery, repair and clinical outcomes in multiple sclerosis.

Imaging Core

The Translational and Molecular Imaging Institute (TMII) is responsible for providing support for all in vivo imaging research at The Mount Sinai Medical Center. TMII Imaging Core is the backbone of the Translational and Molecular Imaging Institute and is responsible for coordinating, supporting and executing imaging research at Mount Sinai including, neuroimaging, cardiovascular imaging, cancer imaging, nanomedicine (molecular imaging and drug delivery), and image processing in the preclinical and clinical settings.

The Core is fully staffed to support all the image acquisition, image analysis, scheduling, and performance of the proposed experiments. The Core has an extensive and expanding inventory of preclinical (large and small) and clinical research imaging facilities and equipment, including ancillary support which encompasses exam rooms, imaging processing workstations, laboratories (wet lab space, cell and chemistry preparation and a radionuclear lab), animal preparation and holding rooms, and testing rooms. The Core's resources are fully supported by user fees drawn from research grants, instrumentation grants, industry contracts, and agreements. Our core facilities are available for use to all qualified investigators from academic, medical, government, and industry laboratories. We do not offer a clinical imaging service.

Our current instrumentation and services include:

- Human Imaging (3T MRI, 7T MRI, 3T MR/PET, CT)
- Human Mock MRI
- Human and Animal Imaging Peripherals
- Human and Animal Anesthesia and Monitoring
- Large Animal Imaging (3T MRI, 7T MRI, 3T MR/PET)
- Small Animal MRI (9.4T, 7T)
- Small Animal US
- Small Animal Optical Imaging (Fluorescence, Bioluminescence and Near-infrared)
- Dissecting Microscope with Digital Camera
- Staff-Assisted Imaging (imaging technologists, nurse, etc.)
- Imaging Processing and Data Analysis
- Scheduling
- Training
- Consultation

Abstracts Selected for Oral Presentation

DREAMM: *In vivo* cell type-specific functional whole-brain circuit mapping of limbic networks in freely-moving animals

Michael Michaelides[1], Sarah Ann Anderson[2], Mala Ananth[3], Panayotis K. Thanos[3, 4], John F. Neumaier[5], Gene-Jack Wang[1, 3], Nora D. Volkow[4], Yasmin L. Hurd[1, 2, 6]

[1]Departments of Psychiatry and [2]Neuroscience, Icahn School of Medicine at Mount Sinai, New York, NY, [3]Biosciences Department, Brookhaven National Laboratory, Upton, NY, [4]Laboratory of Neuroimaging, National Institute on Alcohol Abuse and Alcoholism, Bethesda, MD, [5]Psychiatry and Behavioral Sciences and Pharmacology, University of Washington, Seattle, WA, [6]James J Peters VA Medical Center, Bronx, NY.

Introduction: The mammalian brain is a complex organ with billions of heterogeneous cells whose local and long-range functional connections regulate behavior and physiology. Traditional approaches used for mapping functional brain anatomy do not provide information on long-range, global (i.e. intact whole-brain) circuits. The ability to map the functional connectivity of discrete cell types in the intact mammalian brain during behavior is crucial for advancing our understanding of brain function in normal and disease states.

Methods & Results: We combined designer receptor exclusively activated by designer drug (DREADD) technology and behavioral imaging with micro-positron emission tomography (μPET) and $[^{18}\mathrm{F}]$fluorodeoxyglucose (FDG) to allow, for the first time, whole-brain metabolic mapping of cell-specific functional circuits during the awake, freely-moving state. We term this approach DREADD-assisted metabolic mapping (DREAMM) and document its ability to map whole-brain functional anatomy associated with inhibition of prodynorphin (*Pdyn*)- and of proenkephalin (*Penk*)-expressing medium spiny neurons (MSNs) of the nucleus accumbens shell (NAcSh) implicated in neuropsychiatric disorders. After validating our dynamic imaging methodology (Figure 1), we examined the capacity of DREAMM to provide *in vivo* information regarding the direct anatomical connectivity of *Pdyn*- or *Penk*-expressing MSNs, as well as the time-dependent response of downstream circuits recruited after inhibition of each MSN subtype (Figure 2). Moreover, we evaluated DREAMM during awake FDG uptake in freely-moving rats to assess behaviorally-relevant functional connectivity specific to altering the activity of each MSN (Figure 3). DREAMM revealed discrete behavioral manifestations and concurrent engagement of distinct corticolimbic networks aligned with dysregulation of *Pdyn* and *Penk* NAcSh MSNs.

Conclusion: Our findings illustrate the potential of DREAMM to quantitatively delineate: (i) dynamic changes in discrete whole-brain neuronal circuits *in vivo*, even with one minute resolution in anesthetized animals, and (ii) cell-type specific whole-brain neuronal circuits recruited during the awake, behaving state. Overall, DREAMM fills a technological niche providing unbiased, direct, quantitative and longitudinal information of a well-understood measure of cellular activity (i.e. glucose utilization) to inform on whole-brain functional connectivity. DREAMM can thus be an important reverse-engineering research strategy to dissect *in vivo* specific neuronal networks associated with normal and pathologic behavior.

Clinical Relevance: *Pdyn*- and *Penk-expressing* MSNs synergistically regulate approach and avoidance behaviors and impairments in these neurons are observed in many psychiatric diseases. Delineating discrete yet overlapping neuronal circuits associated with these neurons is of fundamental importance to expand neurobiological insights underlying normal behavior and neuropsychiatric pathology.

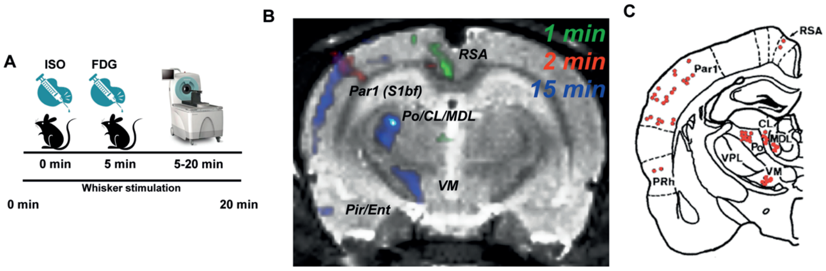

Figure 1. Vibrissae stimulation leads to time-dependent brain activation in barrel field circuitry. (A) µPET imaging protocol. Rats were anesthetized with isoflurane (ISO), placed on the scanner bed and unilateral vibrissae stimulation was initiated. Five minutes later rats were injected intravenously with ~0.6 mCi of FDG and scanning commenced. Stimulation lasted for 15 minutes. (B) time-dependent increases in contralateral FDG uptake in response to unilateral vibrissae stimulation, (C) afferent and efferent connectivity of the vibrissal motor cortex (adapted from Miyashita et al 1994, used with permission). Abbreviations: parietal cortex (Par1), primary somatosensory cortex barrel field (S1bf), agranular retrosplenial cortex (RSA), posterolateral thalamus (Po), centrolateral thalamus (CL), lateral part of mediodorsal thalamus (MDL), lateral part of ventroposterior thalamus (VPL), ventromedial thalamus (VM), piriform cortex (Pir), entorhinal cortex (Ent), perirhinal cortex (PRh).

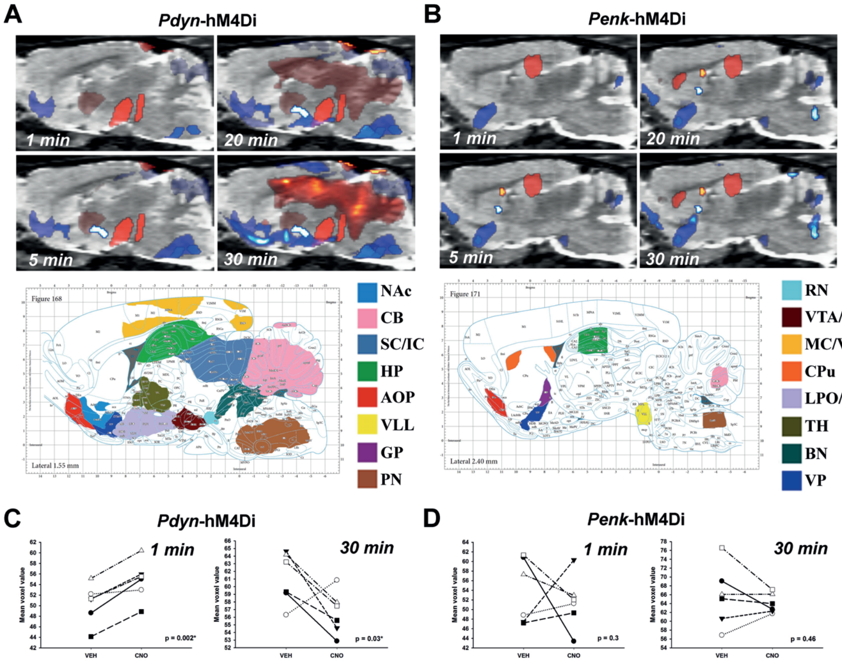

Figure 2. Cell-type-specific, time-dependent control of local and long range signaling is detected using DREADD-assisted metabolic mapping (DREAMM) in anesthetized rats. Time-dependent DREAMM responses after (A) *Pdyn*- and (B) *Penk*-expressing medium spiny neuron (MSN) inhibition (p=0.05; relative increase (red) and decrease (blue) in FDG uptake). Individual subject voxel values in the ventral tegmental area (VTA) showing that *Pdyn*-MSN inhibition significantly increases FDG uptake at 1 minute and decreases FDG uptake at 30 minutes (C), while *Penk*-MSN inhibition does not (D). Abbreviations: nucleus accumbens (NAc), cerebellum (CB), superior colliculus (SC), inferior colliculus (IC), hippocampus (HP), anterior olfactory nucleus (AOP), ventral nucleus of lateral lemniscus (VLL), globus pallidus (GP), pontine nuclei (PN), reticular nuclei (RN), substanita nigra (SN), motor cortex (MC), visual cortex (VC), retrosplenial cortex (RS), caudate putamen (CPu), lateral preoptic area (LPO), lateral hypothalamus (LH), thalamus (TH), brainstem nuclei (BN), ventral pallidum (VP).

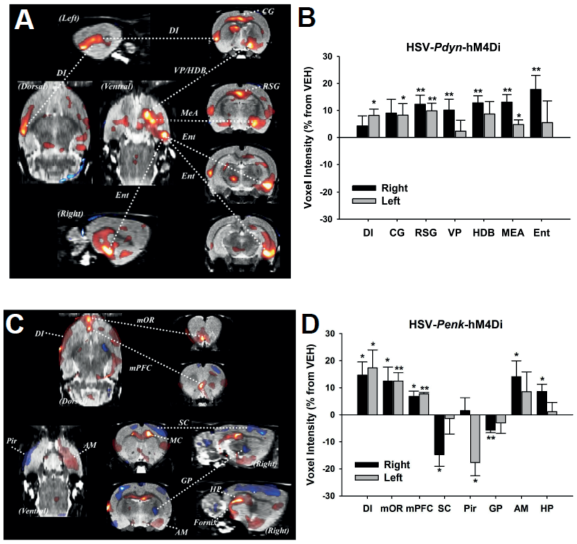

Figure 3. Unilateral inhibition of spatially overlapping *Pdyn- and Penk*-expressing neurons in nucleus accumbens shell of freely moving rats leads to changes in distinct neural circuits. (A) *Pdyn*-MSN inhibition increased FDG uptake in specific corticolimbic regions including the entorhinal cortex (Ent), dysgranular insula (DI), cingulate (CG) and medial amygdala (MEA) as well as ventral pallidum/diagonal band (VP/HDB) as visualized in coronal, sagittal and horizontal planes and (B) as plotted as percent change in signal response *p<0.05, **p<0.01. (C) *Penk*-MSN inhibition led to profound activation of the dysgranular insula (DI), medial orbital prefrontal cortices (mOR and mPFC), hippocampus/fornix (HP) circuit, amygdala (AM), ventral pallidum (VP), and decreased activity of sensorimotor (SC) and piriform cortices (Pir), and globus pallidus as visualized in coronal, sagittal and horizontal planes and (D) as plotted as percent change in signal response *p<0.05, **p<0.01.

Quantitative Susceptibility Mapping of Contrast Agent in a Mouse Prostate Cancer Model

Tian Liu[1], Zhuxian Zhou[2], Zhengrong Lu[2], Yi Wang[3,4]

1 MedImageMetric LL, New York, NY. 2 Biomedical Engineering, Case Western Reserve University, Cleveland, OH.
3 Biomedical Engineering and 4 Radiology, Cornell University, New York, NY.

Introduction: Accurate detection and quantification of contrast agent concentration [CA] not only allows tumor localization in diagnostic cancer imaging, but may also indicate tumor malignancy. MRI has great potential for non-invasive [CA] quantification, but current T1/T2/T2* based methods for estimating [CA] may subject to many error sources including the relaxation quenching caused by limited neighboring free water, the flip angle profile, the ill-conditioning of the signal equation, and other effects in the pulse sequence. These problems are avoidable by analyzing MR signal phase, such as in Quantitative Susceptibility Mapping, which is sensitive to paramagnetic contrast agents such as Gadolinium (Gd) and superparamagnetic iron oxide (SPIO) nanoparticles. Here, we report using QSM to quantify [Gd] in a mouse prostate cancer model.

Methods & Results: PC-3 human prostate adenocarcinoma cells were inoculated to the left dorsal flank of 4-5 weeks old NIH athymic male nude mice [1]. After tumors have grown to 3-5mm in diameter in three weeks, mice were imaged at a Bruker Biospec 7T scanner. Peptide-Targeted MRI contrast agents were administrered in the tail vein at a dose of 0.1mmol Gd/kg for one mouse, and 0.5mmol Gd/kg for the other 2 mice. The mice were scanned before and immediately after injection using a T1 weighted (T1w) gradient echo sequence with a relatively low spatial resolution (150um isotrpoic), and each scan was 20minutes. After the second scan, the mice were euthanized through isoflurance injection, and scanned again at a high resolution (100um isotropic). Other scanning parameters are: TE/TR=15/24ms; flip angle=15; bandwidth=32 kHz; FOV=32x18x20mm^3; number of averaging = 4. The low resolution images were used to confirm existence of CA in the tumor. The high resolution images were used for deriving QSM using a morphology enabled dipole inversion (MEDI) method [2-4]. Susceptibility values in each pixel was converted to [Gd] by dividing 326ppm/M, and the total amount of Gd was calculated by spatially integrating the concentration over the entire tumor. As a validation of the QSM quantification, the tumor was excised and digested with nitric acid. The total amount of Gd was determined using Inductively Coupled Plasma Mass Spectrometer (ICP-MS).

Representative T1w images are shown in Figs. 1a&b, showing Gd enhancement in the tumor. The corresponding high resolution T1w and QSM are shown in Figs. c&d. It is observed that the tumor has an enhanced rim suggesting angiogenesis in the periphery, and heterogeneous enhancement in the middle. The [Gd] and total amount of Gd for these 3 mice are summarized in Table 2. QSM and ICP showed reasonable agreement.

Conclusion: In this study, we demonstrated the feasibility of using QSM to quantify the Gd distribution in a mouse prostate cancer model. QSM is able to quantify high concentration of Gd where traditional T1/T2/T2* based method suffer from relaxation quenching effect.

Clinical Relevance: Prostate tumor has a high prevalence in men over 50 years old, and requires proper treatment before it metastasize and becomes untreatable. Quantification of Gd using MRI renders early and accurate detection and diagnosis of prostate cancer, which is critical for the treatment and management.

Figures and tables:

Figure. 1.
T1w image of the tumor (dash arrow in a) before and immediately after Gd injection is shown in a and b, respectively. In the high resolution T1w image (c), the tumor demonstrated a periphery enhancement (thin arrow in c) with a hyperintense core, which is also seen in the high resolution QSM image (thick arrow in d).

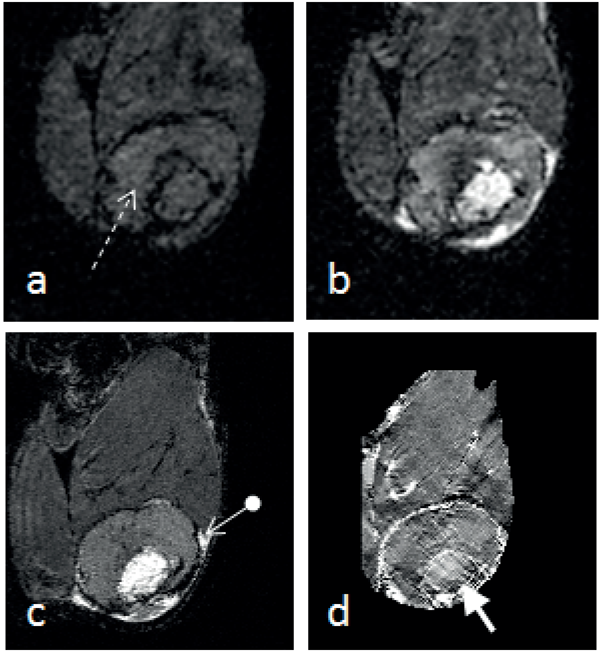

Table 1. Estimated gadolinium

Mouse index	1	2	3
Injected dose (mmol/kg)	0.1	0.5	0.5
QSM			
Tumor volume (uL)	69.6	198.3	143.5
Total Gd (umol)	**0.0056**	**0.024**	**0.0172**
Average [Gd] (mM)	0.081	0.12	0.12
ICP-MS			
Tumor weight (mg)	71.7	185.4	120
Total Gd (umol)	**0.0049**	**0.0135**	**0.0202**

A Multi-Functional Nanoplatform for Imaging, Radiotherapy, and the Prediction of Therapeutic Response

Ajlan Al Zaki*[1], Casey McQuade[1]*, Rob Hickey[2], Daniel Joh[3], So-Jung Park[2], Gary Kao[3], Jay Dorsey[3], and Andrew Tsourkas[1]

Department of Bioengineering, Department of Chemistry, Department of Radiation Oncology, University of Pennsylvania

Introduction: Current radiation-based therapies are often limited by the maximum allowable dose tolerated by adjacent healthy tissues. Challenges associated with accurate tumor margin delineation often exacerbate efforts to maximize tumor dosage while minimizing the damaging off-target effects of radiation. To help overcome this shortcoming, Gold and Superparamagentic iron oxide (SPIO)-loaded polymeric Micelles (GSMs) were designed to help demarcate tumor boundaries by magnetic resonance imaging (MRI) and enhance radiosensitization via a gold-mediated photoelectric effect.

Methods & Results: Micelles were prepared using microemulsions. Briefly, 1.9 nm dodecanethiol stabilized AuNPs and oleic acid stabilized iron oxide nanoparticles were dissolved in toluene and mixed with poly(ethylene glycol)-block-poly(epsilon caprolactone) methyl ether. This solution was added to millipore water and subsequently sonicated. The emulsion was left uncapped overnight in a dessicator to allow phase separation and evaporation of toluene. The particles were then pelleted and purified via centrifugation followed by 0.2 micron filtration. All concentrations were determined using ICP-OES and size measurements were carried out using dynamic light scattering and electron microscopy. X-ray CT and MR phantom images were acquired using various concentration of GSM dispersed in PBS. In vitro X-ray irradiation experiments were carried out on HT 1080 cells (human fibrosarcomma cell line) with a GPM gold concentration of 100 ug/ml using the Small Animal Research Radiation Platform (SARRP) at 150kVp, 15 mA. Athymic nude mice were used for the evaluation of GSMs pharmacokinetics, imaging and irradiation experiments. Magnetic resonance imaging was performed before injection and 24 hr post-injection, prior to radiation therapy.
Cells incubated with GSMs show a higher frequency of gh2ax foci 12 hrs after the administration of orthovoltage radiation. Further, intravenous injection of GSMs into fibrosarcoma-bearing mice led to selective accumulation of GSMs in the tumors, enabling non-invasive MRI imaging and tumor delineation followed by 150 kVp X-ray therapy. Ninety day survival of GSM-injected, irradiated mice was 71% versus 29% with x-rays alone, and 0% with GSM alone. Finally, the rate of volume decrease of irradiated tumors correlates linearly with the amount of GSM-generated contrast visualized on MRI scans.

Conclusion: The presence of gold nanoparticles within the hydrophobic core results in tumor cell sensitization to ionizing radiation. Further, the incorporation of SPIO nanoparticles into the micelles enables ultrasensitive MRI contrast and, notably, the prediction of the rate of tumor volume decrease following GSM-sensitized external-beam radiation therapy based upon the amount of tumor contrast achieved

Clinical Relevance: The combined therapeutic, diagnostic, and prognostic characteristics of this dual-metal nanoparticle micelle system could enable a more personalized approach to a patient’s cancer therapy, based upon their tumoral uptake of GSMs.

Figures and tables:

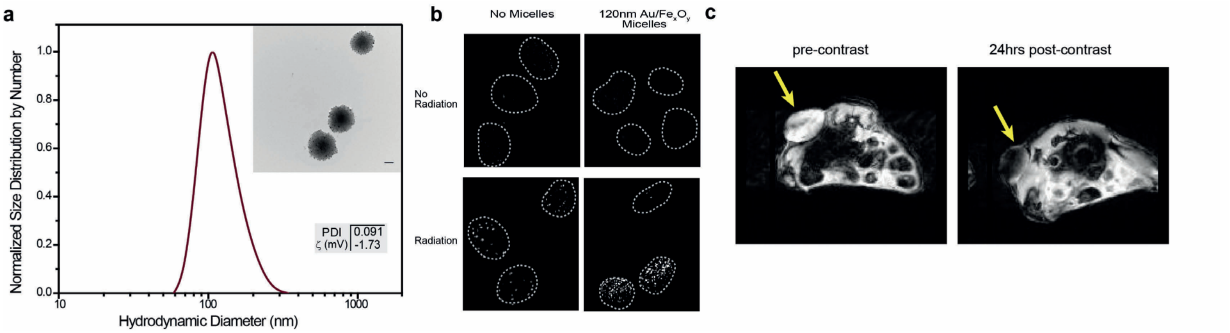

Figure

Figure 1. Gold and SPIO-loaded polymeric micelles. (a) GSMs have a peak size of 120nm and low polydispersity, as determined by dynamic light scattering. Inset. TEM of GSMs (AuNPs and SPIO are visible). **(b)** In vitro irradiation studies. Immunofluorescent imaging of double strand breaks (i.e. gh2ax foci) in HT1080 cells that have been incubated with and without GSMs in the absence (top row) or presence (bottom row) of radiation (4 Gy). **(c)** In vivo MR imaging. Representative T2* weighted MR images in the axial plane prior to injection (pre-contrast) and 24 hours after injection (post-contrast) of GSMs (n=3). Tumor location is indicated by yellow arrows.

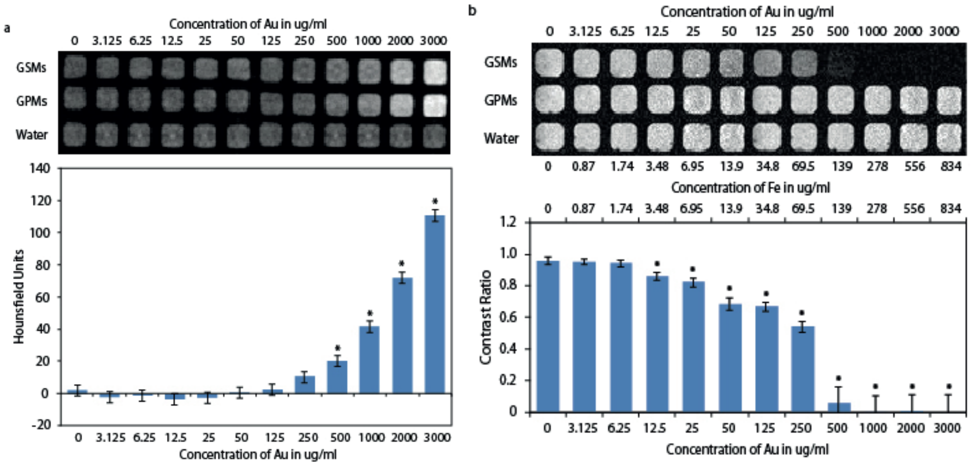

Figure 2. a. (Top image) CT image of GSMs (top row), GPMs (middle row) and a water control (bottom row) as a function of gold and iron concentrations. (Bottom image). Hounsfield units of GSMs as a function of gold and iron concentrations. **b.** (Top image) T_2 weighted image of GSMs (top row), gold-loaded polymeric micelles (GPMs; middle row) and a water control (bottom row) as a function of gold and iron concentrations. (Bottom image) Contrast ratio of GSMs as a function of gold and iron concentrations.

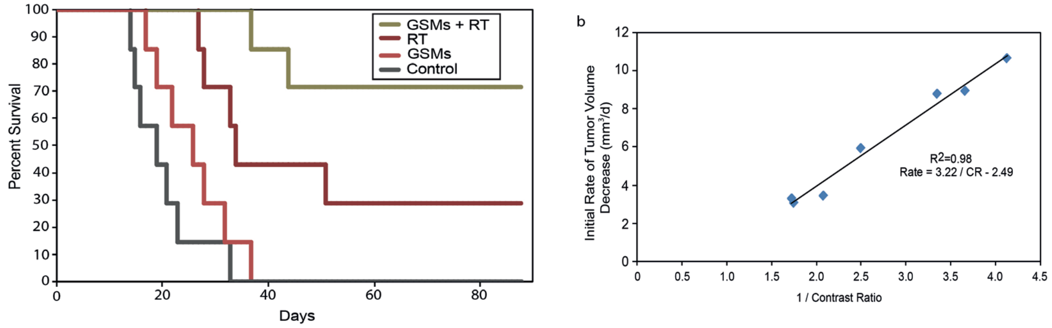

Figure 3. a. Survival curves of tumor bearing mice that received radiation therapy (RT) (6 Gy), GSMs + RT, GSMs only, and no treatment (control). Survival of GPMs + RT > 70%, survival of RT alone < 30%. n=7 for each cohort. **b.** Plot of rate of tumor decrease vs 1/Contrast Ratio. There is a linear correlation between the amount of contrast (pre-GSM relative signal intensity / post-GSM relative signal intensity) seen in MR tumor imaging and the initial rate of tumor decrease after the administration of radiation therapy.

Role of chronic stress on experimental atherosclerosis

Chiara Giannarelli[1,2], David T. Rodriguez[1], M. Urooj Zafar[1,2], Artiom Petrov[2], Dan Christoffel[3], Vincent Vialou[3], Hans J. de Haas[2], Giulia Villa[1], Jagat Narula[2], Scott Russo[3], Eric J. Nestler[3], Juan J. Badimon[1,2]

[1]Atherothrombosis Research Unit, [2]Cardiovascular Institute, [3]Neuroscience Department, Friedman Brain Institute, Icahn School of Medicine at Mount Sinai, New York/USA

Introduction: Cardiovascular disease (CVD) and mood disorders remain the leading cause of mortality and hospitalization in industrialized countries. Co-morbidity between mood disorders and severity of cardiovascular disease is well known; however, the existence of a causal link is unclear. In this abstract we aimed to investigate if mood disorders raise the risk of cardiovascular events by increasing atherosclerotic plaque instability and platelet aggregation in a mouse experimental model of atherosclerosis.

Methods: ApoE−/− mice (n=28) were exposed to chronic social defeat stress while on Western diet for 6 months. ApoE−/− (n=8) not exposed to chronic social defeat served as controls (C). Defeated animals were categorized as either susceptible (S, n=13; depression/anxiety) or resilient (R, n=7; anxiety) phenotypes based on social interaction test. Platelet reactivity to Serotonin:ADP (5-HT:ADP;10μM:6.5μM) or Serotonin:epinephrine (5HT:EPI;10μM: 5μM) was tested acutely after social defeat and at 6 months, using Multiplate Analyzer . Micro-SPECT Annexin A^5 served to image plaque's apoptosis. Uptake of ^{99m}Tc-Annexin A^5 in plaques was quantified by γ-scintillation counting. Aortas and aortic roots were harvested and stained for MOMA-2 (Macrophages, Mac), α-actin (vascular smooth muscle cells, VSMCs), TUNEL and active caspase-3.

Results: Figure 1 summarizes the results from our study. Increased macrophage infiltration was observed in resilient (R) vs. susceptible (S) and Control (C) groups. A trend toward increased macrophage density was observed in S vs. C (Panel A). Vascular smooth muscle cell (VSMC) density was similar in the atherosclerotic lesions of both S and R but significantly lower vs. C (Panel B). VSMC-to-macrophage ratio was significantly lower in S and R vs. C (Panel C). Panel D shows representative images of lesions stained for MOMA-2 (left) and α-actin (right) from R, S and C mice. Maximum uptake of Annexin A5 was significantly lower in S vs. C (Panel E). Resilient mice showed a trend (P=0.057) towards increased uptake of Annexin A5 vs. S. Panel F shows representative SPECT images of R, S and C mice confirming higher apoptosis in R vs C mice. Active Caspase-3 staining confirmed increased apoptosis in R and C vs. S (Panel G). Panel H shows representative active caspase-3 staining of lesions from R, S, and C. Increased platelet reactivity to 5HT:EPI was observed acutely after social defeat in R vs. S and C (Panel I).

Conclusions: Our data demonstrate increased features of plaque vulnerability and platelet reactivity in resilient vs. susceptible mice in an experimental model of mood disorders and atherosclerosis. These data suggest a major role of stress on the progression and thrombotic complications of atherosclerosis.

Figures and tables

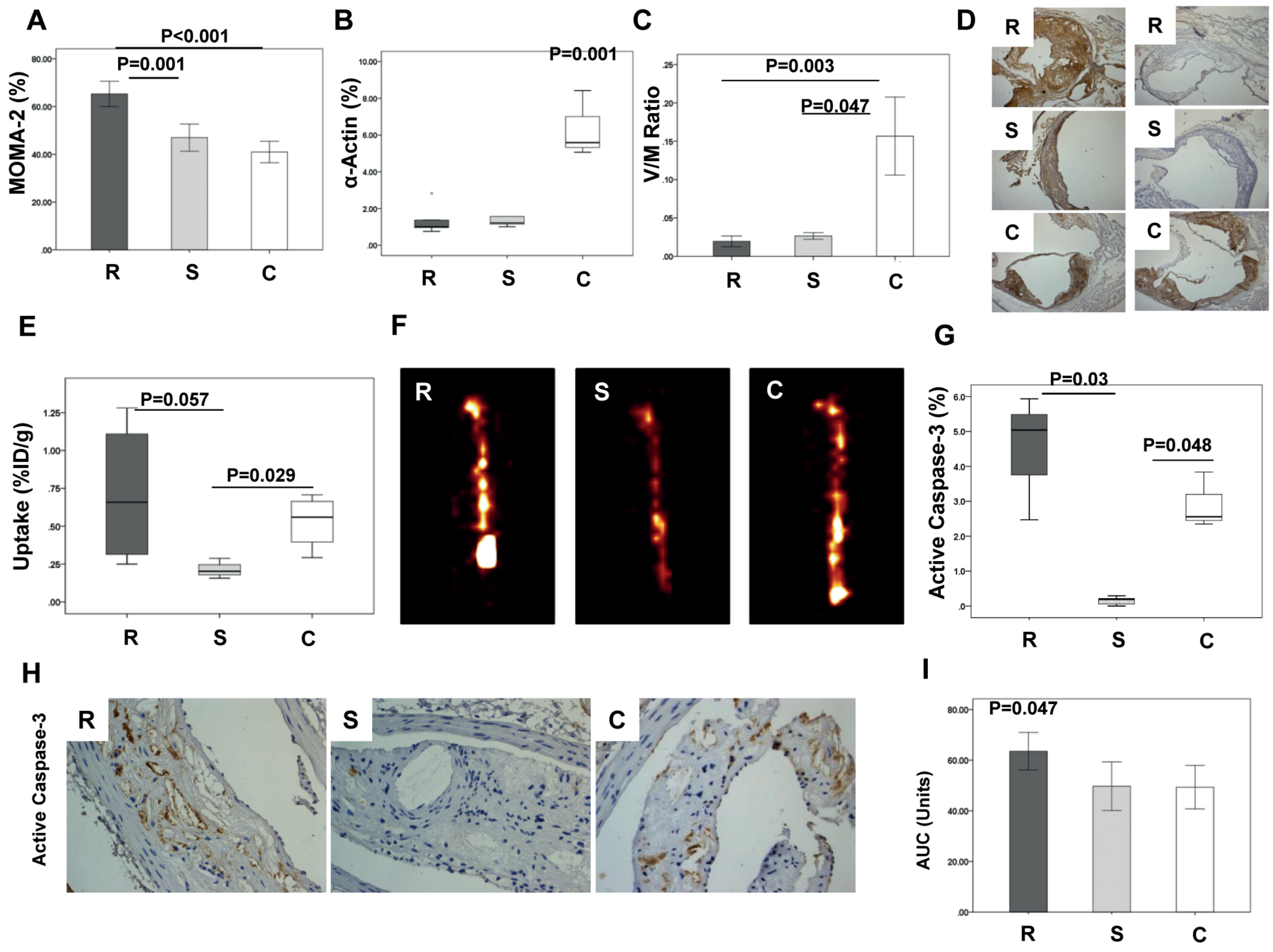

Figure 1. Results of the study. Description of the panels can be found in the Results section.

Abstracts, Neuro Imaging Category

The neural correlates of visual-spatial working memory in youth with and without ADHD: An fMRI study of brain activation

A.-C. V. Bédard[1]; J. H. Newcorn[1]; S. M. Clerkin[1]; B. Krone[1]; J. M. Halperin[1,2]; K. P. Schulz[1]
[1]Department of Psychiatry, Icahn School of Medicine at Mount Sinai; [2]Queens College, City University of New York

Introduction

Visual-spatial working memory refers to the ability to temporarily hold and manipulate visual nonverbal information in mind. Deficits in visual-spatial working memory have been linked with Attention-Deficit/Hyperactivity Disorder (ADHD), academic difficulty and long-term problems in both employment and quality-of-life. This study investigated the underlying brain circuits involved in visual-spatial working memory in youth with ADHD as compared to typically-developing children.

Methods & Results

24 children, ages 9 – 15 years, with ADHD, and 21 well-matched typically-developing youth were scanned using a 3.0 T Siemens Allegra scanner while performing a block design N-Back task, adapted from Chang et al. (2004). Participants had to determine if a stimulus was in the center of the screen (control condition) or in the same location as it was 1 (1 back condition) or 2 (2 back condition) trials previously. Individual contrast images were computed for each experimental condition minus the control condition and were entered into group analyses. The ADHD and control groups performed comparably on the task. Both groups activated the intraparietal sulcal area, precuneus, dorsolateral prefrontal cortex (DLPFC) and anterior cingulate cortex (ACC) during the visual-spatial working memory task, with greater activation as the working memory load increased (i.e. 2back > 1back). However, youth with ADHD had greater activation of DLPFC and paracentral lobule during the 2back condition than controls (Figure 1).

Conclusion

Findings showed parametric effects of working memory load on brain activation that mirrored behavioral task performance. Children with ADHD and control youth seem to activate a similar fronto-parietal circuit when performing a visual-spatial working memory task, but to a greater extent in youth with ADHD. Differences in brain activation were not due to differences in behavioral performance.

Clinical Relevance

This differential activation suggests that children with ADHD require greater mental effort to keep objects online comparable to controls, and is in line with findings from animal studies.

Figure 1.

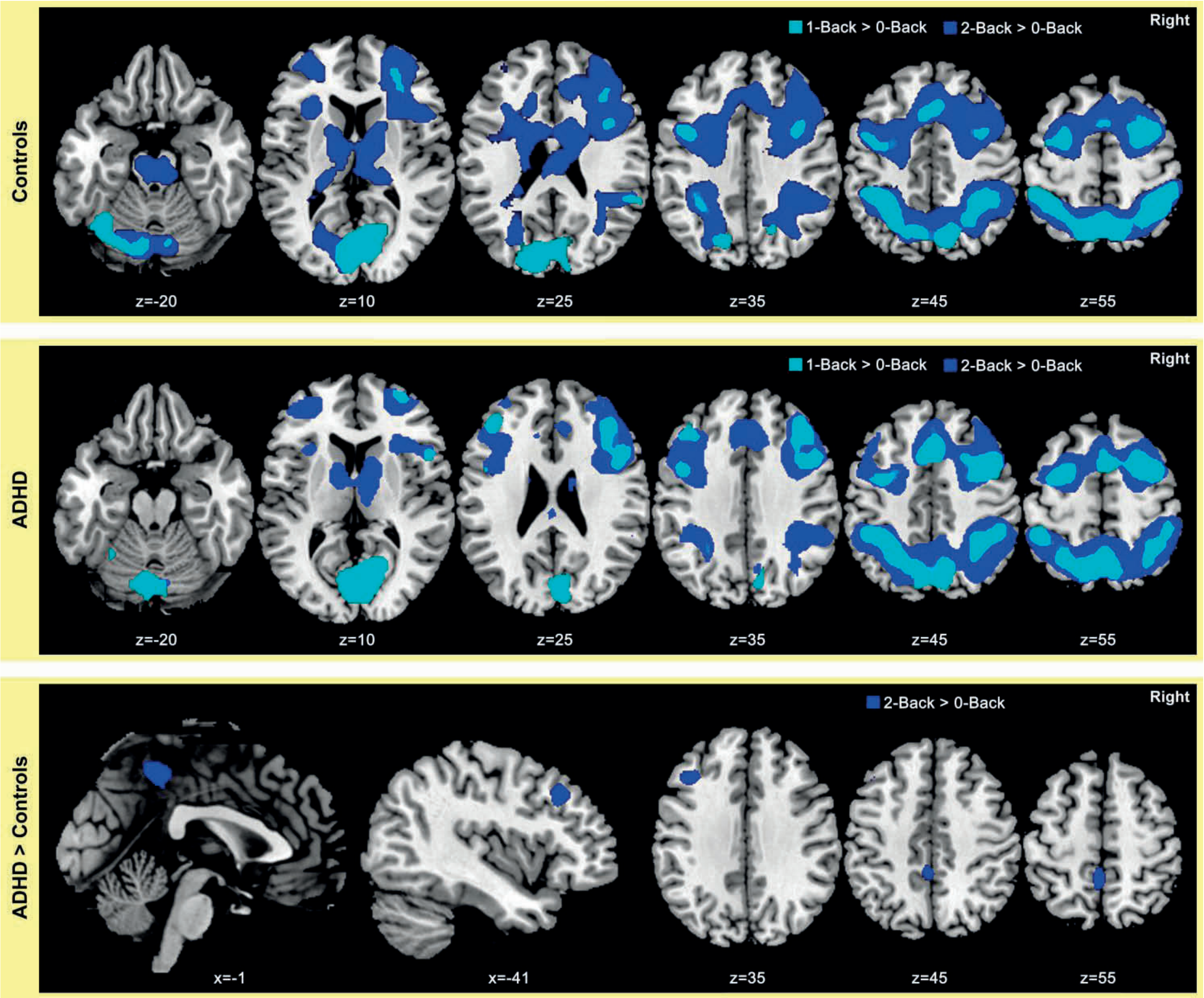
Controls
1-Back > 0-Back
2-Back > 0-Back
Right
z=-20
z=10
z=25
z=35
z=45
z=55
ADHD
1-Back > 0-Back
2-Back > 0-Back
Right
z=-20
z=10
z=25
z=35
z=45
z=55
ADHD > Controls
2-Back > 0-Back
Right
x=-1
x=-41
z=35
z=45
z=55

Diffusional Kurtosis Imaging study of experimental models of demyelination and remyelination

César A. Berríos-Otero[1], Lazar Fleysher[2], Els Fieremans[4], Jingya Zhang[1], , Gareth John[1], and Matilde Inglese[1,2,3]
[1]Department of Neurology, [2]Radiology and [3]Neuroscience, Mt. Sinai School of Medicine, New York, NY.
[4]Center for Biomedical Imaging, Department of Radiology, NYU School of Medicine, New York, NY.

Introduction

Diffusion tensor imaging (DTI) is very sensitive to microscopic injury in anisotropic tissues such as white matter (WM) but not in gray matter (GM). Diffusion kurtosis imaging (DKI) measures non-Gaussian diffusion properties and provides the quantification of mean kurtosis (MK), a marker of tissue architecture complexity independent from diffusion directionality well suited for GM investigation. A recent diffusion model of WM suitable for DKI analysis allows the quantification of intra- and extra-axonal diffusivities, axonal water fraction (AWF), and tortuosity (α) of the extra-axonal space. These parameters may be more specific to particular pathological processes than standard DTI/DKI-parameters. Our aim was to validate DKI biomarkers of de- and remyelination, and neuroaxonal loss in lysolecithin (LPC) and AdII-1 injected mice.

Methods & Results

Methods: WM and GM lesions were induced by stereotactic injection of 1% LPC into the corpus callosum and AdII-1 into the cortex of 12 week-old female C57BL6 mice. In vivo brain MRI was performed on a 7.0T Bruker scanner at 7 and 14 dpi. DKI data were acquired using a 4-shot DW EPI. Mice were perfused with 4% PFA and brains were processed for cryostat embedding. 20μm-thick sections were immunostained using antibodies for Olig2, CD11b, CC1, NG2, and APP and GFAP. Samples were examined with a Leica Microsystems confocal microscope.

Results: ROI analysis showed a significant decrease in AWF, and α at 7dpi and a decreasing trend in intra-axonal diffusivity Daxon in LPC injected mice (n=3; 0.40±0.03 vs 0.34±0.03;p<0.05; 1.60±0.04 vs 1.39±0.07;p<0.01; 0.38±0.03 vs 0.29±0.03;p=0.18; respectively). No significant differences were observed between controls and LPC injected mice at 14dpi in AWF, α, or Daxon (n=3; 0.37±0.02 vs 0.36±0.01;p=0.34; 1.59±0.04 vs 1.61±0.08;p=0.60; 0.39±0.04 vs 0.37±0.05;p=0.80; respectively). A significant increase was observed in MK at 7dpi and 14dpi in AdII-1 injected mice (n=3; 0.70±0.09 vs 1.10±0.09;p<0.01; 0.70±0.09 vs 1.16±0.14;p<0.01; respectively). Immunohistochemistry showed an increase of markers analyzed in both LPC and AdII-1 injected animals in comparison to controls except for a decrease in NeuN in AdII-1 mice.

Conclusion

The decrease in WM tortuosity at 7dpi and the partial increase at 14dpi can be explained by demyelination and remyelination respectively, whereas the decrease in Daxon can be explained by axonal beading. The increase in GM MK can be explained by persistent cellular infiltration.

Clinical Relevance

Based on the use of an idealized no exchange two compartment diffusion model, estimates obtained of the intra- and extra- axonal diffusivities, the axonal water fraction, and the tortuosity of the extra-axonal space should provide insight of axonal and myelin density, which may be useful in assessing myelin-associated neuropathologies. Furthermore, MK measurements may provide valuable information related to GM pathology. In summary, our study shows the potential of DKI measurements as in vivo surrogate markers for WM demyelination and cortical GM damage.

Singular Behavior of Time-Dependent Diffusion in a Fiber Bundle Geometry Due to Disordered Packing

Lauren M. Burcaw, Els Fieremans, Dmitry S. Novikov

Center for Biomedical Imaging, NYU School of Medicine, 660 First Ave, New York NY 10016

Introduction: We show that the randomness in axonal arrangement inside a fiber bundle crucially affects diffusion in the extra-axonal space transverse to the fiber, with implications for pulse-gradient methods of characterizing white matter fiber integrity. We focus on the time-dependence of the diffusion coefficient, $D(t)$, by diffusion measurements in a phantom for extra-axonal diffusion made of randomly packed parallel aligned impermeable fibers, and Monte-Carlo simulations. We show that $D(t)$ transverse to a fiber bundle has a *logarithmic singularity* at long diffusion times, $D(t) \equiv \langle x^2\rangle/2t \simeq D_\infty + c\ln(t/t_0)\,/\,t,\ \ t \gg t_0$. This singularity is a consequence of *short-range disorder* in the fiber packing. It may significantly affect the interpretation of time-dependent diffusion-based methods of interpreting white matter integrity and axon diameter.

Methods & Results: *MRI Measurements.* Imaging was performed at 15°C on a 7T Siemens clinical MRI scanner using a 28 channel knee coil. DTI was carried out using a STEAM sequence. 25 measurements were performed at $b = 0$ and 500 in 20 directions, each with diffusion times, t, of 38.5 ms to 1028.5 ms. Three slices of resolution 3mm × 3mm × 10mm were used. The fiber bundle was placed parallel to the B_0 field to reduce internal field inhomogeneities. *Results:* The DTI eigenvalues are plotted *vs* t in Fig 1a. Fig 1b shows a plot of $D(t)-D_\infty$ vs t on a log-log scale, along with a fit to $c\ln(t/t_0)/t$ (black dashed line) and a fit to c/t (red solid line), showing clearly that the c/t fit is insufficient to properly describe the data. Fig 1c and d show the same $D(t)$ data plotted with respect to $1/t$ and $\ln(t/t_0)/t$, respectively. In Fig 1c, a slight curve can be seen in the data indicating the logarithmic singularity. Fig 1d shows that the bend is removed when plotted with respect to $\ln(t/t_0)/t$, t_0 = 25ms. Fig 1e and f show Monte Carlo simulation data using a free diffusion coefficient of 2 μm^2/s, and fiber size distribution centered around 17 μm. The restricted diffusion inside axons, giving the $1/t$ contribution, is used[1] to probe internal diameter distribution. However, as we have shown, the t-dependence in the extra-axonal space is more relevant, as $\ln(t)/t$ eventually exceeds $1/t$ in long-t limit. Hence, modeling the disorder in extra-axonal space is essential for interpreting such measurements.

Conclusion: The logarithmic singularity in two-dimensional diffusion has been demonstrated for a first time as a hallmark of disordered packing geometries. This singularity dominates the time-dependence of diffusion across axonal fiber bundles and should be included in any quantification scheme for adequate fiber characterization.

Clinical Relevance: Many papers aiming at quantifying axon diameters utilizemethods that require gradient strengths unobtainable in a typical clinical system. Such strong gradients will suppress the signal from the more quickly diffusing water in the extra-axonal space, causing the intra-axonal water to dominate the total diffusion. However, at clinical gradient strengths, the extra-axonal signal is not suppressed, and the logarithmic singularity present in the extra-axonal component of diffusion will dominate. Indeed, Fig 2 shows the intra- and extra-axonal contributions to the total diffusion $D(t)$using simulated diffusion data with fiber sizes based on those found in sector 6 of a rhesus monkey corpus callosum. Sector 6 was chosen as it contained the highest axonal density of 58%; for other ROIs, the role of extra-axonal water would be even more pronounced. From the figure, one can see that as t increases, the contribution to $D(t)$ (black line) from the extra-axonal diffusion (blue line) will begin to dominate the signal after approximately 5 ms. While the effect is subtle, it has greater consequences with increasing t. Indeed, we see that at a diffusion time of 30 ms, $D_{ext}(t)$ will encompass 70% of $D(t)$. This $D_{ext}(t)$ dominance in $D(t)$ will result in the overestimation of axonal diameters.This bias has been empiricallyobserved yet unexplained in the literature.We show that the disordered axonal packing could explain this bias.

Figures and tables

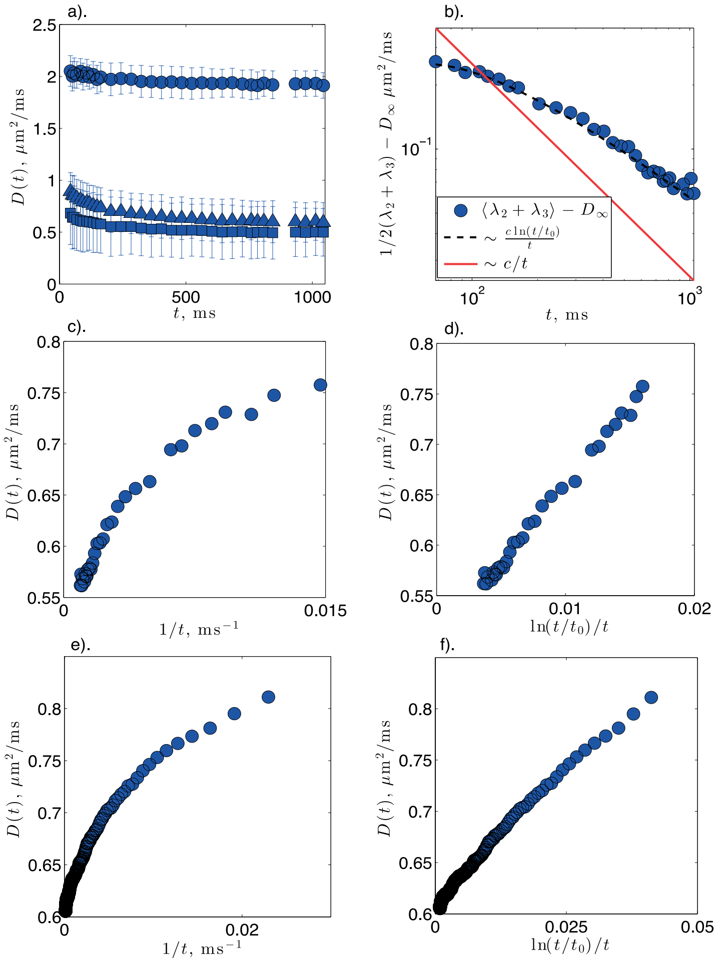

Figure 1:a) Diffusion tensor eigenvalues $\lambda_1 > \lambda_2 > \lambda_3$ measured in the phantom, as function of diffusion time *t*. **b)** We fit the transverse $D(t)=(\lambda_2+\lambda_3)/2$ to Eq (1), and plot the results in log-log scale. The systematic slope change relative to the 1/*t* fit is a hallmark of logarithmic singularity. **c)** This singularity is also manifest in the "bend" in transverse *D*(*t*) vs. 1/*t*. **d)** The logarithmic "bend" straightens up when *D*(*t*) is replotted with respect to $\ln(t/t_0)/t$.**e) and f)** The same as for c and b, but with Monte Carlo simulated data.

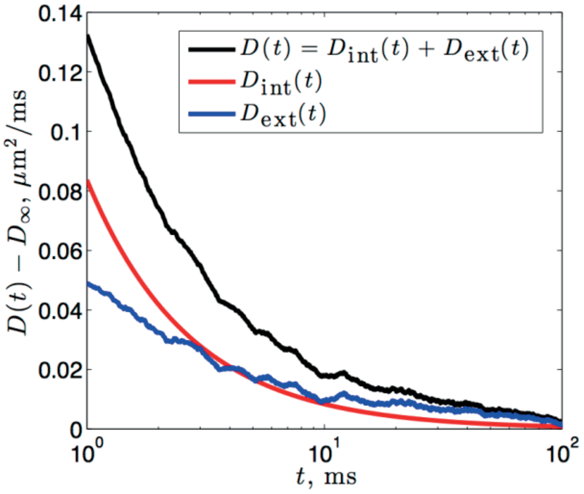

Figure 2: The intra- and extra-axonal components of the long time diffusion coefficient, *D*(*t*),using data from a simulation of diffusion through a ensemble of fiber radii based on sector 6 of the rhesus monkey corpus callosum. The intra-axonal component, $D_{\text{int}}(t)$, is given by the solid red line, and the extra-axonal component, $D_{\text{ext}}(t)$, is given by the solid blue line. Note that at diffusion times, *t*, greater than 5 ms, $D_{\text{ext}}(t)$ will overtake $D_{\text{int}}(t)$ and comprise the majority of the contribution to *D*(*t*), resulting in an overestimation of axon size.

Functional connectivity between insula and amygdala predicts habituation to repeated negative images

Bryan T. Denny1, Jin Fan1,2, Xun Liu3, Stephanie Guerreri1, Sarah Jo Mayson1, Liza Rimsky1, Antonia S. New1,4, Larry J. Siever1,4, Harold W. Koenigsberg1,4

1 Mount Sinai School of Medicine, New York, NY
2 Queens College, City University of New York, New York, NY
3 Institute of Psychology, Chinese Academy of Sciences, Beijing, China
4 James J Peters VA Medical Center, Bronx, NY

Introduction

Behavioral habituation during repeated exposure to aversive stimuli is an adaptive process and represents a key component of many desensitization-based psychotherapies. However, the way in which changes in self-reported emotional experience are related to the neural mechanisms supporting habituation remains unclear. We addressed this question using functional neuroimaging.

Methods & Results

We aimed to probe the mechanisms linking the neural correlates of habituation with self-reported emotional experience in healthy adult participants by repeatedly presenting negative images and recording behavioral and neural responses using functional magnetic resonance imaging (fMRI). We were particularly interested in the role of amygdala and insula activity, given their strong association with bottom-up emotion reactivity in prior work. Results from 25 healthy participants indicated significant habituation behaviorally as well as in amygdala, occipital cortex, and ventral prefrontal cortex (PFC) activity, whereas bilateral posterior insula, dorsolateral PFC, and precuneus showed sensitization. Parametric analyses indicated that posterior insula activation during image presentation predicted greater negative affect ratings for both novel and repeated negative images. Further, repeated negative image presentation was associated with increasing functional connectivity between posterior insula and amygdala, and this increasing connectivity predicted both attenuated insula sensitization and increasing behavioral habituation.

Conclusion

These results indicate that habituation is subserved in part by insula-amygdala connectivity. Given the role of insula and amygdala in emotional reactivity, these results also show that habituation involves a change in the activity of bottom-up affective networks.

Clinical Relevance

Impaired habituation is implicated in many affective disorders, and we have taken an individual differences approach in the present work in understanding the neural mechanisms driving relatively proficient habituators. Further, this work is also serving as a model paradigm in which to study how habituation processes are altered in those diagnosed with various mood and personality disorders (including borderline personality disorder). We are examining these processes in our laboratory in borderline personality disorder patients.

Neurobiological Basis of Response to Lisdexamfetamine (Vyvanse®) in Adults with ADHD

Duhoux S[1], Schulz KP[1], Krone B[1], Bédard AC[1], Pedraza J[1], White SF[2], Blair JR[2], Newcorn JH[1]
[1]Department of Psychiatry, Mount Sinai School of Medicine, New York, NY 10029, [2]National Institute of Mental Health, Bethesda, MD 20892

Introduction

Attention-deficit/hyperactivity disorder (ADHD) is a common and impairing neuropsychiatric disorder which begins in childhood and often persists into adulthood. Several leading investigators have posited that ADHD symptoms are attributable to cognitive and behavioral manifestations of inhibitory control deficits, however, recent evidence also implicates dysfunction in dopaminergic neurotransmission in regions within the motivation-reward related system – which may account for the problems in emotion regulation that are also often present. Stimulant medications, widely prescribed for ADHD, are thought to decrease core symptoms by increasing the level of synaptic dopamine in regions within the fronto-striatal-parietal attention network. However, given recent findings implicating motivation-reward mechanisms to the pathophysiology and symptomatic presentation of ADHD, it is essential to better understand the effects of stimulants on this network. Thus, the objectives of this ongoing event-related fMRI study are to determine the effects of Lisdexamfetamine (LDX), an FDA-approved stimulant medication, on components of the brain motivation-reward system, and to examine the relationship of these effects to clinical improvement over the course of treatment.

Methods & Results

Eleven adults with ADHD (age range: 19-50, 6 males) were treated with LDX and Placebo in a randomized, placebo-controlled, cross-over design. Each participant received active drug for at least 4 weeks via an escalating stepped dose titration (30, 50, 70mg). Subjects were scanned twice, once after 3 – 5 weeks on either Placebo or LDX (with two weeks on best tolerated dose) using a passive-avoidance learning task. In this task, participants were presented with animal line drawings, and had to learn to respond to images associated with a higher chance to win points, and to avoid responding to those associated with a higher chance of losing points. The blood-oxygen-level-dependent (BOLD) signal was modeled using regressors for the images at the time of the decision (chosen vs. refused), and also for the outcome (reward or punishment). Decision-related regressors were weighted by the expected value that the participant had for the image, and outcome-related regressors were weighted by the prediction error, i.e. the difference between the outcome received and the expectation. Preliminary results show that, compared to Placebo, LDX increased modulation of BOLD responses in: 1) striatum and ventromedial prefrontal cortex, when choosing to respond, and 2) insular/inferior frontal cortex, when refusing to respond. We also found that LDX increased the modulation of BOLD responses by prediction error in the caudate, when a reward was received.

Conclusion

These preliminary findings suggest that LDX may act by increasing sensitivity to reward, and therefore, by reinforcing the ability to respond to favorable or rewarding stimuli, and to avoid stimuli viewed as less favorable or rewarding. If confirmed (the study is ongoing; target n = 20), these results would provide support for the hypothesis that stimulant treatment of ADHD can restore balance to dysfunction within motivation-reward related brain circuitry.

Clinical Relevance

This study of the effect of a stimulant drug (Lisdexamfetamine) on reward-related brain circuitry could have significant clinical implications for elucidating the mechanism of action of pharmacological and behavioral treatments for ADHD on this neural network, and in so doing enhance our understanding of the pathophysiology underlying this complex and multi-faceted disorder. Finding optimal ways of targeting the reward system in treatment could ultimately help individuals with ADHD to better represent expected values of choices, and make more “reasonable” decisions.

Figures and tables

Figure 1: Lisdexamfetamine (LDX) effect on the modulation of regional brain activity by expected value, A) in the striatum when objects are chosen, and B) in the insular/inferior frontal cortex when objects are avoided (Note: Figure was created using the initial number of 6 subjects, but data analysis is ongoing, and will be reported on 11 subjects at the meeting).

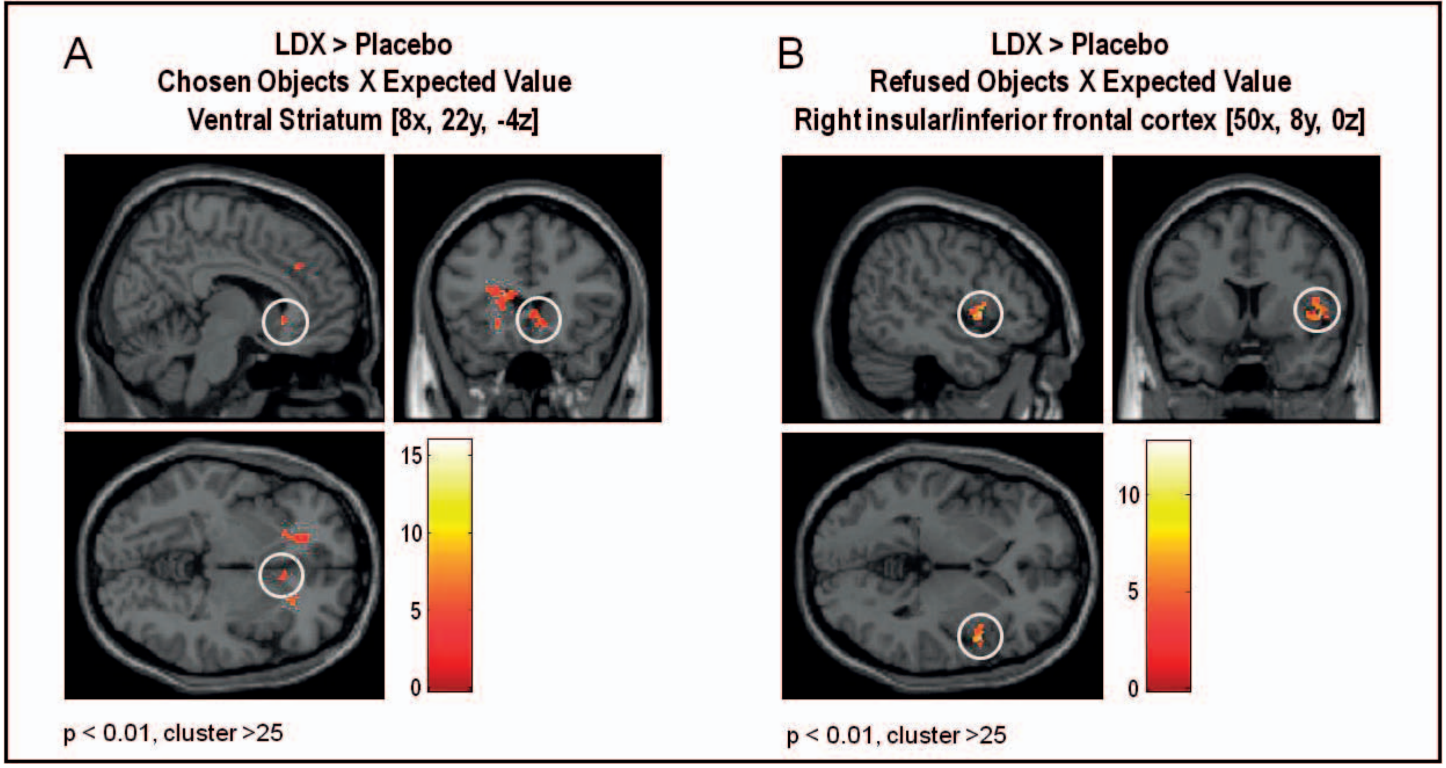

Abnormal associations between spontaneous autonomic activity and brain fluctuations during rest in autism spectrum disorders

Tehila Eilam-Stock[1,2,3], Pengfei Xu[6], Miao Cao[6], Xiaosi Gu[7], Nicholas T. Van Dam[1,3], Evdokia Anagnostou[3,5], Alexander Kolevzon[3,5], Latha Soorya[3,5], Yunsoo Park[3], Michael Siller[8], Yong He[6], Patrick R. Hof[4], Jin Fan[1,2,3,4,5]

[1]Department of Psychology, Queens College, City University of New York, Flushing, NY 11367, USA, [2]The Graduate Center, City University of New York, New York, NY 10016, USA, [3]Department of Psychiatry, [4]Fishberg Department of Neuroscience and Friedman Brain Institute, and [5]Seaver Autism Center for Research and Treatment, Icahn School of Medicine at Mount Sinai, New York, NY 10029, USA, [6]State Key Laboratory of Cognitive Neuroscience and Learning, Beijing Normal University, Beijing, 100875, China, [7]Wellcome Trust Centre for Neuroimaging, University College LondonLondon WC1N 3BG, UK, [8]Department of Psychology, Hunter College, City University of New York, New York, NY 10065, USA

Introduction

Autism Spectrum Disorders (ASD) are characterized by deficits in social interaction and communication, as well as repetitive behaviors and restricted interests. Previous studies have demonstrated that people with ASD have difficulties in processing and interpreting emotions. However, the neural correlates of the socio-emotional deficits, and their pathophysiological basis in ASD, are not well understood. The autonomic nervous system (ANS) has been recognized as having fundamental contributions to emotional and social abilities, by providing physiological signals essential to emotional and subjective states. We, therefore, hypothesized that differences in brain processing of autonomic signals contribute to socio-emotional deficits in ASD.

Methods & Results

Here, we investigated the relationship between non-specific skin conductance responses (SCR), an objective index of autonomic activity, and brain fluctuations during rest in 17 high-functioning adults with ASD and 15 neurotypical controls (NC). Between group differences in SCR-related brain activity, default mode network and whole brain connectivity were examined. Compared to NC, individuals with ASD showed less SCR overall, but no significant difference in skin conductance level was found. The ASD group also showed weaker correlations between skin conductance responses and frontal brain regions, including the anterior cingulate and anterior insular cortices. Additionally, weaker default mode network connectivity was found in ASD relative to NC. Finally, while SCR significantly contributed to default network connectivity in the NC group, no such contributions were found in ASD.

Conclusion

Our data provides evidence for abnormal associations between spontaneous SCR and brain activity and connectivity during rest in ASD. The observed autonomic abnormalities may contribute to the socio-emotional deficits in ASD because ANS signals are essential in emotional processing.

Clinical Relevance

Autonomic measures are relatively easy and inexpensive to obtain, even at a very young age. Detecting autonomic abnormalities may aid in an early diagnosis of ASD, a process that could be critical to the effectiveness of existing behavioral treatments. In addition, treatments targeting autonomic abnormalities may reduce autistic symptoms as well. More research is needed, however, to determine the benefits of such treatments for ASD.

Figures and Table

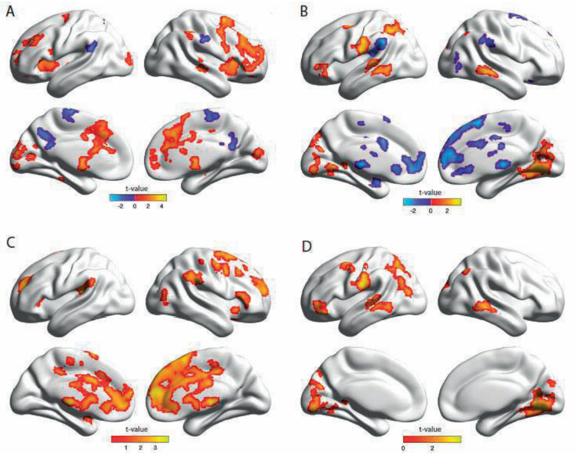

Figure 1. Positive and negative correlations between non-specific skin conductance response (SCR) and brain fluctuations during rest in (**A**) neurotypical controls (NC), and (**B**) adults with autism spectrum disorders (ASD). Red indicates voxels with positive correlations, while blue indicates voxels with negative correlations. (**C**) Stronger correlations in NC compared to ASD (NC > ASD), and (**D**) Stronger correlations in ASD compared to NC (ASD > NC).

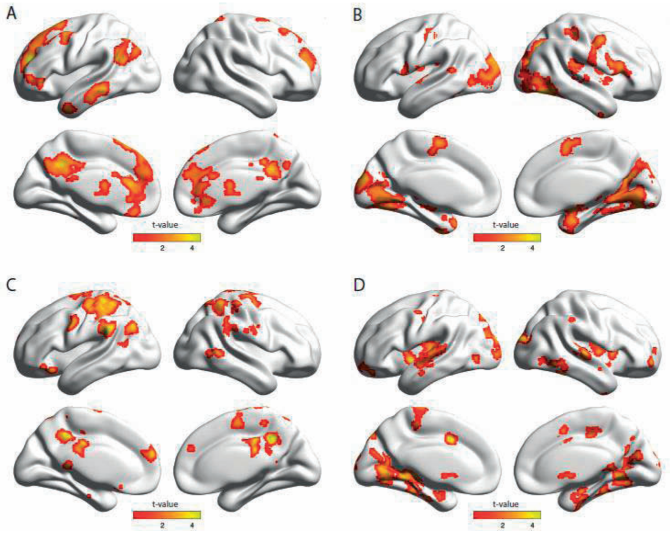

Figure 2. Functional connectivity of the PCC, and an interaction between group (NC vs. ASD) and functional connectivity condition (before vs. after regressing out SCR signal) on PCC connectivity. (**A**) Stronger connectivity in NC compared to ASD (NC > ASD). (**B**) Stronger connectivity in ASD, compared to NC (ASD > NC). (**C**) Stronger effects of SCR on PCC connectivity in NC compared to ASD [NC(with-without SCR) > ASD(with-without SCR)]. (**D**) Stronger effects of SCR on PCC connectivity in ASD compared to NC [ASD(with-without SCR) > NC(with-without SCR)].

Intracellular sodium concentration and cell volume fraction in multiple sclerosis

Lazar Fleysher[1], Roxana Teodorescu[2], Laura Jonkman[2], Matilde Inglese[1,2,3]

[1]Department of Radiology, [2]Neurology and [3]Neuroscience, Mount Sinai School of Medicine, New York, NY, USA.

Introduction: Inflammation, demyelination and axonal degeneration occur within the white matter in the brain in Multiple Sclerosis (MS). While action potential propagation cannot be supported by demyelinated axons efficiently, the expression of Na channels along demyelinated axon regions can lead to restoration of the conduction even in the absence of remyelination. Unfortunately, sodium influx through persistently activated Na channels may lead to an accumulation of intra-axonal sodium, promote reversal of the sodium/calcium exchanger and may lead to a lethal overload in intra-axonal calcium. Therefore, sodium MRI may provide an indicator of cellular and metabolic integrity and ion homeostasis in patients with MS.

Methods & Results: Previous Na-MRI studies in MS patients reported an increase (compared to healthy controls) of brain tissue sodium concentration which represents a weighted average of the extracellular and intracellular sodium content. In this study, we use single-quantum and triple-quantum filtered Na-MRI at 7T to quantify intracellular sodium concentration (ISC) and intracellular sodium volume fraction (ISVF) in 26 MS patients (16F; 44.81±12.5 yrs) and in 26 age and gender matched healthy controls (15F; 44.23±14.7yrs).

Conclusion: Our preliminary results show an increase in ISC and decrease in ISVF in MS patients compared to healthy controls. These results are in agreement with the hypothesis of accumulation of intracellular sodium and tissue damage in MS.

Clinical Relevance: The developed technique allows non-invasive quantitative mapping of the intracellular sodium molar fraction (ISMF), ISC and ISVF in-vivo opening many possibilities for structural functional and metabolic studies of healthy and diseased brain, to monitor disease progression and response to current and experimental treatments.

Figures and tables

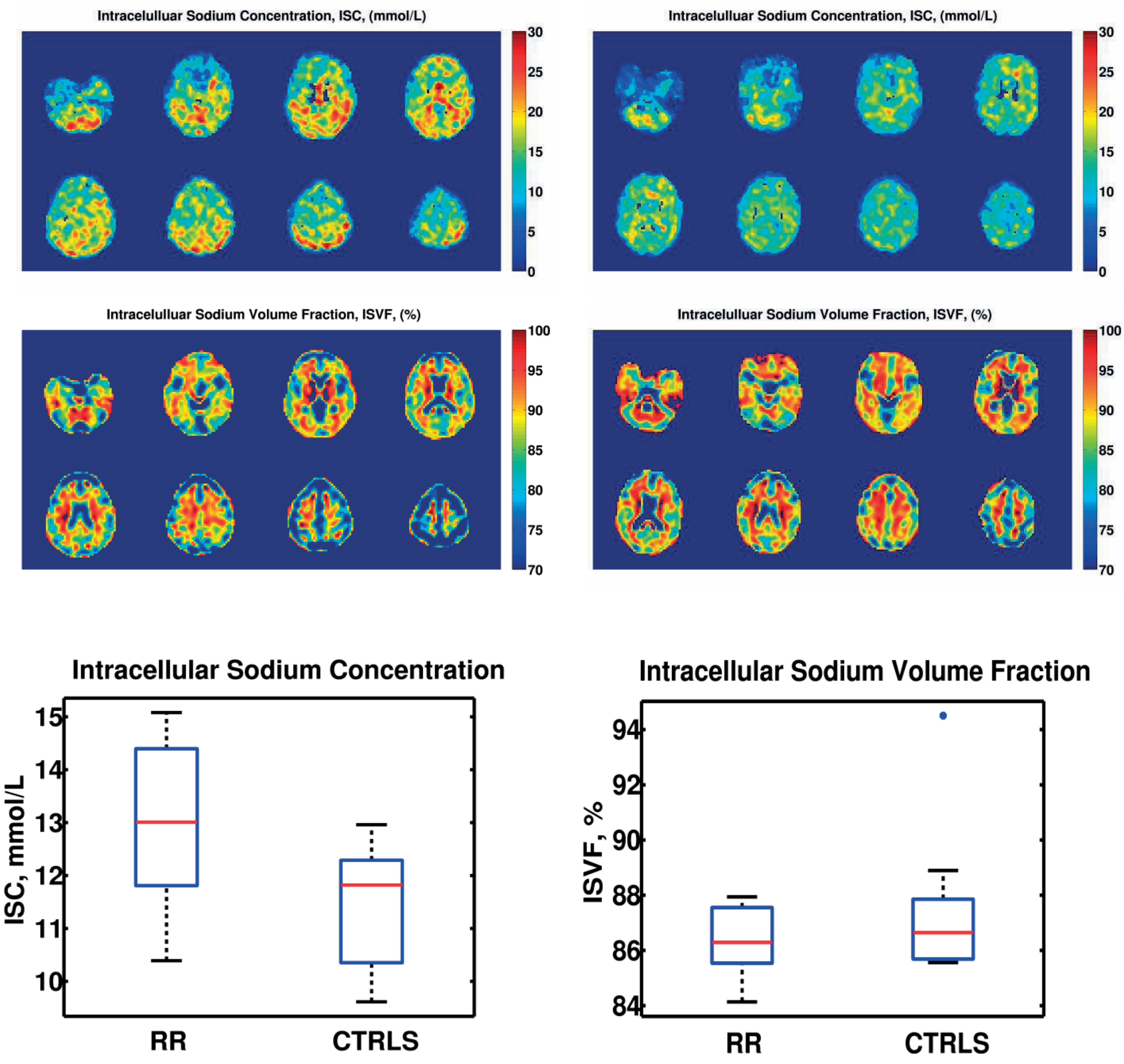

ISC and ISVF maps derived from MRI measurements in a 42 year-old RR-MS patient (top left) and healthy 40-year-old volunteer (top right). Bottom box-plots show group comparison results.

Serial proton MR spectroscopy of gray and white matter in relapsing-remitting multiple sclerosis

Ivan I. Kirov[1], Assaf Tal[1], James Babb[1], Joseph Herbert[2], Oded Gonen[1]

[1]Radiology, New York University, New York, NY, USA, [2]Neurology, New York University, New York, NY, USA

Introduction: In multiple sclerosis (MS), conventional MRI is sensitive to gray and white matter (GM/WM) atrophy and can distinguish active from chronic lesions, but lacks specificity to gliosis, inflammation, demyelination, and neuronal dysfunction. These can be examined with proton magnetic resonance spectroscopy (^{1}H-MRS) quantification of *N*-acetylaspartate (NAA) for neuronal health, creatine (Cr) for glial cell density, choline (Cho) for membrane turnover, and *myo*-inositol (*m*I) for astrocyte status. Although conclusions on disease course are drawn from cross-sectional ^{1}H-MRS studies, only follow-up allows direct observation of disease progress. As a result, there is a reiterated need for longitudinal ^{1}H-MRS, in particular of diffuse pathology in normal-appearing tissue. Our goal was to characterize the diffuse component of early relapsing-remitting (RR) MS with respect to GM and WM metabolism and follow its evolution over 3 years.

Methods: 29 patients (20 women) with clinically definite RR MS for less than 6 years, were recruited prospectively to be scanned semi-annually for 3 years (7 scans each). 10 age- and gender-matched (8 women) healthy volunteers were to be scanned annually (4 scans each). *Post-hoc* exclusion criterion was <5 scans for patients and <4 for controls.
Measurements were done at 3 T. MP-RAGE images were acquired for ^{1}H-MRS volume-of-interest (VOI) guidance and for tissue segmentation. Axial T_2-weighted FLAIR images were acquired for lesion volumetry. The $10\times8\times4.5=360$ cm^3 ^{1}H-MRS VOI (TE/TR=35/1800 ms, 6 slices, 480 voxels, 0.75 cm^3 each) was image-guided over the corpus callosum, as shown in Fig. 1A-B. At two averages, the ^{1}H-MRS took 34 minutes and the entire protocol less than an hour.
The cerebro-spinal fluid (CSF), GM and WM masks were co-registered with the ^{1}H-MRS grid using in-house software. The VOI fractions: GM_f, WM_f, CSF_f were defined as the respective mask volume in all 480 voxels divided by the 360 cm^3 VOI volume. Absolute metabolite amounts were obtained using phantom replacement with correction for T_1 and T_2 relaxation time differences between *in vivo* and *in vitro*. Global GM and WM concentrations were calculated using linear regression. Two-way analysis of variance was used to compare patients to controls in cross-sectional comparisons and random coefficients regression was used to model longitudinal changes. Linear regression was used to test for correlations between changes in metabolites and in CSF_f, GM_f, WM_f, lesion volume, Expanded Disability Status Scale (EDSS) scores and relapses.

Results: 18 patients (13 women) and all controls met the enrollment criteria.
Cross-sectional: The average (over all time points) patients' WM Cr, Cho and *m*I concentrations were higher than the controls' (all $p\leq0.01$). Patients' values were higher at all time points, by a range of 8-16% for Cr, 4-13% for Cho, and 7-17% for *m*I. The patients' WM NAA was lower with a trend on average (p=0.07), but statistically lower at 4/7 time points (Fig. 2, right panel). In GM, there were no differences in the average concentrations over all time points, but there were differences at single time points in three metabolites (Fig. 2, left panel). The patients' average CSF_f was higher than controls'. Patients' VOI T_2 lesion load was 2.1±6.1 cm^3 (median±standard deviation).
Longitudinal: There were significant intra-cohort rates of change only for patients: (*i*) increasing WM Cr, Cho and NAA, decreasing GM Cho and *m*I (all $p\leq0.05$); and (*ii*) increasing CSF_f and lesion volume and decreasing WM_f (all $p\leq0.01$). There were no significantly different inter-cohort (patients' *versus* controls') rates of change, but there was a trend for different CSF_f rates (p=0.06). Finally, the rates of change in GM or WM metabolite levels did not correlate with the rates of change of CSF_f, GM_f, WM_f, lesion volume, EDSS or relapses, with no trends observed.

Conclusion: To our knowledge, the data here represents the most frequent ^{1}H-MRS MS follow-up for the longest duration. In contrast to previous serial ^{1}H-MRS, this study: (*i*) assessed metabolism of a large brain volume; (*ii*) accounted for partial volume effects; and (*iii*) investigated diffuse involvement. We found that WM glial abnormalities were larger in magnitude than the axonal and increased over time independently of conventional clinical or imaging metrics and despite treatment. In contrast, the axonal abnormalities showed partial recovery, suggesting that patients' lower WM NAA levels represented a dysfunction, which may abate with treatment. Absence of widespread diffuse changes in GM suggests that injury there is minimal, focal, or heterogeneous between cortex and deep GM nuclei.

Clinical Relevance: In treated patients with early RR MS, the progressing ^{1}H-MRS-detected abnormalities were glia-related and in the white matter. Axonal deficits tended to recover, presumably due to treatment. This different time course of glial and neuronal metabolism has implications for understanding the natural history of MS, as well as for monitoring response to treatment paradigms.

Figures and tables:

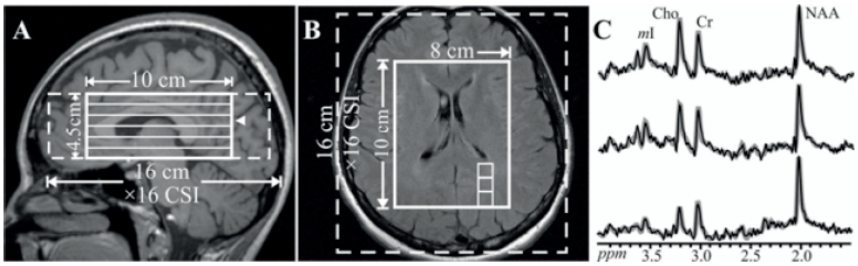

Fig. 1: Sagittal T_1-weighted (**A**) and axial FLAIR (**B**) MRI of a patient overlaid with the ^{1}H-MRS VOI (solid white lines) and field-of-view (dashed lines). The location of **B** is indicated on **A** by an arrowhead. CSI=chemical shift imaging. (**C**) Real part of the ^{1}H spectra from the voxels indicated on (**B**), superimposed with their fitted model functions (gray lines).

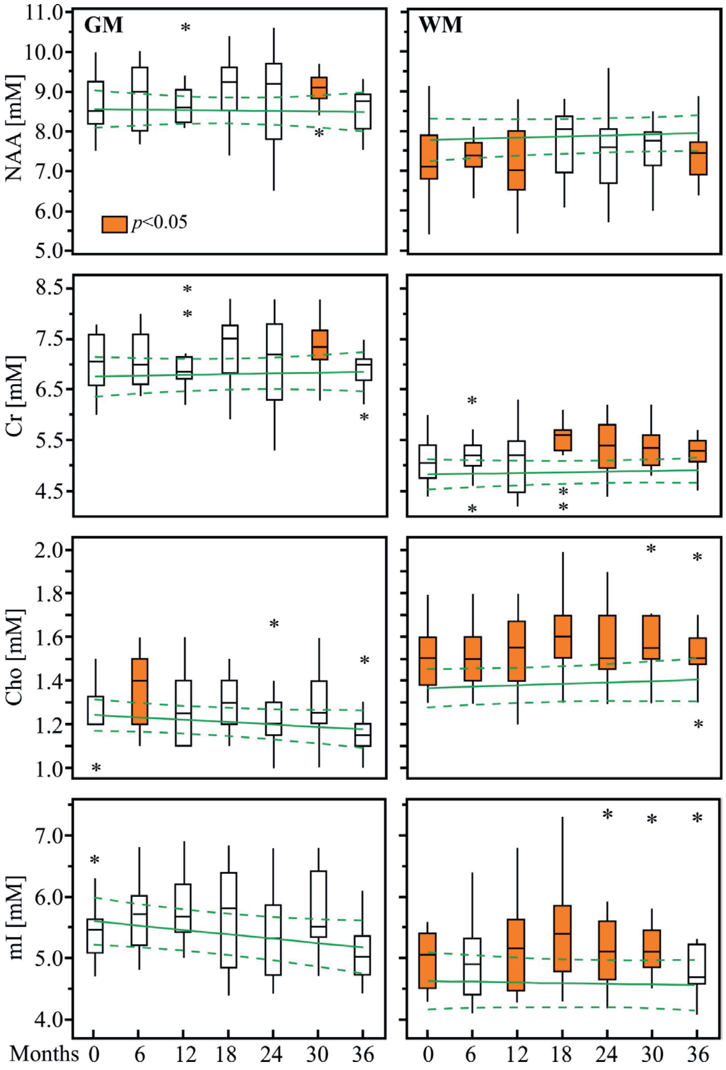

Fig. 2: Box plots of the patients GM and WM NAA, Cr, Cho and *m*I concentrations distributions, overlaid on the regression line of the corresponding average concentrations and 95% confidence intervals (dotted lines) of the controls. Orange fill: patients' distributions significantly different from the controls'.

Methylphenidate and Brain Activity in a Reward/Conflict Paradigm

Iliyan Ivanov, Xun Liu, Suzanne Clerkin, Kurt Schulz, Jin Fan, Jeffrey Newcorn

Icahn School of Medicine at Mount Sinai, New York NY

Introduction: Methylphenidate (MPH) is an indirect agonist that increases intra-synaptic concentrations of dopamine (DA) and noradrenalin (NA) by blocking their reuptake (Kuczenski & Segal, 1977) leading to enhanced cognitive performance (Mehta et al., 2000; Berridge et al., 2006). However, improved task performance with MPH has been linked to inconsistent changes in regional cerebral blood flow and blood oxygen level dependent (BOLD) signal in networks of attention, working memory and reward processing detected by functional magnetic resonance (fMRI). In this study we aim to test the effect of MPH on performance and associated brain activity using a novel hybrid Anticipation, Conflict, Reward (ACR) task that indexes activation in motivational and behavioral control networks associated with reward incentives and conflict resolution. We hypothesized that MPH would decrease activation in components of the motivation-reward network (i.e., insula and ortbito-frontal cortex) during reward trials and in attention-activation networks, including the thalamus, middle frontal gyrus and basal ganglia, during conflict compared to placebo (PL).

Methods & Results: Sixteen healthy adult volunteers, ages 21-45 (Mean =30.6 ±7.4; M-8, F-6) were scanned twice using functional magnetic resonance imaging (fMRI) and performing the ACR task with PL vs. MPH. Instruments included SCID, CAARS, SCL-90R, MAST-AD, WASI; Placebo and MPH (dosed at 0.5mg per kg) were administered 60min before scans and were randomized for order. **Results showed** that MPH improved accuracy ($F_{1,15}$)=4.469, *p* <0.05) in all trial types except non-reward cue with incongruent target trials. MPH decreased activation in both attention and motivational networks (e.g. insula, putamen) compared to PL.

Conclusion: MPH was also associated with lower task-related activity in components of the reward motivation system, particularly the insula, during reward trials irrespective of target difficulty. MPH was associated with lower task-related activity in components of attention-activation system irrespective of the reward cue.

Clinical Relevance: These results suggest that with PL subjects committed most effort to minimize loses whereas with MPH most efforts were committed to obtain as many money wins as possible.

Figures and tables

Figure 1.

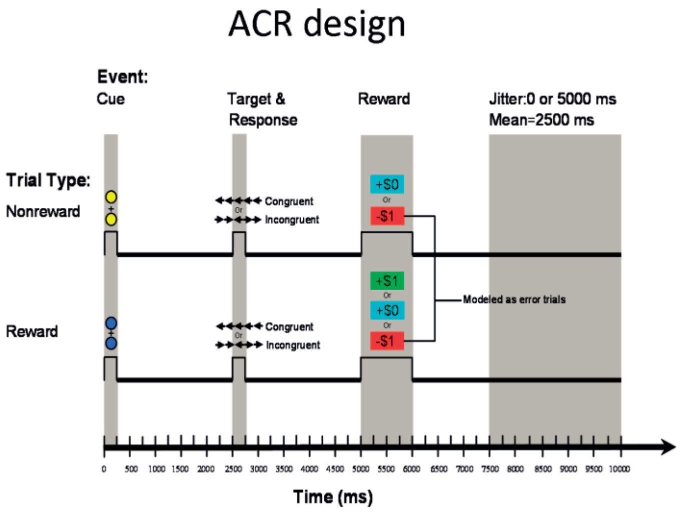

Figure 2. PL > MPH activation in Right Insula

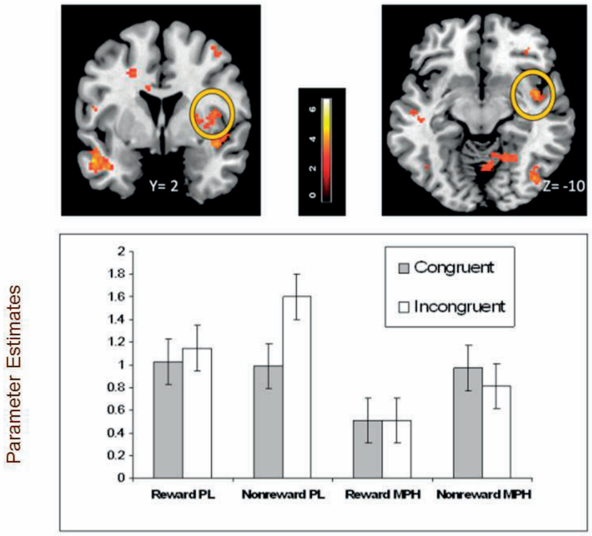

Reduced functional connectivity between insula and amygdala underlies diminished habituation to aversive stimuli in borderline personality disorder

Harold W. Koenigsberg, MD[1,2], Bryan Denny, Ph.D.[1] Jin Fan, Ph.D[1]. Xun Liu, Ph.D.[3],
Liza Rimsky[1], Antonia Mcmaster[1], Antonia New, M.D.[1,2], Larry J. Siever, MD[1,2]

[1] Icahn School of Medicine at Mount Sinai
[2]James J Peters VA Medical Center
[3] Institute of Psychology, Chinese Academy of Sciences

Introduction

Affective instability (AI) is a core feature of BPD, yet its neural underpinnings have not been clearly identified. We hypothesized that a contributor to AI is impairment in engagement of adaptive emotional habituation processes to reduce negative affect.

Methods & Results

METHOD: 19 BPD patients, 25 healthy volunteers (HC) and 23 avoidant personality disorder patients (AvPD) viewed emotionally negative pictures two times, 5 minutes apart, as fMRI images were obtained. Group comparisons of novel vs. repeat picture viewing were carried out. Changes in functional connectivity to a left insula seed region, when viewing repeat vs. novel pictures were examined using psychophysiological interaction analysis.

RESULTS: Consistent with psychological habituation, HC subjects rated repeat significantly less negatively than novel negative pictures ($p = 0.01$), but BPD and AvPD subjects did not. BPD subjects showed larger decreases in activation for repeat vs. novel pictures than HCs in dorsal anterior cingulate cortex and several temporal regions. This failure to increase dACC activity was associated with greater affective instability in BPD subjects (figure 1). HC subjects demonstrated increased insula-amygdala connectivity when viewing repeat vs. novel pictures and, consistent with the observed behavioral habituation, increased left insula-amygdala connectivity was associated with decreased negative affect ($r = 0.490$, $p = 0.015$). In contrast, BPD patients showed less increased insula-amygdala connectivity than HC’s ($p< .05$, whole-brain corrected FWE) (figure 2). Distinguished from both BPDs and HCs, AvPD patients showed the opposite correlation between change in insula-amygdala connectivity and change in negative affect ($r = - 0.516$, $p = 0.014$).

Conclusion

This study provides evidence that anomalies in prefrontal activation and insula-amygdala connectivity are associated with impaired emotional habituation and affective instability in borderline patients.

Clinical Relevance

Extreme emotional reactivity is a defining feature of borderline personality disorder (BPD), yet the neural-behavioral mechanisms underlying this affective instability are poorly understood. This study suggests that anomalous neural activity during habituation contributes to affective instability in BPD. Since emotional habituation is a common implict emotion regulation mechanism and plays a role in psychotherapy, itentifying its neural correlates may help better target treatment for affective instability.

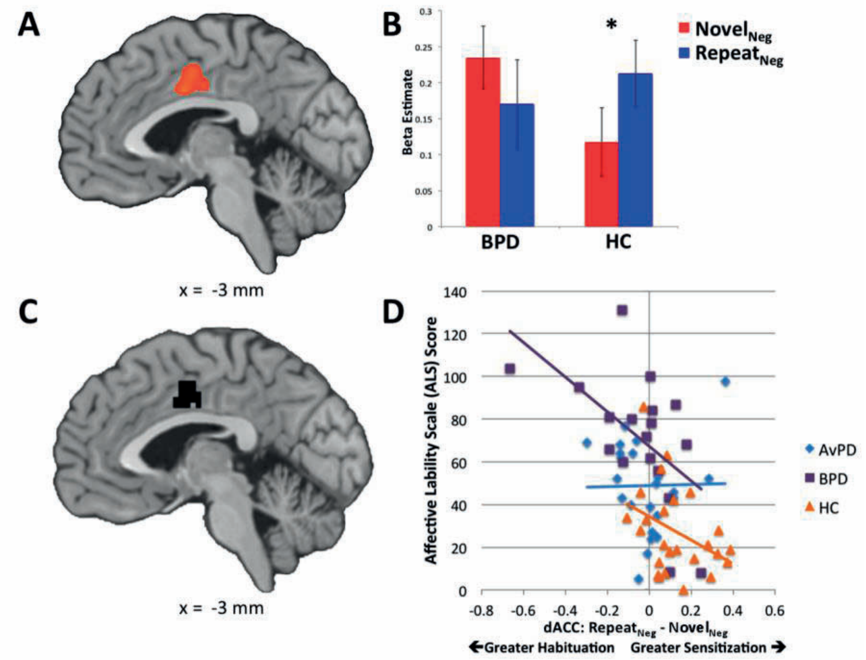

Figure 1 - Engagement of the dorsal anterior cingulate (dACC) when viewing repeat vs. novel negative pictures. A.) The map shows a 156 voxel dACC cluster indicating a significant difference between HC and BPD groups for Repeat$_{Neg}$ vs. Novel$_{Neg}$ activity ($p<0.05$, $k=150$, FWE-corrected), B.) Extracted beta-weights for each group when viewing novel and repeat negative pictures, C.) Unbiased 65 voxel dACC region-of-interest (ROI) derived from conjunction of voxels showing significant between-group differences for repeat vs. novel negative picture viewing for BPD vs. HC and AvPD vs. HC contrasts ($p<0.05$), D.) Correlation of repeat vs. novel activation differences in the independently-defined dACC ROI with affective instability for each group.

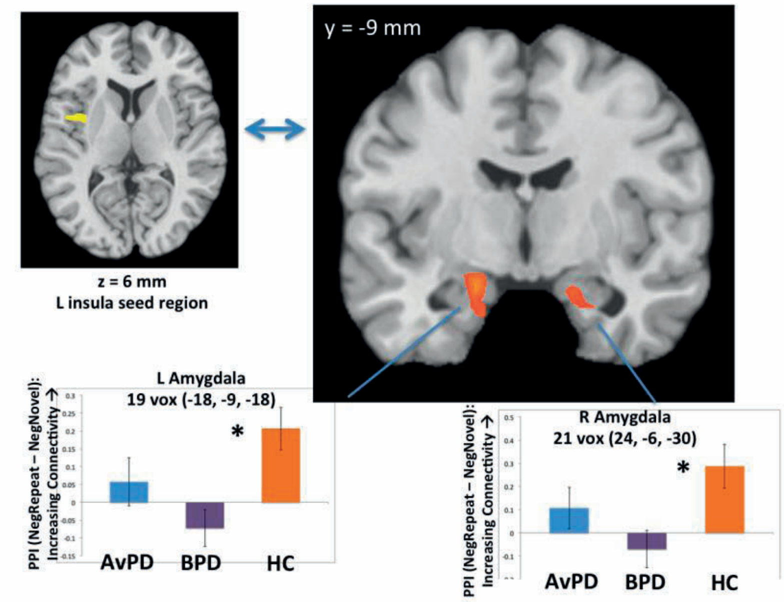

Figure 2 – Group Differences in Insula-Amygdala Connectivity When Viewing Repat vs. Novel Negative Pictures

Effects of chronic and acute stimulant exposure on brain connectivity hubs

Anna B. Konova[1,2], Scott J. Moeller[1], Dardo Tomasi[3], Rita Z. Goldstein[1]

[1]Departments of Psychiatry and Neuroscience, Icahn School of Medicine at Mount Sinai, New York, NY 10029; [2]Department of Psychology, Stony Brook University, Stony Brook, NY 11794; [3]National Institute on Alcohol Abuse and Alcoholism, Bethesda, MD 20892.

Introduction

The spatial distribution and strength of 'hubs' that facilitate information processing are essential features of the brain's network topology, and are particularly susceptible to neuropsychiatric disease. Despite growing evidence that drug addiction alters functioning and connectivity of discrete brain regions, little is known about whether chronic drug use affects this network-level organization, or if it can be further modified by therapeutic agents acting on dopamine. We used functional connectivity density (FCD) mapping to evaluate the effects of chronic and acute stimulant exposure on brain hubs, i.e., regions with high numbers of long- and/or short-range functional connections.

Methods & Results

19 individuals with cocaine use disorders (CUD) and 15 healthy controls completed resting-state fMRI scans following oral methylphenidate (20 mg) or placebo in randomized order. Long- and short-range FCD maps were computed for each subject and medication condition. The effects of diagnosis and methylphenidate on FCD were examined with 2 (Group) × 2 (Medication) ANCOVAs, covarying for age. Results indicated that a diagnosis of CUD was associated with increased long- and short-range FCD in the ventromedial prefrontal cortex, posterior cingulate/precuneus, and putamen/amygdala. Across all participants, methylphenidate decreased long-range FCD in the sensorimotor cortex and short-range FCD in the bilateral putamen/thalamus.

Conclusion

These results show that chronic cocaine use is associated with an abnormal count of long- and short-range functional connections to several brain hubs, particularly those part of the default mode network, suggesting that there is an inefficient overrepresentation of these energy-expensive topological components in addiction. In contrast, the dose of methylphenidate reduced the number of short-range connections to hubs relevant to the formation of habits and more severe patterns of drug use, suggesting that abnormalities in these hubs could be potentially modified by treatment.

Clinical Relevance

Therapeutic doses of methylphenidate can modify altered connectivity density in cocaine addiction in brain hubs associated with more severe patterns of drug use.

Figure 1. Effects of chronic cocaine use and single dose of oral methylphenidate on FCD. Three dimensional planes are shown at X=-2, Y=-11, and Z=-9. K density maps are shown in spectrum and T-maps are shown in red at a $P<0.005$ voxel-level uncorrected and 45 contiguous voxels threshold. No brain regions showed higher FCD in controls>CUD or during methylphenidate>placebo. There were also no group-by-medication interactions.

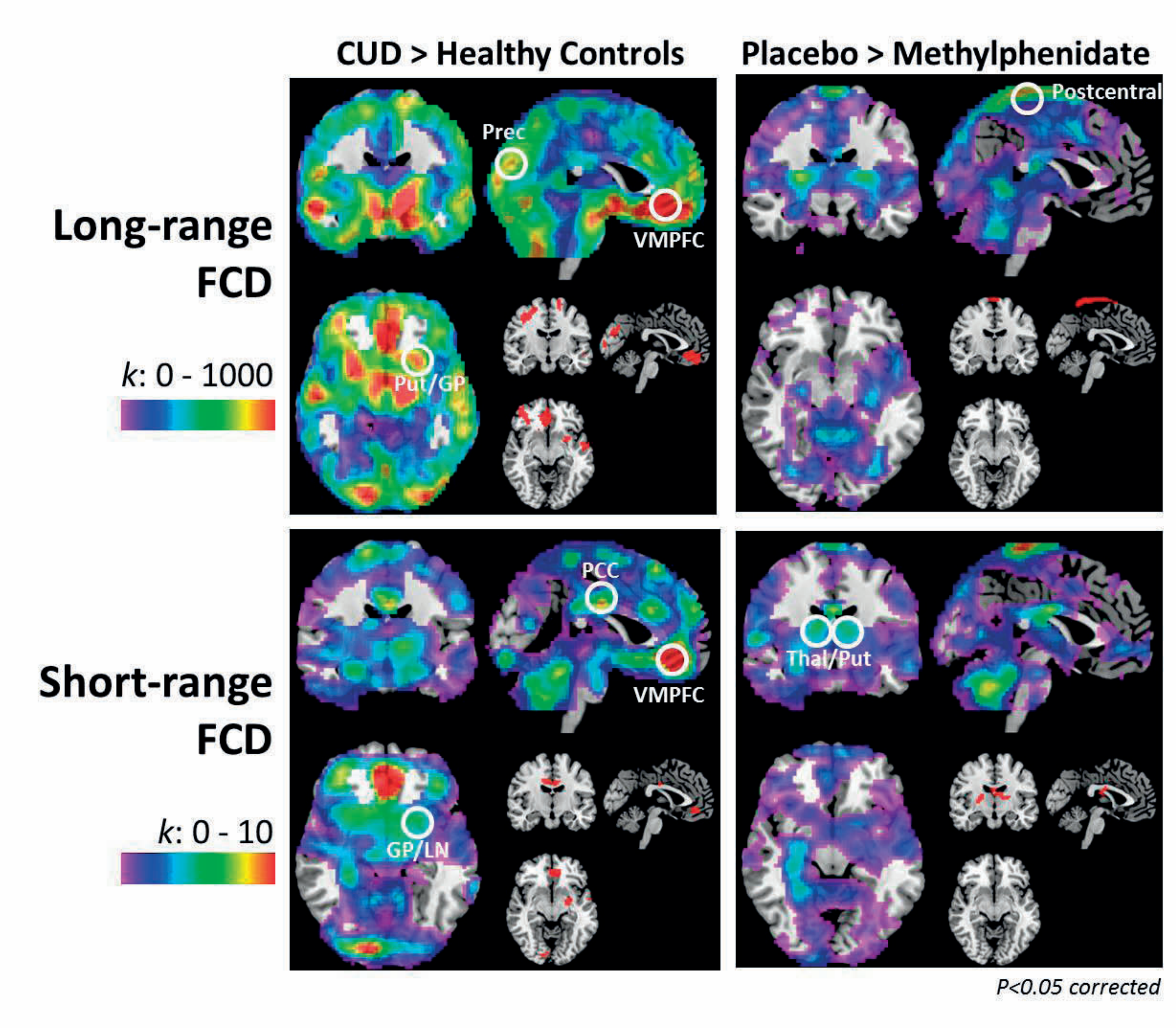

Striatal biomarkers of differential therapeutic response to stimulant and non-stimulant medications for ADHD

K. P. Schulz[1]; A.-C. V. Bédard[1]; J. Fan[1,2]; S. M. Clerkin[1]; I. Ivanov[1]; J. M. Halperin[1,2]; J. H. Newcorn[1]

[1]Department of Psychiatry, Icahn School of Medicine at Mount Sinai; [2]Queens College, City University of New York

Introduction: The increasing number of stimulant and non-stimulant medications for attention-deficit/hyperactivity disorder (ADHD) highlights the need for biomarker strategies to inform treatment selection. The affinity of the stimulant methylphenidate, but not the non-stimulant atomoxetine, for the dopamine transporter manifests most prominently in dissociable effects on neural function in striatum that may predict differential response to the two treatments. The predictive utility of striatal biomarkers may be further influenced by polymorphic variation in the 3' untranslated region (UTR) of the dopamine transporter gene (*DAT1*).

Methods & Results: We used functional magnetic resonance imaging (fMRI) to test the predictive value of baseline neural activation in 36 youth with ADHD (mean age 11.0 ± 2.4 years; 30 males) recruited from a larger comparator trial. Youth were scanned with fMRI during a go/no-go task while off-medication, and treated with both methylphenidate and atomoxetine in randomized order in a double-blind cross-over design. Clinical response was measured using the ADHD Rating Scale-IV-Parent Version (ADHDRS-IV). Three multiple regression analyses with treatment order as a covariate were used to test for activation differentially related to: i) response to methylphenidate versus atomoxetine; ii) methylphenidate response as a function of *DAT1* 3' UTR genotype; and iii) improvement of inattentive versus hyperactive-impulsive symptoms. Whole-brain analysis found that elevated activation for response inhibition in right caudate nucleus predicted superior therapeutic response to methylphenidate over atomoxetine (**Figure 1**). The relationship of right caudate nucleus activation to methylphenidate response was further moderated by polymorphic variation in the *DAT1* 3' UTR locus; caudate nucleus activation was positively correlated with symptomatic improvement in carriers of the 9-repeat allele of *DAT1*, but not in homozygotes for the 10-repeat allele (**Figure 2**). Finally, elevated activation in right caudate nucleus was predominantly but not exclusively associated with improvement of inattention symptoms for methylphenidate (**Figure 3**).

Conclusion: Findings corroborate caudate nucleus activation as a candidate biomarker of differential response to methylphenidate over atomoxetine, and suggest that a subpopulation of youth with ADHD – specifically, those who present with increased caudate activation – respond preferentially to the dopaminergic effects of methylphenidate. The moderation of the predictive utility of caudate nucleus activation for methylphenidate response by *DAT1* 3' UTR genotype challenges the notion that striatum is the primary site of therapeutic action for stimulant medications for all individuals with ADHD.

Clinical Relevance: The identification of a biomarker that predicts preferential response to stimulant over non-stimulant medications, in association with a specific neural function in a particular brain region (i.e., caudate nucleus), addressing a distinct set of symptoms (i.e., inattention) in a subgroup of youth with ADHD (carriers of th *DAT1* 3'UTR 9-repeat allele), is a potentially ground-breaking step in the development of targeted approaches to treatment.

Figures and Tables

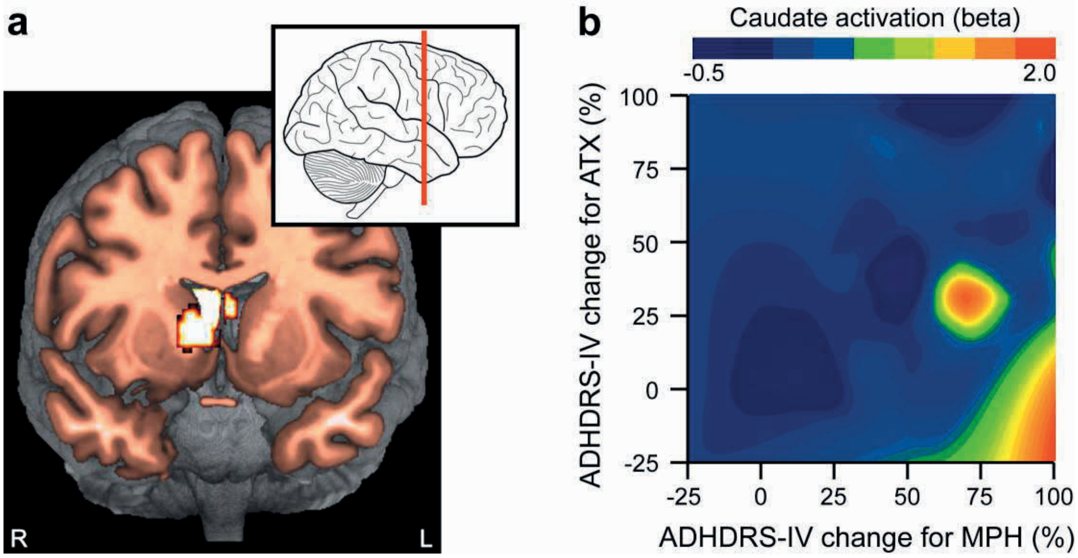

Figure 1. Elevated baseline caudate nucleus activation for response inhibition predicts superior clinical improvement for methylphenidate (MPH) versus atomoxetine (ATX) in 36 youth with ADHD. (**a**) Differential symptomatic improvement for MPH and ATX was associated with activation in right caudate nucleus. (**b**) Plotting right caudate nucleus activation against percent change on the ADHD Rating Scale-IV-Parent Version (ADHDRS-IV) for both MPH and ATX reveals that elevated right caudate activation predicts robust improvement for MPH and little to no improvement for ATX.

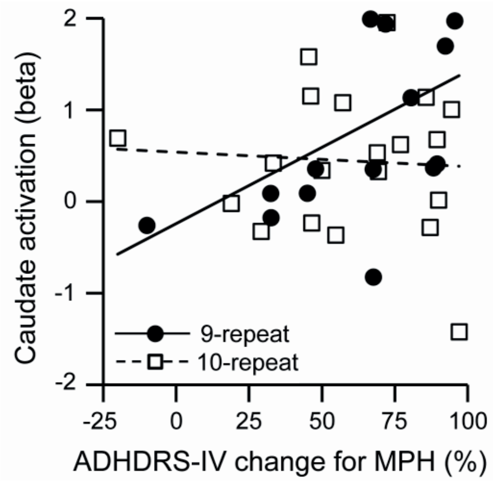

Figure 2. Plotting right caudate nucleus activation against percent change on the ADHD Rating Scale-IV-Parent Version (ADHDRS-IV) for MPH in the two *DAT1* 3’ UTR genotype groups reveals that right caudate activation predicts improvement in carriers of the 9-repeat allele of the polymorphism (n = 15), but not in homozygotes for the 10-repeat allele (n = 20).

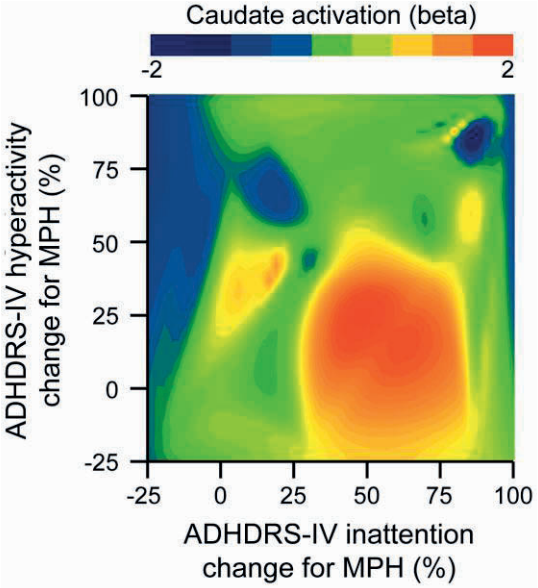

Figure 3. Plotting right caudate nucleus activation against the percent change in both inattention and hyperactivity-impulsivity symptoms on the ADHD Rating Scale-IV-Parent Version (ADHDRS-IV) for MPH reveals that elevated right caudate activation was associated with a preponderance of improvement in inattention symptoms.

Neural Dysfunction Associated with Pleasure in Postpartum Depression and its Relationship to Reported Sleep Disturbance

Michael E. Silverman[1], Holly Loudon[2], Casey Mauro[1] and Martin A. Goldstein[3]
1. Icahn School of Medicine at Mount Sinai, Department of Psychiatry
2. Icahn School of Medicine at Mount Sinai, Department of Obstetrics, Gynecology and Reproductive Science
3. Icahn School of Medicine at Mount Sinai, Department of Neurology

Introduction

Postpartum depression (PPD), the most common complication of childbearing, is a potentially catastrophic condition that follows pregnancy, affecting both the mother and the newborn. Nosologically classified as a specifier of a major depressive disorder, symptoms of PDD are distinguished not by their phenomenology of diminished mood and decreased positive affect, but rather by their timing of onset. Because a core symptom of depression is loss of pleasure, we hypothesized that subjects with increased PPD symptomatology would show diminished neural responsivity to positive stimuli in the ventral striatum, a brain region associated with positive experience and reward. We further postulated that because physiologic dysregulation is a key marker in PPD and that sleep loss is a conspicuous feature of early motherhood, the observed neural dysregulation associated with pleasure would be strongly associated with the subject's reported level of early maternal sleep disturbance.

Methods & Results

Twenty women, each between 6-8 weeks postpartum, underwent structural and functional magnetic resonance imaging acquired with a research-dedicated Siemens Allegra Magnetron 3 Tesla head dedicated MRI scanner (maximum gradient strength ~60mT/m, max gradient slew ~600T/m/s). Three subjects were subsequently discarded due to head movements greater than 1 voxel (3-4mm), leaving 17 subjects (mean age = 27 years). Gradient echo planar imaging - blood oxygen level dependent (EPI-BOLD) fMRI were acquired (TR=2000msec, TE=30msec, flip angle=90°;FoV=210mm, 32 slices; 3mm thickness; 1mm gap) as an index of neuronal activity during the neuropsychological activation paradigm.

The fMRI activation paradigm consisted of an emotional word probe, with semantic specificity, allowing for a complementary higher-level examination of the hypothesized circuitry. This paradigm employed stimuli in which emotional qualities were *incidental* relative to the explicit nature of a word/scrambled-word (i.e., nonsense letter clusters) determination behavioral task demand (2AFC finger button-press). Using this technique, the evocation of potentially confounding cognitive processes (*e.g.,* semantic categorization) could be minimized.

The task was presented in a block design. Presentation was counterbalanced to control for order and time effects. Each block was comprised of 10 novel stimuli of the same valence (positive, neutral, negative depressive, and negative threat); there were 100 trials per condition, 400 total trials per study session. Blocks were counterbalanced to include 1, 2 or 3 scrambled stimulus words. Each stimulus appeared for 1.5 second, followed by a jittered inter-stimulus interval averaging 1900msec., for a total block duration of 34 seconds. Each block was followed by 12 seconds of rest. Each run was preceded and followed by an additional 36-second rest. During rests, subjects were instructed to look at a centered fixation cross with their minds floating freely.

Differences in neural responses specific to the ventral striatum, a key brain region associated with pleasure, were assessed in relation to stimulus, overall depressive symptomatology, and reported maternal sleep disturbance. Responses significant at $p<.05$ corrected for multiple comparisons revealed significantly greater BOLD response to positive stimuli in the right ($F=6.838$, $p<.020$) but not left ($F=2.981$, $p<.105$) nucleus accumbens (right: [20,12,-12], left: [-15,15,-14]). Secondary correlational analyses associated with the primary hypothesis demonstrated a BOLD response for positive words in the right nucleus accumbens that was moderately correlated (negative) with severity of PPD symptoms ($r=-.531$, two-tailed $p_{corr}\leq.028$, volume=33 voxels of 2x2x2mm^3), and a stronger correlation (negative) with severity of reported sleep disturbance ($r=-.621$, $p_{corr}\leq.008$, volume=33 voxels of 2x2x2mm^3).

Conclusion

While the overwhelming majority of studies exploring depression have focused on the processing differences in negative stimuli, relatively few have specifically addressed the diminished response to pleasure. Notably, pleasure which is a key component to approach motivation is also associated with the maintenance of the maternal drives necessary for healthy infant/child development. The importance of the current finding lies in the support they lend to understanding the specific nature of emotional processing and behavioral abnormalities in early maternal depression and prove helpful in laying the groundwork for determining the mechanisms responsible for changes in mood during the perinatal period.

Clinical Relevance

Among the most commonly expressed complaints of early motherhood is the sleep fragmentation associated with newborn care and feeding. Even in instances when the newborn sleeps, maternal insomnia is a frequently reported complaint. The relationship between sleep disturbance and the onset of major depression in people with no prior history of psychiatric disturbance has been well documented. While the relationship between sleep deprivation and mood remains a causality dilemma, the fact that sleep deprivation is most commonly precedes depression, and that normal sleep patters are disrupted during the perinatal and postpartum period, is at least suggestive of a causal direction. Further research is needed to determine if early recognition and treatment of sleep disturbances can prevent the onset or minimize the impact of parinatal depression.

Figures and tables

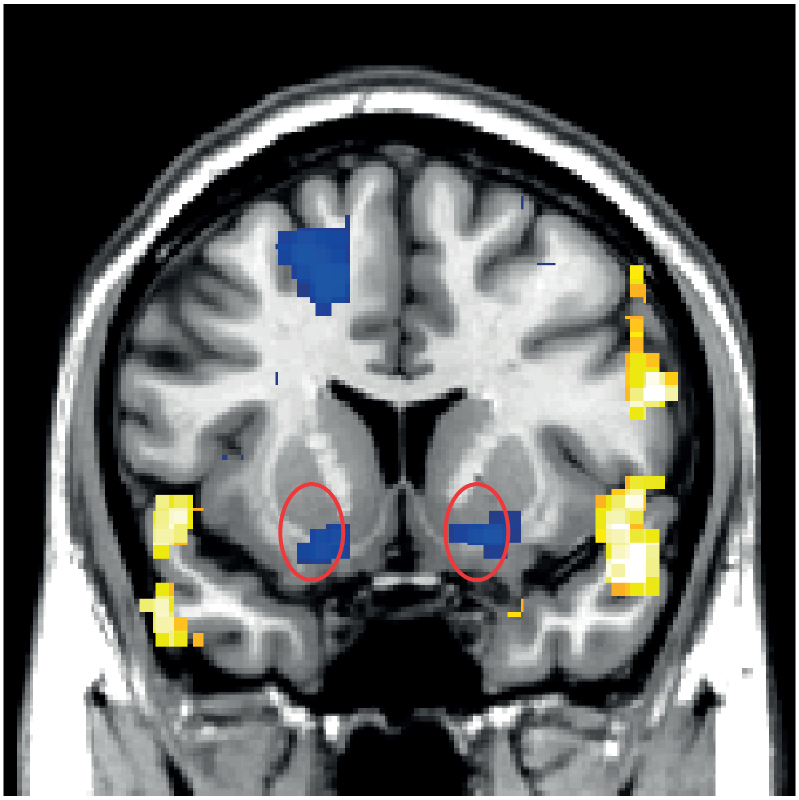

Presented at p≤.05 for visualization.

Quiet PROPELLER MR Techniques Provide Equivalent Quality for Routine Brain MR Imaging

Idoia Corcuera-Solano, A. Doshi, M. Fung, D. Gui, A. Gaddipati, L. Tanenbaum

Icahn School of Medicine at Mount Sinai

Introduction: Switching magnetic field gradients is the primary source of acoustic noise in MRI. Sound pressure levels can run as high as 100-120dB, potentially producing physical discomfort and temporary hearing loss, mandating hearing protection. Two methods have been used to reduce noise - dampen/isolate the gradient coil from the patient bore, or reduce switching rate. Both have drawbacks, the first resulting in reduction of bore space, the second reducing performance. New technology has made quieter techniques feasible. “Quiet” PROPELLER uses a standard 2D PROPELLER sampling scheme. The k-space trajectory and data-sampling scheme are optimized such that gradient steps are smaller and result in a scan that produces less noise. We aim to evaluate the quality of “Quiet” T2 PROPELLER acquisitions in comparison to techniques in current day to day practice for brain imaging

Methods & Results: Thirty-four consecutive subjects who underwent brain MR imaging examination in our institution were prospectively enrolled in this study. They were 18 men and 16 women, mean age of 54 years (range 19–96). All subjects were scanned with the pre-clinical “Quiet” T2 PROPELLER techniques in addition to routine T2 PROPELLER and T2 FLAIR PROPELLER imaging approaches on a clinical 1.5 T MR scanner. Two experienced neuroradiologists independently analyzed the MR images and assessed the images qualitatively (table 1). A non-parametric paired Wilcoxon test was used to compare the image qualitativey parameters between “Quiet” T2 and conventional T2 protocols. Statistical analysis was performed using commercially available software (SPSS version 20). A $p < 0.05$ indicated a statistically significant difference. No differences were observed in image quality, white/grey matter differentiation or blurring perception. No differences were found in overall preferences

Conclusion: “Quiet” PROPELLER T2 and T2 FLAIR were comparable in quality to conventional PROPELLER acquisitions with no significant tradeoffs aside from longer scan times.

Clinical Relevance: “Quiet” PROPELLER T2 and T2 FLAIR provide equivalent quality at comfortable sound pressure levels and can replace conventional sequences for routine evaluations of the brain.

Figures and tables

Table 1. MR images were evaluated using 3 criteria:

Criterion	Interpretation	Score
Overall Quality	Inferior Equivalent Superior	1 2 3
Grey-White matter differentiation	Inferior Equivalent Superior	1 2 3
Blurring perception	Yes No	1 2
Overall Preference	Quiet T2 FLAIR vs T2 FLAIR Quiet T2 PROP vs T2 PROP	

Figure 1. Comparison between conventional T2 PROPELLER and “Quiet” T2 PROPELLER sequences (left) and conventional T2 FLAIR PROPELLER and “Quiet” T2 FLAIR PROPELLER (right) of a patient with post craniofacial recurrent tumor resection with postsurgical changes.

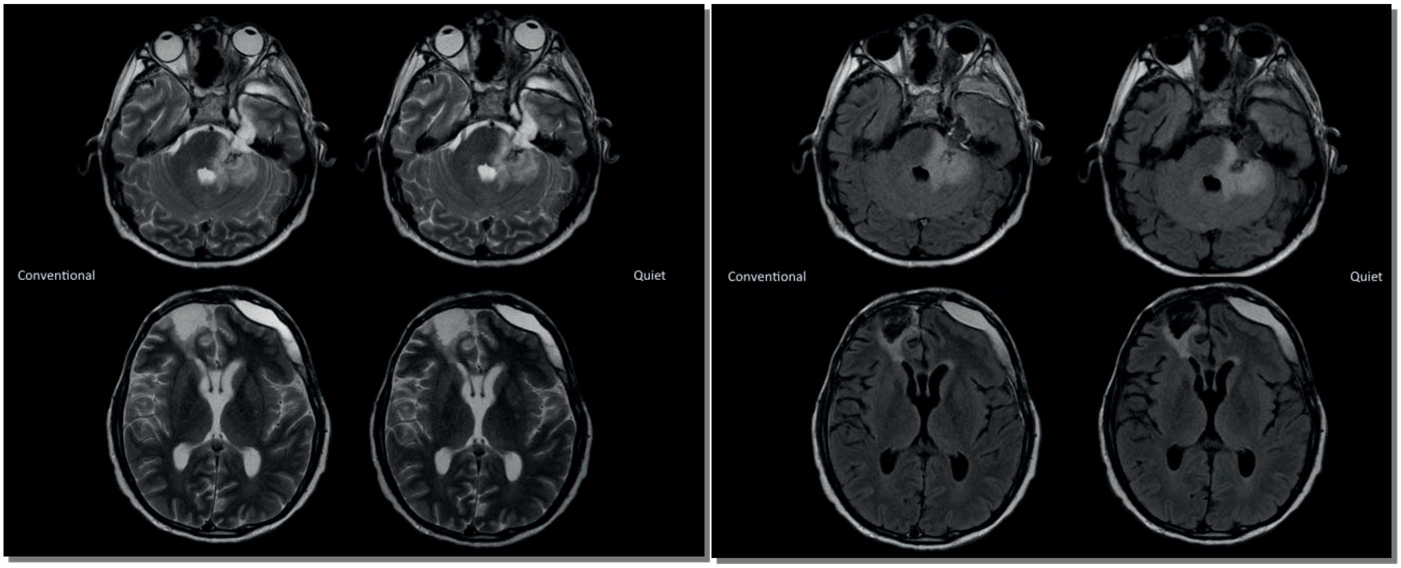

“Silent - Zero TE” MR Techniques Provide Equivalent Quality for Routine T1 Weighted MRI of the brain

Idoia Corcuera-Solano, A. Doshi, M. Fung, G. McKinnon, W. Sun, J. Akao, K. King, L. Tanenbaum

Icahn School of Medicine at Mount Sinai.

Introduction: Switching magnetic field gradients is the primary source of acoustic noise in MRI. Sound pressure levels can run as high as 100-120dB, potentially producing physical discomfort and temporary hearing loss, mandating hearing protection. Two methods have been used to reduce noise - dampen/isolate the gradient coil from the patient bore, or reduce switching rate. Both have drawbacks, the first resulting in reduction of bore space, the second reducing performance. New technology has made quieter techniques feasible. We aim to evaluate the quality of nearly silent MR T1-weighted GRE acquisitions compared to current techniques in brain imaging. This technique is a silent 3D isotropic gradient echo acquisition with a nearly zero TE and low flip angles. It uses a 3D spiral radial sampling scheme with no in-plane phase and frequency direction, and no slice selection phase. Due to the K-Space trajectory and data-sampling scheme, the gradient steps are small, accounting for the quiet behavior.

Methods & Results: Twenty-nine consecutive subjects who were undergoing brain MR imaging at our institution were prospectively enrolled in this study. There were 13 men and 19 women, mean age of 56 years (range 20–98) and were imaged for a variety of clinical indications. All subjects were scanned with the pre-clinical “Silent” T1 technique in addition to routine T1 CUBE and T1 FLAIR PROPELLER sequences on a clinical 1.5 T MR scanner. Two experienced neuroradiologists independently analyzed the MR images and assessed the images qualitatively (table 1).A non-parametric paired Wilcoxon test was used to compare the qualitative parameters between “Silent” T1 and conventional T1 protocols. Statistical analysis was performed using commercially available software (SPSS version 20). A $p < 0.05$ indicated a statistically significant difference. Both readers preferred “Silent” T1 over the T1 CUBE and the T1 PROPELLER. “Silent” T1 was comparable in quality to conventional T1 acquisitions with no significant tradeoffs aside from longer scan times. G-W matter differentiation was significantly better in Silent T1 than conventional T1 (table 2).

Conclusion: “Silent” T1 weighted scans provide equivalent quality at nearly zero sound pressure levels and can replace conventional sequences for routine T1W evaluations of the brain

Clinical Relevance: “Silent” T1 weighted scan is an useful approach for routine clinical use to avoid the acoustic noise generated during MR imaging, an unwanted side effect that cause discomfort in patients and healthcare professionals.

Figures and tables

Table 1. MR images were evaluated using 3 criteria:

Criterion	Interpretation	Score
Overall Quality	Much worse than expected Worse than expected As expected Better than expected Much better than expected	1 2 3 4 5
Grey-White matter differentiation	Much worse than expected Worse than expected As expected Better than expected Much better than expected	1 2 3 4 5
Overall Preference	Silent T1 vs T1 CUBE Silent T1 vs T1 FLAIR PROPELLER	

Table 2. Qualitative analysis results

Reader 1	**"Silent" T1**	**T1 FLAIR PROP**	**p**	**"Silent" T1**	**T1 CUBE**	**p**
G-W matter differentiation	4.24±0.74	2.86±0.35	<0.01	4.28±0.59	2.58±0.51	0.03
Overall Quality	3.48±0.74	2.97±0.18	0.07	3.48±0.74	2.33±0.49	0.02
Reader 2	**"Silent" T1**	**T1 FLAIR PROP**	**p**	**"Silent" T1**	**T1 CUBE**	**p**
G-W matter differentiation	4.34±0.77	2.86±0.35	<0.01	4.34±0.77	2.67±0.49	0.03
Overall Quality	3.76±0.79	2.93±0.53	0.004	3.41±0.78	3.76±0.79	0.01

Figure 1. Comparison between T1 FLAIR PROPELLER, "Silent" T1 and T1 CUBE

Neurosurgical ICU: Ultra-low dose SAFIRE based Head CT satisfactory for Repeated Surveillance Exams

I Corcuera Solano, MD; A Noor, MD; A H Doshi, MD; L N Tanenbaum, MD. New York, NY

Introduction

Neurosurgical ICU patients undergo frequent and repeated head CT imaging, resulting in high cumulative doses. As a result, we adopted an ultra-low dose head CT protocol (ULDCT) for follow-up use in this patient population. Our purpose was to quantitatively and qualitatively assess the quality of ULDCT exams against perceived standards of quality as well as with respect to LDCT and SDCT examinations of the same patient.

Methods & Results

Due to practical considerations and scanner availability, NICU patients undergo CT exams on a variety of scanners and many will undergo low-dose CT (LDCT) and standard-dose (SDCT) along with ULDCT examinations creating the opportunity assess quality across exam types. A retrospective analysis of 60 head CT during 2012-2013 was performed with 28 ULDCT (avg CTDIvol =15.55 mGy, 79% < ACR standards of 75 mGy), 12 LDCT (36.46 mGy) ,and 20 SDCT (48.38 mGy). SDCT exams were performed on a variety of clinical Siemens scanners using filtered back projection (FBP). LDCT exams utilized clinical iterative reconstruction (IR) techniques (ASIR-60 (GE LIGHTSPEED VCT) or SAFIRE-3 (Siemens AS+ 128). All ULDCT exams were performed with SAFIRE-3 on a Siemens Definition AS+ 128 scanner.

Studies were independently evaluated by two neuroradiologists for image quality (granularity, grey-white differentiation, and overall quality) against expected standards. A quantitative assessment of image noise was made. Data were analyzed as medians and groups were compared with the use of the Wilcoxon signed-rank test.

With ULDCT the CTDIvol of head CT is reduced from routine SDCT by 68% (table 2) (79% below ACR guidelines), while maintaining comparable quality and similar noise levels to SDCT images. LDCT offers higher image quality compared with SDCT with no differences in noise. When compared to ULDCT, LDCT significantly reduces image noise ($p=0.008$) and improves qualitative measures of image quality ($p< 0.05$) (Table 1).

Conclusion

ULDCT allows substantially lower dose while maintaining quality for surveillance studies from the NICU.

Clinical Relevance

ULDCT provides satisfactory studies, comparing favorably with SDCT. This technique should be considered for surveillance evaluations in the NICU.

Table 1. Qualitative and Quantitative Analysis

Qualitative Analysis		ULDCT	LDCT	p	LDCT	SDCT	p	ULDCT	SDCT	p
Granularity	Av Observers	2.82±0.47	4±0.42	0.003	4±0.42	3.38±0.58	0.032	2.82±0.47	3.38±0.58	0.23
GW matter diff	Av Observers	3.50±0.67	3.79±0.49	0.277	3.79±0.49	2.90±0.59	0.034	3.50±0.67	2.90±0.59	0.004
Overall quality	Av Observers	3.25±0.45	4.08±0.51	0.003	4.08±0.51	3.25±0.52	0.022	3.25±0.45	3.25±0.52	0.908

Granularity	Gray-White differentiation	Overall quality
1= much more granularity than expected	1= much worse than expected	1= much worse than expected
2= more granularity than expected	2= worse than expected	2= worse than expected
3= normal, as expected	3= normal, as expected	3= normal, as expected
4= less than expected	4= better than expected	4= better than expected
5= much less than expected	5= much better than expected	5= much better than expected

Quantitative Analysis		ULDCT	LDCT	p	LDCT	SDCT	p	ULDCT	SDCT	p
White matter	Av	29.15±8.52	31.59±2.48	0.099	31.59±2.48	29.64±3.95	0.037	29.15±8.52	29.64±3.95	0.22
	Std	7.14±4.40	6.12±2.93	0.003	6.12±2.93	4.86±1.10	0.644	7.14±4.40	4.86±1.10	0.002
	SNR	5.37±2.54	6.24±2.20	0.008	6.24±2.20	6.48±1.27	0.31	5.37±2.54	6.48±1.27	0.49

Table 2. Radiation Dose

total dose of CTDIvol (mGy)				Difference CTDI vol					
	uLDCT (n=28)	LDCT (n=12)	SDCT (n=20)	uLDCT-LDCT	%	SDCT-LDCT	%	uLDCT-SDCT	%
Max	20.46	54.7	60.69	34.24	62	5.99	10	40.23	56
Min	11.77	26.8	33.8	15.03	56	7	20	22.03	65
Mean	15.55	36.46	48.38	20.91	57	11.92	24	32.83	68

Methods of Peripheral Nerve Tissue Preparation for Second Harmonic Generation Imaging Of Collagen Fibers

Surabhi Vijayaraghavan, Rumana Huq, Michael Hausman
Leni & Peter W. May Department of Orthopaedics, Microscopy Shared Resource Facility,
Icahn School of Medicine at Mount Sinai

Introduction

Second Harmonic Generation (SHG) imaging of the peripheral nerve using multi-photon microscopy is a novel technique with little documentation. It affords the significant possibility of non-destructive imaging of internal nerve anatomy. The nature of nerve tissue, especially its size and viscoelastic properties, presents special challenges for microscopy. While nerves are under an innate *in situ* strain, they retract once dissected, thus distorting microscopic structure. The challenge is to preserve the nerve in its natural strain range to obtain images that most truly reveal its structure.

Methods & Results

This study examined SHG images of rat median nerve prepared by several different methods to compare image quality and content. Nerve segments were fixed under strained (constant load or length) and unstrained conditions and imaged as fresh whole mount nerves as well as plastic (methyl methacrylate) and paraffin embedded sections. (Table 1) These were tested for optimal excitation wavelength, quantitative image contrast, and overall quality. Root mean squared (RMS) contrast was calculated for all conditions and compared to the qualitative rankings.

RMS contrast calculation proved to be a reliable measure of the level of image contrast that can be detected by eye. We concluded that images obtained from tissue sections (plastic and paraffin) provided the most accurate and revealing SHG images of peripheral nerve structure. Plastic embedding yielded slightly better image quality, being a superior process in terms of principle and material. However, it is a complex and time-consuming process. Hence the choice of paraffin as an embedding medium for SHG imaging of peripheral nerve is a reasonable compromise between image quality and feasibility. (Figure 1) Further, nerve preparation by straining under constant load stretched the nerve beyond *in situ* levels. Fresh tissue preparation by straining under constant length more closely reflected *in vivo* conditions. (Figure 1) Lastly, removing the embedding material prior to imaging significantly improved image quality. (Figure 2) Optimal excitation wavelengths were consistent regardless of the preparation method.

Conclusion

This study answers all the preliminary questions needed for any study that endeavors to image nerve collagen fibers by SHG. Embedded sections were most conducive for capturing nerve structure and collagen fibers. The choice of plastic embedding medium improves image quality, but not significantly when compared to paraffin sections. Removing the medium prior to imaging (i.e. de-paraffinization or de-plasticization) yields a higher RMS contrast, and consequently better images. The optimal wavelength for excitation for SHG was found to be 860nm across all embedded samples. Hence, we speculate that the optimal imaging wavelength for SHG is independent of the nature of the embedding process.

Clinical Relevance

These answers lay the groundwork for furthering non-destructive imaging of the peripheral nerve, an important clinical dilemma that is key to successful diagnosis and recovery from peripheral nerve injury.

Figures and tables

Table 1. Preparation conditions

	Zero Strain/ Passive Preparation	Strain by Constant Length	Strain by Constant Load
Paraffin embedding	X	X	X
Plastic embedding	X	X	
Fresh whole mount	X	X	

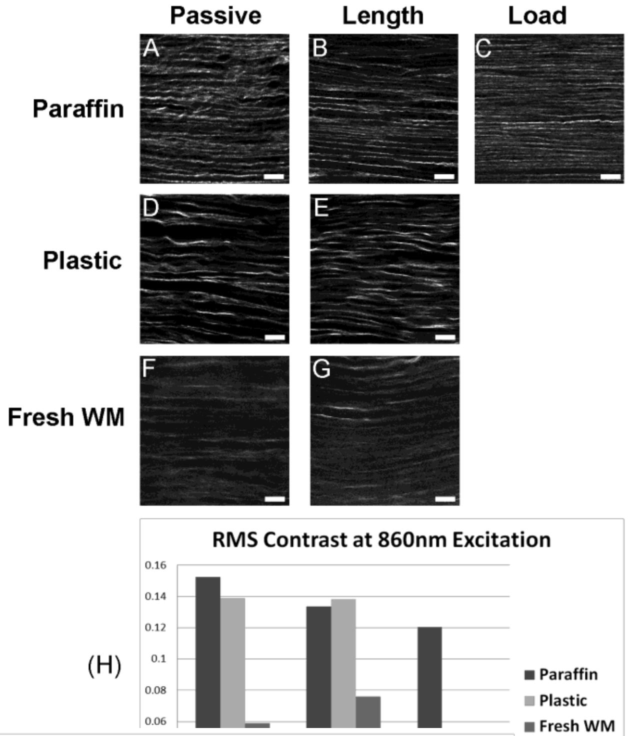

Figure 1. SHG images acquired with an excitation wavelength of 860nm with optimized imaging parameters. Images (A-C) are of paraffin embedded sample fixed under zero strain, length, and load conditions respectively. Images (D-E) are of MMA samples fixed under zero strain and length respectively. (F-G) are fresh whole mount samples fixed under zero strain and length respectively. No scaling has been applied to any of the images. The full 12-bit grayscale range is visible. Scale bars are 20μm. Graph (H) shows the RMS contrast calculated for each image.

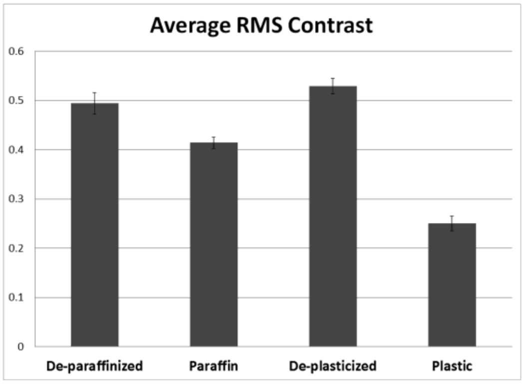

Figure 2. Graph of average RMS contrast for SHG images of slides either with or without the respective embedding material.

Design of a Multi-Nuclear Histology MRI Probe for Direct Imaging of Pre-mounted Tissue Sections.

D. M. Hoang[1], E. Voura[1,2], and Y. Z. Wadghiri[1]
[1] Radiology, NYU School of Medicine, NY, NY, USA; [2] Biology, Dominican College, Orangeburg, New York, USA.

Introduction

The validation of MRI findings with histology, the gold standard, is an ongoing challenge. In this study, we designed and tested a set of planar MRI probes to examine the sensitivity limits achievable at 7-Tesla and to achieve a near-perfect co-registration with optical microscopy. Our simple in-house probe design allowed for imaging of any type of tissue section pre-mounted under standard coverslips. Several organs tissues were examined demonstrating an unprecedented match between MRI and histology opening up the opportunity to test novel molecular MRI probes within their tissue targets.

Methods & Results

The design of our histology coil was based on off-the-shelve materials requiring a simple construction as depicted in Figure 1. The assembly was made in-house using Plexiglas as a support, copper tape to conduct the current, and thermo-glue to keep the structure together as shown in Figure 1b,d. The size of the resulting planar coil structure was dictated by the size of the tissue sections examined, as well as by the width and thickness of the glass support available. For samples encased by two coverslips, a coil with an opening height of 450-µm housed sections as thick as 130-µm. The surface area covering the imaging of the tissue depended on the width (W) of the flat copper strip (Fig. 1a). For this work, three widths (W=12, 26, and 52 mm) were chosen to image a variety of tissue sections ranging from organ subsections from the mouse olfactory bulb, to large samples such as whole mouse organ slices or human specimens. The 150-µm-thick glass coverslips used in our study were either 12 or 24 mm wide resulting in the design of coils with the same corresponding inner length of the insert (IL=12 and 24 mm) in order to accommodate the encased samples (Fig. 1c). The U-shaped slotted resonator outer length (OL) was extended by an adequate length of the Teflon-based capacitor to ensure the even spread of the surface current within the copper tape before reaching the edge of the opening. The choice of a capacitor of equal length to the IL of the insert was based on a simulation by Meadowcroft *et al*. (1). The adjustment of the resonance frequency was achieved by a homemade T/M circuit based on two variable capacitors (Voltronics Corps., Salisbury, MD) (Fig. 1f). Our setup was designed to ensure that all of our probes could easily interface the same T/M circuit via a RG223 double-shielded coaxial cable using a BNC connector. The combination of the various dimensions (W, IL, OL, and H) led to the design of five distinct histology coils comprised of three planar coil dimensions (WxIL, referred to as small: 12x12 mm; medium: 26x24 mm; and large: 52x24 mm, respectively) as depicted in Figure 2a. The systematic choice of OL=2xIL demonstrated a homogeneous RF field coverage throughout the cavity housing the tissue sample for all the coils. Two opening heights (H=450 and 1350 mm) were included in the coil set to enable the insertion of either two type of encasing (slide or dual coverslip) covering tissue thicknesses ranging from 5 to 1000 mm.

MRI data acquired with our various RF histology coils from thin mouse and human tissue sections perfectly matched with light microscopic images as shown in Figure 3. The smallest and most sensitive dual-coverslip histology coil (W=12 mm, IL=12 mm, OL=24 mm, H=450-µm) can accommodate tissue portions to give the highest anatomical detail as illustrated in Figure 3. The examples shown in (a) and (b) correspond to T2*- & T1-weighted images from an excised 60 mm mouse olfactory bulb mounted on dual coverslips, respectively.

Conclusion

In conclusion, our results demonstrate that the flat coils designed for this study are unique structures for the direct imaging of histology slides by offering an unrivaled trade-offs between an excellent homogenous RF coverage and an optimal sensitivity. Large tissue samples (FOV=20-mmx40-mm) can be imaged in less than 8-hours with the largest coil with a minimum 60-µm section (in-plane: 60-µm). Under similar conditions, tissues that can fit a FOV=10-mm x 8-mm could be acquired in less than 2-hours using the smallest coil we have designed. Doping the buffer solution with 5-mM GdDTPA leads to 2.4x gain in SNR enabling the possibility to acquire tissue section as thin as 10-um thickness in 8-hours when combined with our smallest histology coil.

Clinical Relevance

This probe design offers the unique opportunity for unparalleled image co-registration between MRI and light microscopy that would be otherwise unachievable using conventional resonators. The considerable gain in sensitivity (up to 6.7-fold) obtained relative to any conventional CP coil will enable the acquisition of highly resolved images using tissue section thicknesses commonly used for histology within their standard mounting that can be obtained from typical biopsies.

Figures and tables

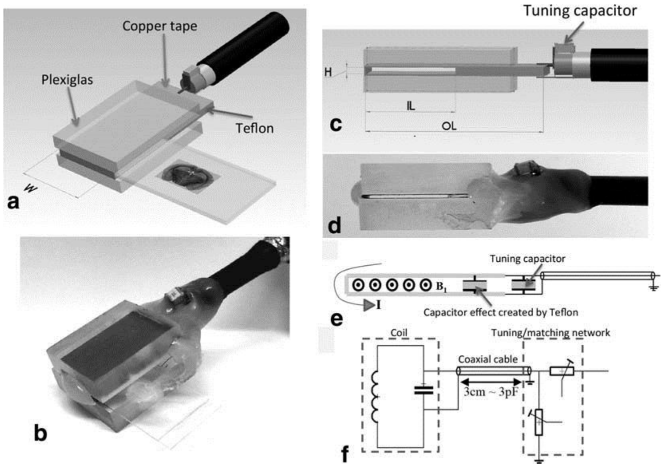

Figure 1: Principle and overview of the histology slide probe. a: Schematic of the planar coil structure to accommodate histology tissue section. The choice of the width (W) defines the extent of the homogeneous RF field of interest covering the tissue sample to be imaged within a slide. b: The height (H) of the opening was chosen to insert a tissue encasing slide setup to accommodate the pairing of either a glass/coverslip (_1350 mm) or two coverslips (_450 mm). c: The inner length (IL) comes in two dimensions to house commercially available 12-mm-wide coverslips or 25-mm-wide slides. The resulting OL of the probe is approximately twice the IL as prescribed by Meadowcroft et al. (2007). For the sake of simplicity of the design, the construction of the structures described in this work was made in-house using thermo-glue as in (b and d). e: The current traversing the slotted resonator induces a transverse B1 RF field after crossing a square Teflon-based capacitive insert extending throughout the whole unused but required OL of the coil. f: The tuning/matching (T/M) of all the probes is insured by two variable capacitors (Voltronics Corps., Salisbury, MD) via a double-shielded coaxial cable. All probes can be easily interchanged with the same T/M circuit.

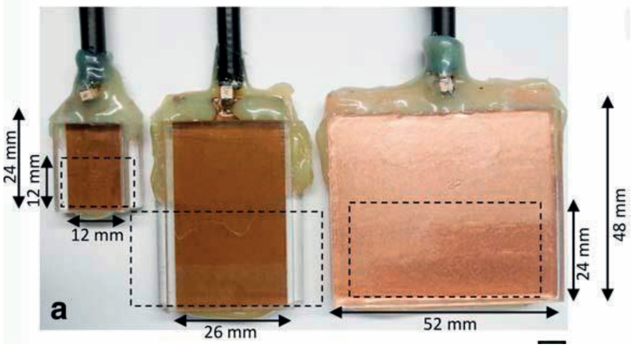

Figure 2: A set of five histological slide coils were developed to accommodate both different sample sizes and slide setup. a: The coils were designed in three sizes to house encasing based on dual coverslips for tissue sections up to 100 mm thick (insert H≈450 mm). The smallest coil (W= IL=12 mm, OL=24 mm) was designed to insert 24x12 mm coverslips. The middle coil shown is of similar size (W=26 mm, IL=24 mm, OL=48 mm) to the structure previously reported (35) to enable the partial examination of standard size slides (50x24 mm). The larger structure (W=52 mm, IL=24 mm, OL =48 mm) shown at right permits the full coverage of slides of the same size. All the coils proved to have an excellent RF planar homogeneity assessed experimentally using MRI with a phantom composed by a thin layer of water doped with 2.5 mM Gd-DTPA sandwiched between two coverslips.

Figure 3: Highly detailed examples obtained from 60-μm tissue sections using the smallest and most sensitive coverslip histology coil designed (W =12 mm, IL=12 mm, OL=24 mm, H=450μm). The first image set (a) and (b) correspond respectively to T2*- and T1-weighted images with 30 mm in-plane resolution obtained from the mouse olfactory bulb coregistered with the corresponding light microscopy (c). The MRI contrast on both images helps identify the following cell layers: (1) olfactory ventricle, (2) combines the internal plexiform layer, granule cell layer and ependymal layer, (3) mitral cell layer, (4) external plexiform layer, (5) glomerular layer, (6) olfactory nerve layer. The coil can also accommodate coronal mouse brain sections depicted by the example of a 50-mm in-plane MRI showing clearly the white matter track and different small tissue structures in (d) T2*- and (e) T1-weighted images in perfect alignment with (f) histology.

Magnetic Characteristics of Multiple Sclerosis by Quantitative Susceptibility Mapping

W Chen[1], S Gauthier[2], T Liu[1], C Langkammer[3], S Ropele[3], J Communale[1], A Gupta[1], and Yi Wang[1]
[1]Radiology and [2]Neurology, Cornell University, New York, USA
[3]Neurology, Medical University of Graz, Austria

Introduction

Iron as a transition metal with a unique chemical property that it can readily donate or receive an electron is an essential facilitator of basic biochemical activities of cells. Excessive iron may present in deep gray matter structures including basal ganglia. Pathological iron deposits may present in white matter inflammation sites. The incompletely known iron deposition may be both consequence and promotion of MS pathogenesis. Activated microglia/macrophages express ferritin due to up-regulation of transferrin receptor in response to inflammatory stimuli. Iron overload can lead to oxidative stress damaging macromolecules including proteins, lipids and DNA, and can cause activated microglia increase production of proinflammatory mediators in MS. Additionally, demyelination may also contribute to magnetic susceptibility increase.

Methods & Results

Tissue magnetism is a property of molecular electrons that respond to an applied magnetic field. For example, unpaired electrons in ferric iron make it highly paramagnetic. Magnetic susceptibility can be detected as a hypointensity in traditional gradient echo (GRE) MRI. However, this blooming T2*/SWI hypointensity varies easily with imaging parameters including TE, B0, object orientation, and voxel size. We have developed quantitative susceptibility mapping (QSM) from the typically ignored phase data in MRI by solving the magnetic field to susceptibility source inverse problem. The deconvolution in QSM removes the blooming artifacts and enables accurate localization and quantification of susceptibility sources. We apply QSM to study in brains of multiple sclerosis (MS) patients. All subjects underwent 3T MRI including 3D multiecho GRE, from which QSM was constructed.

I) Mean susceptibilities in the basal ganglia were measured on 68 patients (26 with clinically isolated syndrome, 42 with relapsing-remitting MS) and 23 control subjects, and were compared between MS phenotypes (clinically isolated syndrome, MS) and the control subjects by using analysis of variance. Compared with control subjects, patients with MS and clinically isolated syndrome had increased (more paramagnetic, $p<.01$) magnetic susceptibilities in the basal ganglia with patient neurological deficits (Fig.1).

II) Magnetic susceptibilities of MS lesions were studied on 32 clinically confirmed MS patients. To estimate the ages of MS lesions (hypointense on T2 weighted images), all available prior MRIs (performed 0.3 – 10.6 years ago) were examined. MS lesions' susceptibilities relative to normal appearing white matter (NAWM) were obtained from QSM images. We found 162 MS lesions being age measurable with 6 becoming only visible on QSM. The relative susceptibility on average was 1, 35, 42, -2, 1, and 1 ppb (part per billion) for early enhancing lesions (0y), early non-enhancing lesions (0 –2y), lesions aged 2 –4y (none aged 4–6y), 6 –8y, 8 –10y, and >10y respectively (Fig.2).

Conclusion

Magnetic susceptibilities of basal ganglia in MS brains increase with neurological deficits, which may reflect neurodegeneration. Magnetic susceptibilities of MS lesions increase rapidly as lesions change from enhancing to non-enhancing, gain high susceptibility relative to NAWM and gradually dissipate as lesions age, which may reflect demyelination activities in MS lesions.

Clinical Relevance

Quantitative susceptibility mapping (QSM) enables accurate noninvasive measurement of tissue magnetic property. Magnetic susceptibility is a biomarker for iron deposition in neurodegeneration and for demyelination in multiple sclerosis and may serve as an outcome measurement point for anti-inflammatory, neuroprotective and neuroregenerative treatments.

Figures and tables

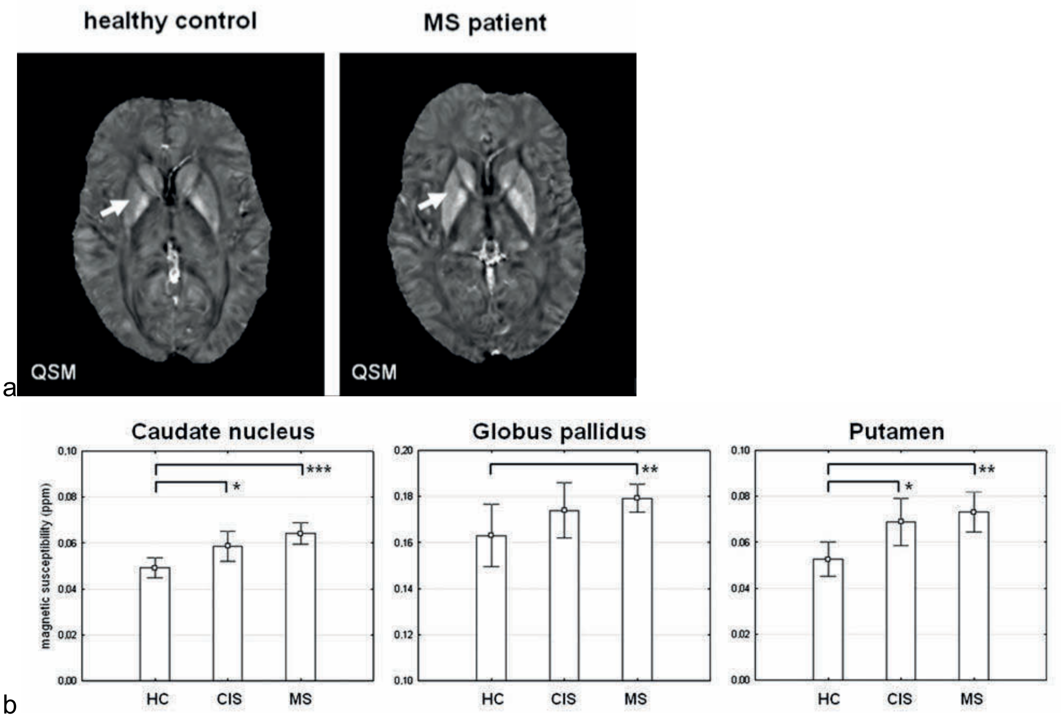

Fig.1. a) iron deposition measured on QSM in healthy control and MS patients. b) iron increases significantly with neurologicla deficit (HC=healthy control, CIS=clinical isolated symptom, MS=relapsing/remitting MS).

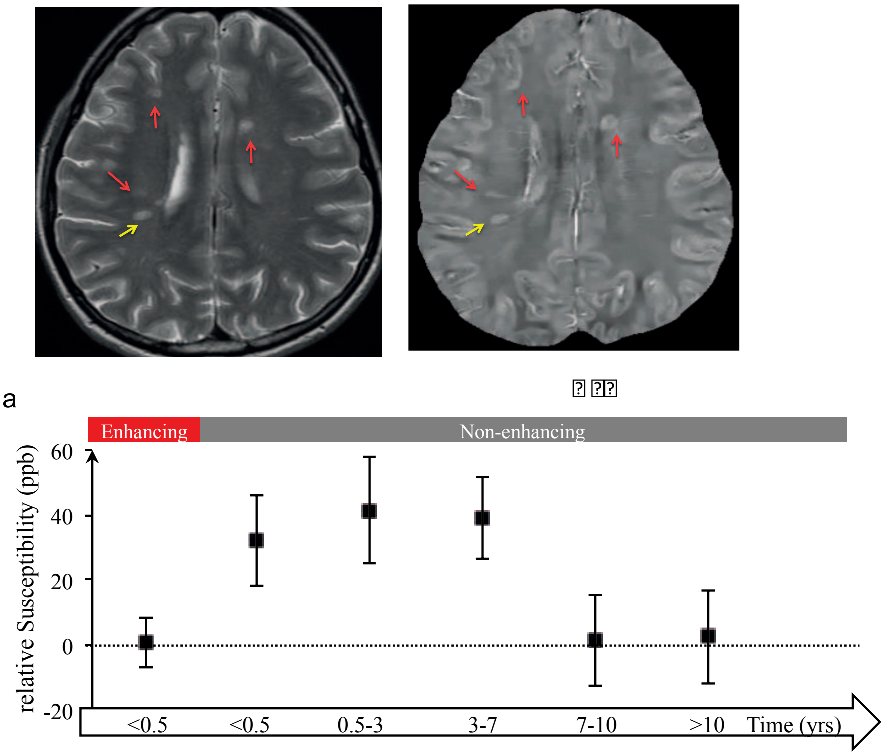

Fig.2. a) MS lesions in standard T2 weighted imaging (T2w) and QSM, with different features showing on QSM. b) MS lesion susceptibility relative to NAWM at various lesion ages.

Brain Perfusion MRI with Dynamic Quantitative Susceptibility Mapping

Bo Xu[1,2], Pascal Spincemaille[2], Tian Liu[3], Nandadeepa Thimmappa[2], Silvina Dutruel[2] Martin Prince[2], Yi Wang[1,2]
[1]Cornell University, Ithaca, USA; [2]Weill Cornell Medical College, NY, USA; [3]MedImageMetric LLC, NY, USA

Introduction

Quantitative Susceptibility Mapping (QSM) measures the susceptibility which can be used to directly quantify contrast agent concentration in perfusion MRI. In this work, we proposed a multi-echo spiral GRE sequence combined with TRACER reconstruction to get high temporal frame rate dynamic phase images, which are used to generate dynamic susceptibility maps with MEDI, a dipole inversion algorithm. Perfusion CBF, CBV and MTT maps are computed based on [Gd] time courses as in standard DSC MRI.

Methods & Results

***Pulse sequence*:** A 5-echo 3D stack spirals GRE sequence was developed (Fig.1) with gradient moment nulling on all axes. Consecutive spiral leaves were rotated over the golden ratio angle.
Data acquisition: *N*=3 healthy volunteers were scanned using an 8-channel head coil. Ten ml of Gadovist (1mM) injection at 3ml/s was initiated 20s after scan start. $TR/TE_{min}/TE_{max}$ = 32.3/0.8/26.3ms, FA=15˚, BW=±125KHz, matrix size = 200×200×24, voxel size = 1.1×1.1×3mm^3.
Multi-echo complex image frame: the complex MR image was reconstructed with TRACER at a temporal frame rate of 0.7s by constraining the temporal change between consecutive frames.
Dynamic QSM: The phase data of the first frame was sutracted from all frames to obtain field map induced by Gd. This field map was feed into MEDI to compute susceptibility map and [Gd] was obtained by scaling the susceptibility map with the Gd^{3+} mol susceptibility (308 ppm/mol). All the [Gd] map was baseline corrected assuming the concentration of CSF is zero. **Results:** In all volunteers, sub-second dynamic susceptibility maps were successfully obtained. Fig. 2 shows the arterial input function obtained from the middle cerebral artery. The peak concentration is about 5mM and gets t o1mM after 90s. As the concentration is computed directly from susceptibility, no conversion is needed. Fig.3 shows the perfusion CBF, CBV and MTT maps obtained from the AIF and tissue concentration time courses[3]. The residual function is computed by performing SVD deconvolution without a cutoff threshold of 30%.

Conclusion

We present a dynamic QSM technique for 3D [Gd] mapping at sub-second frame rate for quantiative perfusion MRI. This techqniue exploits the linear relationship between susceptibility and Gd concentration, providing a direct way for absolution perfusion quantification. Multi-echo acquisition increases the sensitivity for phase measurment. TRACER reconstruction with sub-second temporal frame rate is more likely to capture the peak time and less prone to error.

Clinical Relevance

This work aims to improve the current brain perfusion quantification by using quantitative susceptibility mapping technique. This method can potentially increase the accuracy of brain perfusion by improving the arterial input function measurement and absolute quantification of tissue contrast enhancement. These will be useful in brain stroke and cancer patient.

Figures and tables

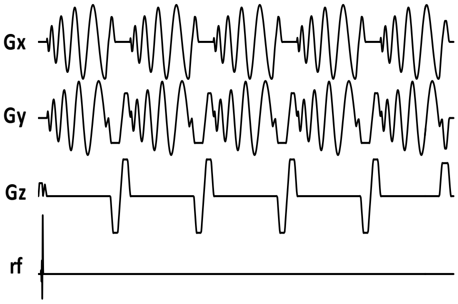

Fig. 1 Multi-echo spiral GRE sequence

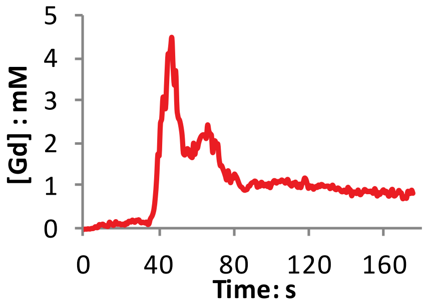

Fig. 2 Arterial input function

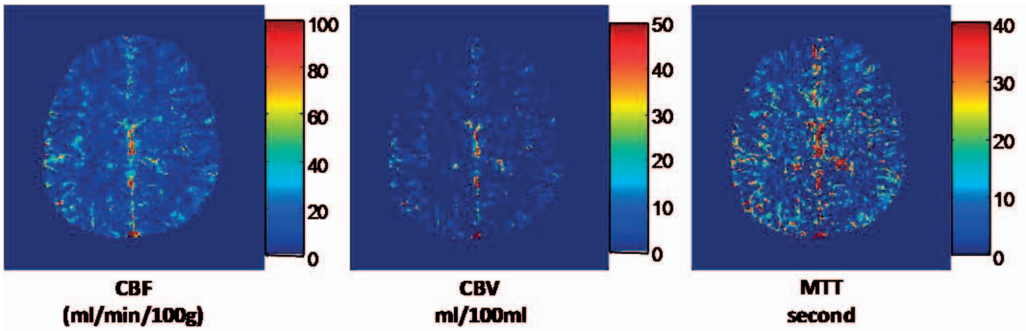

Fig. 3 CBF, CBV and MTT maps

Cerebovascular Reactivity at Hypercapnia Measured with Arterial Spin Labeling in Multiple Sclerosis

Yongxia Zhou, Hina Jaggi[1], Joseph Herbert[1], Robert I. Grossman[1], Yulin Ge[1]
[1]Radiology/Center for Biomedical Imaging, New York University School of Medicine, New York, NY, United States

Introduction

Measuring cerebro-vascular reactivity (CVR) with cerebro-blood flow (CBF) using ASL technique had just been reported in controls [1]; but the CVR imaging of MS patients has not been evaluated before. The objective of this study was to examine patients with early MS to address whether there is CVR impairment and whether this correlates with lesion or other non-invasive MRI imaging features.

Methods & Results

Twenty-one MS patients with clinically definite relapsing-remitting MS and 20 demographically-similar healthy volunteers were recruited. EPI-based ASL was performed on a 3T whole-body MR scanner (Siemens Magnetom Tim Trio; Siemens Healthcare, Erlangen, Germany) using a 12-channel head coil with a gradient echo EPI sequence. CO_2 is a potent vasodilator, and an increase of CO_2 tension in blood (referred to as hypercapnia) is known to cause CBF increase. Such CBF changes were measured with a standard pseudo-continuous arterial spin labeling (pCASL) MRI at 3T, with quantitative CBF (ml/min/100g) maps generated during both room air and hypercapnia (mixed 5%CO_2, 21%O_2, and 74%N_2) exposure. The CVR was calculated as % (percentage change in CBF comparing CO_2 inhalation to room-air breathing) divided by $\Delta EtCO_2$ (mmHg).

There were significantly increases of CBF with CO_2 challenge in both groups; and the percentage change of CBF at CO_2 condition compared to room air was correlated significantly with the $EtCO_2$ pressure in control group. There was significantly correlation (r=0.55, P=0.0002) between the CBF measured with ASL and with phase-contrast at baseline. The global CVR (average of the normalized CBF-CVR with end-tidal CO_2 in the gray matter and white matter) showed a significantly reduction of the global average in MS patients (3.12±0.52 %/mmHg) compared to control (5.16±0.56 %/mmHg) group (P=0.01) (Figure). There was altered CVR with different types of lesions. We also found that the combination of all five hemodynamic measurements can achieve 98% of classification accuracy using the All-Dimensional (AD) tree classifier. There was a significant correlation between the average parenchymal CVR and brain parenchymal ratios in all subjects (r=0.33, P=0.04). In addition, there was a significant correlation between average CVR from gray matter and lesion volumes in MS patients (r=-0.46, P=0.03).

Conclusion

We had shown over 50% decrease of average whole brain parenchymal CVR in MS; as well as a tight correlation between CVR in MS and lesion load. The WM lesions, as expected, showed a low CBF at baseline and almost no change of CBF after CO_2; suggesting a loss of cerebrovascular response. The combinations of all the hemodynamic measurements for accurately classifying MS from controls indicated that CVR (together with age, and $CMRO_2$) was the most essential feature among all the measurements.

Clinical Relevance

Our results suggest that the impaired cerebrovascular response during neuronal activities may affect the effective oxygen delivery particularly to the previously active healthy neurons with increased oxygen demand (activity-induced hypoxia). And CVR impairment reflecting the hemodynamic deficits might lead to neurodegeneration in MS over time.

Figures and tables

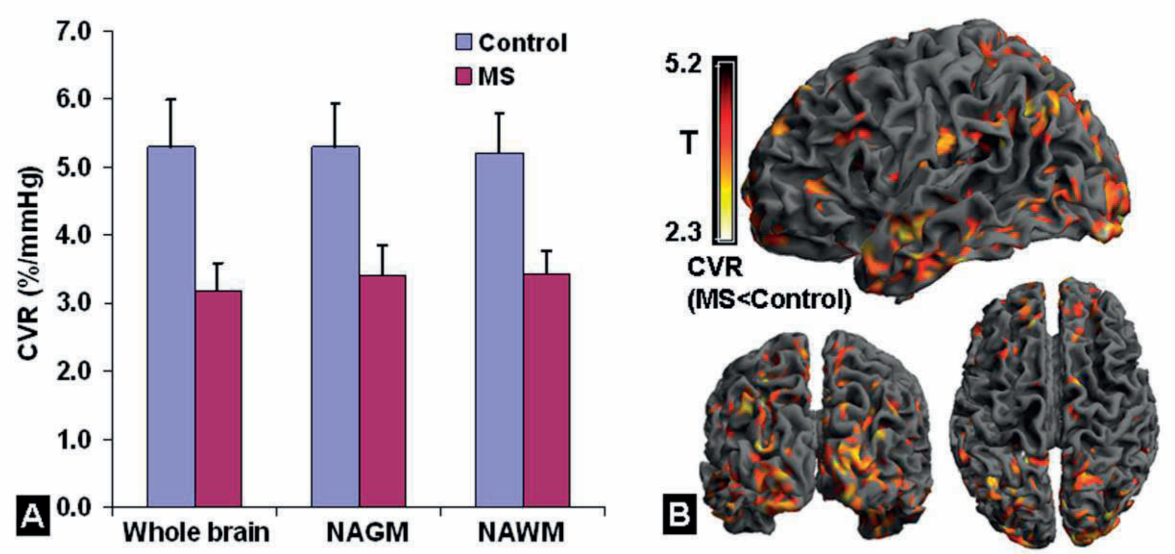

Figure. CVR differences in controls and MS patients. **A**: significantly reduced global whole brain (P=0.01), NAGM (P=0.01) and NAWM (P=0.02) CVR in MS compared to control group. The CVR, however, was not statistically different between GM and WM at either control or MS group (P>0.7). The CVR in lesions are close to zero with a 0.03%/mmHg mean and 0.10%/mmHg standard deviation. **B**: Voxel-wise group comparisons of f normalized CVR responses between two groups, with regional CVR of MS less than of control in the occipital, somatosensory, temporal, parietal and frontal regions (P<0.05).

Longitudinal Regional Brain Volume Changes in Mild Traumatic Brain Injury

Yongxia Zhou, Andrea Kierans, Damon Kenul, Yulin Ge, Joseph Rath, Joseph Reaume,
Robert I. Grossman, Yvonne W. Lui

Radiology/Center for Biomedical Imaging,
New York University School of Medicine, New York, NY, United States

Introduction

About 20% of patients have persistent post-concussive syndrome (PCS) within 6 months to 1-year after mild traumatic brain injury (MTBI), and there is recent evidence showing that these patients have microstructural, metabolic and functional changes to the brain using a variety of new neuroimaging techniques [1]. Whether a single concussive episode and the resultant microstructural, metabolic and functional changes that have been associated with such an injury culminate in chronic brain alterations such as atrophy is not known. The purpose of this study is to examine longitudinal changes in regional brain volume using automated whole brain parcellation in a well-defined cohort of MTBI patients and correlate regions of brain atrophy with quantitative neurocognitive assessment as well as clinical symptom scale measures.

Methods & Results

Of a group of 28 MTBI patients, 19 were followed for one year. These were compared with 22 matched controls, and 12 of whom were followed for one year. All MRI experiments were performed at the 3T Trio body MRI scanner (Siemens Tim Trio, Erlangen, Germany) using a 12-channel head coil. The 3D gradient echo T1-weighted MPRAGE protocol with the following parameters: (TR/TE/TI=2300/2.98/900ms, flip angle=9^o, resolution=1x1x1mm^3) was used to obtain structural images.To validate the results obtained using FreeSurfer, two additional commonly-used algorithms were used. For comparison between MTBI patients and controls, based on MPRAGE data, whole-brain voxel-based morphometry (VBM) package in FSL (http://www.fmrib.ox.ac.uk/fsl/vbm) was used for segmentation and gray matter density analysis. For longitudinal comparison of intra-subject initial and follow-up regional brain volume, after removing extracranial tissues using AFNI (http://afni.nimh.nih.gov/afni/), the boundary shift integral (BSI) method [3] was applied to measure the global atrophy rate and ventricular enlargement.

In patients, there was significant decrease in WM volume of the bilateral anterior cingulate, the cingulate isthmus and GM of precuneus regions over one-year (corrected P<0.05). No volumetric differences were found between MTBI patients at the time of their initial visit and controls after normalization. Almost no changes in volume were detected in any regions in controls followed for one year (*Figure 1A*). Corroborative results comparing patients at one-year follow-up to controls showed lower WM volume in the rostral anterior cingulate (rAC), caudal anterior cingulate (cAC) and left isthmus of cingulate, as well as lower GM volume in right precuneus (*Figure 1B*). These cross-sectional differences still remain after accounting for individual brain size differences and adjustment for multiple comparisons with Bonferonni correction (corrected P<0.05). Group analyses based on VBM method between MTBI patients at one-year follow-up and controls (corrected P<0.05) confirmed the pattern of regional atrophy seen using Freesurfer (bilateral rAC and cAC, and posterior precuneus regions; *Figure 1C*). Consistent with Freesurfer regional findings, group analyses based on VBM method between MTBI patients at initial visit and controls showed no significant group difference.
BSI results using longitudinal data in MTBI patients showed significant correlations between the whole-brain boundary shift and the ventricular enlargement (r=0.62, P=0.003). The average BSI between MTBI patients at one-year follow-up and initial visits is 7.6 CC (longitudinal atrophy), which is about two times the BSI of controls. And there was significant correlation between the supartentorial volumetric change measured from Freesurfer and the whole-brain BSI (r=0.54, P=0.042).

Conclusion: Our observations demonstrate that regional brain atrophy is not exclusive to moderate and severe TBI, but may be seen following mild injury as early as one year after injury. The anterior and isthmus of the cingulum and precuneal regions may be distinctively vulnerable. We find an association between regional volume loss and neurocognitive performance / clinical symptom scores. Such associations may relate to dysfunction within these specific brain regions: the anterior cingulum is known to play a role in affective and cognitive domains and the precuneus is highly linked to associative cortex.

Clinical Relevance

A single concussive episode can result in global and regional brain atrophy1 year after injury. Correlations between cingulate WM loss and neurocognitive performance and clinical symptom scales, including the Beck Anxiety Inventory and the Post Concussion Symptom Scale, support the notion that chronic pathophysiologic changes occur to the brain that may manifest as persistent symptoms after mild head injury.

Figures and tables

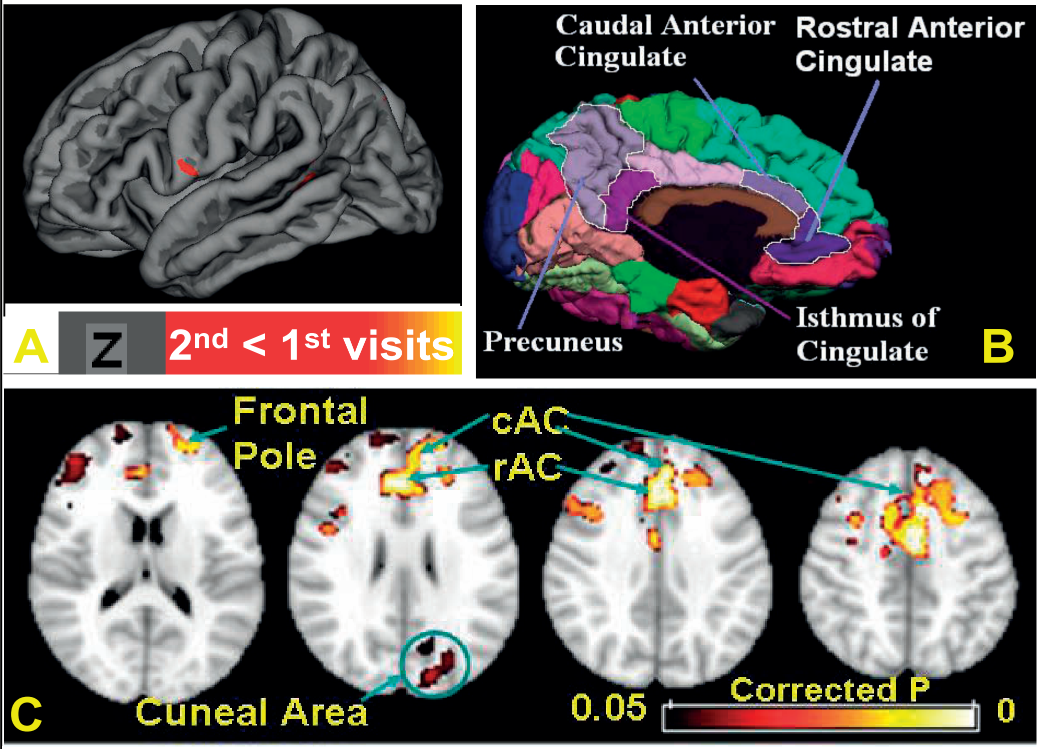

Figure1. **A**: There were no significant changes (minimal |Z|<2, P>0.05) for controls at 1-year follow-up compared to baseline for almost all the brain regions except very mild atrophies in the frontal and temporal areas. **B**: Regional volumetric brain analysis showing the medial surfaces of a volume-rendered image of the left cerebral hemisphere; the labeled regions demonstrated significant volume changes (corrected P<0.05) in MTBI patients after one-year follow-up in comparison to initial visits or controls. **C**: Validation of cross-sectional results based on VBM method between MTBI patients at one-year follow-up and controls (corrected P<0.05): VBM showed similar patterns of regional volumetric atrophies with Freesurfer findings (e.g. atrophies in the regions of rostral /caudal anterior cingulate and precuneus / cuneus areas).

Abstracts, Cancer & Body Imaging Category

Automated Synthesis of PET Imaging Probes for Proliferation of Cancer and Immune Cells

Mark Lazari[1,2], Jeffrey Collins[1,2], Kevin Quinn[1,2], Shane Claggett[1,2], Pei Yuin Keng[1,2], Michael E. Phelps[1,2], Nagichettiar Satyamurthy[1,2], Melissa Esterby[1,2,3], Dave Bates[3], R. Michael van Dam[1,2]

[1]Crump Institute for Molecular Imaging, [2]Department of Molecular & Medical Pharmacology, UCLA, Los Angeles, CA, 90095 USA; [3]Sofie Biosciences, Inc., 6162 Bristol Parkway, Culver City CA 90230

Introduction: Deoxycytidine kinase (dCK), a rate-limiting enzyme in deoxyribonucleoside salvage, phosphorylates and therefore activates nucleoside analogs (ex. Gemcitabine) that are used routinely in anti-cancer therapy; it is often downregulated in many neoplastic cells. Imaging probes that target dCK (ex. 1-(2'-deoxy-2'-[^{18}F]fluoroarabinofuranosyl) cytosine (D-[^{18}F]FAC) may allow the stratification of patients into likely responders and non-responders with dCK-dependent prodrugs however their complex, manual synthesis remains a major hurdle to clinical implementation. Automation of synthesis is the leading strategy to increase availability of commonly produced ^{18}F-labeled PET probes (e.g. 2-[^{18}F]fluoro-2-deoxy-D-glucose ([^{18}F]FDG) and [^{18}F]fluorothymidine ([^{18}F]FLT)) and is critical to the widespread use of valuable molecular imaging probes tied to important biology of disease or therapeutic targets such as the [^{18}F]FAC family of probes. Importantly, due to existing infrastructure considerations of radiopharmacies, automated synthesis modules need to support research, optimization, and routine production of a variety of radiopharmaceuticals. Here we report the development of ELIXYS – an automated, robotic, cassette-based, and multi-pot synthesis module to support both the research and clinical demands for routine production of complex chemical syntheses including D-[^{18}F]FAC.

Methods & Results: Three identical, independent reaction vessels were moved among dedicated 'stations' for reagent addition, sealed reaction, evaporation, and transfer. Exposure of tubing and valves to high pressures was eliminated. Purification with silica cartridges was performed after fluorination, coupling with cytosine, (ie. between reaction vessels), and HPLC for the final product. To facilitate routine synthesis, a cassette-based reagent delivery system that contains all wetted paths and reagents was used. Each cassette is comprised of reagent storage vials, gaskets for sealing the reaction vial, purification cartridges, and disposable valves. Non-optimized decay-corrected radiochemical yields (RCY%) were D-[^{18}F]FAC 31 ± 6 (n=5); L-[^{18}F]FMAU 45 ± 2 (n=3); [^{18}F]FDG 61 ± 13 (n=6); [^{18}F]SFB 70 ± 9 (n=5); [^{18}F]FLT 12 ± 2 (n=5).

Conclusion: With the growing use of PET for *in vivo* molecular imaging, the availability of PET probes will soon become the key-limiting factor for molecular medicine strategies. D-[^{18}F]FAC, L-[^{18}F]FMAU, [^{18}F]FDG, [^{18}F]SFB, and [^{18}F]FLT were successfully synthesized with exactly the same hardware configuration, requiring only changes in software and setup (reagents). Once optimized, we expect ELIXYS to be used for safe, reliable, routine, automated production of essentially all classes of ^{18}F-labeled probes for use in preclinical and clinical environments.

Clinical Relevance: The possibility of applying predictive imaging to patients with late stage disease could save valuable, often critical, treatment time and enable the use of the appropriate treatment to be administered at the appropriate time.
Furthermore, ensuring a flexible solution for the optimization and routine production of a variety of molecular imaging probes will reduce time and cost associated with the translation of such agents for clinical use, ultimately making molecular medicine more accessible.

Figures and tables

Figure 1: Front view of the ELIXYS radiosynthesizer, opened for accessibility prior to a reaction.

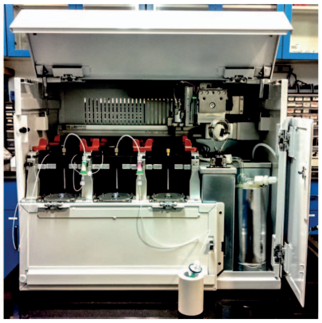

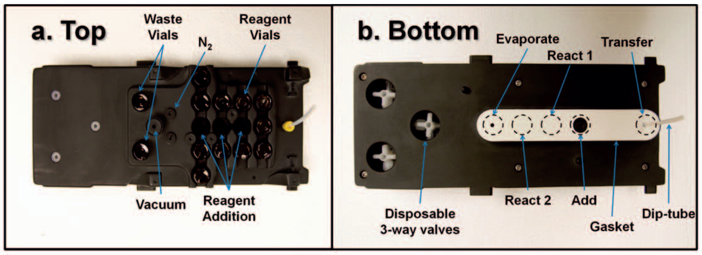

Figure 2: Disposable cassette. **a** Sealed reagent vials are placed upside-down and three empty spaces are reserved for reagent addition. **b** At each station, the reaction vial pneumatically seals against a PTFE coated silicone gasket.

Table 1: Several sample radio-TLC or UV/radio-HPLC chromatograms are listed for each probe. The data shows non-optimized syntheses and purifications adapted from the literature. **Radio-TLC.** Samples of reaction intermediates or products were analyzed via TLC. TLC plates were scanned with a Raytest *mini*Gita. For [^{18}F]FDG, all steps were verified with radio-TLC. The middle chromatogram represents the deprotection efficiency and the right chromatogram is the purified product. Optimization is needed to remove additional residual $^{18}F^-$ ion. **HPLC.** Samples were purified via semi-preparative HPLC (KNAUER), and collected fractions were confirmed by analytical HPLC (KNAUER Smartline) co-injected with the respective cold standard.

D-[^{18}F]FAC	**Chromatogram:** Post-Fluorination Radio-TLC **Stationary Phase:** Silica gel **Mobile Phase:** 95:5 MeCN:H_2O **Mean:** 87 ± 7% (n=5)	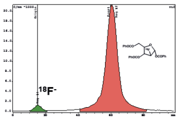	**Chromatogram:** Semi-Preparative HPLC **Stationary Phase:** 5μm C18 (Gemini–NX) **Mobile Phase:** 1:99 EtOH:10mM $NH_4H_2PO_4$ **Flow Rate:** 5.0 mL/min	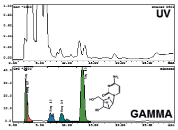	**Chromatogram:** Analytical HPLC **Stationary Phase:** 5μm C18 (Luna) **Mobile Phase:** 10:90 EtOH:50mM NH_4OAc **Flow Rate:** 1.0 mL/min	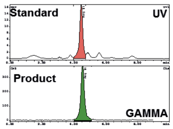
L-[^{18}F]FMAU	**Chromatogram:** Post-Fluorination Radio-TLC **Stationary Phase:** Silica gel **Mobile Phase:** 95:5 MeCN:H_2O **Mean:** 82 ± 0% (n=3)	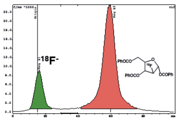	**Chromatogram:** Semi-Preparative HPLC **Stationary Phase:** 5μm C18 (Gemini–NX) **Mobile Phase:** 4:96 MeCN:50mM NH_4OAc **Flow Rate:** 5.0 mL/min	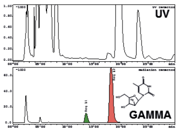		
[^{18}F]FDG	**Chromatogram:** Post-Fluorination Radio-TLC **Stationary Phase:** Silica gel **Mobile Phase:** 95:5 MeCN:H_2O **Mean:** 77 ± 13% (n=6)	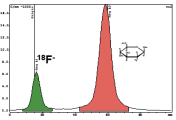	**Chromatogram:** Post-Hydrolysis Radio-TLC **Stationary Phase:** Silica gel **Mobile Phase:** 50:50 EtOAc:Hexane **Mean:** 98 ± 3%	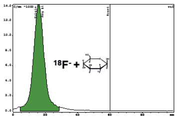	**Chromatogram:** Post-Purification Radio-TLC **Stationary Phase:** Silica gel **Mobile Phase:** 95:5 MeCN:H_2O **Mean:** 88 ± 7%	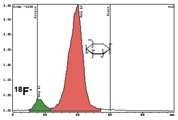
[^{18}F]SFB	**Chromatogram:** Post-Fluorination Radio-TLC **Stationary Phase:** Silica gel **Mobile Phase:** 95:5 MeCN:H_2O **Mean:** 95 ± 3% (n=5)	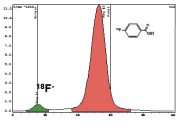	**Chromatogram:** Semi-Preparative HPLC **Stationary Phase:** 5μm C18 (Luna) **Mobile Phase:** 50:50 MeCN:H_2O 0.1% TFA **Flow Rate:** 3.0 mL/min	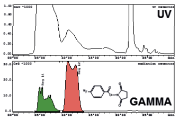	**Chromatogram:** Analytical HPLC **Stationary Phase:** 5μm C18 (Luna) **Mobile Phase:** 50:50 MeCN:H_2O 0.1% TFA **Flow Rate:** 1.0 mL/min	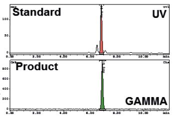
[^{18}F]FLT	**Chromatogram:** Post-Fluorination Radio-TLC **Stationary Phase:** Silica gel **Mobile Phase:** 50:50 EtOAc:EtOH	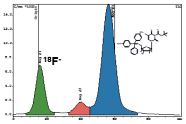	**Chromatogram:** Semi-Preparative HPLC **Stationary Phase:** 5μm C18 (Luna) **Mobile Phase:** 8:92 EtOH:20mM KH_2PO_4 **Flow Rate:** 5.0 mL/min	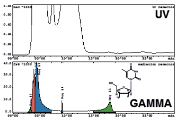	**Chromatogram:** Analytical HPLC **Stationary Phase:** 5μm C18 (Luna) **Mobile Phase:** 10:90 EtOH:H_2O **Flow Rate:** 1.0 mL/min	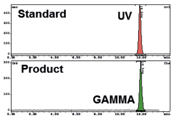

Table 2: Decay-corrected radiochemical yield (RCY) for each probe. In most cases, non-optimized results are comparable to other reports.

Probe	Decay-corrected RCY (%)
D-[^{18}F]FAC	31 ± 6 (n=5)
L-[^{18}F]FMAU	45 ± 2 (n=3)
[^{18}F]FDG	61 ± 13 (n=6)
[^{18}F]SFB	70 ± 9 (n=5)
[^{18}F]FLT	12 ± 2 (n=5)

Diagnostic performance of delayed hepatobiliary imaging post gadoxetic acid combined with DWI vs. dynamic contrast-enhanced imaging for HCC detection: Pilot Data

Cecilia Besa MD, Nancy Cooper MD, Sara Lewis MD, Amita Kamath, Sasan Roayaie MD, Isabel Fiel, Bachir Taouli MD

Icahn School of Medicine at Mount Sinai

Purpose: To compare the diagnostic performance of hepatobiliary phase imaging (HBP) post gadoxetic acid combined with DWI vs. dynamic contrast-enhanced (CE) MRI for hepatocellular carcinoma (HCC) detection.

Methods: 203 consecutive patients with liver disease who underwent gadoxetic acid-enhanced MRI for HCC screening from 01/2011 to 12/2011 were included in this IRB approved retrospective single center study. 96 patients with HCC and 107 patients without HCC (controls) were identified. Two sets of images were analyzed independently by 3 readers: HBP/DW-set (HBP at 20 min post injection + DWI using b 0-50-500-1000) and dynamic CE-set (CE imaging including pre-contrast, arterial, portal venous and late venous 3D T1WI after the administration of 10 mL of gadoxetic acid). Readers had access to T2WI and T1 in- and opposed-phase sequences for both data sets to allow differentiation of common benign lesions such as hemangiomas and cysts. Reference standard was represented by consensus interpretation of 2 separate readers using combination of imaging, clinical and pathologic data. HCCs were defined as lesions > 1 cm with hypointensity on HBP and/or restricted diffusion (hyperintensity on b500/1000 and low ADC) on the HBP/DW-set and typical wash-in/wash-out on the CE-set. Per lesion and per patient sensitivity, specificity, PPV and NPV were calculated for each image set.

Results: Pilot data is presented here. 101 initial patients with 75 HCCs (mean size 22 ± 9 mm, range, 11-63 mm) were evaluated by two independent readers. 63/75 (84%) HCCs demonstrated hypointensity on HBP with restricted diffusion and 60/75 (80%) had typical wash-in/wash-out. A combination of hypointensity and restricted diffusion yielded a per patient sensitivity, specificity, PPV and NPV of 80%, 92.6%, 90.9% and 82.4% for reader 1 and 84%, 96%, 95.5% and 85.9% for reader 2 for the HBP/DW-set and 88%, 98%, 97.7% and 89.2% for reader 1 and 92%, 100%, 100% and 92.73% for reader 2 for AASLD criteria, respectively. When a combination of hypointensity on HBP and/or restricted diffusion was evaluated, sensitivity increased from 80% to 90% for reader 1 and 84% and 92% for reader2 for the HBP/DW-set, with slightly decreased in specificity. False positive rate on HBP/DW-set for lesions with hypointensity and restricted DWI was 5/101 (0.05%) and 2/101 (0.02%) for readers 1 and 2 respectively, with false positives corresponding to hemangiomas, nodular confluent fibrosis, perfusional abnormalities and dysplastic nodule.

Conclusion: Pilot data demonstrate similar sensitivity, slightly lower specificity and equivalent NPV when using a combination of HBP imaging post gadoxetic acid and DWI compared to dynamic phase images for detection of HCC > 1 cm. This combination has potential for HCC screening.

Clinical Relevance: Use a fast post-contrast liver MRI protocol consisting of gadoxetic acid injection outside the MRI room with DWI can be proposed for HCC screening, which could provide shorter and possibly less expensive MRI exams.

Figures and tables:

Figure 1: Hypovascular HCC (arrows) in the right hepatic lobe showing lack of arterial enhancement (a) with hypovascularity on portal venous phase (b). The lesion demonstrates restricted diffusion on b1000 (c) and hypointensity on HBP post Gd-EOB-DTPA (d).

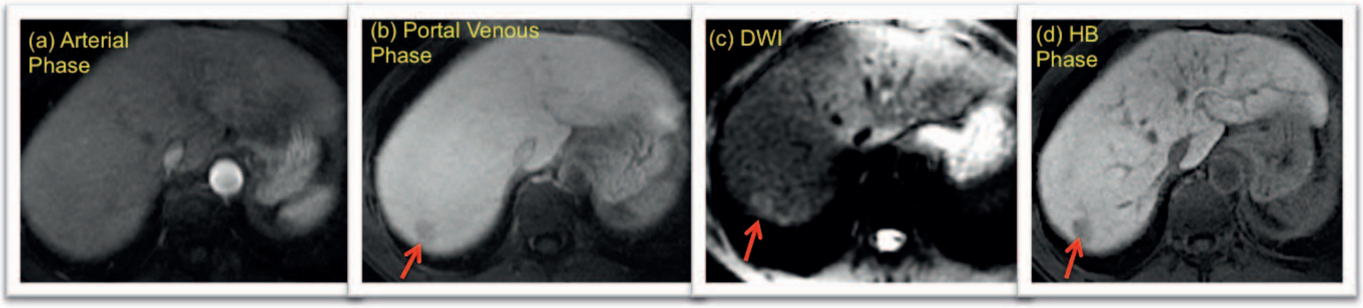

Table 1: Sensitivity, specificity, PP and NPV of MRI for HCC detection per-patient (101 patients with 75 HCCs)

	Sensitivity	Specificity	PPV	NPV
Observer 1				
CE-Set	88%	98%	97.7%	89.2%
HBP/DW-set*	80%	92.6%	90.9%	82.4%
HBP/DW-set**	90%	90.2%	90%	90.2%
Observer 2				
CE-Set	92%	100%	100%	92.73%
HBP/DW-set*	84%	96%	95.5%	85.9%
HBP/DW-set**	92%	88.2%	88.4%	91.8%

Noninvasive Detection of liver fibrosis with multiparametric Magnetic Resonance Imaging compared to Transient Elastography and ELF markers

H. A. Dyvorne[1], G.H. Jajamovich[1], C. Calcagno[1], M.I. Fiel[2], D. Dieterich[3], S. Friedman[3], C. Donnerhack[1], R.L. Ehman[2] and B. Taouli[1]

[1]Translational and Molecular Imaging Institute, [2]Department of Pathology, [3]Department of Medicine, Division of Liver Diseases at Icahn School of Medicine at Mount Sinai, New York, NY, USA and [4]Mayo Clinic, Rochester, MN, USA

Introduction: The purpose of this study is to assess the diagnostic value of multiparametric Magnetic Resonance Imaging (MRI) including diffusion-weighted imaging (DWI), dynamic contrast-enhanced MRI (DCE MRI), MR elastography (MRE) compared to transient elastography (TE) and ELF markers for detection of liver fibrosis.

Methods: This IRB approved prospective study included 48 subjects (9 healthy volunteers and 39 with chronic liver disease) who underwent multiparametric MRI, TE and ELF tests. DWI was performed using 16 b values and diffusion decay was fit to the intravoxel incoherent motion model to yield hepatic D (true diffusion), PF (perfusion fraction), D* (pseudo diffusion) and ADC (apparent diffusion coefficient). DCE MRI was acquired after injection of gadolinium chelate and processed using a dual input single compartment model to yield arterial, portal and hepatic flow (Fa, Fp, Ft), arterial fraction (ART), distribution volume (DV), mean transit time (MTT) and time to peak (TTP). MRE was performed using a motion sensitive gradient echo sequence with 50Hz waves propagating through the liver via a passive driver. Liver stiffness (LS-MRE) was measured. TE used a 3.5 MHz probe and 50 Hz transient waves, and the liver stiffness (LS-TE) was the median value of 10 successful measurements with interquartile range ≤ 30%. Comparisons between noninvasive modalities and fibrosis METAVIR stage on histopathology (obtained in patients) were performed using Spearman correlation. ROC analysis was performed to assess the performance of each technique for the detection of moderate (F2-F4) or advanced (F3-F4) fibrosis.

Results: Correlation with fibrosis stage were significant for D ($r = -0.58$, $p<0.001$), MTT ($r = 0.44$, $p=0.011$), TTP ($r = 0.47$, $p=0.005$), LS-MRE ($r = 0.77$, $p<0.001$) and LS-TE ($r = 0.66$, $p<0.001$). ROC curves are given in **figure 1**. For detection of F2-F4, AUROC were 0.803, 0.640, 0.869, 0.836 and 0.809 for D, MTT, TTP, LS-MRE and LS-TE respectively. For detection of F3-F4, AUROC were 0.815, 0,719, 0.696, 0.970 and 0.809 for D, MTT, TTP, LS-MRE and LS-TE respectively. Examples of parametric maps are given in **figure 2**.

Conclusion: Using MRI and TE, excellent diagnostic performance was obtained for the detection of liver fibrosis. MRE had the highest performance for detection of F3-F4, and excellent performance for detection of F2-F4.

Clinical Relevance: Noninvasive assessment of liver fibrosis, using DWI, TE and MRE alone or in combination, may help reduce the burden associated with liver biopsy.

Figures and tables:

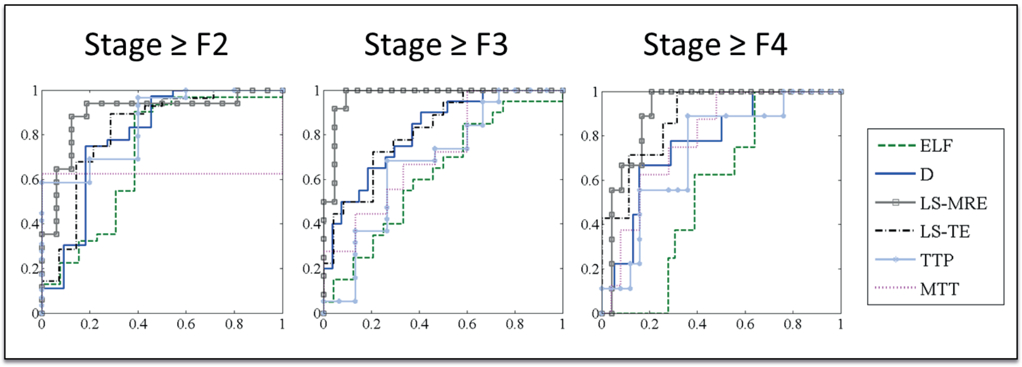

Figure 1: ROC curves for the detection of METAVIR stages 2-4 or stages 3-4.

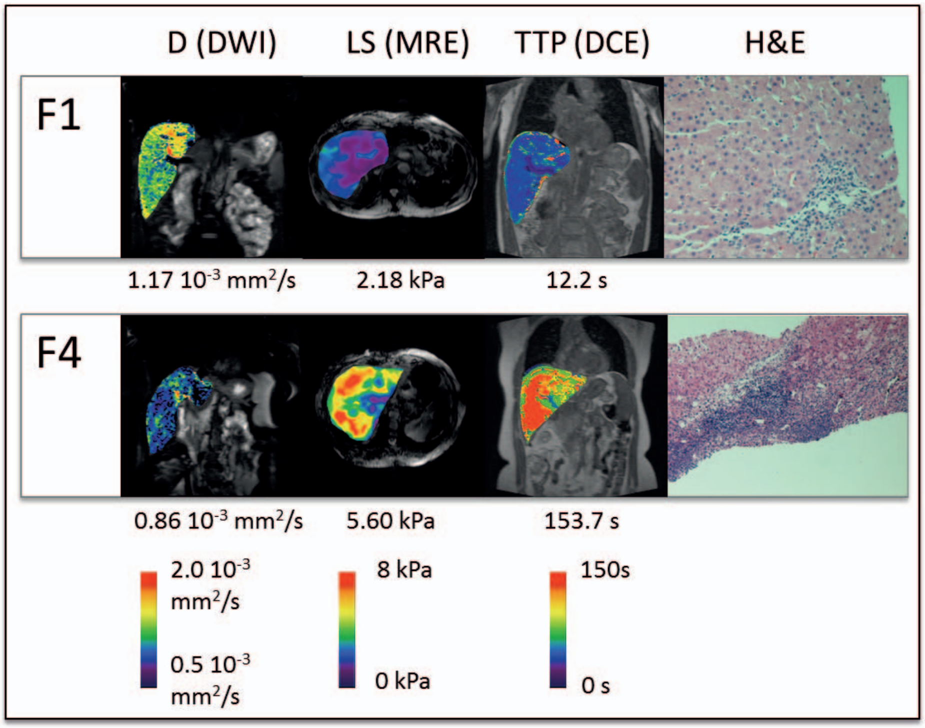

Figure 2: Example of parametric maps for D, LS-MRE and TTP (left to right) and histopathology (H&E staining, right) in a subject with fibrosis stage 1 (top) and fibrosis stage 4 (bottom)

Quantification of hepatic blood flow using a high-resolution phase-contrast MR imaging sequence

Hadrien A. Dyvorne[1], Ashley Knight-Greenfield[1], Cecilia Besa[1], Nancy Cooper[1], Thomas D. Schiano[2] and Bachir Taouli[1]

[1]Translational and Molecular Imaging Institute and [2]Department of Medicine, Division of Liver Diseases at Icahn School of Medicine at Mount Sinai, New York, NY, USA.

Introduction: Portal hypertension (PH) is a serious complication of cirrhosis. Definitive diagnosis of PH is accomplished with hepatic venous pressure gradient (HVPG) measurement, which is highly invasive. Phase contrast Magnetic Resonance Imaging (PC-MRI) can be used to noninvasively measure hepatic blood flow, which may reflect the presence of PH. However long acquisition times can limit its use in the clinic. The purpose of this study is to measure blood flow in the portal vein (PV) and hepatic artery (HA) using a high resolution highly accelerated compressed sensing (PC-SPARSE) technique and to correlate hepatic flow parameters with the presence of PH.

Methods: This was a retrospective, IRB approved study in 76 patients (M/F 48/28, mean age 54 y) who underwent MRI including PC-MRI. Flow, mean velocity, and vessel area were measured in the PV and HA using a highly undersampled (R=6) PC-MRI technique with random sampling and dynamic compressed sensing reconstruction (**figure 1**). Arterial fraction (ART = HA flow/[HA flow + PV flow]*100) was calculated from the flow curves (**figure 2**). PH score was calculated based on MRI findings (observation of ascites, varices and splenomegaly). Mann Whitney test and Spearman rank correlation coefficient were used to test sensitivity to PH and Child-Pugh class. ROC analysis was performed for detection of PH and Child-Pugh class B and C.

Results: 40/76 patients were cirrhotic, among which 37 had signs of PH. PV velocity and flow were significantly lower in PH (velocity: 8.9 ± 3.1 vs. 12.3 ± 2.8, $p < 0.001$; flow: 16.3 ± 7.7 vs. 19.7 ± 7.0, $p = 0.03$). PV velocity was also lower in patients with Child-Pugh class B and C vs. class A (7.7 ± 3.9 vs. 10.1 ± 2.1, $p = 0.047$). PV velocity correlated negatively with PH score ($r = -0.516$, $p < 0.001$), and ART correlated positively with Child-Pugh class ($r = 0.491$, $p = 0.045$). PV velocity had an AUC of 0.795 for detection of PH.

Conclusion: A highly accelerated compressed sensing phase-contrast MRI technique produces high-resolution images for hepatic flow measurement. PV velocity and ART are promising for detection of PH and monitoring of PH treatment. Prospective studies establishing correlation of PC-MRI with HVPG should be performed.

Clinical Relevance: Assessment of portal hypertension using accelerated phase contrast imaging may offer a noninvasive alternative to the HVPG technique for screening of patients with advanced cirrhosis and for monitoring of response to therapy for portal hypertension.

Figures and tables:

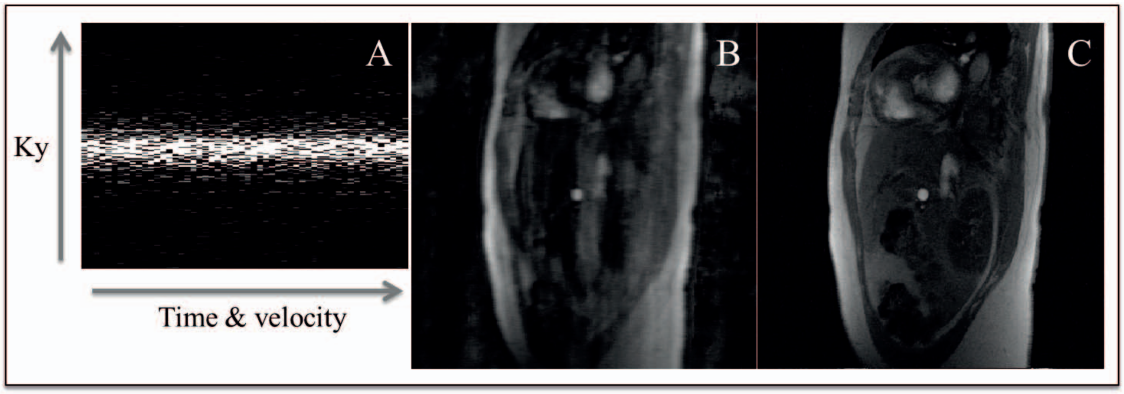

Figure 1: Dynamic compressed sensing framework: Random undersampling mask (A), magnitude images before (B) and after (C) compressed sensing reconstruction.

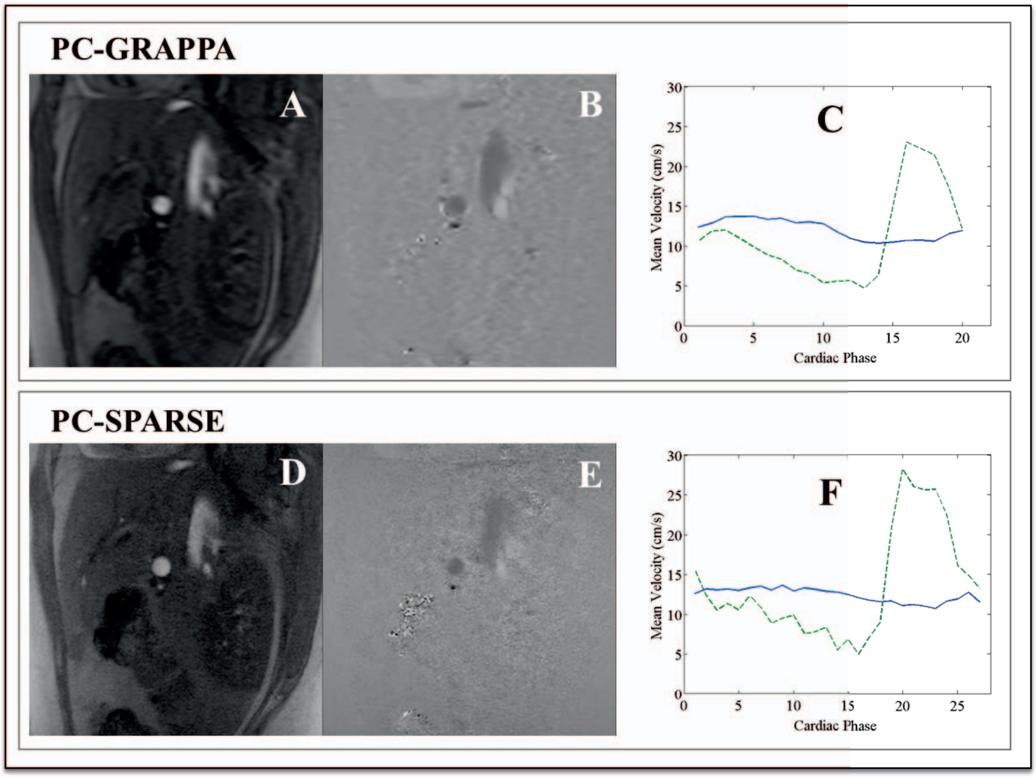

Figure 2: PC-GRAPPA (A, B and C) and PC-SPARSE (D, E and F) magnitude (A, D) and phase difference images (B, E) in a 54-year old female patient without liver cirrhosis. Mean vessel velocity curves (C, F) are displayed for the PV (solid line) and HA (dashed line).

Arterial input function reconstruction for DCE-MRI of the liver using pre-bolus acquisition with low dose gadolinium contrast

Guido H. Jajamovich[1], Claudia Calcagno[1], Hadrien Dyvorne[1], Henry Rusinek[2], Shimon Aronhime[1] and Bachir Taouli[1]

[1] Translational and Molecular Imaging Institute, Icahn School of Medicine at Mount Sinai
[2] New York University Langone Medical Center

Introduction: Changes in liver perfusion and flow quantified with DCE-MRI have been observed in advanced liver fibrosis and cirrhosis. Quantification of liver perfusion modeled parameters depends on the determination of the contrast agent concentration in the blood plasma (the so called arterial input function, AIF), which is typically challenging because of several possible artifacts, for example signal saturation. In this study we assessed the quality of a reconstructed AIF using a pre-bolus injection of low-dose gadolinium contrast and we compared it with the measured AIF after the injection of the main gadolinium bolus during DCE-MRI of the liver.

Methods & Results: In this prospective IRB approved study, 23 DCE-MRI examinations were performed in 20 patients with liver disease (M/F 16/4, mean age 56.9 y), including 3 patients scanned twice (on different days) at 1.5T (Siemens Avanto). As shown in Fig., a pre-bolus of 1.3 ml of Gd-BOPTA (Multihance) was injected for AIF acquisition using a high temporal resolution coronal oblique (parallel to abdominal aorta) 2D-TurboFLASH sequence (TR/TE/FA 198.9/0.21/12°, matrix 128x93, slice thickness 1 cm, temporal resolution 0.2 s, acquisition time 1 min). The main bolus consisting of 0.05 mmol/kg of Gd-BOPTA was then injected, and DCE-MRI was obtained with a coronal 3D-FLASH sequence covering the whole liver and the aorta (TR/TE/FA 2.96/0.95/12°, matrix 192x121, slice thickness 4 mm, mean temporal resolution 2.7s, 64 volumes acquired). ROIs were placed in the abdominal aorta and signal intensity was converted to gadolinium concentration by using SPGR signal equation [1]. Pre-bolus AIF was reconstructed by shifting, adding and scaling the concentration-curve in the aorta after the pre-bolus injection (Fig.) [2]. Two observers assessed blindly and independently pre-bolus and main bolus AIF curves qualitatively (for peak and width). Quantitative AIF curve features including peak concentration, time to peak (TTP), upslope, area under the time activity curve of gadolinium contrast at 60 s (AUC60) and the full width at half maximum (FWHM) were calculated and compared between pre-bolus and main bolus data.

Pre-bolus curve quality was significantly better than main bolus AIF curves (in 19/23 for observer 1, and 20/23 for observer 2). AUC60, peak concentration and upslope of pre-bolus AIF were significantly higher and FWHM was significantly lower than those of main bolus (Table). In the 3 patients that underwent test-retest studies, all parameters showed better reproducibility using pre-bolus AIF (CV 9.5-42.5% for pre-bolus AIF and 26.2-67.7% for main bolus AIF).

Conclusion: Estimation of the AIF using a pre-bolus gadolinium injection has the potential to overcome the low temporal resolution and saturation effects shown in the measured AIF after the main dose of contrast agent is injected. The high temporal resolution used during the pre-bolus injection preserves the AIF signal intensity peak, while the high spatial resolution used after the main bolus misrepresents the AIF due to temporal undersampling. Moreover, the lower-dose used for the pre-bolus resides in the linear regime between observed MR signal intensity and concentration, away from saturation.

Clinical Relevance: Estimation of the AIF using a pre-bolus injection of gadolinium decouples the AIF and liver imaging acquisition protocols, allowing for a more precise AIF determination and a higher spatial resolution imaging of the liver after main bolus injection.

Figures and tables:

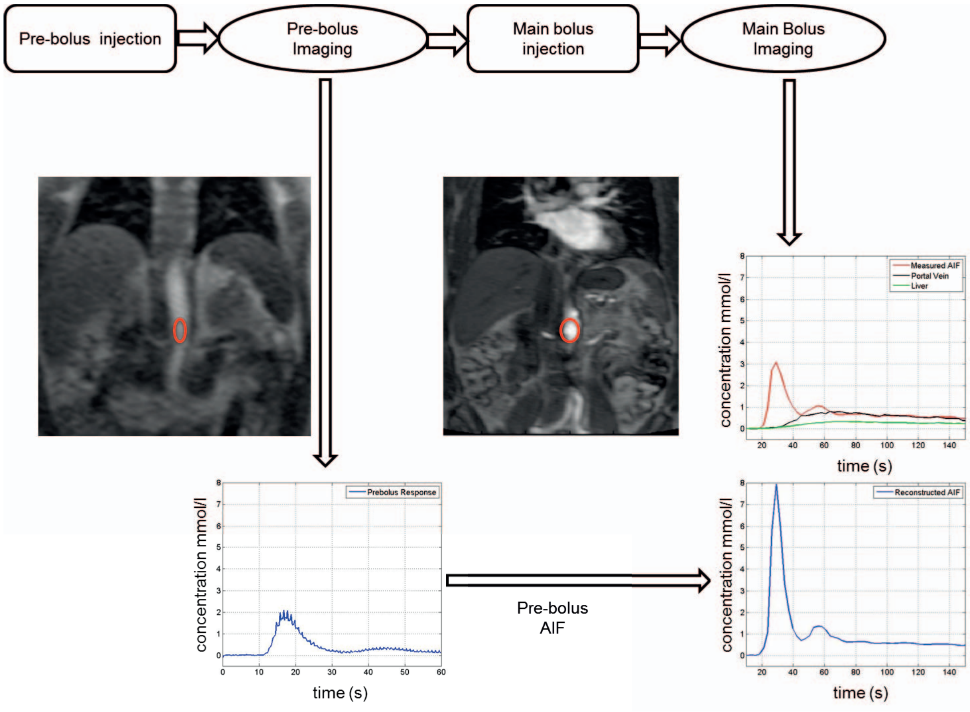

Flow diagram showing the reconstructed and measured AIF using first low dose gadolinium injection before main bolus.

	Pre-bolus AIF	Main bolus AIF	p
Peak (mmol)	7.69 ± 4.56	3.45 ± 1.53	**< 0.001**
Time to Peak (s)	8.68 ± 2.7	10.14 ± 5.11	0.07
Upslope (mmol/s)	0.96 ± 0.6	0.42 ± 0.22	**< 0.001**
AUC60 (mM.s)	99.04 ± 26.91	72.7 ± 21.2	**< 0.001**
FWHM (s)	8.98 ± 2.67	12.21 ± 6.01	**< 0.001**

Mean values ± SD for parameters of the pre-bolus and main bolus AIFs

References

1. Schabel, M.C. Phys Med Biol., 2008. **53**: p. 2345-73.
2. Koestler, H., et al. Magn. Reson. Med, 2004. 52(2): p. 296-299

This work was supported by NIDDK grant 1R01DK087877

Quantitative liver MRI combining Phase Contrast imaging, Elastography, and DWI: assessment of test-retest and post-prandial effect. Prospective study at 3T

G. H. Jajamovich[1], H. Dyvorne[1], C. Donnerhack[1], R. Ehman[2] and B. Taouli[1]

[1] Translational and Molecular Imaging Institute, Icahn School of Medicine at Mount Sinai
[2] Department of Diagnostic Radiology, Mayo Clinic College of Medicine

Introduction: Techniques such as MR Elastography (MRE), phase contrast (PC) and diffusion-weighted imaging (DWI) have potential for non-invasive detection of liver fibrosis, cirrhosis and portal hypertension associated with chronic liver disease. Since portal flow and liver stiffness (LS) may be altered by food intake [1, 2], changes in LS, portal vein (PV) flow, PV velocity and liver ADC (which is affected by flow) might be observed and may lead to decreased reproducibility. This prospective study quantifies reproducibility (in fasting conditions) and post-prandial changes in PV flow/velocity, LS, and liver ADC at 3T.

Methods & Results: 9 healthy volunteers and 2 patients with HCV and cirrhosis (M/F 8/3, mean age 35 y) were enrolled in this prospective IRB approved study. All subjects underwent 3T MRI (MR750, GE Healthcare), including 2D PC (pulse triggered with VENC=50 cm/s, slice perpendicular to the portal vein), axial SS EPI DWI (free breathing, 16 b-values from 0 to 800 mm2/s) and MRE (4 slices through the liver). All subjects were initially scanned twice after 6 hours of fasting to assess reproducibility of each technique (subjects were removed from the scanner and re-scanned). The subjects were then scanned again in postprandial conditions, 20 min. after a 700 Kcal liquid meal (Ensure Plus). To quantify PV flow and velocity, a ROI was drawn in the PV on PC images. Mean LS and liver ADC were obtained by placing a ROI in the right hepatic lobe on LS maps and diffusion images. A mono-exponential fitting was used to compute the ADC. The coefficients of variation (CV) for PV flow, PV velocity, LS and liver ADC were computed for the two scans in fasting state. Wilcoxon paired tests were performed to assess differences in these metrics before and after caloric intake (average from the 2 fasting scans was used for comparison).

PV flow, PV velocity, liver ADC and LS showed good to excellent reproducibility in fasting state, with CVs ranging from 4.5%-17.4% (Table). PV flow, PV velocity and LS were all significantly higher in postprandial state (Table, Fig.). The two cirrhotic patients showed an average increase of 16.6% in LS (4.0 to 4.6 kPa for 1st patient, and 3.2 to 3.8 kPa for 2nd patient), while the healthy volunteers had an average increase of 10.3% in LS. Average increase in PV flow and PV velocity was 61.5% and 27.5%, respectively. Liver ADC did not significantly change before and after caloric intake.

Conclusion: These results indicate that caloric intake is a factor to consider in interpreting PC-based PV flow/velocity and MRE-based hepatic stiffness measurements. The difference in LS between fasting and postprandial states is elevated in patients with liver disease and the diagnostic significance of this observation needs to be verified further.

Clinical Relevance: Liver blood flow and metabolism are altered in the postprandial state. Portal venous flow/velocity and liver stiffness increased significantly after a caloric intake, showing the importance of undergoing MRI in a controlled state.

Figures and tables:

	PV Flow	PV Velocity	ADC	LS
Fasting #1	16.1 ± 3.9	11.6 ± 3.0	1.5 ± 0.4	2.1 ± 0.8
Fasting #2	16.3 ± 4.5	11.5 ± 2.3	1.6 ± 0.3	2.1 ± 0.7
CV	17.4%	11.7%	10.1%	4.5%
Postprandial	25.5 ± 6.9	14.5 ± 3.5	1.6 ± 0.3	2.4 ± 0.9
p*	0.001	0.007	0.3	0.01

PV flow, PV velocity, liver ADC and LS (liver stiffness) for all subjects (mean ± SD) in fasting and post-prandial states. CV is calculated to assess reproducibility in fasting conditions. PV Flow (ml/s), PV Velocity (cm/s), ADC (x10^{-3} mm^2/s), LS (kPa). *: comparison of average fasting values and postprandial values.

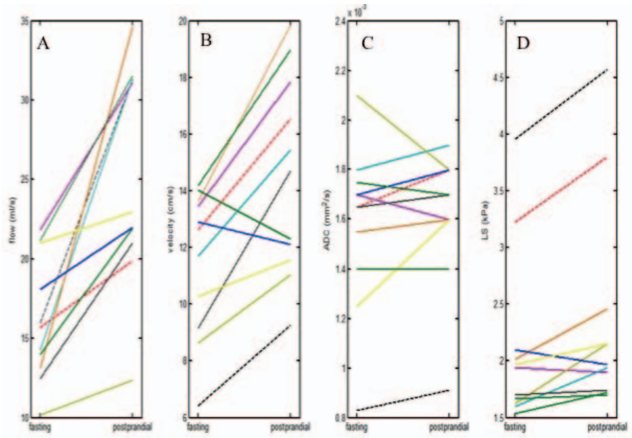

Changes in PV flow (A), PV velocity (B), liver ADC (C) and liver stiffness (D) in fasting and postprandial conditions in 11 subjects (the 2 fasting values are averaged). The two cirrhotic patients have higher LS (dashed lines).

References
1. Sadek, A.G., et al. J Magn Reson Imaging, 1996. 6(1): 90-93
2. Yin, M., et al. AJR Am J Roentgenol, 2011. 197(1): 64-70
3. Yin, M., et al.. Clin Gastroenterol Hepatol, 2007. **5**(10): 1207-1213

This work was supported by NIDDK grant 1R01DK087877

Dental filling artifacts in head and neck PET/MRI imaging. Comparison with PET/CT images

K. Knešaurek1, D. Izquierdo-Garcia2, J. Machac1, Z. A. Fayad2

1 Division of Nuclear Medicine/ Department of Radiology, 2Transitional and Molecular Imaging Institute, The Mount Sinai Medical Center, New York, USA

Introduction: The purpose of our study was to explore the influence of dental filling artifacts in head and neck PET/MRI imaging.

Methods & Results: In an ongoing study, several patients were imaged on a GE DLS 16 slice PET/CT system. Approximately 20 minutes later, the same patient was imaged on a Philips PET/MRI system. The data were reconstructed using vendors' software. For PET/MRI data a binary attenuation map was created from MRI images and applied for attenuation correction (AC). The data were transferred to a common platform and compared using in house software. Two approaches were used to match PET data. First, MRI and CT data were co-registrated and the transformation was saved and used to match the PET data. The second approach was a direct match of the PET data. In both cases, matching was done using maximization of mutual information (Viola and Wells, Int. J. Com. Vis., 137-154, 1997). The differences in CT and MRI generated attenuation maps were significant, more than 30% of average values. However, the differences in the reconstructed images were 20% or less of the average activity in the area and did not cause major diagnostic problem.

Conclusion: Our results indicate, that PET clinical images are not significantly affected by dental filling artifacts, when MRI derived AC is used in head and neck PET/MRI imaging.

Clinical Relevance: PET/MRI can be utilized in head and neck imaging in a very similar way as PET/CT does.

Figures and tables:

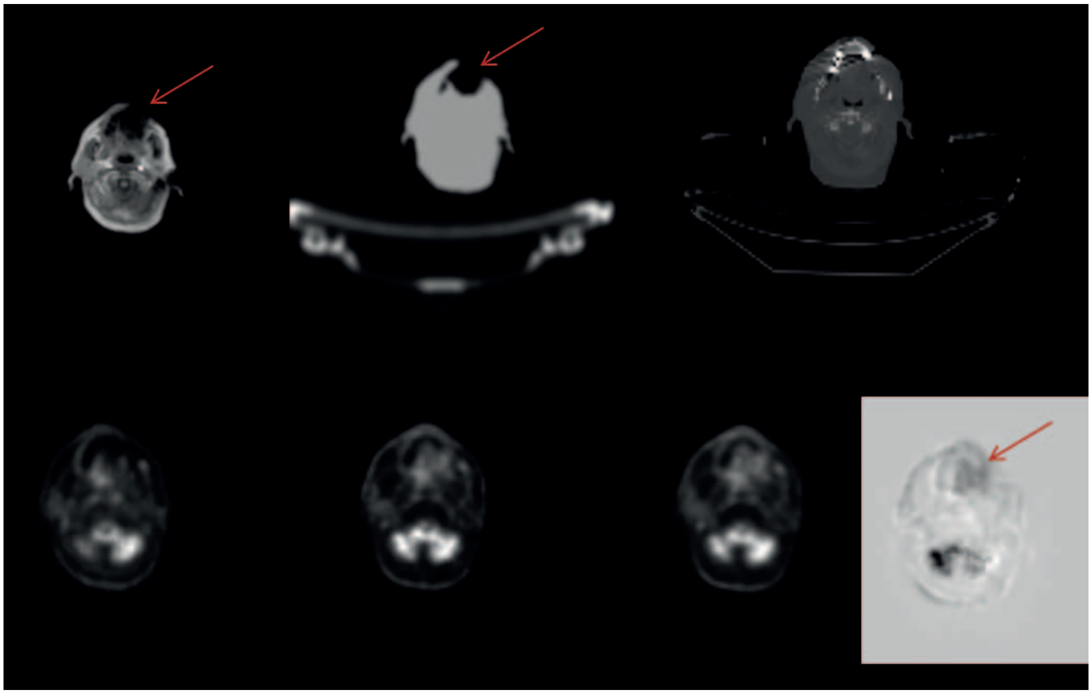

Fig.1 Upper row from left; MRI image, MRI AC binary map and corresponding CT image. Lower row from left; PET image obtained with MRI AC and matched PET images from PET/CT obtained with MRI-CT matching and PET-PET matching. Last image shows the difference between the first and the second PET image. The arrows indicate the area affected by dental filling artifacts. Differences shown in right inferior cerebellum area are due to small missregistration between the PET images.

Interim FDG PET/CT Predicts Response and Progression Free Survival (PFS) Better than Clinical and Baseline Metabolic Measurements in Hodgkin's Lymphoma (cHL): Correlation of Various Methodologies

Knight-Greenfield, Ashley[1]; Cotter, Ryan[1]; Marshall, Richard A[1]; Hutchings, Martin[2]; Lamonica, Dominick[3]; Doucette, John[1]; Stern, Jamie[1]; Kostakoglu, Lale[1]

[1]Nuclear Medicine, Mount Sinai School of Medicine, New York, NY, United States; [2]Haematology/Oncology, Rigshospitalet, Copenhagen, Denmark; [3]Roswell Park Cancer Center, Buffalo, NY, United States

Introduction: Previous studies have demonstrated that conventional methods to predict PFS in cHL, including clinical criteria, may not be sufficient. While several metabolic parameters have been examined, an algorithm to best predict PFS remains unclear. The Purpose of this study is to determine the best predictor of response and PFS among various methods and variables of tm metabolic measurements at baseline and at interim PET/CT compared to conventional methods in cHL.

Methods & Results: Retrospective evaluation of prospectively acquired data in 40 cHL pts, all stages. Eligibility: PET/CT prior to and after 1 cycle (PET1), ABVD therapy, imaging at 60min+15min. Baseline parameters included clinical data (stage, IPS, unfavorable vs favorable), metabolic tm volume (MTV), total lesion glycolysis (TLG), SUVmax, SULpeak determined using gradient method (PETVCAR2, GE Healthcare). Data were evaluated at PET1 using Deauville 5-PS, %Δ in MTV, SUVmax, TLG, and SULpeak (PERCIST). Variables were correlated with PFS and response evaluated by rIWG3. Median follow-up for non-relapsing patients was 33.83 mo. Of 66 pts, 15 relapsed (median time to progression: 6.5 mo.). Best predictor of response was PERCIST followed by Deauville and %ΔSUVmax at PET1. PERCIST was the most sensitive and the most specific, with good PPV and NPV. The best predictor of PFS was Deauville 5-PS followed by %ΔSUVmax, %ΔTLG and PERCIST at PET1. PERCIST was most sensitive in the prediction of PFS and had high specificity and NPV. Deauville was most specific in the prediction of PFS. No parameters had good PPV. No baseline conventional (stage, IPS, UF vs. F) or PET variable was associated with PFS or response (See tables and figure).

Conclusions: Combining Deauville with PERCIST/%ΔSUVmax adds prognostic information and may dictate early changes in therapy in the future. Combinatorial evaluation in future cHL trials, such as Deauville with quantitative measurements may help dictate when to escalate or deescalate treatments. Risk-stratification of cHL using tumor metabolic volumetry and PERCIST criteria may require larger prospective studies to validate thresholding method and cut-offs.

Clinical Relevance: Disease stage dictates treatment in cHL. If response to therapy can be evaluated early on and correlates with progression free survival, treatment can be adapted and individualized with potential improvement in survival.

Figures and tables:

Prediction of Best Response

Variable (dichotomous)	OR	CUT-OFF (ROC)	p-value
Gradient Method (n=66)			
Baseline MTV (mL)	0.87	118.5	0.85
Baseline SUVMAX (g/ml)	2.48	15.45	0.23
Baseline TLG (g/ml x cm$^{3)}$	1.08	697	0.91
%ΔMTV	4.88	98%	**0.04**
%ΔSUVmax	10.22	62%	**0.003**
%ΔTLG	6.46	99%	**0.02**
PERCIST Criteria (n=38)			
%ΔSULpeak	75	61%	**0.001**
Deauville PET1 >3 (n=66)	12.25		**0.002**
Conventional (n=66)			
Stage III or IV	0.52		0.38
IPS >3	1.50		0.75
F vs. UF (early stage only)	2.83		0.27

Prediction of Progression Free Survival

Variable (dichotomous)	HR	CUT-OFF (ROC)	p-value
Gradient Method (n= 66)			
Baseline MTV (mL)	1.66	131.5	0.34
Baseline SUVMAX (g/ml)	1.81	15.5	0.26
Baseline TLG (g/ml x cm$^{3)}$	1.24	545	0.70
%ΔMTV	3.20	98%	**0.03**
%ΔSUVmax	3.83	77%	**0.01**
%ΔTLG	4.09	99%	**0.01**
PERCIST Criteria (n=38)			
%ΔSULpeak	9.40	75%	**0.01**
Deauville PET1 >3 (n=66)	6.13		**0.0005**
Conventional (n=66)			
Stage III or IV	1.07		0.90
IPS >3	1.25		0.77
F vs. UF (early stage only)	1.28		0.73

Kaplan-Meier Analysis

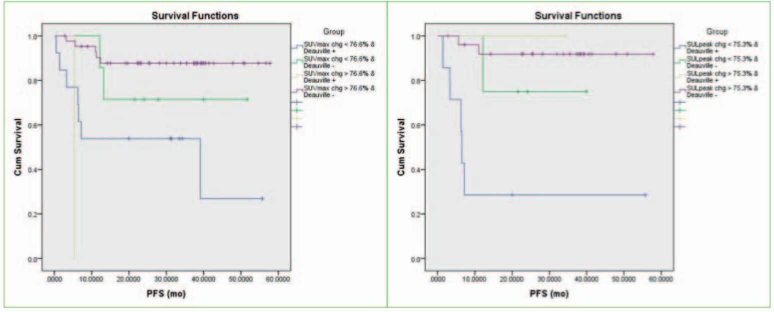

Quantitative Comparison of Lesion FDG Uptake on a Whole Body PET-MR system with PET-CT

Machac, Josef(1); Izquierdo-Garcia, David(2); Knesaurek, Karin(1); Rafique, Ash(1); Davies, Olufunke(2); Fuster, Valentin(3); Fayad, Zahi(2)

1. Div of Nuclear Medicine, Dept of Radiology, Mount Sinai Medical Center, New York, NY, 2.Translational and Molecular Imaging Institute, Mount Sinai Medical Center, New York, NY, 3. Cardiovascular Institute, Mount Sinai Medical Center, New York, NY

Introduction: PET-MR is a potential alternative to PET-CT. We presented previously a clinical evaluation of the first combined whole-body PET-MR unit in the US, in comparison with PET-CT. We present a quantitative comparison between PET-MR and PET-CT of FDG uptake by benign and malignant lesions.

Methods & Results: After injection of F-18 FDG, 36 patients had routine PET-CT at 1.2 +/-0.4 hrs, (PET(1)-CT) followed by imaging at 2.7 hrs, with a Philips TF PET-MR scanner, T1 MR in coregistration were segmented into air, lungs, or soft tissues for attenuation correction of the PET images (PET(2)-MR). In 14 patients with either benign or malignant lesions, the PET images obtained with the PET-MR system were also reconstructed with the attenuation correction provided by CT from the PET(1)-CT acquisition (PET(2)-CT). The FDG uptake, measured as SUVmax on the same workstation, was compared for each lesion from PET(2)-MR with PET(1)-CT images, and the PET(2)-CT images.

83 abnormal lesions were identified in 14 patients; 15 lesions in 5 patients were considered benign arthritic inflammatory lesions, a mean 3 lesions (range 1 to 7) per patient; 68 lesions in 11 patients were considered or suspected as malignant, a mean 6.2 lesions (range 1 to 14) per patient. The mean SUVmax was higher for PET(2)-MR and PET(2)-CT, acquired at a later time after injection, than compared to PET(1)-CT, but there was no significant difference in mean SUVmax between PET(2)-MR and PET(2)-CT by Bland-Altman analysis and paired Ttest. This was true for both benign and malignant lesions separately, too.

Conclusion: Although the SUVmax for both benign and malignant lesions was higher for PET(2)-MR compared to PET(1)-CT, due to the greater time between injection and acquisition, there was no significant difference between lesion FDG SUVmax measured from the same PET(2) scan whether corrected for attenuation by either the MR map obtained from the PET(2)-MR or the CT map obtained from the PET(1)-CT.

Clinical Relevance: This work supports the use of the Phillips PET-MR system for clinical oncological purposes, when quantification of focal lesion uptake is involved.

Figures and tables

	PET(1)-CT		PET(2)-MR		PET(2)-CT
Mean SUVmax	5.0		6.6		6.6
SD	3.5		3.3		3.2
P		<0.001		ns	
2 SD of difference		5.2		1.6	

Quantitative Histogram Analysis of Liver MR Elastography

Yuan-Shuo Wang, Hadrien Dyvorne, Guido Jajamovich, Bachir Taouli

Translational and Molecular Imaging Institute, Division of Liver Diseases, Mount Sinai School of Medicine

Introduction: Liver fibrosis and cirrhosis is a major health challenge in the US. While needle liver biopsy has been the gold standard for diagnosing fibrosis and cirrhosis, it has poor patient-acceptability and significant sampling and interpretation errors. A non-invasive alternative shown to accurately diagnose fibrosis and cirrhosis is measuring liver stiffness (LS) using magnetic resonance elastography (MRE). Current work relating fibrosis and MRE-derived LS examines mainly averaged LS over a large liver area, which overlooks the heterogeneous distribution of LS and fibrosis at pathology. The objective of the study is to perform quantitative histogram analysis of liver MRE data and to correlate these derived histogram metrics with histopathologic stage of liver fibrosis.

Methods & Results: This prospective IRB-approved study is an ancillary study of a NIDDK-funded proposal at Mount Sinai. 12 healthy volunteers and 27 patients with chronic liver disease and concomitant liver biopsy within 3 months were enrolled. An axial MRE sequence was performed at 3T (GE 750) (TR/TE 50/22, 1.4x2.8x10mm, 4 slices, 50Hz, ASSET 2) during 4 breath holds. LS was measured by placing ROIs in liver parenchyma using MRE Quant software, and pixels with confidence indices <95% were excluded. LS was plotted in frequency histograms, and histogram metrics (including entropy, standard deviation (SD), median, mode, skewness, kurtosis, peak histogram height, area under histogram curve within one standard deviation, and mean LS) were correlated with histopathologic stage of fibrosis.

SD and entropy of LS increased with increasing degree of fibrosis. AUCs were 0.88-0.95 for LS mean, 0.88-0.96 for LS median, 0.87-0.95 for LS max, 0.89-0.95 for LS SD, and 0.85-0.95 for LS entropy for F0-F1 vs. F2-F4 and F0-F2 vs. F3-F4, respectively. Combinations of mean LS with another LS histogram metric were minimally better than mean LS alone in assessing fibrosis stage.

Conclusion: Median, SD, entropy, and max LS are equally as good as mean LS in fibrosis assessment. High SD and entropy are observed in F3-F4 patients indicating increased stiffness heterogeneity, likely due to heterogeneous fibrosis distribution.

Clinical Relevance: Histogram metrics of liver MRE data could prove extremely valuable in distinguishing histopathologic stages of liver fibrosis compared or combined to mean LS, likely due to heterogeneous distribution of LS. This would give more accurate estimates of liver heterogeneity and more accurate correlation of LS to fibrosis stage.

Extent of Measurement Error in the Context of Assessment of Tumor Response to Treatment

David Yankelevitz, Ricardo Avila, Claudia Henschke

Mount Sinai, Kitware, Mount Sinai

Introduction: Response of tumors to treatment both in the context of clinical trials as well as during routine clinical care is often based on change in size measured by imaging. While these measurements are generally made either uni-dimensionally or even bi-dimensionally there has in recent years been recognition of the potential advantage of three-dimensional imaging for volumetric assessment. However, while many groups are now advocating for this change, there is only now beginning to be realization of the extent that measurement error plays in making these types of estimates, and that they may actually be even more severe with volumetric measures than simple in-plane measurements.

Methods & Results: Error in measurement can come from three main sources. This includes the device used to produce the image, the software used to extract the image from background and inherent uncertainty related to the boundary of tumor tissue as it invades adjacent non-tumor tissue. In this instance we seek to evaluate the error introduced by the machine and in particular CT scanners. We use a novel calibration device we refer to as a “pocket phantom” and have shown that it can be used to measure resolution and other fundamental image quality characteristics, with results that are comparable to a traditional CT calibration device [1]. As the device has three precision manufactured and highly calibrated spheres with diameters of 15.9mm, we are able to measure volume based on the CT measurement and compare it to an actual truth. In a previous study conducted in Europe we found that certain 16 slice CT scanners at multiple independent locations were producing high-resolution CT images with up to 44% volumetric change error due to warping along the trans-axial dimension [2]. In this smaller study we sought to reproduce this issue at an independent site with the same CT scanner and using the same high resolution CT scanning protocol as originally observed. The site received a package containing three regularly spaced pocket phantoms and CT scanned the package using multiple scan sequences and positioning the device at different distances from iso-center. Fully automated pocket phantom detection and measurement software provided objective image quality measurements.

We found that a new set of high-resolution CT acquisitions from a 16-slice CT scanner showed significant levels of volumetric error. Maximum volumetric change observed between measurements of the precision calibrated Teflon spheres was 43.8%. Visual inspection of the images revealed a similar warping of the CT images along the trans-axial dimension resulting in volumetric variability. Further inspection of this data revealed a potential relationship between trans-axial image warping and the distance of an object from scanner iso-center.

Conclusion: Measurement error directly related to the CT scanner may not be readily apparent when performing a scan yet it can dramatically affect volume measurements. The extent of this effect can be so great as to actually mislead either a clinician or researcher into believing a tumor has either progressed or responded based on criteria equivalent to that used in standard RECIST. These findings suggest that there is a need for ongoing calibration of images when measurements are being made and that especially when subtle changes are being considered. Error introduced by the machine itself needs to be accounted for, and even this represents only a portion of the extent of potential error.

Clinical Relevance: As we become further dependent on medical imaging to determine response to treatment, there needs to be much greater recognition of the extent of measurement error. Currently, there is no attempt at quantifying this parameter other than to include a large threshold as representing change. An approach that includes a calibration device incorporated into the scanning protocol will allow for an individualized assessment of the extent of machine error which can provide a basis for setting some boundaries on the degree to which a measurement can be relied on.

A method to detect weak bioluminescent optical imaging signals in a mouse cancer metastasis model

Yu Zhou[1,2], Inge van Rooy[2], Johnny Ng[2], Cheuk Ying Tang[1,2]

1. Shared Research Facility; 2. Translational and Molecular Imaging Institute

Introduction: In vivo bioluminescent imaging technology is a method for investigating cancer metastasis in preclinical animal models. It is of interest to know how and when cancer cells migrate from primary tumors to metastatic sites. However, during the cancer's early stage development, the population of the metastatic tumor cells is much lower than in the late stages, so the bioluminescent imaging signal from the metastatic area is very weak. As a result, acquiring good quality images becomes very challenging. Here we discuss a technique on how to extract weak signals from suspected early stage metastatic sites in the upper body region of a mouse cancer model.

Methods & Results: Athymic, nude female mice (N=4) with A-431 cells (a GFP/firefly luciferase clone, A-431/D4) were used in this study. Two primary tumors with 5 million cells were injected into the lower mammary fat pads in each mouse. The mice were imaged 20 days after injection.

In this research, IVIS-Spectrum optical imaging system (Camera: IVIS 23240) was from PerkinElmer. XGI-8 Gas Anesthesia System was set at 0.2~0.25 LPM oxygen gas flow, and Isoflurane vaporizer was set at 1.5-2.0 percent. 15 mg/ml luciferin (XenoLight D-Luciferin Potassium Salt, P/N 122796, PerkinElmer) was used by Intra-Peritoneal (IP) injection with 10 µl/1 gram of body weight.

1. The mice were scanned before luciferin injection to acquire the baseline image. IVIS-Spectrum was set by exposure time 60 s, binning (M) 8, FOV 17.6 cm, f1, and focus height 1.5 cm (Figure 1A).
2. After luciferin injection, the signal of the image was saturated (Figure 1B) using the baseline setting.
3. Mice were monitored until the luciferin/luciferase bioluminescent reaction reached a plateau (Figure 1C) by using exposure time 2 s, binning (HR)4, FOV 17.6 cm, and f8, but the weak signal in the upper body area could not be detected.
4. All primary tumors (exposure time 2 s, Figure 1D) were covered, but still no signal was seen in the upper body areas. When the parameters were chosen the same as the background setting, another issue occurred as shown in Figure 1E. There was too much light leaking from the primary tumors. It was hard to cover the primary tumors well enough to prevent leaking.
5. When the lower body of a single mouse was covered completely (Figure 1F), a clear weak signal emerged from the upper body area.

Figure 2 shows the total photon flux per second, derived from the matrix ROIs from the background and the bioluminescent signal images respectively (1B and 1F). The more photons per second (p/s) in each small grid, the more tumor cells were in there. The weak metastatic bioluminescent signal was extracted successfully. It shows a metastasis in the upper body area of the mouse, most probably in either the lung or the axillary lymph node.

Conclusion: The bioluminescent signal from metastatic tumor cells cannot be monitored if primary tumors are not sealed completely or are removed in the early metastatic stage. The optical imaging system parameters can be optimized to extract the weak bioluminescent signal.

Clinical Relevance: Tracking tumor cells with luciferase is one of the important imaging methods to investigate cancer metastasis.

Figures and Tables:

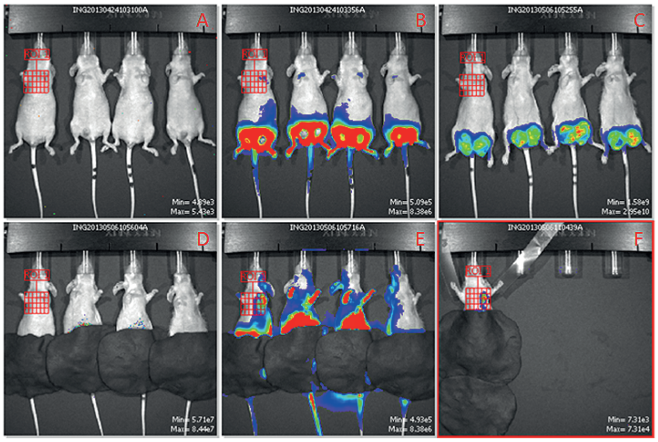

Figure 1. Bioluminescent images. 1A) background image before luciferin injection with exposure time 60 s, binning (M) 8, FOV 17.6 cm, f1, and focus height 1.5 cm. 1B) image saturation after luciferin injection with baseline settings. 1C) unsaturated peak signal image with exposure time 2 s, binning (HR) 4, FOV 17.6 cm, and f8. 1D) image of covered primary tumor sites with exposure time 2 s. 1E) image of covered primary tumor sites with exposure time 60 s. 1F) image of single mouse with completely sealed primary tumor sites with exposure time 60 s. The weak metastatic bioluminescent signal was observed.

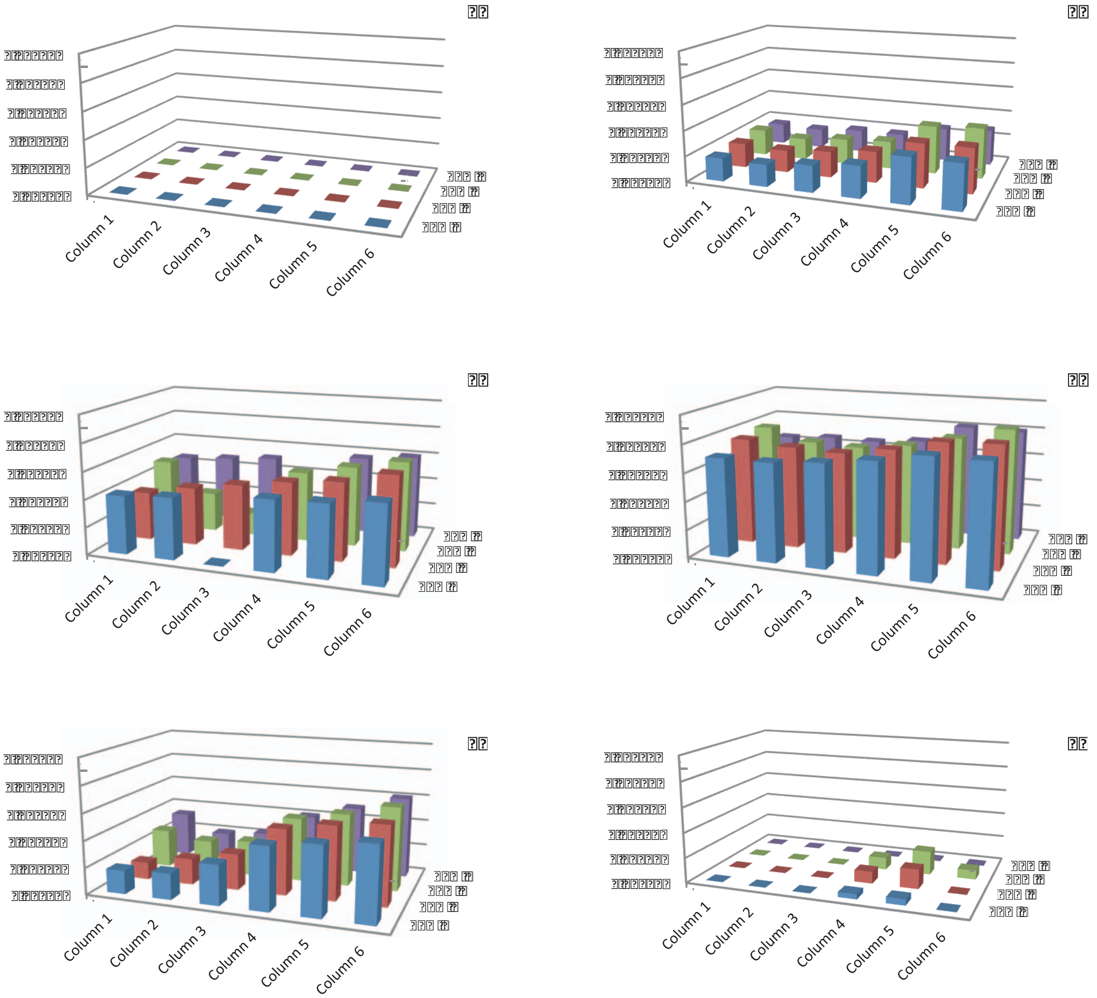

Figure 2. Matrix ROI measurements of the total flux (photons/second) corresponding to Figure 1A-F. 2A) Background signal. 2B) Saturated signal immediately after luciferin injection. 2C, D, E) Signal acquired during the maximum signal intensity plateau period. 2F) Weak metastatic bioluminescent signal.

Abstracts, Nanomedicine Category

3D DCE-MRI for the extensive quantification of microvasculature permeability and nanoparticles uptake in atherosclerotic rabbits

Calcagno C, Lobatto ME, Millon A, Senders M, Fay F, Robson PM, Ramachandran S, Mani V, Mulder WJM, Fayad ZA

Translational and Molecular Imaging Institute, Icahn School of Medicine at Mount Sinai, New York, NY

Introduction: The proliferation of micro- and neovessels with increased permeability is an important feature of vulnerable, high-risk atherosclerotic plaques. The permeable micro- and neovessels in high-risk plaques are not only a marker of vulnerability, but can also be exploited to deliver targeted treatments to the vessel wall. For example, novel nanotherapeutics based on the enhanced permeability and retention effect selectively extravasate in tissues with increased permeability, such as high-risk atheroscerotic plaques. We have already showed that anti-inflammatory nanoparticles can reduce plaque microvasculature/permeability as quantified non invasively by 2D dynamic contrast enhanced (DCE) MRI. A limitation of 2D DCE-MRI is the restricted coverage at only few specific anatomical locations along an artery. This limits the evaluation of the overall disease burden as well as the evaluation of the response to therapy, which severely impacts the significance of these findings. Here we describe a novel 3D black blood DCE-MRI acquisition for the extensive evaluation of permeability of atherosclerotic plaques. We validate this approach using ex vivo Evans Blue fluorescence, a marker of vascular permeability, and compare microvascular permeability assessed by 3D DCE-MRI with nanoparticles uptake in the aorta of atherosclerotic rabbits.

Methods & Results: Six atherosclerotic rabbits and four non-atherosclerotic controls were imaged on a 3T MR magnet using a T1 weighted black blood 3D Motion SensitizedDrivenEquilibrium (MSDE) prepared Rapid Gradient Echo (3D-MERGE) sequencefor DCE-MRI of the abdominal aorta. Contrast agent uptake in the aortic vessel wall was quantified by calculating the area under the concentration curve (AUC). After imaging, animals were injected with Evans Blue (EB) dye to evaluate microvascular permeability by ex vivo fluorescence imaging. EB binds to albumin and extravasates at sites with enhanced endothelial permeability. AUC maps of control rabbits displayed little or no uptake of contrast agent (**Figure1A**), while atherosclerotic rabbits revealed marked and inhomogeneous uptake of contrast agent in the abdominal aorta (**Figure1B**). AUC was significantly higher in atherosclerotic compared to control rabbits (unpaired t-test, $p< 0.0001$, **Figure2A**). Additionally there was a significant correlation between AUC by 3D DCE-MRI and ex vivo EB fluorescence (**Figure1C**), indicating that 3D DCE-MRI can measure microvascular permeability along an entire vascular bed (**Figure2B**; $R^2=0.19$; $p=0.0039$). To assess the correlation between microvascular permeability and 3D DCE-MRI, 2 atherosclerotic rabbits were sacrificed 6 hours after injection of fluorescent nanoparticles and 30 minutes after injection of EB to evaluate microvascular permeability. We found that nanoparticle signal strongly correlated with both AUC by 3D DCE-MRI ($r^2= 0.56$, $p=0.0018$) and EB ($r^2= 0.47$,$p=0.0007$, **Figure3**).

Conclusion: This novel 3D DCE-MRI approach allowsfor the in vivo assessment of plaque permeability with coverage over a large vascular territory. Quantitative comparison of AUC maps from atherosclerotic and control rabbits revealed significantly higher contrast agent uptake in atherosclerotic rabbits, indicating increased vessel permeability. Additionally, we established a significant correlation between in vivo quantification of permeabilityby DCE-MRI and ex vivo permeability with Evans Blue, andwith nanoparticles uptake.

Clinical Relevance: This non-invasive technology may be used in the future clinical practice to identify patients that may specifically benefit from nanoparticles therapies. Additionally, it may be used in future clinical studies to stratify patients' risk base on microvasculature/permeability and to assess their changes after therapeutic intervention.

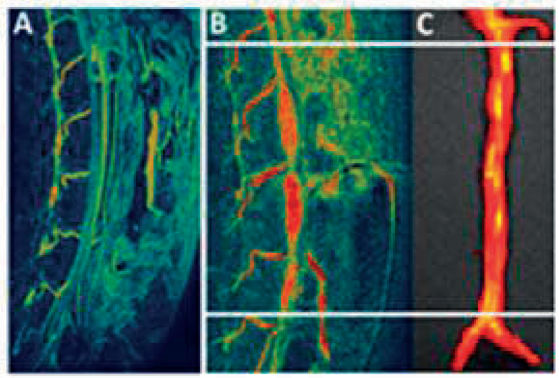

Figure 1: **A**, maximum intensity projection (MIP) of AUC (mmol*min/l) map of a control rabbit. **B**, MIP of AUC map of an atheroscleroticrabbit.**C**, Evans Blue fluorescence of the same atherosclerotic rabbit in **B**.

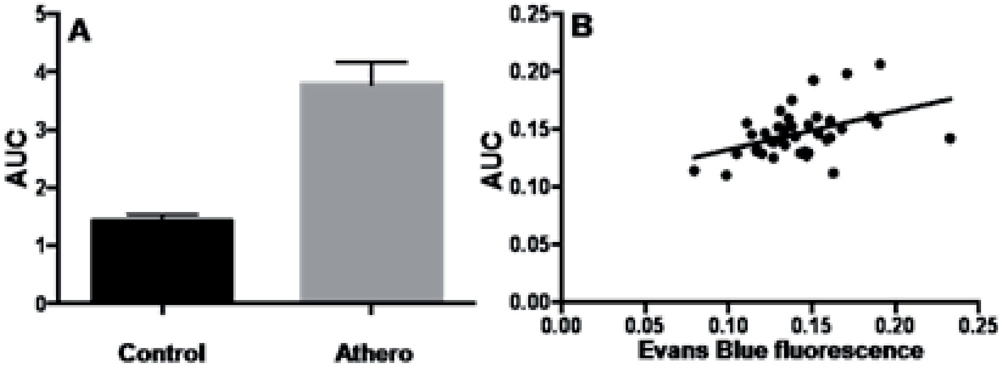

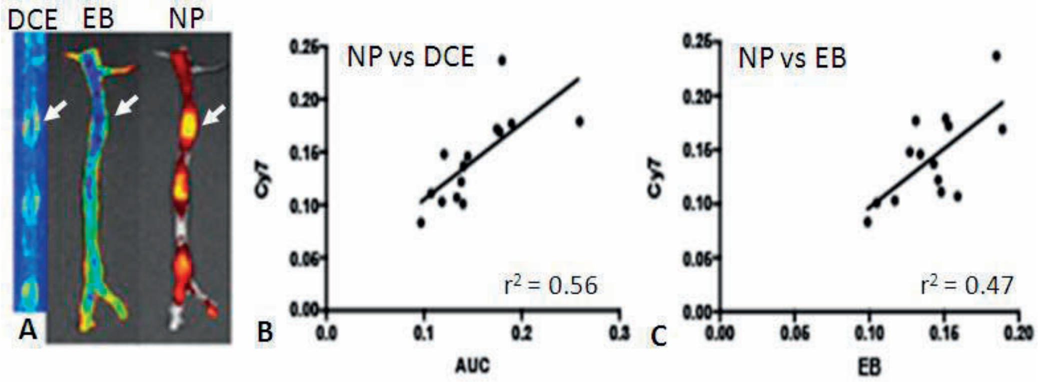

Figure 3: **A**, representative DCE maps, and fluorescence imaging with EB and nanoparticles. Corresponding areas of high permeability by DCE and EB, and high nanoparticle uptake are indicated by white arrows. The other panels show the correlation between nanoparticle uptake with DCE (**B**) and EB (**C**).

Gold nanoparticles for atherosclerotic plaque characterization via monocyte tracking using computed tomography

Peter Chhour,[1] Pratap C. Naha,[1] Muredach Reilly,[2] Victor A. Ferrari,[2] David P. Cormode[1,2]

1. Radiology Department, University of Pennsylvania; 2. Cardiology Department, University of Pennsylvania

Introduction: Atherosclerosis is characterized by the development of plaques in the arterial wall. The migration of monocytes into the arterial wall is a key process in the early development of atherosclerotic plaques. Soon after migrating into the intima, monocytes differentiate into macrophages, then foam cells, which cause instability in the plaque and eventually lead to plaque rupture. When these events occur in a coronary artery, it can lead to myocardial infarction and death. Computed tomography (CT) is one of the best techniques for imaging the coronary arteries. The use of gold nanoparticles as a CT contrast agent is a recently explored field due to gold's high biocompatibility and strong X-ray absorption. The development of gold nanoparticles for monocyte tracking via CT may lead to early detection of rupture prone atherosclerotic plaques, informing therapeutic strategies.

Methods & Results: Gold nanoparticles (AuNPs) were synthesized through the Turkevich method. Briefly, chloroauric acid was boiled with disodium citrate for 15 minutes. The resulting nanoparticles are not stable in salt based solutions such as phosphate buffered saline (PBS), but were stabilized through surface ligand exchange. AuNPs were treated with various ω-thiol ligands at a final concentration 0.47 mM of ligand for 1 hour. AuNPs were purified via centrifugation and stabilization was examined by resuspension in PBS. The final concentrations of AuNPs were determined with ICP-OES. TEM images of AuNPs were taken with a JEOL 1010 electron microscope. To assess cell viability, RAW 264.7 monocytes incubated for 24 hours with various concentrations of AuNPs were stained with LIVE DEAD solution and imaged with fluorescence microscopy. To determine monocyte uptake of AuNPs, RAW 264.7 cells were treated with ligand stabilized AuNPs for 24 hours, washed, fixed with paraformaldehyde, formed into pellets and imaged with a clinical CT scanner. ELISA was used to study cytokine release, as a measure of monocyte function.TEM of AuNPs revealed them to have an average diameter of 15 nm. From a range of ω-thiol ligands, a group of five stabilized AuNPs were further studied, i.e. 11-mercaptoundecanoic acid (11-MUA), 16-mercaptohexadecanoic acid (16-MHDA), 4-mercapto-1-butanol (4-MB), poly(ethyleneimine) (PEI), and 11-mercaptoundecyl-tetra(ethylene glycol) (MTEG). Stabilization of AuNPs can be visualized as a color change. The X-ray attenuation of monocytes resulting from uptake of AuNPs can clearly be seen in CT images (A). Internalization of AuNP was confirmed with TEM. Analysis of CT images revealed high uptake of 4-MB and 11-MUA stabilized AuNPS compared to the others. Our experiments showed that AuNPs are well tolerated by monocytes, for example, concentrations of 11-MUA AuNPs up to 1 mg/ml did not affect cell viability (C), nor did they affect cytokine release (D).

Conclusion: We have identified a variety of ligands that provide robust stability to AuNPs in biological media. Our results demonstrate that some of these ligands result in low AuNP toxicity and high uptake/CT contrast in monocytes. This work presents the basic principle of labeling monocytes for CT detection. Future work will include further analysis of cell function and in vivo experiments.

Clinical Relevance: Monocyte labeling for CT imaging may eventually be used to identify patients at high risk for a heart attack. In the meantime, it can be used to study atherosclerosis and the effect of novel treatments preclinically.

Figures and tables

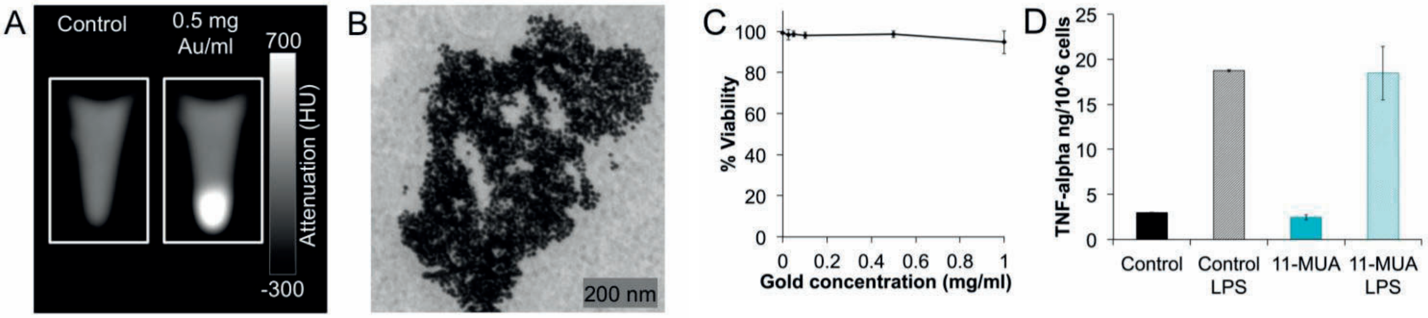

Single step reconstitution of multifunctional high-density lipoprotein-derived nanomaterials using microfluidics

Francois Fay[1§], YongTae Kim[2†§], David P. Cormode[1], Brenda L. Sanchez[1], Jun Tang[1], Mingming Ma[2], Omid C. Farokhzad[3], Kathryn J. Moore[4], Edward A. Fisher[4], Willem J. M. Mulder[2, 5], Robert Langer[2*] and Zahi A. Fayad[1*]

1) Translational and Molecular Imaging Institute, Icahn School of Medicine at Mount Sinai, 2) David H. Koch Institute for Integrative Cancer Research, Massachusetts Institute of Technology, 3) Department of Anesthesiology, Brigham and Women's Hospital, Harvard Medical School, 4) Departments of Medicine (Cardiology) and Cell Biology, NYU School of Medicine. 5) Department of Vascular Medicine, Academic Medical Center, Amsterdam, The Netherlands,
[§]Equally contributed

Introduction: High Density Lipoprotein (HDL) is a natural nanoparticle involved in the transport of cholesterol throughout the body. HDL has been shown to exhibit atheroprotective properties as it promotes cholesterol efflux from atherosclerotic plaque macrophages in the arterial wall. A recent effort centers around the use of rHDL as a natural nanoparticle platform for the delivery of contrast agents such as gadolinium chelates, iron oxide or gold nanoparticles, and employing them as molecular imaging contrast agents. To date, multistep production protocols pose a limit on the synthesis of batch quantities and are sensitive to inter-batch variations. In order to scale up the production process and to judiciously control rHDL's composition we have developed a modular single-step approach based on recently introduced microfluidics technology that enables the standardized mass production of such lipoprotein-based nanoparticles.

Methods & Results: Organic solutions containing phospholipids and imaging agents (QD, FeO-NP, Au-NP, DiO) or therapeutic model drug (simvastatin) were injected into a microfluidic chip alongside an aqueous solution containing ApoA1. Within the chip the controlled flow streams generate microvortices where fast mixing of the solutions leads to the instantaneous formation of HDL-like nanoparticles (Figure 1). HDL particles produced by this microfluidics method, which we refer to as μHDL, had similar physicochemical properties (size, morphology) to particles produced by conventional methods and natural HDL. Moreover cell based assays demonstrated that μHDL nanoparticles displayed a similar bioactivity profile to natural HDL. Incubation of macrophages of simvastatin loaded μHDL s resulted in a significant decrease in the secretion of pro-inflammatory cytokine demonstrating the potential of our new microfluidic method to produce therapeutic HDL based nanoparticles. Additionally μHDL that encapsulated hydrophobic dies (DiO) or nanocrystals such as quantum dots (QD), gold (Au) or iron oxide (FeO) nanoparticles were characterized and evaluated in model murine macrophage cell line. We observed all the different versions to have excellent diagnostic properties, to be specifically taken up by macrophages and rendered these cells visible for either magnetic resonance imaging (FeO-μHDL), computed tomography (Au-μHDL), or fluorescence imaging (QD-μHDL).

Conclusion: We have developed a microfluidics-based method to produce bioactive multifunctional HDL-like nanoparticles that can be used for molecular imaging. This single step production process will facilitate the optimization of existing HDL nanoparticle platforms and could accelerate the development of new formulations and applications.

Figures and tables

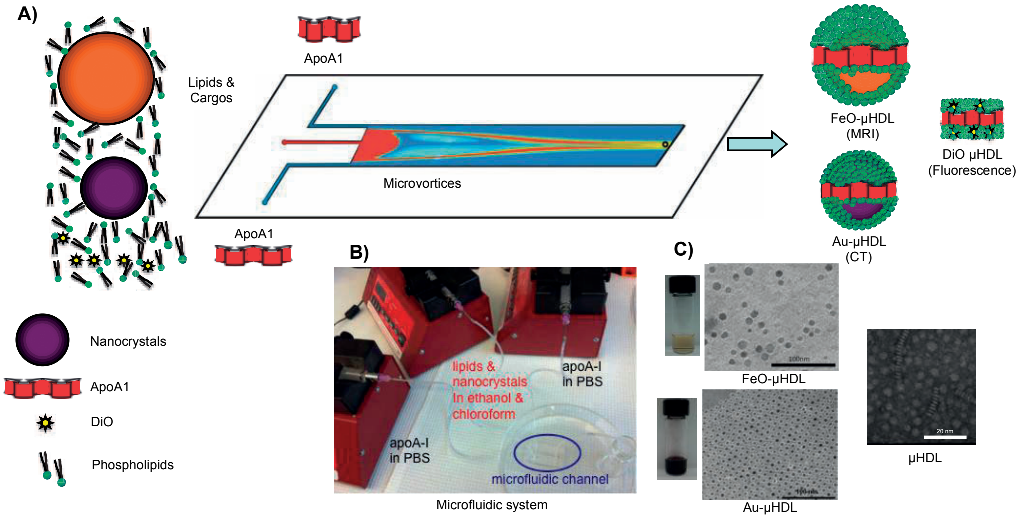

Figure 1 Microfluidic-based synthesis of HDL-derived nanomaterials (μHDLs). A) The microfluidic platform allows single-step and large-scale production of the multimodal μHDL. B) Photographs of the microfluidic device. C) Photographs and negative stain TEM images of FeO-μHDL, Au-μHDL, FeO-μHDL, and μHDL.

Development of Therapeutic Polymeric Nanoparticles containing the LXR agonist GW3965 for the Resolution of Inflammation

Suresh Gadde[1‡], Orli Even-Or[2‡], Krishna Harsha Adusumilli[1], Andrea Erakovic[1], Edward A. Fisher[2], Omid C. Farokhzad[1]

[1]Laboratory of Nanomedicine and Biomaterials, Brigham and Women's Hospital, Harvard Medical School, Boston, MA 02115, USA
[2]Department of Cell Biology and the Leon H. Charney Division of Cardiology, New York University School of Medicine, New York, NY 10016.
[‡]These authors contributed equally to this work

Introduction: Studies have shown that activation of liver X receptors (LXR) can attenuate inflammation and inflammatory gene expression, which makes them particularly attractive targets for intervention of cardiovascular, metabolic, and/or inflammatory diseases in humans. In this study, we developed a nanoparticle (NPs) library containing synthetic LXR agonist GW3965 (GW) and studied the anti-inflammatory effects of these NPs *in vitro* and *in vivo* .

Methods & Results: The library of LXR agonist containing NPs (LXR-NPS) were synthesized via self-assembly of biodegradable PLGA, PLA based polymeric derivatives. Our library contains more than 70 distinct NP formulations, with variations in critical parameters such as size, surface charge, drug loading and drug release (Fig 1), which can affect pharmacokinetics and biodistribution of GW. The LXR-NPs with ideal physicochemical properties were further evaluated for their anti-inflammatory effects *in vitro* by inhibiting lipopolysaccharide (LPS) induced inflammatory response in peritoneal macrophages. The macrophages were pretreated with GW and LXR-NPs and then stimulated with LPS to induce a pro-inflammatory response. Macrophages treated with either GW or LXR-NPs substantially suppressed the secretion of pro inflammatory mediators MCP-1, and TNFα. Over all, LXR-NPs have shown higher efficacy than GW alone, and formulation PpcPgGW (PLGA-PEG/PLGA-GW/GW) was further evaluated *in vivo*. The capacity of PpcPgGW to prevent inflammation was also evaluated in a zymosan-induced peritonitis model in wild type C57BL/6 mice. The mice were intravenously (i.v.) treated with controls and PpcPgGW, 1h before Intraperitoneal injection (i.p.) of zymosan. Treatment with the PpcGW formulation resulted in a significant reduction of the PMN cell infiltration into the inflammation site as assessed 4 h after Zymosan injection (Fig.2). Also, the treatment with PpcPgGW significantly suppressed gene expression and secretion of pro-inflammatory factors MCP-1 and TNFα.

Conclusion: We have successfully developed a library of nanoparticles containing LXR agonist GW3965 and results shows that our nanoparticles are capable of resolving inflammation.

Clinical Relevance: LXRs plays important role in resolving inflammation and LXR agonists are promising candidates for treatment of inflammation. Here in our study, we developed biodegradable nanoparticles that can deliver LXR agonist in a controlled fashion, and suppress pro-inflammatory mediators. These proresolving NPs have potential for treatment of a wide array of diseases involving inflammation.

Figures and tables:

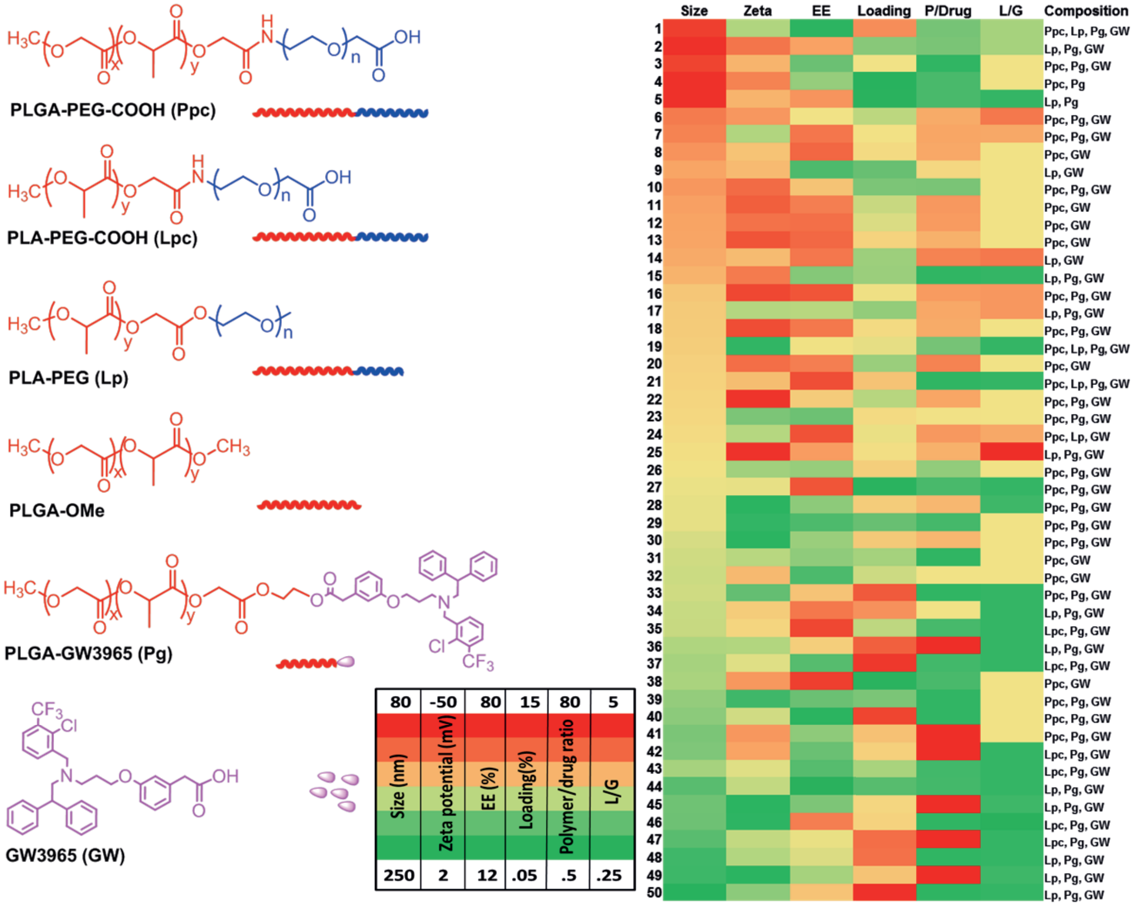

Figure 1: Chemical structure of polymers and polymer drug conjugate used in the generation of particle library (Left panel). Assortment of nanoparticle library (Right panel). Heat map illustrates formulation parameters (% of encapsulation efficiency, % of loading, and polymer/drug ratio) and physicochemical properties (hydrodynamic size, surface charge) of NPs.

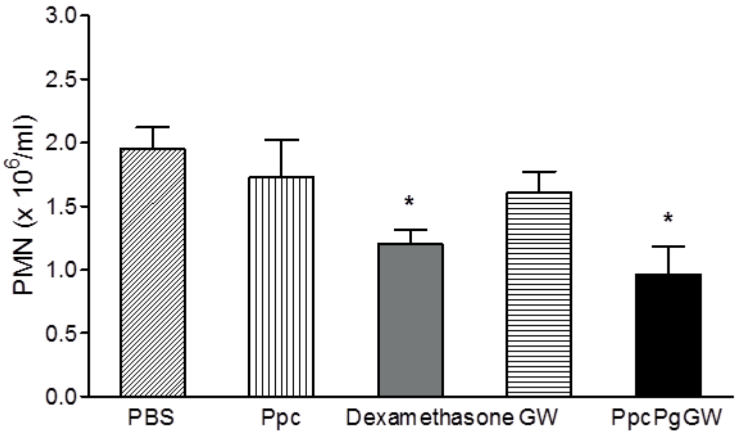

Figure 2: WT male mice (n=5) were administrated i.v with the respective regimens and after one hour mice were injected i.p. with Zymosan. Four hours afterwards, the cells were harvested and analyzed by FACS. (Each bar represents the Mean ± SEM. **P<0.05* vs PBS and Ppc)

Silica-encapsulated silver nanoparticles as contrast agents for contrast-enhanced dual-energy x-ray breast imaging

Roshan Karunamuni, Ajlan Al-Zaki, David Cormode, Anatoliy Popov, Jim Delikatny, Andrew Tsourkas, Andrew D.A. Maidment

University of Pennsylvania, Philadelphia, PA 19104

Introduction: Contrast-enhanced (CE) dual-energy (DE) x-ray breast imaging encompasses an emerging group of modalities used to increase the contrast of radiographic imaging agents by suppressing the anatomical signal variation in the body. By reducing the effect of this soft tissue “anatomical noise”, it is then possible to segment and quantify the signal from an exogenous imaging agent. Traditionally, CEDE breast imaging has been employed with an iodinated contrast agents.These are typically small tri-iodobenzene compounds with substitutions for improved solubility. While these iodinated agents are extremely stable and resist biodegradation, they are plagued with several limitations: low circulation time, off-target accumulation, and contrastmedia related nephropathy. We have previously demonstrated through theoretical analysis that silver may be used as an alternative to iodine as an imaging agent due to the favorable position of its k-edge (26 keV) in the mammographic energy range. In this work, we design, manufacture, and test a silica-encapsulated silver nanoparticle (AgNP)imaging agent for use in CEDE imaging.

Methods & Results: Synthesis: The silver core is synthesized by reduction of silver nitrate using polyvinylpyrriodine (PVP) at elevated temperature. The PVP-stabilized silver cores are then encapsulated within a silica shell by mixing with tetraethoxysilane for 12 hours. Finally, the silica-silver nanoparticles are made biologically-compatible by the addition of a polyethylene glycol (PEG) surface layer. This is a two-step process, in which the nanoparticles are first made lipophilic by covalently linking octadecanol to the silica surface. Next, an amphiphilic ligand that contains a lipophilic polycaprolactone chain and a hydrophilic PEG chain is bound to the surface of the nanoparticle. Transmission electron micrographs of the particles showed a solid silver core with an average diameter of 39 ± 6 nm and a total diameter (including the silica shell) of 102 ± 9 nm (Figure 1). Testing in living systems:Immunocompromised mice were injected with 600 mg/kg of silica-silver nanoparticles. Immediately post-injection, the animals were imaged initially using a small animal, micro-CT scanner at 45 kVp. The images demonstrated significant enhancement in the heart, liver, and primary and peripheral blood vessels (Figure 2). The mice were re-imaged 24 hours after the injection, and the majority of the particles were located in the spleen and liver, with minimum enhancement observed in the heart and other organs. Testing the contrast in a clinical system: The contrast-to-noise ratio (CNR) of the silica-silver nanoparticles was compared to that of clinically-used Omnipaque in the Hologic Selenia dimensions CEDE clinical system for the same volumetric concentration. The nanoparticles and iodinated contrast agent were injected into a breast tissue phantom and imaged. For several combinations ofclinically-feasible imaging parameters, the CNR of the AgNP was comparable and in some cases superior (70%) to that of iodine(Figure 3).

Conclusion: Silver nanoparticles were successfully encapsulated with a silica shell and stabilized within a biocompatible polymeric micelle. The particles showed significant enhancement within the heart, liver, and primary blood vessels of immunocompromised mice. Using breast phantom experiments, the contrast-to-noise ratio of the silver nanoparticles were found to be comparable or in some cases superior to that of iodine for several combinations of spectral pairs.

Clinical Relevance: The implementation of a nanoparticle-based imaging agent for CEDE imaging provides opportunities to obtain surface characteristics and molecular boundaries of breast lesions. The unique combination of functional and high-resolution anatomical informationin a single imaging procedure represents a powerful breast imaging tool for morphological and vascular characterization of breast lesions.

Figures and tables

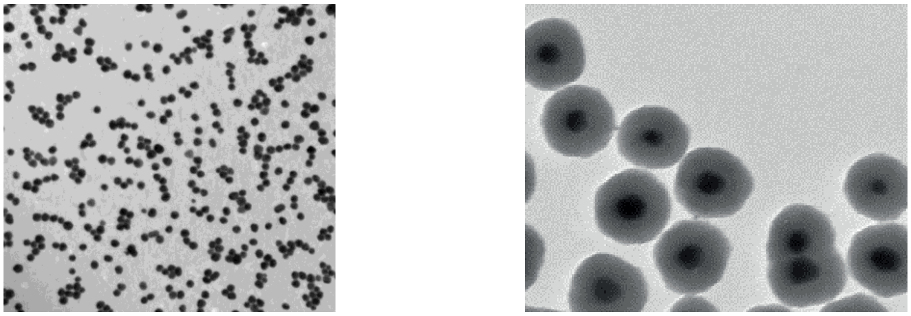

Figure 1. TEM images of (**left**) PVP-stabilized silver core, 39 nm in diameter and (**right**) Si-encapsulated silver cores with a total diameter of 102 nm. The PEG-PCL layer on the final AgNP is electron-transparent and thus does not appear in the TEM image.

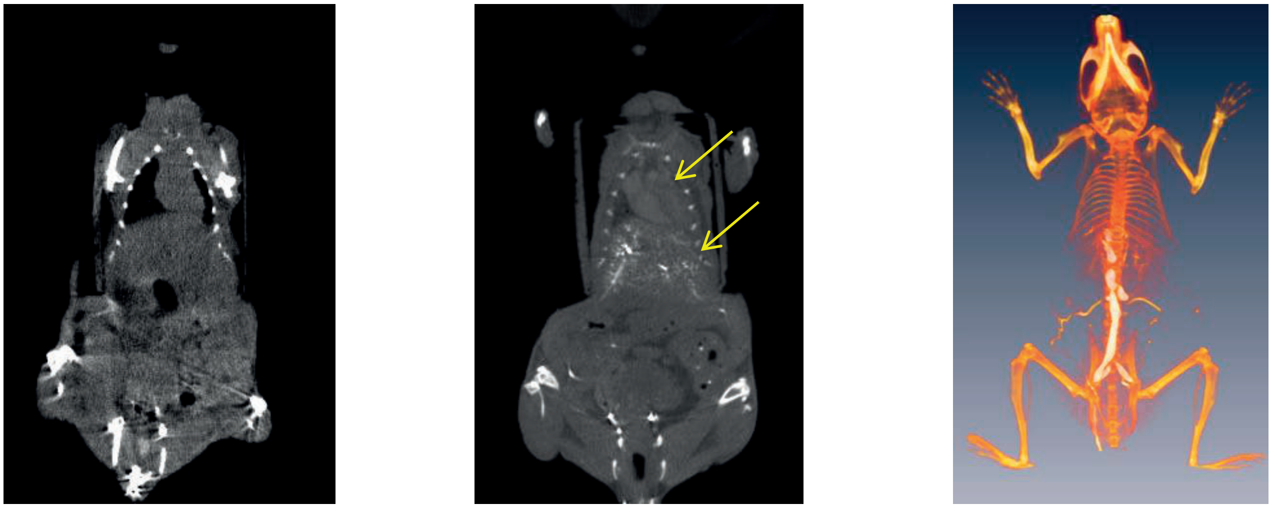

Figure 2. Left: Reconstructed slice of micro-CT volumetric data set obtained before injection of AgNP. **Middle:** Reconstructed slice obtained immediately post-injection of AgNP at a dose of 600 mg silver/kg of body weight. Significant contrast is observed immediately post-injection in both the heart and liver (yellow arrows). **Right:** False color image of volumetric data showing significant enhancement in peripheral and primary blood vessels.

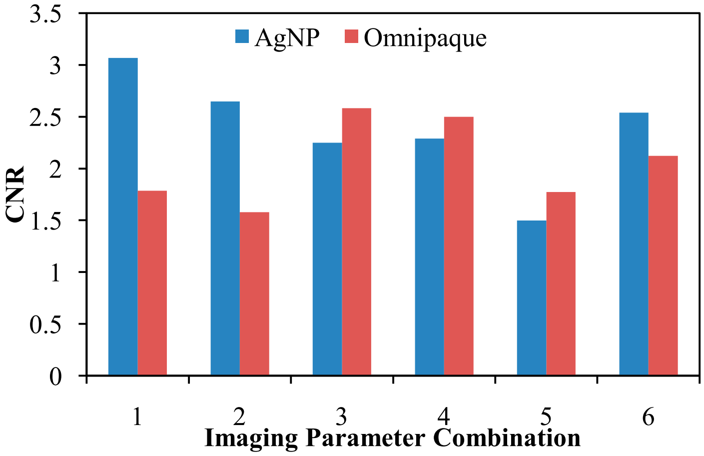

Figure 3. CNR comparison between silica-silver nanoparticles (AgNP)and clinically used Omnipaque on the Hologic Selenia Dimensions CEDE system. The contrast was compared for the same volumetric concentration for six unique combinations of imaging parameters. The nanoparticles exhibited similar, and in some case, superior contrast to the iodinated agent.

Radiolabeled Liposomes: Toward Personalized Medicine.

Carlos Perez-Medina[1,2,3], Willem J. Mulder[3], Valentin Fuster[2,4], Jason S. Lewis[5], Zahi. A. Fayad[3], Thomas Reiner[5]

1 Centro de Investigación en Red de Enfermedades Respiratorias, Spain. 2 Centro Nacional de Investigaciones Cardiovasculares, Madrid, Spain, 3 Translational and Molecular Imaging Institute, Icahn School of Medicine at Mount Sinai, New York, 4 Zena and Michael A. Wiener Cardiovascular Institute, Icahn School of Medicine at Mount Sinai, New York, 5 Department of Radiology, Memorial Sloan-Kettering Cancer Center, New York

Introduction: Nanotherapy holds great promise in the fight against cancer. More recently, its exploitation for atherosclerotic disease has been shown in preclinical studies. However, due to the heterogeneity of vascular permeability in the aforementioned diseases, the potential benefits of nanotherapy vary immensely between patients. Therefore, an imaging-based screening process to verify amenability of nanotherapy for individual patients would be of tremendous value and would render it a unique personalized medicine treatment modality. In the current study we explore strategies to radiolabel lipid-based nanoparticulate platforms in a modular fashion, which simultaneously allows prescreening subjects for nanotherapy amenability and biodistribution. Specifically we focused on an integrated approach to label liposomes with ^{89}Zr that satisfies the required criteria for tracer development in terms of labeling efficiency and label stability.

Modular labeling approach: Three new different approaches will be tested exploiting three conjugation reactions. These will be directly compared to a traditional direct labeling approach of the liposomes employing a lipid-chelator conjugate. This stage is already ongoing and the modified clickable lipid building blocks and chelators (Deferoxamine, DFO) are being synthesized and characterized.

Conclusion: This project is aimed at developing novel labeling strategies that allow the visualization lipid nanoparticles. In the future we will exploit the approach to assess nanoparticle accumulation in atherosclerotic lesions in a rabbit model as well as patients.

Clinical Relevance: The new materials will enable selection of patients amenable for nanotherapy.

Figures and Tables

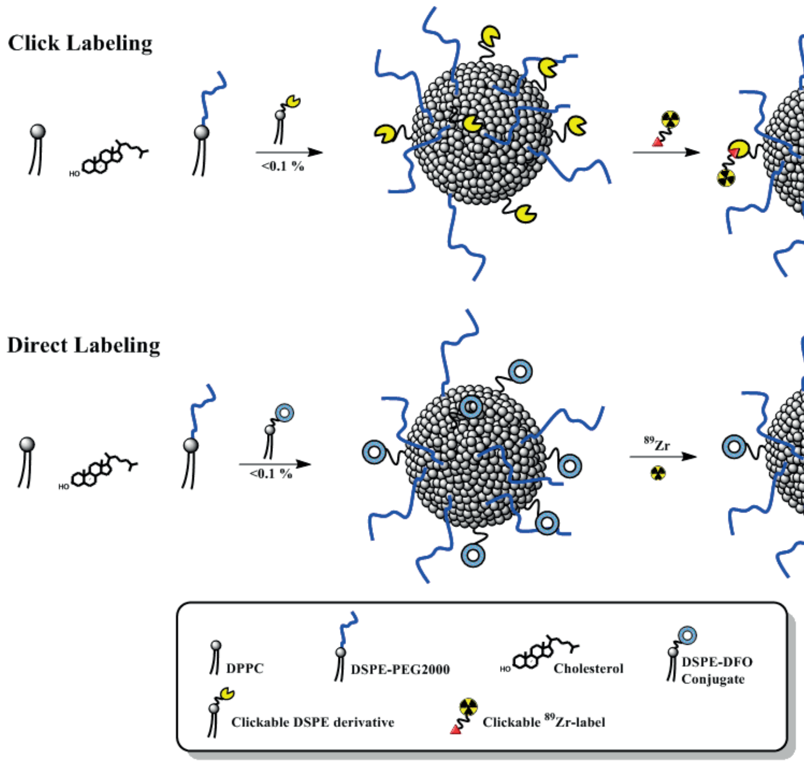

Nanoparticle formulations of cannabinoids for targeted treatment of cancer

Bram Priem, Brenda Sanchez, Francois Fay, Willem J. Mulder

TMII Nanomedicine department, Department of Radiology, Icahn School of Medicine, New York

Introduction: The cannabinoid receptor (CB) is well-known for regulating neutrotransmitter release in the brain. Recently, CBs have been found to play a critical role in many non-neurological diseases including cancer. Activation of the cannabinoid receptors by their agonists, have been shown to inhibit the growth of tumors and produce beneficial effects on cardiovascular disease in experimental settings. Δ9-tetrahydrocannabinol (THC) is one of the most well-known agonists to CB1 and CB2. Another cannabinoid named cannabidiol(CBD) is reported to be effective against cancer and to enhance the effect of THC. However, the therapeutic effects of these compounds have not been explored due to their undesirable psychoactive effects, high hydrophobicity, and poor bioavailability to diseased tissues after systemic administration. In this study, we used lipid-based nanoparticles as a drug carrier to circumvent these hurdles by increasing the compound bioavailability and realizing targeted delivery.

Methods and results: Polylactic-co-glycolic acid(PLGA) based lipid nanoparticles were used in a cell viability assay to assess the effectiveness of the formulation compared to free drug on a variety of cell lines. Particle drug concentrations were measured with high-performance liquid chromatography to assure equal amount of drug was given in vitro. Results show a significant decrease in cell viability for the nanoparticle formulation at equivalent doses of free drug in a variety of cancer cell lines.

Conclusion: Our results clearly showed that nanoparticles formulations with either THC or CBD have significantly higher efficacy than free drugs in vitro. In the future, we will further examine these results with the use of flow cytometry and with the use of in vivo experiments

Figures and tables

MDA-MB 231

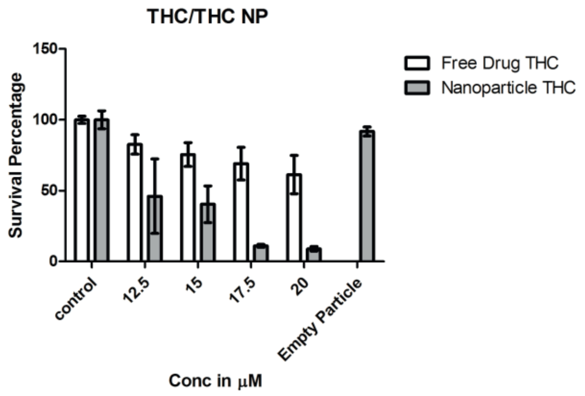
THC/THC NP

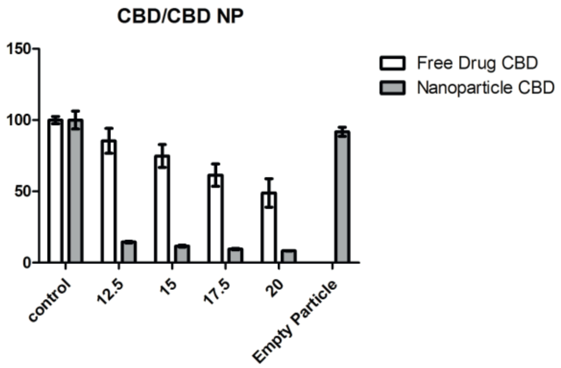
CBD/CBD NP

A Multifunctional Lipoprotein/Polymer Hybrid Nanoparticle for Controlled Release Drug Delivery to Atherosclerotic Plaques

Brenda L. Sanchez-Gaytan[1], Mark E. Lobatto[1,2], Jun Tang[1], Francois Fay[1], Canturk Ozcan[1], YongTae Kim[3], Omid C. Farokhzad[4], Edward A. Fisher[5], Robert Langer[3], Zahi A. Fayad[1], Willem J.M. Mulder[1,2]

[1]TMII, Icahn School of Medicine of Mount Sinai, NY, USA. [2]Department of Vascular Medicine, Academic Medical Center, Amsterdam, The Netherlands, [3]Department of Chemical Engineering, MIT, Cambridge, MA, USA. [4] Laboratory of Nanomedicine and Biomaterials, Department of Anesthesiology, Brigham & Women's Hospital, Boston, MA, USA. [5] Department of Medicine and Cell Biology, NYU School of Medicine, NY, USA.

Introduction: 2nd generation polymeric nanoparticles have shown significant advantages in drug delivery. They can be loaded with poorly water soluble drugs, their size can be judiciously controlled[2] and their surface can be functionalized with a stealth coating and targeting ligands. Importantly, the polymeric core can be loaded with drugs and/or contrast agents for which the release rates can be controlled by the choice of polymer composition. High-density lipoprotein (HDL) is a natural nanoparticle that transports fats through the body, which has an inherent affinity for atherosclerotic plaques. In this study we developed a novel HDL-like hybrid nanoparticle using recently developed microfluidics technology. The nanoparticle is comprised of a HDL coating that encapsulates a poly(lactic-co-glycolic acid) (PLGA) core suitable for the delivery of drugs in a controlled manner. The versatility of the approach allows the incorporation of functional lipids to render multifunctional nanoparticles with imaging, therapeutic and atherosclerosis targeting properties.

Methods and Results: Hybrid polymer-HDL nanoparticles with a PLGA core and a coating comprised of lipids and apolipoprotein A1 (PLGA-HDL) were synthesized using microfluidics. The synthetic approach consists of the rapid injection of the components in three different channels of a microfluidics chip. Amphiphilic phospholipids and PLGA were dissolved in a mixture of ethanol and acetonitrile. This solution was injected in the middle channel of the microfluidic chip and mixed with an aqueous apoprotein A1 (ApoA1) solution injected in the two outer channels. Inside the chip, controlled nanoprecipitation occurred through microvortices, resulting in the instantaneous and continuous production of hybrid PLGA-HDL nanoparticles with high reproducibility (Fig 1A, B). he resulting PLGA-HDL nanoparticles had a hydrodynamic diameter of 75 nm with a polydispersity of 0.205 (Fig 1D). PLGA-HDL nanoparticles with imaging capabilities were formed by introducing Gd-DTPA-lipids and/or fluorescent lipids in the formulation. This allows their visualization in *in vitro* and *in vivo* studies (Fig 1E-G). Cells tolerated the PLGA-HDL nanoparticles very well and displayed a particular affinity for macrophages over other cells (Fig 1E). Moreover, the selective nanoparticle uptake by macrophages could be decreased by a competitive incubation with native HDL. In vivo studies carried out on ApoE knockout mouse showed a clear accumulation of the nanoparticles within the atherosclerotic lesions. Also, a high degree of colocalization of PLGA-HDL with macrophages was observed.

Conclusions: We developed a hybrid HDL-like nanoparticle platform with both *in vivo* and *in vitro* imaging capabilities. The nanoparticle design allows the incorporation of water soluble drugs in the polymeric core. PLGA-HDL nanoparticles displayed similar behavior as native HDLs.

Clinical Relevance: HDL-like nanoparticles labeled with contrast agents have been shown suitable for molecular imaging as they effectively target atherosclerotic plaque. The hybrid HDL-like nanoparticle presented here provides additional capabilities as a theranostic nanoparticle with controlled drug release.

Figures and tables

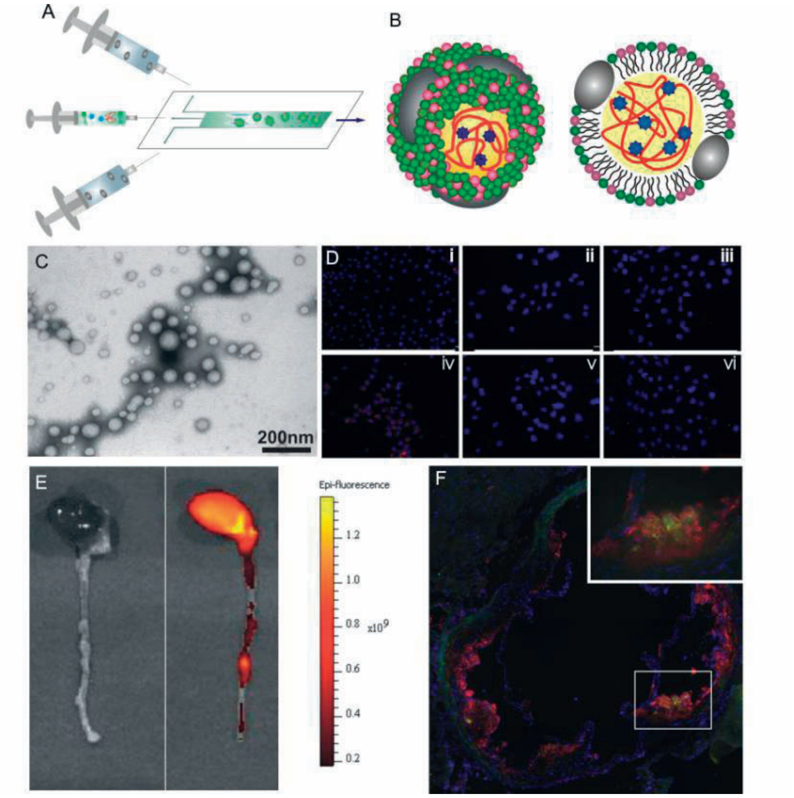

Figure 1. A) Schematic representation of the synthesis of PLGA-HDL nanoparticles using microfluidics. B) 3-D and cross-sectional view of multifunctional HDL-like nanoparticles containing functional lipids in the corona and drug molecules incorporated in the PLGA core. C) TEM image of the HDL-PLGA nanoparticles negatively stained with phosphotungstic acid. D) Micrograph of macrophages (i, iv), hepatocytes (ii, v) and pancreatic endothelial cells (iii,vi) incubated with Rhodamine-labeled HDL-PLGA (iv-vi) and Rhodamine-labelled PEG lipids in the corona and PLGA in the core (i-iii). After 2 hours of nanoparticle incubation at 37 °C, macrophages showed a preferential uptake of Rhodamine-labeled HDL-PLGA nanoparticles (iv). E) IVIS optical imaging of atherosclerotic aorta excised from a ApoE KO mice injected with saline (left) or HDL-PLGA (right). F) Fluorescence microscopy of the aortic root of ApoE KO mice revealed colocalization of HDL-PLGA (FITC) and CD68-macrophages (TRITC) 24 hours after injection.

A nanomedicine-based treatment regimen to induce plaque remodeling to a favorable phenotype in mice with advanced atherosclerosis

Jun Tang[1], Mark E. Lobatto[1], Wei Leong[1], Hendrik Sager[2], Susanne van der Staay[1], Sarian M. van Rijs[1], Sarayu Ramachandran[1], Yaritzy M. Astudillo[3], Raphael Duivenvoorden[4], Ying Wang[5], Valentin Fuster[6], Ira Tabas[5], David P. Cormode[7], Matthias Nahrendorf[2], Edward A. Fisher[3], Zahi A. Fayad[1], Willem J.M. Mulder[1]

[1]Translational and Molecular Imaging Institute, Icahn School of Medicine at Mount Sinai, New York, NY, USA. [2]Center for System Biology, Massachusetts General Hospital, Boston, MA, 02114. [3]Department of Medicine (Cardiology) and Cell Biology, Marc and Ruti Bell Program in Vascular Biology, NYU School of Medicine, New York, USA. [4]Department of Vascular Medicine, Academic Medical Center, Amsterdam, The Netherlands. [5]Department of Medicine, Columbia University, New York, NY, USA. [6]Department of Cardiology, Icahn School of Medicine at Mount Sinai, New York, NY, USA. [7]Department of Radiology, University of Pennsylvania Perelman School of Medicine, Philadelphia, PA, USA

Introduction: Inflammatory macrophages contribute to an increased chance of atherosclerotic plaque rupture. Previously, we developed a simvastatin loaded high-density lipoprotein ([S]-rHDL) nanoparticle to decrease plaque macrophages in apolipoprotein E$^{-/-}$ (ApoE$^{-/-}$) mice. In this study, we investigated if a short-term aggressive [S]-rHDL treatment followed by a subsequent mild treatment regimen could induce favorable plaque remodeling.

Methods & Results: 99 ApoE$^{-/-}$ mice with advanced atherosclerotic plaques received 4 intravenous (i.v.) doses of [S]-rHDL (60 mg/kg statin, 40 mg/kg ApoA-1) in one week. Subsequently, the mice received either 8-week treatment of oral statin (15 mg/kg/day), low dose [S]-rHDL (15 mg/kg statin, i.v. twice/week) or placebo **(A)**. Macrophage levels (CD68 stain), collagen (trichrome stain) content and plaque size (hematoxylin phloxine saffron stain + CD68 stain) were quantified in aortic root sections. One-week [S]-rHDL treatment resulted in a 68% decrease of macrophage levels (**B**). Subsequent 8-week oral statin or low dose [S]-rHDL treatment maintained the low macrophage levels **(C)**. Importantly, the collagen/macrophage ratio, an indicator for plaque stability, was significantly higher in these two groups than control **(D)**. Liver, muscle and kidney damage markers were not affected by the treatment. In addition, *in vivo* fluorescence molecular tomography imaging showed that one week [S]-rHDL treatment reduces protease activity in aorit roots by 58% (p=0.0088).

Conclusion: This novel two-pronged nanomedicine/oral statin regimen rapidly reduced macrophage content in advanced atherosclerotic plaques in the first week, while a subsequent moderate 8-week treatment resulted in plaque remodeling towards a high collagen/macrophage ratio.

Clinical Relevance: The current nanomedicine-based regimen can potentially induce rapid remodeling to a more favorable plaque phenotype and sustain it over time, which might reduce the risk of recurrent events.

Figures and tables

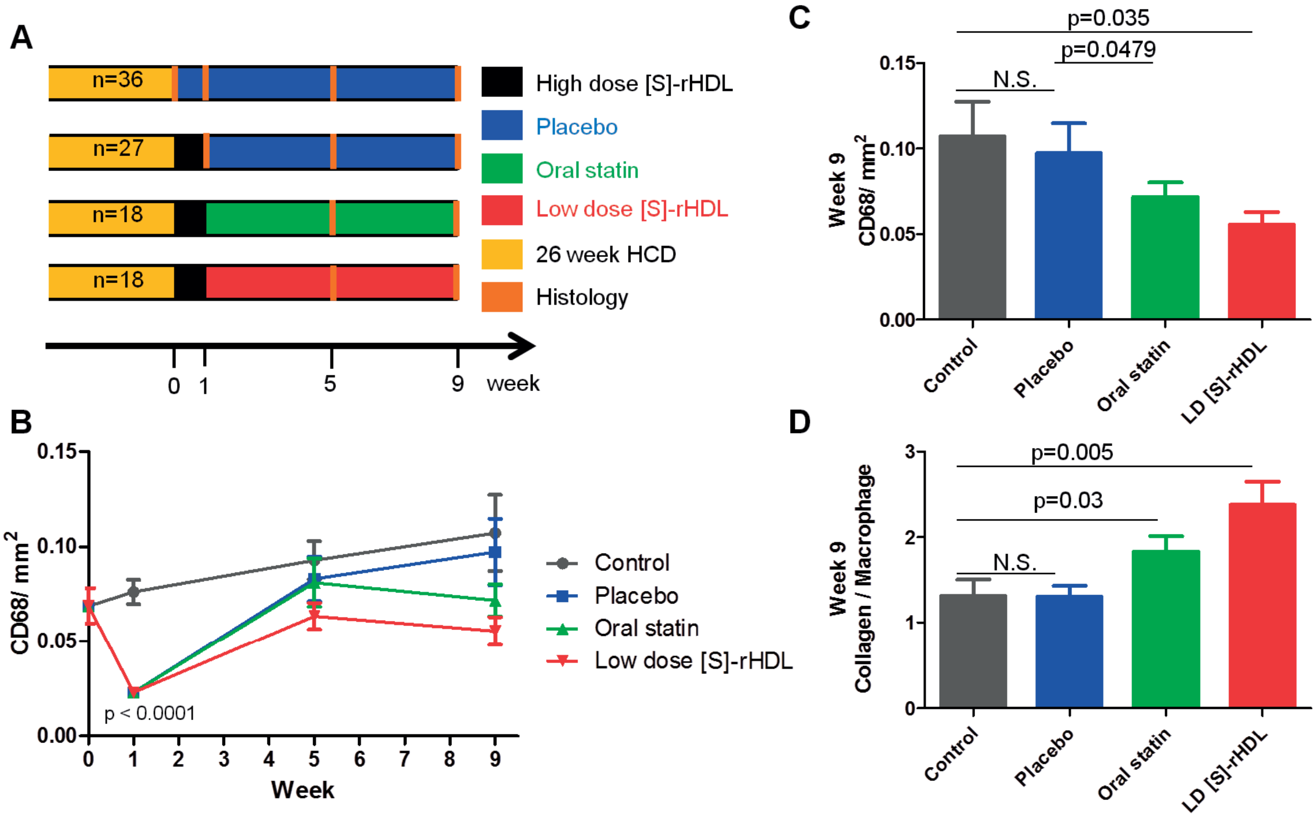

Lipidoid Nanoparticle mRNA Delivery to Myocardium for Controlled Expression of Novel Regenerative Therapeutics

I.C. Turnbull[1], A.A. Eltoukhy[2], K.M. Fish[1], A.R. Kontorovich[1], J. Chen[1], R.J. Hajjar[1], D.G. Anderson[2], K.D. Costa[1]

[1]Cardiovascular Research Institute, Icahn School of Medicine at Mount Sinai (New York, NY).
[2]David H Koch Institute for Integrative Cancer Research, Massachusetts Institute of Technology (Cambridge, MA).

Introduction: Modified mRNAs interact and assemble with lipidoid mixtures resulting in nanoparticles (NPs) that can be used to deliver growth factor message to cells, resulting in translation and protein expression. Such NPs offer a potential alternative to viral vectors for gene therapy, but efficacy has not been demonstrated in the heart. We have recently explored lipidoid nanoparticle mediated eGFP mRNA delivery to cardiomyocytes *in vitro* and in rat myocardium as proof of concept for stem cell stimulatory growth factor delivery to drive regeneration of the infarcted heart.

Methods & Results: Stemfect (SF, Stemgent, Cambridge, MA) and modified lipidoid formulations (FLNP) were used to create metastable and stable nanoparticles containing modified eGFP. These nanoparticles were delivered to cultured cardiomyocytes as well as living rat heart via direct intramyocardial injection (IM) or by intracoronary delivery with aortic cross-clamping (CC). Expression of mRNA in harvested tissue samples was monitored by real time-PCR, and eGFP protein product was detected by immunofluorescence. Cultured neonatal rat cardiomyocytes were efficiently transduced by incubation with SF-eGFPmRNA, outperforming Lipofectamine (Life Technologies) (Figs. 1, 2a), whereas FLNPs were ineffective under matched *in vitro* conditions (Fig. 2b). Interestingly, adult rat myocardium was successfully transduced by both NP formulations via IM delivery using dosages of 1ug to 10ug eGFPmRNA (Fig. 3), with sacrifice at 20 hours after the injection. Compared to saline-treated negative controls, the fold increase in eGFPmRNA levels for the SF was 726x to 1393x (n=1), whereas FLNP increased dramatically from 142x at 1ug (n=3) to >5000x at 5 and 10ug (n=3). With CC delivery, eGFPmRNA expression was lower than for IM (420x at 10ug) but still significant. Fluorescence microscopy revealed GFP positive cells in the subepicardium of all treated hearts (Fig. 5), mirroring the mRNA expression data. Biodistribution was evaluated by analyzing eGFP mRNA expression levels in lung, liver, spleen, kidney, skeletal muscle and brain, and compared to heart levels (Fig. 4). While IM injection of SF-eGFP mRNA resulted in some expression in the lung and spleen, IM injection using FLNP was almost entirely restricted to the heart with <1% off-target expression. As expected for intracoronary delivery to healthy myocardium, biodistribution was more pronounced with CC delivery of FLNP, particularly in the lung, liver and spleen; results could be very different for CC delivery to infarcted myocardium with compromised coronary flow. Preliminary assessment of expression kinetics was also performed using IM injection of FLNP at the 5ug dosage, revealing high levels of eGFPmRNA expression in the heart at 6h post-delivery (18380x ± 5457, n=2), compared to 20h (5628x ± 1291, n=3) and 48h (6537x, n=1), with no detectable expression at 2 weeks post-delivery (53x ±26, n=3); there were also no overt signs of longer term toxicity (data not shown).

Conclusion: We have completed proof of concept studies supporting our hypothesis that lipidoid nanoparticles carrying modified eGFP mRNA can be used for message delivery to cardiac cells *in vitro* and *in vivo*. This transient expression is readily detectable on a time scale from several hours to several days, with limited off-target biodistribution for IM delivery, and is therefore suitable for delivery of growth factors, such as stem cell factor, to stimulate cardiac stem cell homing, proliferation, and differentiation for cardiac regeneration applications (Fig. 6).

Clinical Relevance: The incidence of heart failure (HF) and associated emergency room visits continues to increase worldwide despite significant advances in pharmacological therapy and assist devices. Thus, there is an urgent need for novel approaches to address the etiology of HF after acute coronary events that often, ultimately lead to HF. Recent discoveries of cardiac stem cell (CSC) populations in the infarcted heart and de-differentiated cardiomyocytes in the hypertrophic heart present an opportunity for novel regenerative therapies with the potential to decrease the rate of, or mitigate the progression to heart failure. Nanoparticle-based delivery of modified mRNA for transient expression of key growth factors that induce stem cell proliferation, adhesion, angiogenesis in addition to anti-apoptotic signaling and cell survival pathways may prove to be an efficacious approach to leveraging CSC potential.

Figures and Tables

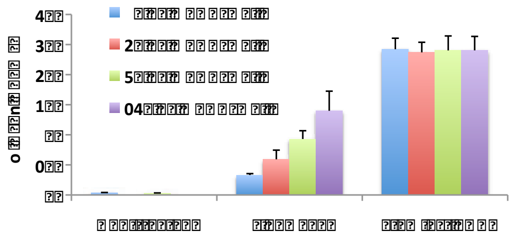

Figure 1. Neonatal rat cardiomyocytes (NRCM) in culture, were successfully transduced with Stemfect eGFP-mRNA.

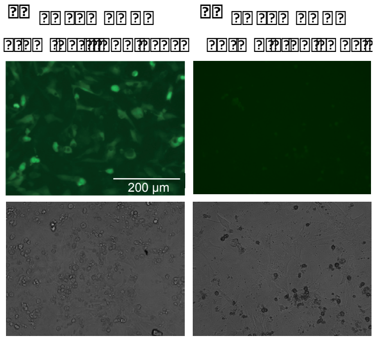

Figure 2. Cultured neonatal rat cardiomyocytes 24h after incubation with lipid nanoparticles.

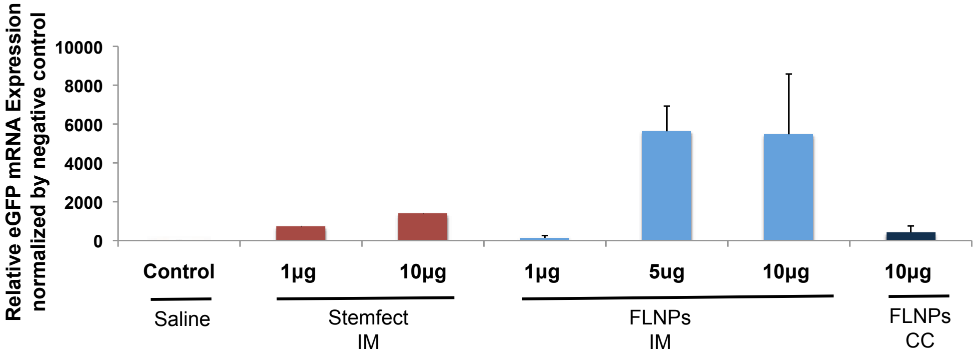

Figure 3. eGFPmRNA levels in rat myocardium 20 hours after lipid nanoparticle delivery, using Stemfect lipoplexes or Formulated lipid nanoparticles (FLNPs), via direct intramyocardial injection (IM) or aortic cross clamping (CC).

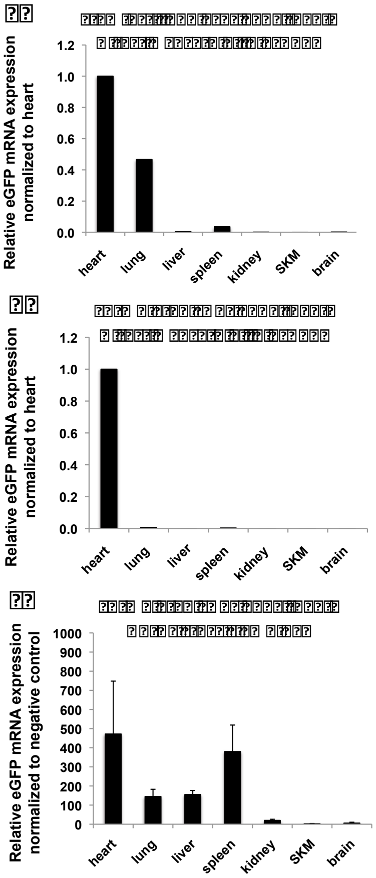

Figure 4. Biodistribution of FLNPs/eGFPmRNA .

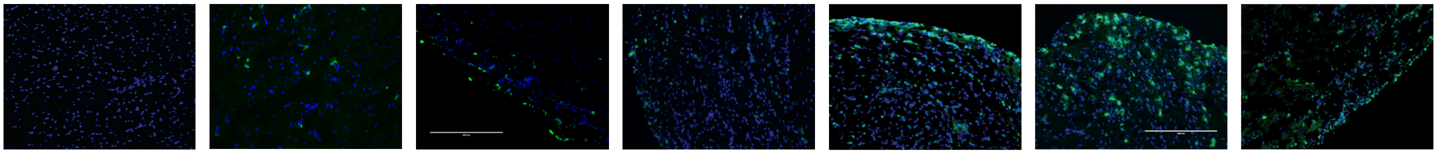

a) negative control

b) 1µg mRNA Stemfect lipoplexes

c) 10µg mRNA Stemfect lipoplexes

d) 1µg mRNA FLNPs

e) 5µg mRNA FLNPs

f) 10µg mRNA FLNPs

g) 10µg mRNA FLNPs Cross clamping

Figure 5. Immunofluorescence of rat myocardium 20 after injection of lipid nanoparticles, via direct intramyocardial injection (b-f) or cross clamping (g). Sections incubated with anti-GFP antibody (green), and nuclei stained with DAPI (blue).

Figure 6. Conceptual model of nanoparticle mediated mRNA delivery to the infarcted heart vie Direct introduction of nanoparticles to the heart either via intramyocardial injection, or by non-invasive intra-coronary delivery.

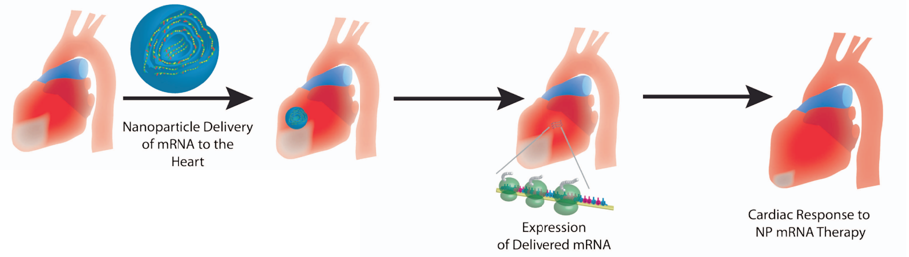

Abstracts, Cardiovascular Imaging Category

Reproducibility of analysis of a simple multicenter protocol for evaluation of deep vein thrombosis

Nadia Alie, Sarayu Ramachandran, Philip M. Robson, Daniel D. Samber, Zahi A. Fayad, Venkatesh Mani
Translational and Molecular Imaging Institute, Icahn School of Medicine at Mount Sinai

Introduction: Venous thromboembolism (VTE) is a complex multifactorial disease that affects 300,000-600,000 individuals in the United States every year. Deep vein thrombosis (DVT) is the most common presentation of VTE, and manifests in the form of blood clots in the deep veins of the body, typically of the calf, thigh and lower pelvis. The diagnosis, therapeutic management and follow-up of subjects with DVT cannot be based solely on clinical examinations, since the signs and symptoms of this disease are not specific. Here, we propose the use of magnetic resonance (MR) venography using a blood pool contrast agent (Ablavar) to robustly quantify the volume of deep vein thrombosis in a multi-center setting.

Methods & Results: From a subset of 90 subjects projected to be enrolled in a study evaluating the efficacy of DVT treatment, DVT volumes were computed. Deep veins evaluated included the external iliac vein, common femoral vein, superficial femoral vein, deep femoral vein, popliteal vein, anterior tibial vein, posterior tibial veins, gastrocnemius veins, and the peroneal veins.
Acquisition: Subjects were imaged in a feet first, supine position. Three segments were acquired, encompassing a) pelvis b) thigh and c) calf sections (Figure 1) using a T1W 3D gradient echo sequence before and 5 minutes after injection of 0.03mmol/kg of Ablavar contrast agent.
Analysis: Coronal post contrast images were reformatted using the curved 3D MPR tool in OsiriX, as shown in Figure 2. The DVT was visualized as lower signal intensity compared to the surroundings. A curved path following the centerline of each vein being analyzed was calculated. The vessel with the DVT was then straightened, and the dataset was reformatted to obtain multiple images perpendicular to the vein. The DVT was segmented by two observers by placing regions of interest on each reformatted imaging slice to obtain volumetric measurements of the DVT.
Reproducibility assessment: Intra class correlation and Bland Altman analysis were performed to compare the results obtained by the two readers.
Results: Figure 3 shows the Bland Altman and intra class correlation (ICC) plots showing the agreement between the two readers. The ICC between the two readers was excellent (ICC = 0.98, $p < 0.001$).

Conclusion: MR venography with Ablavar can robustly and reproducibly quantify DVT volumes in a multi-center setting. It could potentially be used as a readout for treatment efficacy.

Clinical Relevance: MR venography with Ablavar can be accurately used to diagnose the presence and extensiveness of DVT in the proximal veins as compared to compression ultrasound (CUS). CUS is currently the most common imaging test used in the diagnosis of suspected acute DVT. However, CUS cannot reliably assess the proximal deep veins in the thigh and lower pelvis, which are the most common sources of PE. MR venography can potentially be used to determine patients' response to various treatments targeting VTE and compare the effectiveness of the treatments.

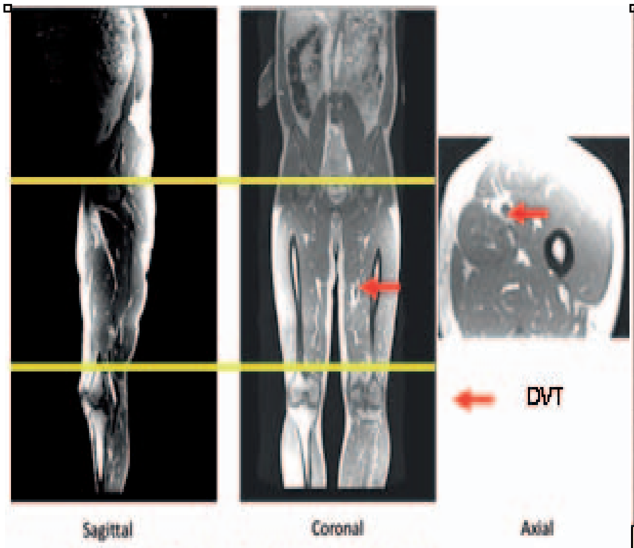

Figure 1: Imaging coverage for evaluating DVT

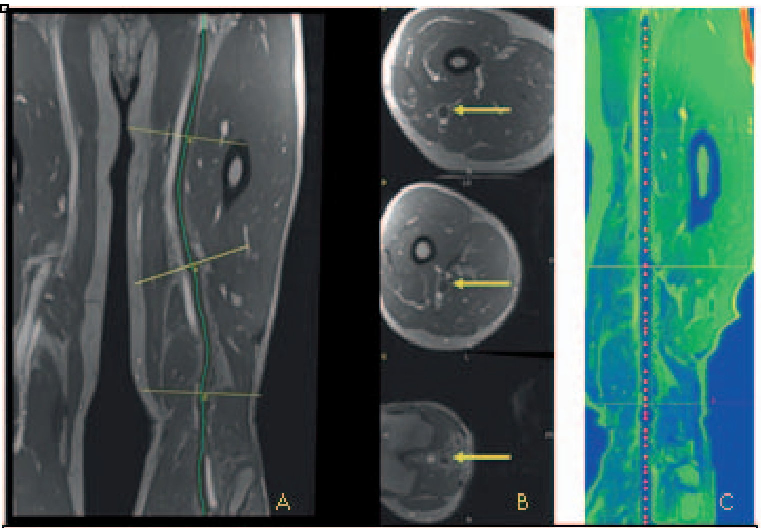

Figure 2: (A) 3D curved multiplanar reconstruction of DVT in a 59 year old male subject. (B) Corresponding axial images clearly delineating DVT as the black region filling the vessel lumen (yellow arrows) (C) Straightened vessel for analysis

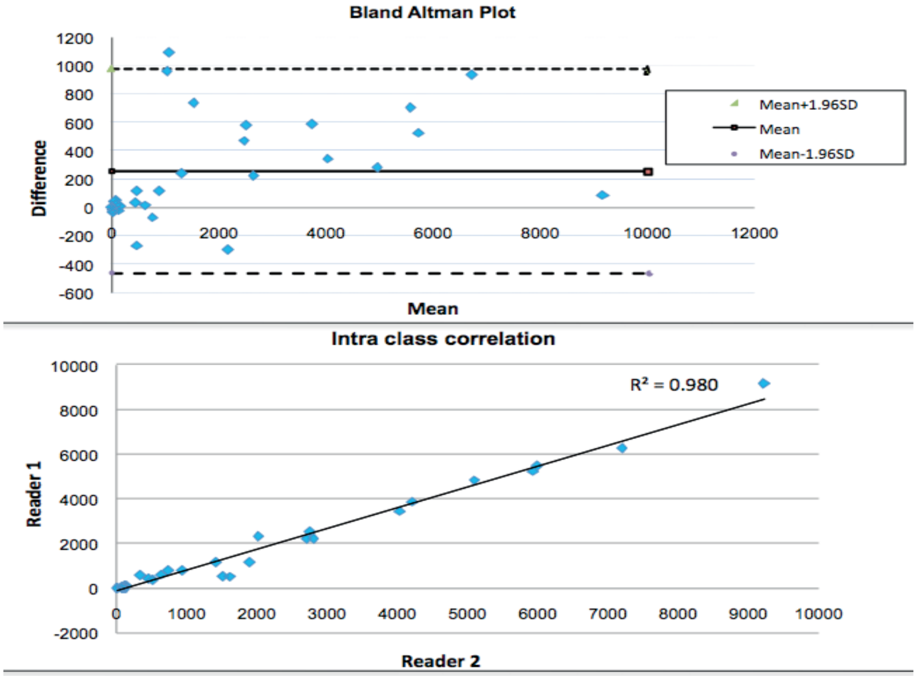

Figure 3: Bland Altman and ICC plots showing agreement between two readers

Study of ^{123}I-Galectin-3 as a SPECT Agent for Myocardial Infarction Imaging in Rats

Teresa Arias[1,2], Artiom Petrov[1], Hans de Haas[1], Carlos Perez[1,2], Zahi Fayad[1], Valentín Fuster[1,2], Jagat Narula[1].

[1] Zena and Michael A. Wiener Cardiovascular Institute
Icahn School of Medicine at Mount Sinai, New York. USA.
[2] Centro Nacional de Investigaciones Cardiovasculares (CNIC), Madrid. Spain.

Introduction: Galectin-3 is a ß-galactoside-binding animal lectin expressed in most of the tissues in normal conditions and overexpressed in myocardium since earlier stages of heart failure, including myocardial infarction (MI). In this context, Galectin-3 is a known biomarker associated with extracellular matrix (ECM) turnover what makes it a very promising imaging diagnostic tool to assess myocardial fibrosis.

Methods: Human Galectin-3 was labeled with Na^{123}I and *in vitro* solid-phase binding assays were conducted to test ^{123}I-Galectin-3 ability to bind to its targets. For *in vivo* studies, rats (n=6) underwent permanent left anterior descending artery (LAD) ligation and sham rats as controls (n=6). All animals were subjected to both, (i) cardiac magnetic resonance and (ii) nuclear imaging (µSPECT/µCT) after 2 or 4 weeks of MI. Pharmacokinetics and biodistribution studies were also conducted in those rats.

Results: *In vitro* studies showed that ^{123}I-Galectin-3 kept binding properties after radiolabeling. Specific activity bound of ^{123}I-Galectin-3 to laminin, fibronectin and rat collagen type I was significantly higher ($p<0.05$) compared to BSA (Figure 1). Quantitative ^{123}I-Galectin-3 injected dose per gram uptake was significantly higher in the apex of 2-weeks-old MI rats (0.15 ± 0.04%) (Figure 2) compared to sham (0.05 ± 0.03%) and 4-weeks-old MI (0.08 ± 0.06%) rats (Figure 3). Nevertheless, moderate uptake was observed during *in vivo* nuclear imaging in all the rats, in agreement with the important ^{123}I-Galectin-3 degradation observed in blood and heart samples.

Conclusion: This study demonstrates that ^{123}I-Galectin-3 allows cardiac imaging of the myocardial remodeling after MI in rats. If proven clinically, using Galectin-3 as an imaging tool may progress in the assessment and treatment of MI patients. However, strategies to avoid ^{123}I-Galectin-3 *in vivo* degradation need to be sought to improve non-invasively cardiac imaging.

Clinical Relevance: Imaging of myocardial fibrosis is one of the main research topics in most of the cardiovascular imaging institutes over the world. This study of ^{123}I-Galectin-3 as a potential agent for nuclear imaging may allow the assessment of the myocardial fibrosis described during cardiac remodeling in the clinical practice.

Figures

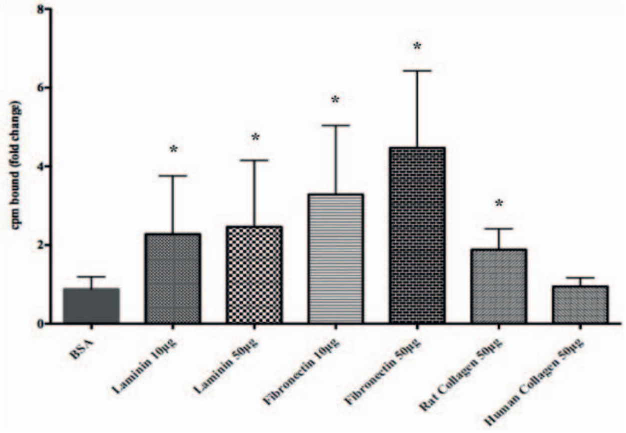

Figure 1. ^{123}I-Galectin-3 binding *in vitro* experiments. ^{123}I-Galectin-3 binding properties measured as specific activity bound. Values are given as mean ± SD of duplicates measurements from seven independent experiments. cmp means counts per minute.*$p < 0.05$ vs. background.

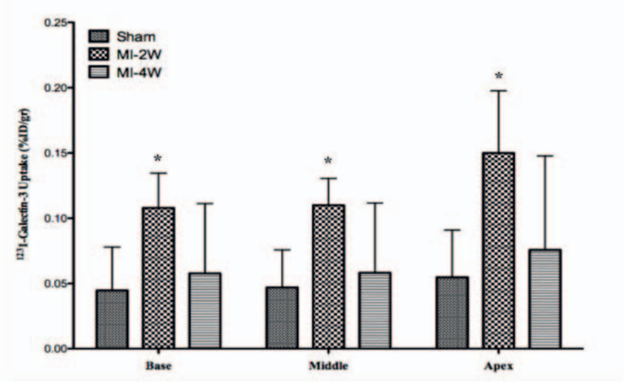

Figure 2. ^{123}I-Galectin-3 heart uptake. Values are given as mean ± SD of duplicates measurements from twelve independent experiments. MI-2W means 2-weeks-old-myocardial infarction and MI-4W, 4-weeks-old-myocardial infarction. *$p < 0.05$ vs. Sham.

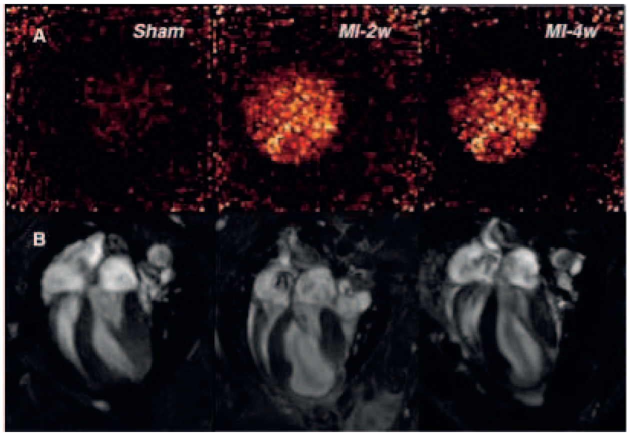

Figure 3. *Ex vivo* nuclear imaging (µSPECT) and *in vivo* Cardiac Magnetic Resonance (CMR): A) Ex vivo ^{123}I-Galectin heart uptake and B) CMR for infarct size and functional heart analysis. MI-2W means 2-weeks-old-myocardial infarction and MI-4W, 4-weeks-old-myocardial infarction.

Ultrashort Echo Time- and Dixon-based Magnetic Resonance Attenuation Correction for MR/PET Quantification in Animal Abdomen Imaging

Jason Bini, Wouter Nijhof, Philip M. Robson, Claudia Calcagno, Antoine Millon, Mark Lobatto, Mootaz Eldib, Zahi A. Fayad.
Translational and Molecular Imaging Institute, Icahn School of Medicine at Mount Sinai

Introduction: Attenuation correction is critical for accurate quantitative MR/PET. Current preclinical MR/PET attenuation maps consist of two (air and soft tissue) or three (air, soft tissue and fat) tissue classifications in whole-body MR/PET. Bone is the highest attenuating tissue in the body but is difficult to separate from air using current conventional MR sequences. Previously we have shown that ignoring bone can cause substantial quantitative errors in preclinical imaging. Using ultrashort echo time (UTE) sequences, bone can be detected and separated from air with postprocessing of MR images, as has been shown in the derivation of brain attenuation maps. The objective of the current study was to apply and evaluate feasibility of UTE- and Dixon-based attenuation correction in the abdomen of rabbits.

Methods & Results: CT and MR/PET images of five rabbits were acquired. MR/PET acquisition was performed using a sequential MR/PET scanner (Philips Ingenuity TF). MR imaging consisted of T1-weighted, UTE and Dixon acquisitions. These images were then postprocessed to segment bone and create a fat/water fraction image. MR attenuation correction (MRAC) methods consisted of the system standard two tissue classification map (air and soft tissue; MRAC$_{ST}$), two-three tissue classification maps (air, soft tissue, fat; MRAC$_{DIXON}$) and (air, soft tissue, bone; MRAC$_{UTE}$) and a four tissue classification map (air, soft tissue, fat, bone; MRAC$_{UTEDIX}$). The MR attenuation maps were then inserted into the standard PET reconstruction in place of the system standard two tissue classification map. For the CTAC method, CT images were coregistered to the MR and CT attenuation maps were inserted into the standard PET reconstruction in place of the MR map. PET images from CTAC and all MRAC methods were generated. Voxel-by-voxel and region-of-interest (ROI) analysis was performed to determine differences in standardized uptake values (SUV). ROIs were drawn on the coregistered CT images for liver, kidneys, spine and soft tissue (muscle). Voxel-by-voxel comparisons of PET images showed excellent correlation of SUV between all MRAC methods versus the CTAC method [(MRAC$_{ST}$, R=0.99834, p=0.6135), (MRAC$_{DIXON}$, R=0.99841, p=0.0036), (MRAC$_{UTE}$, R=0.99708, p=0.0924), (MRAC$_{UTEDIX}$, R=0.99846, p=0.0077)] with a slight trend toward more quantitative accuracy in overall voxels with increasing number of tissue classes. The ROI-based comparison showed a strong trend toward more accuracy in percent difference and absolute difference (AD) of SUVmean in ROIs with increasing number of tissue classes when compared to CTAC, especially in the spine [(MRAC$_{ST}$, -0.16 AD (-21.35 %diff, p<0.0001); MRAC$_{UTEDIX}$, -0.01 AD (-0.91 %diff, p=0.242)] and back muscles near the spine [(MRAC$_{ST}$, -0.07 AD (-21.65 %diff, p<0.0001); MRAC$_{UTEDIX}$, 0.003 AD (0.26 %diff, p=0.6074)].

Conclusion: In this study, we have derived MR based attenuation maps using UTE- and Dixon-based methods to compare MRAC and CTAC methods for PET attenuation correction. We have demonstrated that it is feasible to segment bone in the abdomen of rabbits and generate an MRAC PET image that is quantitatively accurate to that of CTAC methods. Further clinical studies need to be carried out to validate the clinical use of combined UTE and Dixon MRAC methods.

Clinical Relevance: The spatial distribution of attenuation must be measured in order to permit quantitative evaluation of standard uptake values (SUV) in clinical MR/PET images. Accurate attenuation correction using MR data is important in order to accurately quantify PET tracer uptake in the rabbit aorta for characterization of atherosclerotic plaques using clinical MR/PET scanners.

Figures and tables

Table 1. Summary of CTAC and MRAC attenuation coefficient values for each region-of-interest analyzed.

ROI	CTAC(cm^{-1})	MRAC$_{ST}$(cm^{-1})	MRAC$_{DIXON}$(cm^{-1})	MRAC$_{UTE}$(cm^{-1})	MRAC$_{UTEDIX}$(cm^{-1})
Liver	0.0988	0.0960	0.0970	0.0960	0.0971
Left Kidney	0.0974	0.0960	0.0919	0.0960	0.0919
Right Kidney	0.0975	0.0960	0.0892	0.0960	0.0892
Spine	0.1129	0.0960	0.0982	0.1056	0.1075
Back Muscle	0.0997	0.0960	0.0995	0.0960	0.0995
ALL ROIs	0.1015	0.0960	0.0956	0.0980	0.0976

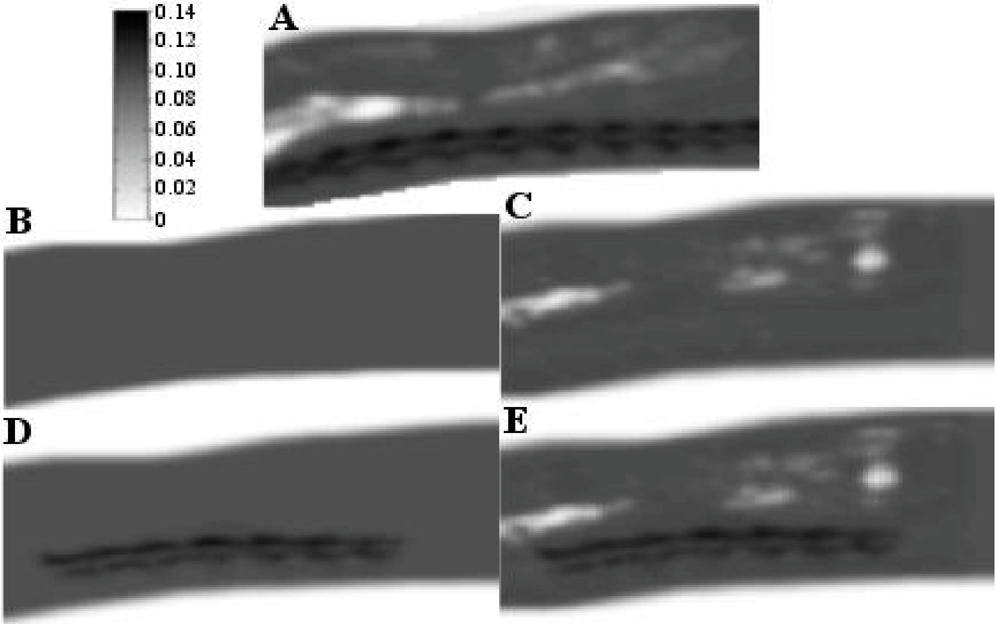

Figure 1. Representative images of attenuation maps used in PET reconstruction (A) CTAC attenuation map (B) MRAC$_{ST}$ attenuation map (C) MRAC$_{DIXON}$ attenuation map (D) MRAC$_{UTE}$ attenuation map E) MRAC$_{UTEDIX}$ attenuation map. Assigned attenuation values were 0.130cm^{-1} for bone[5], 0.096cm^{-1} for the system standard soft tissue values and for the Dixon-based method, a continuous range of values from pure fat (0.090cm^{-1}) to pure water (0.0100cm^{-1}) based on the water/fat fraction.

Table 2. Summary of mean SUVs for regions-of-interest analyzed for each respective reconstructed PET image.

	CTAC	MRAC$_{ST}$	MRAC$_{DIXON}$	MRAC$_{UTE}$	MRAC$_{UTEDIX}$
ROI	**SUV Mean**	**SUV Mean**	**SUV Mean**	**SUV Mean**	**SUV Mean**
Liver	1.85	1.77	1.78	1.80	1.79
Left Kidney	2.00	1.96	1.95	2.00	1.95
Right Kidney	2.06	1.86	1.94	1.98	1.94
Spine	0.75	0.59	0.66	0.72	0.74
Back Muscle	0.32	0.25	0.32	0.28	0.32
ALL ROIs	1.35	1.25	1.29	1.32	1.31

In vivo molecular imaging of apoptosis and necrosis in atherosclerotic plaques using microSPECT-CT and microPET-CT imaging

M. De Saint-Hubert [1,2], J. Bucerius [1,2,3]*, M. Bauwens [1], N. Deckers [4], M. Drummen [1], K. Douma [1,2], P. Granton [5], G. Hendrikx [1,2], D. Kusters [4] , C.P.M. Reutelingsperger [4], F.M. Mottaghy [1,3]

1Department of Nuclear Medicine, MUMC, Maastricht, The Netherlands
2Cardiovascular Research Institute Maastricht (CARIM), MUMC, Maastricht, The Netherlands
5Department of Nuclear Medicine, University Hospital RWTH Aachen, Aachen, Germany
4Department of Biochemistry, Maastricht University, The Netherlands
5Maastro Clinic, Maastricht, The Netherlands
* Presenter

Introduction: To study molecular imaging of apoptosis and necrosis, two key players in atherosclerosis instability, a multi-modal imaging approach combining single photon emission computed tomography (SPECT), positron emission tomography (PET) and computed tomography (CT).

Methods & Results: Collar induced carotid atherosclerosis ApoE knockout mice were imaged with 99mTc-AnxAF568 SPECT-CT to study apoptosis and sequentially with PET-CT following 124I-Hypericin (124I-Hyp) injection to visualize necrosis. SPECT depicted increased 99mTc-AnxAF568 uptake in both atherosclerotic carotid arteries whereas our data suggest that this uptake is not merely apoptosis related. Although PET of 124I-Hyp was hampered by the slow blood clearance in atherosclerotic mice, 124I-Hyp was able to target necrosis in the atherosclerotic plaque.

Conclusion: Both 99mTc-AnxAF568 and 124I-Hyp uptake are increased in atherosclerotic carotid vasculature compared to control arteries. While apoptosis imaging remains challenging, necrosis imaging can be feasible after improving the biodistribution characteristics of the probe.

Clinical Relevance: To study vascular plaque apoptosis and necrosis by means of non-invasive molecular imaging using newly developed radioactive SPECT- and PET tracers and to evaluate their potential for translation into the clinical situation.

Arterial and Fat Tissue Inflammation are Highly Correlated - a Prospective 18F-FDG PET/CT Study

Jan Bucerius [1,2,3,4,5],Venkatesh Mani [1,2,6], Stephanie Wong [1,2], Colin Moncrieff [1,2], David Izquierdo-Garcia [1,2], Josef Machac [7], Valentin Fuster [6,8], Michael E. Farkouh [6,9], James H. F. Rudd [10], Zahi A. Fayad [1,2,6]

1. Translational and Molecular Imaging Institute, Mount Sinai School of Medicine, New York, New York, 2. Department of Radiology, Mount Sinai School of Medicine, New York, New York, 3. Department of Nuclear Medicine, Maastricht University Medical Center, Maastricht; The Netherlands, 4. Cardiovascular Research Institute Maastricht (CARIM), Maastricht University Medical Center, Maastricht; The Netherlands, 5. Department of Nuclear Medicine, University Hospital RWTH Aachen, Aachen; Germany, 6. Department of Cardiology, Zena and Michael A. Weiner Cardiovascular Institute and Marie-Josée and Henry R. Kravis Cardiovascular Health Center, Mount Sinai School of Medicine, New York, New York, 7. Division of Nuclear Medicine, Department of Radiology, Mount Sinai School of Medicine, New York, New York, 8. The Centro Nacional de Investigaciones Cardiovasculares (CNIC), Madrid; Spain, 9. Cardiovascular Imaging Clinical Trials Unit, Mount Sinai School of Medicine, New York, New York, 10. Division of Cardiovascular Medicine, University of Cambridge, Cambridge; United Kingdom

Introduction: There is evidence that the link between obesity and cardiovascular disease might relate to inflammation in both fat tissue and the arterial wall. 18F-fluorodeoxyglucose positron emission tomography (FDG-PET) uptake is a surrogate marker of vessel wall inflammation. The aim of the study was to measure FDG uptake in both regions using PET and identify links between adipose and arterial inflammation.

Methods & Results : 173 cardiovascular patients were prospectively imaged with FDG-PET/CT. Arterial FDG uptake was measured in the carotid arteries and ascending aorta. The same was done in fat tissue in the neck, the pre-sternal region, the abdomen (all subcutaneous) and the pericardium. FDG uptake was quantified as average maximal target-to-background ratio (meanTBRmax). Multivariate regression analyses were performed to identify significant associations between arterial and adipose tissue FDG uptake and clinical variables as given by the standardized correlation coefficient (β). FDG uptake values within all fat tissue regions were highly predictive of vascular FDG uptake in both the carotids (neck subcutaneous: β:0.248, p=0.001) and aorta (chest pericardial: β:0.236, p=0.003; abdomen subcutaneous: β:0.207, p=0.007). Obesity was significantly associated with elevated FDG uptake in adipose tissue (neck subcutaneous: β:0.470, p<0.0001; abdomen subcutaneous: β:0.339, p=0.006; chest subcutaneous: β:0.619, p=0.028; chest pericardial: β:0.978, p=0.035).

Conclusion: FDG uptake in diverse fat tissue regions was significantly associated with arterial FDG uptake, a reasonable surrogate of inflammation. Increasing body weight significantly predicted the level of fatty inflammation. FDG-PET therefore provides imaging evidence for an inflammatory link between fat tissue and the vasculature in patients with cardiovascular disease.

Clinical Relevance

To provide imaging evidence for the well-known link between vascular and fat tissue inflammation in patients with cardiovascular disease.

Optimizing 18F-FDG-PET Imaging of Vessel Wall Inflammation – The Impact of 18F-FDG Circulation Time, Dose, Uptake Parameters, and Fasting Blood Glucose Levels

Jan Bucerius [1,2,3,4], Venkatesh Mani [1,2,5], Colin Moncrieff [1,2], Josef Machac [6], Valentin Fuster [5,7], Michael E. Farkouh [5,8], Ahemd Tawakol [9], James H. F. Rudd [10], Zahi A. Fayad [1,2,5]

1. Translational and Molecular Imaging Institute and Imaging Science Laboratories, Mount Sinai School of Medicine, New York, New York, 2. Department of Radiology, Mount Sinai School of Medicine, New York, New York, 3. Department of Nuclear Medicine, Maastricht University Medical Center; Maastricht, the Netherlands, 4. Cardiovascular Research Institute Maastricht (CARIM), Maastricht University Medical Center; Maastricht, the Netherlands, 5. Department of Cardiology, Zena and Michael A. Weiner Cardiovascular Institute and Marie-Josée and Henry R. Kravis Cardiovascular Health Center, Mount Sinai School of Medicine, New York, New York, 6. Division of Nuclear Medicine, Department of Radiology, Mount Sinai School of Medicine, New York, New York, 7. The Centro Nacional de Investigaciones Cardiovasculares (CNIC), Madrid, Spain, 8. Cardiovascular Imaging Clinical Trials Unit, Mount Sinai School of Medicine, New York, New York, 9. Cardiac MR PET CT Program, Massachusetts General Hospital, Harvard University, Boston, Massachusetts, 10. Division of Cardiovascular Medicine, Cambridge University, Cambridge, United Kingdom

Introduction: 18F-fluorodeoxyglucose (FDG) positron emission tomography (PET) is increasingly used for imaging of vessel wall inflammation. However, limited data is available regarding the impact of methodological variables, i. e. patient's pre-scan fasting glucose, the FDG circulation time, the injected FDG dose, and of different FDG uptake parameters, in vascular FDG-PET imaging.

Methods & Results: 195 patients underwent vascular FDG-PET/CT of the aorta and the carotids. Arterial standard uptake values (meanSUVmax) as well as target-to-background-ratios (meanTBRmax) and the FDG blood pool activity in the superior vein cava (SVC) and the jugular veins (JV) were quantified. Vascular FDG uptake classified according to tertiles of patient's pre-scan fasting glucose levels, the FDG circulation time, and the injected FDG dose was compared using ANOVA. Multivariate regression analyses were performed to identify the potential impact of all variables described on the arterial and blood pool FDG uptake. Tertile analyses revealed FDG circulation times of about 2.5 h and pre-scan glucose levels of less than 7.0 mmol/l showing favorable relations between the arterial and blood pool FDG uptake. FDG circulation times showed negative associations with the aortic meanSUVmax values as well as SVC- and JV FDG blood pool activity but a positive correlation with the aortic- and carotid meanTBRmax values. Pre-scan glucose was negatively associated with aortic- and carotid meanTBRmax and carotid meanSUVmax values, but correlated positively with the SVC blood pool uptake. Injected FDG dose failed to show any significant association with the vascular FDG uptake.

Conclusion: FDG circulation times and pre-scan blood glucose levels significantly impact FDG uptake within the aortic and carotid wall and may bias the results of image interpretation in patients undergoing vascular FDG-PET/CT. FDG dose injected was less critical. Therefore, circulation times of about 2.5 h and pre-scan glucose levels less than 7.0 mmol/l should be preferred in this setting.

Clinical Relevance: To optimize and standardize vascular 18F-FDG imaging protocols for use in clinical routine and clinical research.

Attenuation Correction for Flexible MR Coils in Combined PET/MRI Imaging

Mootaz Eldib, Jason Bini, Claudia Calcagno, Philip M. Robson, Venkatesh Mani,
and Zahi A. Fayad

Translational and Molecular Imaging Institute
Icahn School of Medicine at Mount Sinai

Introduction: Attenuation correction for MR coils is a new challenge that came about with the development of combined MR and PET imaging. This task is challenging since such coils are not directly visible on either PET or MR acquisitions with current combined scanners and therefore are not easily localized in the field of view (FOV). This issue becomes more evident when trying to localize flexible MR coils (e.g. cardiac or body matrix coil) that change position and shape from patient to patient and from one imaging session to another. In this report we propose a novel method to localize and correct for the attenuation and scatter of a flexible MR cardiac coil, using MR fiducial markers placed on the surface of the coil to allow for accurate registration of a template CT based attenuation map.

Methods: To quantify the attenuation properties of the cardiac coil, a uniform cylindrical water phantom doped with 18F-Fluorodeoxyglucose (18F-FDG) was imaged on the sequential MR/PET system without and with the flexible cardiac coil. After establishing the need to correct for attenuation of the coil, we test the feasibility of several registration methods to register a pre-computed attenuation map to correct for attenuation. To accomplish this, MR and CT visible markers were placed on the surface of the cardiac flexible coil. The coil was imaged on a CT scanner at maximum and average bend to represent the range of patient habitus. The average bend coil image was chosen as the reference scan. Using only the markers as a driver for registration, the maximum bend CT image was registered to the reference image by a combination of rigid and deformable registration. The accuracy of several methods was compared for deformable registration including b-spline, and volume spline (figure 1). Finally, we validated our novel approach both in phantom and patient studies.

Results: Our phantom experiments indicated that the presence of the coil resulted in a 13% reduction in measured 18F-FDG activity when compared to the phantom only scan. Furthermore, local underestimation reached 20% in regions of interest (ROIs) close to the coil (fig 2). Having established the need to correct for attenuation of the coil, we tested various registration methods and deemed volume spline registration to be the most accurate, as measured by the Dice similarity metric. Our phantom experiments showed that the bias in 18F-FDG quantification introduced by the presence of the coil could be reduced by using our registration method. A negligible overestimation of <2% of the overall activity for the phantom scan with the coil attenuation map was measured when compared to the baseline phantom scan without coil. A local overestimation of 3% was observed in ROI analysis when using the proposed method to correct for attenuation of the flexible cardiac coil (fig 2). Quantitative results from the patient study agreed well with the phantom findings.

Conclusions: We present and validate an accurate method to localize and register a CT-based attenuation map to correct for the attenuation and scatter of flexible MR coils. This method can easily be translated to clinical use to produce quantitatively accurate measurements with use of flexible MR coils during MR/PET imaging.

Figures and tables

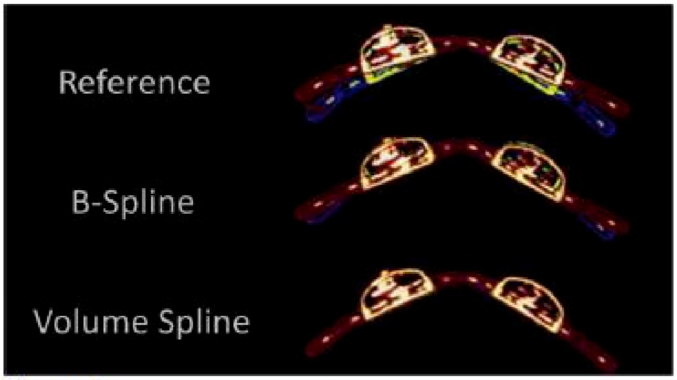

Figure 1.

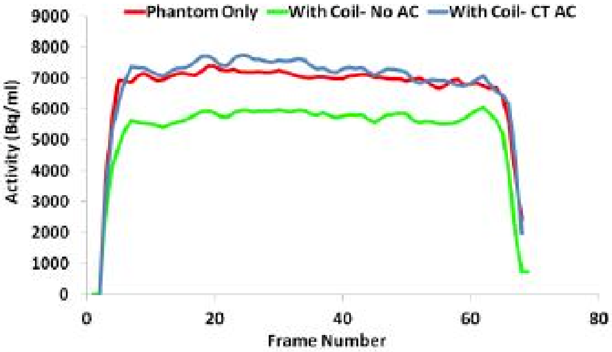

Figure 2.

Controlled Delivery of the LXR Agonist GW3965 to Avoid Lipogenic Effects on the Liver while Improving Atherosclerosis

Orli Even-Or[a], Xue-Qing Zhang[b], Omid C. Farokhzad[b]* , Edward A. Fisher[a]*

[a]Leon H. Charney Division of Cardiology, and Cell Biology, New York University School of Medicine, New York, NY
[b] Laboratory of Nanomedicine and Biomaterials, Brigham and Women's Hospital, Harvard Medical School, Boston, MA

Introduction: Liver X Receptors (LXR) agonists have been shown to have antiatherogenic properties. However, they often induce hypertriglyceridemia and hepatic steatosis. In this study, we demonstrate the activity of PLGA-PEG nanoparticles (NP's) containing a synthetic LXR agonist, GW3965, to inhibit the development of atherosclerosis without affecting the liver.

Methods & Results : Using a Wild Type (WT) mice we investigated the hepatic effects of the LXR agonist (GW3965) either in solution or encapsulated in nanoparticles. In addition, a low density lipoprotein receptor knockout (LDLr -/-) mice model with induced atherosclerotic plaques was used to study the ability of the GW3965-containing NP's to inhibit the progression of atherosclerosis. Both studies consisted of 2 weeks intravenous treatment with GW3965. The first study confirmed that the administration of the LXR agonist in its free form results in hypertriglyceridemia and hepatic steatosis. In contrast, the mice treated with the GW3965-containing NP's show no significant differences as compared to the vehicle (PBS)-treated mice. Then we studied the effect of the different treatments in the plaque and we show that the GW3965-containing NP's were significantly more potent than the free LXR agonist at inducing LXR target gene expression in the plaque. Notably, GW3965-containing NP's markedly reduced the macrophage ($CD68^+$) area in the plaque by 50% in LDLr-/- mice after only two weeks of treatment.

Conclusion: Altogether, our results suggest that the GW3965-containing PLGA-PEG NP's have the abbility to inhibit the progression of atherosclerosis in mice while sparing the toxicity in the liver.

Clinical Relevance: LXR agonists are a promising treatment for atherosclerosis but their negative effects in the liver have delayed their clinical use. Here we show that LXR agonist containing PLGA-PEG NP's are effective in delaying atherosclerosis progression in mice without affecting the liver, supporting further development of these NP's as a potential therapy for atherosclerosis.

Figures and tables

Figure 1. Chemical structure of GW3965-containing NP's. The particle consists of a surface-associated fluorescent molecule, an outer PEG surface, and a biodegradable polymer matrix loaded with hydrophobic GW3965. Size of the NP is 156.5 ± 10.3 nm.

	Control	**Free GW3965**	**NP/GW3965**
Plasma TC	1485±170	1797±87*	1181±150
Plasma TG	873±84	1321±329*	559±190$^{\#}$

Table 1. Plasma total cholesterol (TC) and triglyceride (TG) levels of PBS (Vehicle), free GW3965 or NP/GW3965-treated WT mice. Values are mean ± standard deviation (n=5); **P<0.05* vs control, $^{\#}$ *P<0.05* vs control .

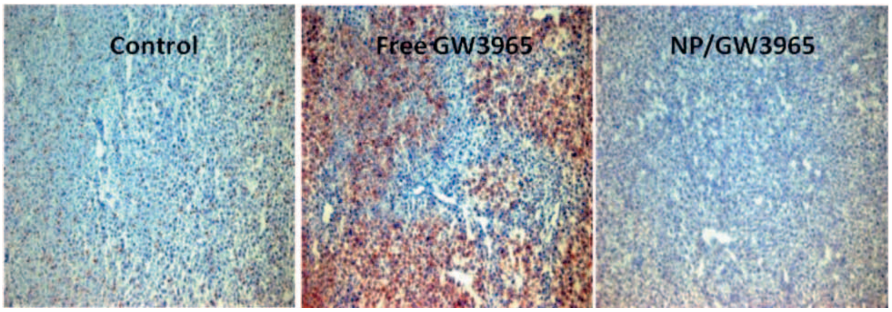

Figure 2. Oil red O staining (which reflects lipid content) of livers of PBS (Control), free GW3965 or or NP/GW3965-treated WT mice. Neutral lipid accumulation is shown in red. Representative liver sections are shown at 10x magnification (n=5).

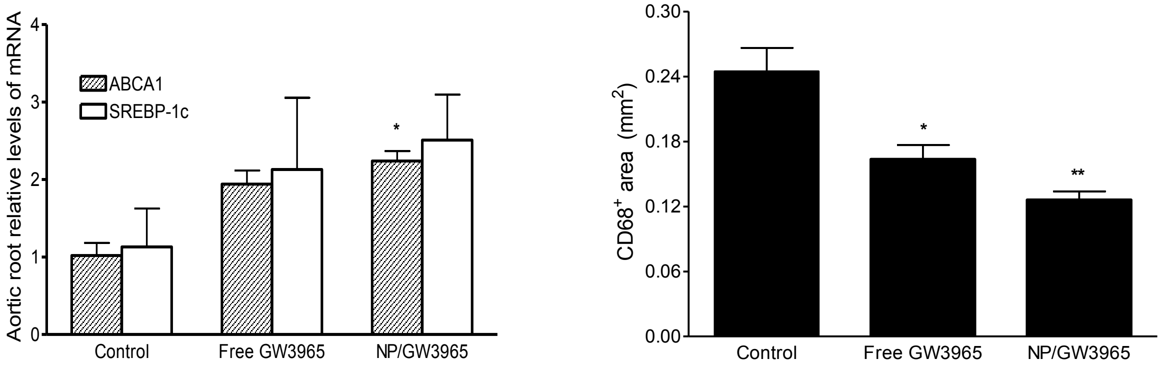

Figure 3. Progression of atherosclerotic lesions of PBS (Control), free GW3965 or NP/GW3965- treated LDLr -/- mice. (A) Aortic arch LXR target gene expression. (B) Quantitative analysis of plaque macrophage (CD68$^+$) area by ImagePro Plus software. Data are represented as the mean ± standard deviation (n=5). **P<0.05* and ***P<0.01*, vs control.

Particulate matter exposure worsens atherogenic profile in "Ground Zero" workers

Venkatesh Mani[1], Simonette T. Sawit[1], Cynara Maceda[1], Claudia Calcagno[1], Sarayu Ramachandran[1], Zahi A. Fayad[1], Jacqueline Moline[1] and Maryann McLaughlin[1]

[1]Translational and Molecular Imaging Institute, Icahn School of Medicine at Mount Sinai
New York/USA

Introduction: Exposure to particulate matter (PM) is associated with adverse health effects leading to increased morbidity. Law enforcement workers were exposed to high levels of particulate pollution after working at "Ground Zero" and may exhibit accelerated atherosclerosis. Peripheral artery tonometry (PAT) can evaluate vascular reactivity, a surrogate for endothelial function. Dynamic contrast enhanced MRI (DCE-MRI) correlates with plaque neovascularization. We hypothesize that DCE-MRI and PAT can be used to evaluate differences in atherosclerosis profiles in patients subjected to **high** (initial dust cloud) and **low** (after September 13, 2001) **PM exposure.**

Methods: 31 subjects (28 male) with high (n=19) or low (n=12) exposure to PM underwent PAT and DCE- MRI. Demographics (age, gender, family history, hypertension, diabetes, BMI, and smoking status), biomarkers (lipid profiles, hs-CRP, BP) and ankle-brachial index measures (left and right) were obtained from all subjects. Differences between the high and low exposures were compared using independent samples t-test. Using linear forward stepwise regression with an information criteria model, independent predictors of increased area under curve (AUC) from DCE were determined using all variables as input. Confidence interval of 95% was used and variables with $p>0.1$ were eliminated. $p < 0.05$ was considered significant.

Results: Subjects with high exposure had significantly lower PAT values (worse endothelial dysfunction) (**PAT: 1.70 +/- 0.23 for high vs. 1.94 +/- 0.38 for low, p= 0.038**), and higher DCE AUC uptake (increased neovascularization) compared to subjects with lower exposure. (**AUC: 2.65 +/- 0.63 for high vs. 1.88 +/- 0.69 for low, p = 0.016).** Except for ankle-brachial index of the right leg, none of the other parameters were significantly different between the two groups. The regression model indicated that only **high exposure to PM, CRP >3.0 and total cholesterol** were independently associated with increased neovascularization (in decreasing order of importance, **all p < 0.026).**

Discussion: High exposure to PM decreases endothelial function, increases plaque neovascularization and thereby worsens atherogenic profile of "ground zero" workers.

Figures and tables

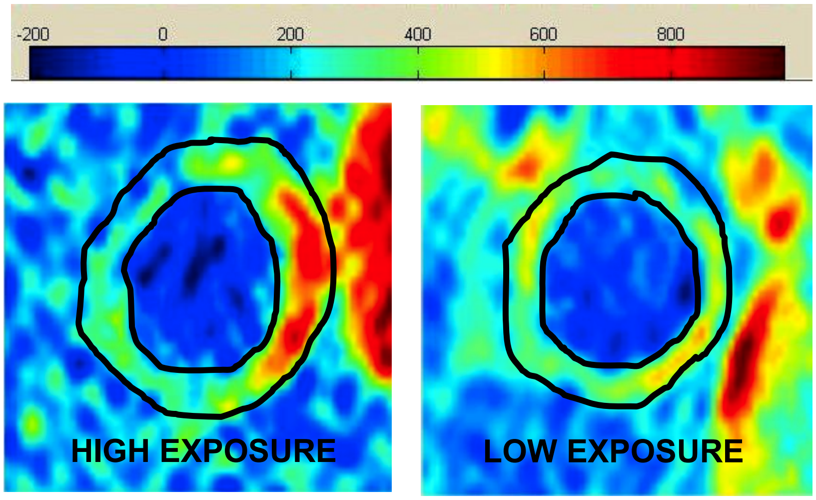

Figure: Sample DCE-MRI AUC (7 minutes) images of a left common carotid artery from high and low PM exposure patients

Molecular assessment of hypoxia in advanced atherosclerosis using ^{18}F-fluoromisonidazole (FMISO) PET imaging. A comparison with ^{18}F-fluorodeoxyglucose (FDG)

Jesus Mateo[1,3], David Izquierdo-Garcia[3], Juan J. Badimon[2], Zahi A. Fayad[3], Valentin Fuster[1,2]
[1]Department of Epidemiology, Atherothrombosis and Imaging, Centro Nacional de Investigaciones Cardiovasculares (CNIC), Madrid 28029, Spain; [2]The Zena and Michael A. Wiener Cardiovascular Institute, Icahn School of Medicine at Mount Sinai, New York, NY 10029, USA; [3]Translational and Molecular Imaging Institute, Icahn School of Medicine at Mount Sinai, New York, NY 10029

Introduction: Hypoxia has been revealed as an important microenvironmental factor influencing atherosclerosis progression. Through the expression of hypoxia-inducible factor-1 (HIF-1), hypoxia promotes the survival and metabolic adaptation of infiltrated macrophages and induces plaque neovascularization, significant hallmarks of vulnerability. Therefore, imaging plaque hypoxia could serve as a marker of lesions at risk.

Methods & Results: Advanced aortic atherosclerosis was induced in 18 rabbits by combination of atherogenic diet and double balloon endothelial denudation. Animals underwent ^{18}F-FMISO PET and ^{18}F-fluorodeoxyglucose (^{18}F-FDG) PET imaging at 6-8 months (atherosclerosis induction) and at 12-16 months (progression) after diet initiation. Four rabbits fed standard chow served as controls. Radiotracer uptake of the abdominal aorta was measured using standardized uptake values (SUV). Following imaging, plaque hypoxia (pimonidazole), macrophages (RAM-11), neovessels (CD31) and hypoxia-inducible factor-1α (HIF-1α) were assessed by immunohistochemistry. ^{18}F-FMISO uptake increased with time on diet [SUVmean of 0.10±0.01 in non-atherosclerotic animals *versus* 0.20±0.03 ($P<0.05$) at induction and 0.26±0.03 ($P<0.01$) at progression]. *Ex vivo* PET imaging corroborated the uptake of ^{18}F-FMISO by the aorta of atherosclerotic rabbits (SUVmax of $0.15\pm0.01 \times 10^{-2}$ in control animals *versus* $3.40\pm0.72 \times 10^{-2}$ at progression, $P<0.01$). ^{18}F-FDG uptake also augmented in atherosclerotic animals, with a SUVmean of 0.43±0.02 at induction *versus* 0.34±0.02 in non-atherosclerotic animals ($P<0.05$). Unlike ^{18}F-FMISO, there was no further increase in ^{18}F-FDG uptake at progression. By immunohistochemistry, hypoxia was predominantly located in the macrophage-rich areas within the atheromatous core, whereas the macrophages close to the lumen were not hypoxic. Intraplaque neovessels were found largely in macrophage-rich hypoxic regions (pimonidazole^{+}/HIF-1α^{+}/RAM-11^{+}).

Conclusion: Plaque hypoxia increases with disease progression and is present in macrophage-rich areas associated with neovascularization. ^{18}F-FMISO PET imaging emerges as a new tool for detection of lesion severity.

Clinical Relevance: Given the marked association between hypoxic macrophages and neovascularization, plaque hypoxia may represent a novel target for noninvasive imaging of plaques at risk, potentially allowing early diagnosis and/or risk prediction of patients with atherosclerosis in the near future.

Figures and tables

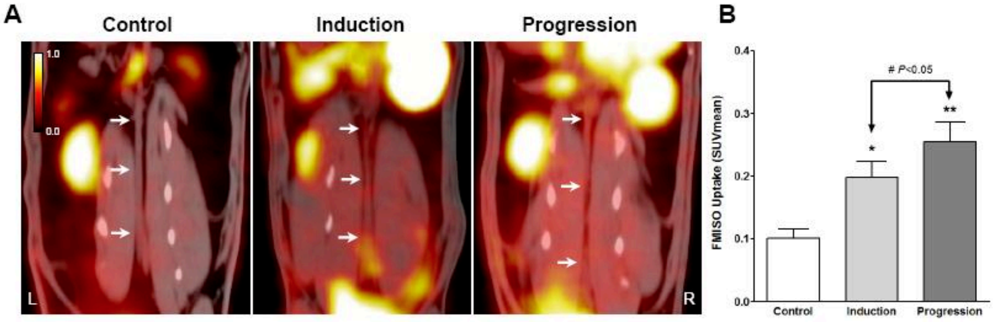

***In vivo* ^{18}F-FMISO PET of hypoxia**. **A**, Combined PET/CT coronal views of the abdominal aorta illustrating the ^{18}F-FMISO uptake of two atherosclerotic rabbits after 8 months (middle panel) and 16 months (right panel) on atherogenic diet, compared with a healthy control animal (left). White arrows denote the abdominal aorta. **B**, Bar-graph comparing the ^{18}F-FMISO uptake (SUVmean) of the abdominal aorta of atherosclerotic rabbits with that of healthy control animals. Bars represent mean±SEM. **P*<0.05, ***P*<0.01, significantly different compared with control. #*P*<0.05, induction *vs*. progression.

Figure 1

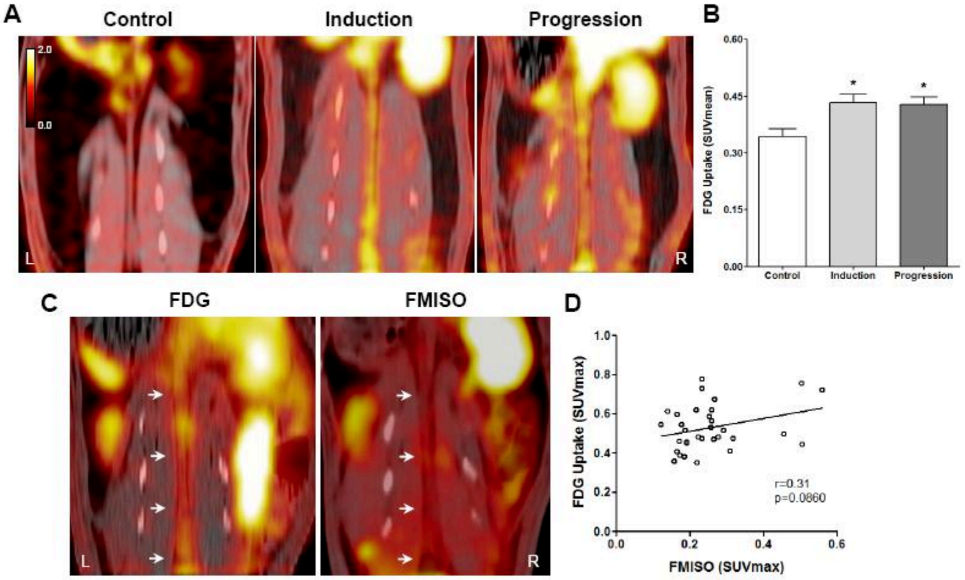

***In vivo* ^{18}F-FDG PET of metabolic rate/inflammation and correlation with ^{18}F-FMISO**. **A**, Combined PET/CT coronal views of the abdominal aorta illustrating the ^{18}F-FDG uptake of two atherosclerotic rabbits after 8 months (middle panel) and >12 months (right panel) on atherogenic diet, compared with a healthy control animal (left). **B**, Bar-graph comparing the ^{18}F-FDG uptake (SUVmean) of the abdominal aorta of atherosclerotic rabbits with that of healthy control animals. Bars represent mean±SEM. **P*<0.05, significantly different compared with control. **C**, Representative ^{18}F-FDG and ^{18}F-FMISO PET studies (fused with CT scans) obtained within a few days of each other from an animal of the progression group. White arrows highlight the abdominal aorta. **D**, Correlation between the uptake of ^{18}F-FMISO and ^{18}F-FDG.

Figure 2

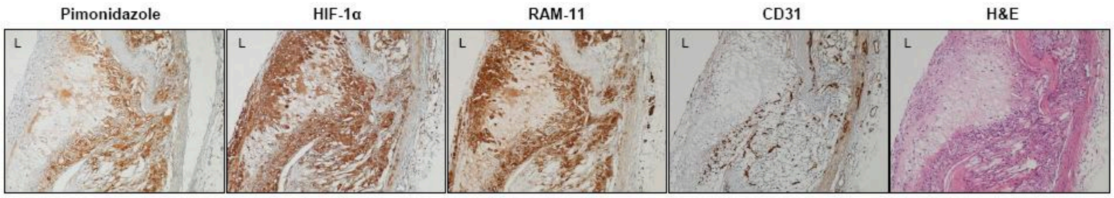

Plaque neovessels colocalize with HIF-1α-positive hypoxic macrophages. Representative staining of hypoxia (pimonidazole), HIF-1α, macrophages (RAM-11), neovessels (CD31) and H&E in serial sections of an advanced atherosclerotic lesion showing colocalization of intimal plaque neovessels with HIF-1α-positive macrophage-rich hypoxic areas (pimonidazole^{+}/HIF-1α^{+}/RAM-11^{+}). Photomicrographs taken at 100x magnification. L, lumen.

Figure 3

Analysis of dynamic contrast-enhanced magnetic resonance images of human carotid arteries with the MARINA software

Sarayu Ramachandran[1], Claudia Calcagno[1], Venkatesh Mani[1], Philip M. Robson[1] and Zahi A. Fayad[1]
[1]Translational and Molecular Imaging Institute, Icahn School of Medicine at Mount Sinai
New York/USA

Introduction: Dynamic contrast-enhanced magnetic resonance imaging (DCE-MRI) is commonly used to study tumor vascularity, and has also been applied to the investigation of atherosclerosis. Inflammation and neovascularization are markers of vulnerable atherosclerotic plaque. By examining the uptake of contrast agent in the walls of major vessels such as the aorta and the carotid arteries it is possible to extract information about the plaque composition. However, quantitative analysis techniques for DCE-MRI, such as area-under-the curve (AUC) measurements and kinetic modelling, require extensive post-processing, and the researcher may be limited by commercially available systems. Here we present a graphical user interface and analysis software called MARINA (MAgnetic Resonance INterface for Analysis) and describe its use in DCE-MRI evaluations. The software is developed in MATLAB (MathWorks Inc., MA) and designed as a flexible, modular package for quantitative analyses on human or animal models.

Methods & Results: The MARINA software consists of separate modules for data import, region-of-interest (ROI) delineation and quantitative analyses. MRI data in the DICOM format can be easily loaded into the software using the intuitive user interface and data import module. If needed for longitudinal data analysis, up to 12 studies can be simultaneously displayed on the main window. ROIs in various different shapes can be drawn on the images and the software will display the average and standard deviation of the signal intensity, as well as the area of the ROI. The ROI masks can also be saved and re-loaded for future review or analysis. Quantitative analysis of DCE-MRI data begins with loading the appropriate series of images and then performing time-series registration using the Registration module. The Registration module performs intra-series motion correction and denoising to prepare the data for further analysis. The AUC module computes pixel-by-pixel AUC maps based on the signal intensities of the registered series. Vessel wall ROIs can be drawn on registered data and used to generate signal intensity versus time curves that show the uptake of contrast agent by the tissue. Using the Concentration module, the signal intensity curves can be converted into contrast agent concentration values. The concentration versus time curves are used as input into the Kinetic modelling module. Kinetic models such as the Patlak, Tofts and modified-Tofts models are implemented in the software which is designed to fit each model to the concentration data and output the fitting parameters.
Figure 1 shows the main user interface window of MARINA and the results of the AUC module for a DCE-MRI study of human carotid arteries. Figure 2 displays the Kinetic modelling module and the various models fit to the concentration versus time data for carotid wall ROIs.

Conclusion: The MARINA software can be a useful tool in the quantitative analysis of DCE-MRI data. As the software accepts input images in the DICOM format it can fit easily into a workflow in which the data is acquired on commercially available MRI scanners. The user can save the results of intermediate analysis steps such as maps and ROI masks, and re-load them in the future for review. The modular design of the software presents users with an opportunity to develop and include newer analyses techniques as their research progresses.

Clinical Relevance: The software described here is a valuable research tool that allows researchers to analyze and display the results of their clinical and pre-clinical analyses. Currently there are multiple users utilizing the software to perform quantitative analyses for research on human and animal models.

Figures and tables

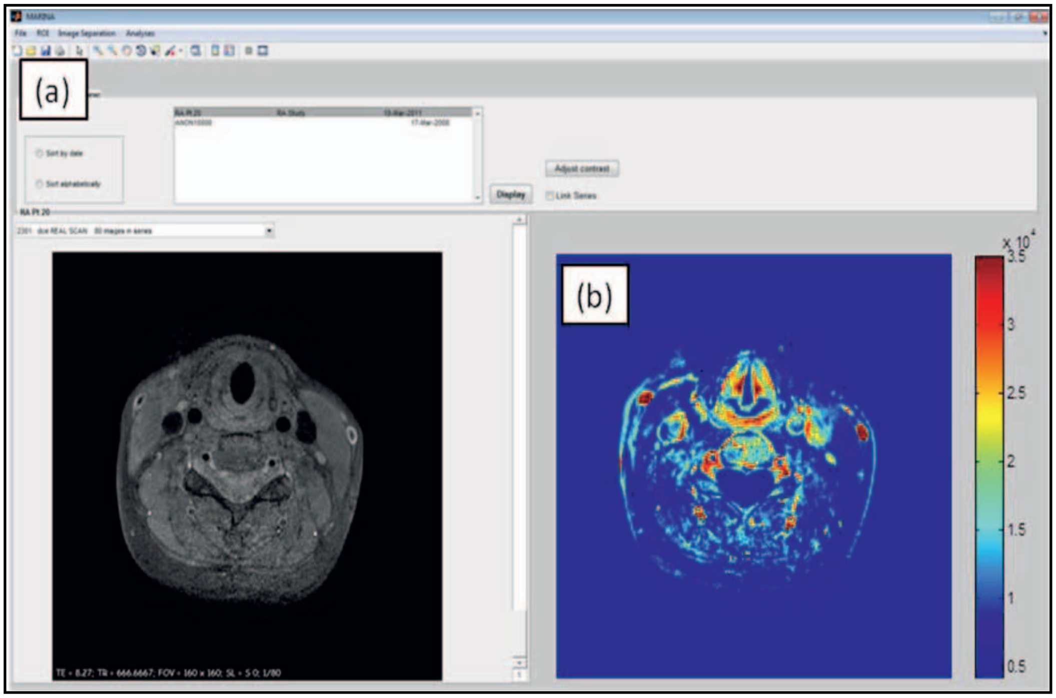

Figure 1. (a) Main user interface window of MARINA showing DCE-MR image from human carotid study overlaid with (b) the AUC map of the DCE-MRI data.

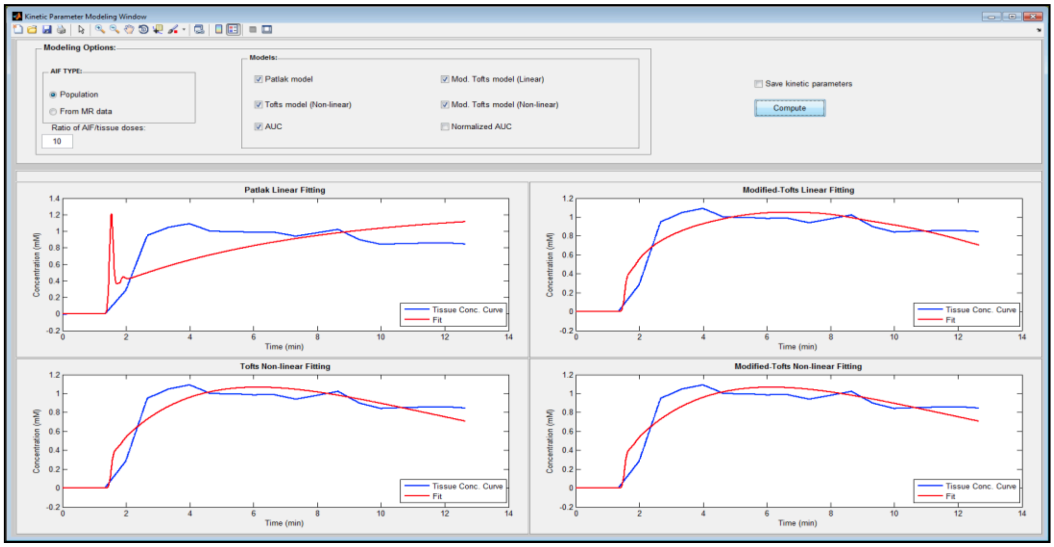
Kinetic Parameter Modeling Window

Modeling Options:

AIF TYPE:
● Population
○ From MR data

Ratio of AIF/tissue doses: 10

Models:
☑ Patlak model
☑ Mod. Tofts model (Linear)
☑ Tofts model (Non-linear)
☑ Mod. Tofts model (Non-linear)
☑ AUC
☐ Normalized AUC

☐ Save kinetic parameters

Figure 2. The Kinetic modelling window depicting the results of various kinetic model fits (red plots) to the DCE-MRI of the left carotid vessel wall (blue plots).

Simultaneous Acquisition of Bright Blood Arterial Input Function and Black Blood Vessel Wall Uptake Yielding Quantitative Concentration-Time Curves for Kinetic Analysis of Dynamic Contrast Enhanced Imaging in the Atherosclerotic Vessel Wall

Philip M. Robson, Claudia Calcagno, Sarayu Ramachandran, Venkatesh Mani, and Zahi A. Fayad

Translational and Molecular Imaging Institute, Mount Sinai School of Medicine, New York, NY

Introduction: The need for simultaneous acquisition of the arterial input function (AIF) and the vessel wall uptake is gaining interest in the field of quantitative kinetic analysis of DCE in the vessel wall. The need to sample the AIF at higher temporal yet lower spatial resolution than the vessel wall, with different dynamic signal range between AIF and tissue curve, and at separate spatial locations requires novel imaging techniques. Furthermore, it is apparent that black blood techniques, which are superior for distinguishing the vessel wall and plaque from the lumen, should be combined with bright blood acquisitions. For carotid imaging, current dual imaging techniques have not provided adequate quantification of the concentration-time curves for subsequent kinetic analysis. This is challenging due to the high concentrations found in the first pass passage of the clinical bolus (0.1 mmol/kg) used for vessel wall DCE imaging. In this work, we demonstrate the acquisition of quantitative concentration-time AIF and tissue curves in a single sequence and provide quantitative kinetic analysis of DCE in the vessel wall.

Methods & Results: The black-blood SHILO dual imaging DCE technique is based on a multi-slice 2D segmented turbo-spin-echo sequence, with double inversion recovery black-blood preparation. Prior to each segment acquisition a low spatial resolution gradient-echo image-frame is acquired giving temporal resolution of 2 sec for the AIF and 32 sec for the tissue curves in this 2-slice acquisition. The AIF image-frame is saturation-prepared and segmented to maintain sensitivity to very short T1 (echo train length 40). The spatial resolutions are 0.5 mm x 1 mm, 6-mm slice (AIF) and 0.5 mm x 0.5 mm, 3-mm slice (vessel wall). Bloch equation simulations were used to compute a conversion from signal to concentration for the AIF. The standard SPGR model was used for the vessel wall uptake curve. Five patients underwent DCE imaging of the carotid artery (0.1 mmol/kg Magnevist, injected at 4 ml/s). Quantitative concentration-time curves for a whole-vessel-wall ROI were found and kinetic parameters for the vessel wall found using the standard modified Tofts-Kermode model. AIF and vessel wall uptake curves were obtained in all subjects. Representative images from one subject are shown: (A) AIF frame, (B) AIF detail, (C) vessel wall image, (D) detail. Quantitative AIF and vessel wall concentration-time curves are shown in (E), concentration of contrast agent for the AIF (left axis) and tissue curves (right axis). Kinetic parameters, average and standard deviation over left and right carotid arteries in two slices, for each subject are given in the Table.

Conclusion: Black-blood SHILO, with suitable signal modelling, is able to acquire quantitative concentration-time curves for the AIF, similar in functional form to those measured by Parker et al.. Vessel wall curves are obtained with a T1-weighted DIR-SE sequence. Kinetic parameters are in broad agreement with those in the literature.

Clinical Relevance: Improved accuracy and robustness in quantitative DCE has the potential to identify increased vascularity in the vessel wall resulting from inflammation associated with the development of atherosclerosis. Early identification of disease would be advantageous for clinical management.

Figures and tables

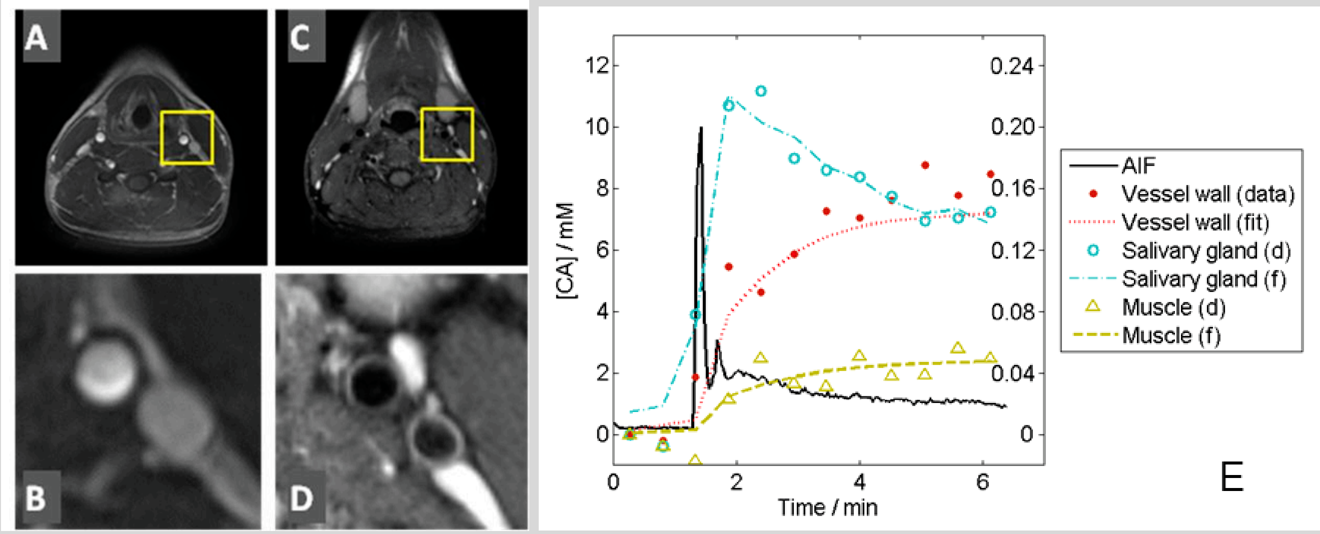

Figure 1: Results from black-blood-SHILO DCE measurements in one representative subject. a) One AIF image frame during bolus passage, and detail of the carotid artery (b). c-d) Black-blood DIR-SE images at later times showing contrast agent uptake, e) Plots of the measured AIF (black solid line) after conversion to blood concentration ([CA]) using the signal model computed from Bloch equation simulations, and the tissue uptake curves for the vessel wall (red, dots), salivary gland (blue, circles), and muscle (green, triangles) after conversion to concentration using the standard SPGR model. For the tissue uptake curves, symbols are measured data, and lines are results from modified Tofts-Kermode fitting routines. Vertical scale is [CA] for the AIF on the left, and for the tissue uptake curves on the right.

Table 1: Kinetic parameters from black-blood SHILO DCE

Subject	v_p	K_{trans} / min^{-1}	v_e	k_{ep} / min^{-1}
1	0.0027 ± 0.003	0.027 ± 0.007	0.11 ± 0.05	0.29 ± 0.17
2	0.0009 ± 0.0012	0.021 ± 0.005	0.089 ± 0.02	0.24 ± 0.05
3	0.0029 ± 0.002	0.019 ± 0.005	0.086 ± 0.018	0.22 ± 0.02
4	0.0016 ± 0.0015	0.016 ± 0.004	0.089 ± 0.03	0.19 ± 0.05
5	0.0006 ± 0.0012	0.018 ± 0.003	0.14 ± 0.11	0.19 ± 0.12

Diffusion Weighted Imaging (DWI) in the Rabbit Model of Atherosclerosis: Distribution of Apparent Diffusion Coefficient (ADC) in Six-Month Old Aortic Plaque

Philip M. Robson, Claudia Calcagno, Sarayu Ramachandran, Venkatesh Mani, and Zahi A. Fayad
Translational and Molecular Imaging Institute, Mount Sinai School of Medicine, New York, NY

Introduction: The rabbit model of atherosclerosis is useful for studying treatment models, drug development and longitudinal studies monitoring response or disease progression. Diffusion imaging has shown promise in atherosclerosis. It has been shown to identify different plaque components in *ex vivo* studies in human and animals , and *in vivo* in human studies , however, it has not previously been demonstrated *in vivo* in the rabbit model. To evaluate the potential of DWI for atherosclerosis in the rabbit aorta, we determined the precision of the diffusion coefficient estimation from in vivo measurements and found the distribution of ADC values in a cohort of 14 rabbits.

Methods & Results: Fourteen male New Zealand White rabbits with atherosclerosis induced by an established method [7,8] were imaged with DWI after 6 months of plaque development. A clinical system (Philips 3 T Achieva) was used with the product 8-channel knee-coil arrayed receiver. The DWI protocol consisted of the following: SE-DW single-shot EPI, TR/TE 3000/68 msec, FOV 160 x 40 mm, 1x1 mm resolution with 3-mm slice thickness, 16 slices in one TR orientated perpendicular to the abdominal aorta inferior to the renal arteries. Images were acquired with 12 different *b*-values equally spaced up to 600 s/mm^2, with diffusion gradients in the slice-select direction. 32 averages were acquired for each image in a total scan time of 19:15 min.

Image quality was good in all rabbits scanned (Fig. 1). Diffusion values ranged between 0.64 and 1.87 x10^{-3} mm^2/s, with an average value of 1.07 x10^{-3} mm^2/s. In 1 rabbit it was possible to identify a bimodal relationship. The fast/slow diffusion components had D = 2.90 and 1.10 x10^{-3} mm^2/s (Fig. 2). The average two-tailed span of the 90% confidence interval for the diffusion coefficient was 0.27 x10^{-3} mm^2/s with this DWI protocol.

The histogram of ADC values in this cohort of rabbits is shown in Fig. 3. The distribution shows a span of approximately 0.8 x10^{-3} mm^2/s, or 3 times the 90% confidence interval of a single measurement of the ADC.

Conclusion: DWI *in vivo* in the rabbit model is feasible with a 20-min protocol giving up to 16 slices. Image quality was acceptable with diffusion weighting in the range up to 600 s/mm^2. Quantification showed diffusion values consistent with others' measurements in normal vessel wall media , the highest diffusion coefficient was less than pure water, which is a physical upper limit for diffusion measurements. DWI was sufficiently sensitive to distinguish bimodal diffusion characteristics in the 6-month old aortic plaque. The precision of diffusion measurements in this study was less than the span of the distribution found in the cohort of rabbits and is sufficient to distinguish normal vessel wall, lipid core, and free water (D = 1.54, 0.26, 3.03 x10^{-3} mm^2/s).

Clinical Relevance: Quantitative DWI may permit identification of early changes in the vessel wall prior to the formation of stenosis and complex plaque. Detection of the early changes in the disease could lead to improved management of patients and guide the use of prophylactic drugs and lifestyle changes. Effective screening of at-risk groups could have advantages for long term clinical outcome and reducing the cost of care.

Figures and tables

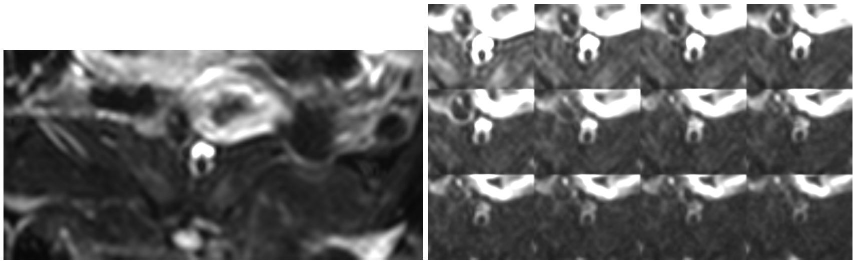

Figure 1: Typical images of diffusion weighting in 6-month old atherosclerotic plaque in the NZW rabbit aorta at a select range of diffusion *b*-values. *Left*: The aorta is shown in the abdomen in a b=0 s/mm^2 image. *Right*: All 12 b-values evenly distributed from 0 to 600 s/mm^2 (left-to-right, top-to-bottom; all images displayed at same greyscale; to show higher b-values well, signal at low b-value is saturated.)

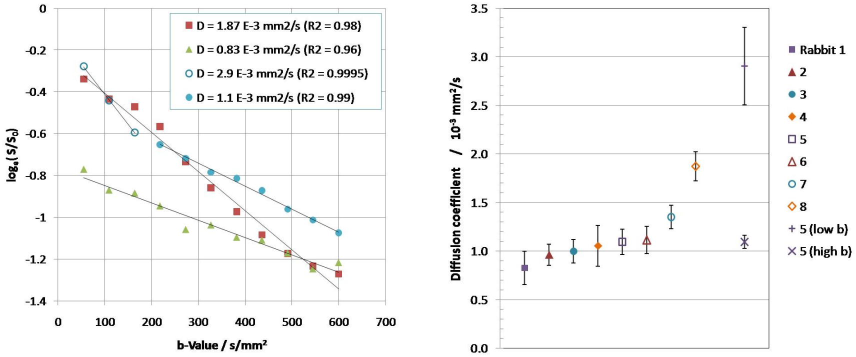

Figure 2: (Left) Diffusion coefficient determination from the plot of log(S/S$_0$) and *b* including the bimodal relationship (circles). (Right) All diffusion coefficient measurements with 90% CI including the separate low and high b-value portions for the bimodal relationship.

Figure 3: Distribution of ADC values in a cohort of 14 rabbits. The 90% confidence interval of the ADC measurement was 0.27 x10^{-3} mm^2/s, smaller than the span of the ADC distribution.

Abstracts, Miscellaneous Category

Microscopy Shared Resource Facility
(Note: This abstract is a summary of the services provided by the Microscopy SRF and presents image data of original research only in the context of the facility services offered.)

Rumana Huq, Victor Friedrich

Mount Sinai School of Medicine

Introduction: The Microscopy Shared Resource Facility (SRF) is a core research and teaching facility dedicated to providing a complete range of light microscopy and image analysis services to the faculty, staff, and students of the Mount Sinai School of Medicine. The Microscopy SRF is available for use 24/7 by all trained users. Free consultation services are offered for immunostaining instruction and protocols, antibody selection, experimental design, microscope selection and image analysis advice.

Methods & Results: The facility services include: confocal, multiphoton, spinning disk confocal, epi-fluorescence, structured illumination, brightfield, stereoscope, deconvolution, and image analysis. (Figure 1)

The Microscopy SRF has several platforms for imaging live cells and tissues. The following microscopes are equipped with incubation chambers that provide CO2, humidity and temperature control for live imaging:

- Leica SP5 DMI Confocal
- Spinning Disk Confocal
- Olympus IX-70 Widefield

All the systems listed above are equipped with motorized focus drives and XY stages to enable automated, Z-stack, time-lapse imaging. Movies are created and analyzed using Metamorph, Volocity, or Image J software. Some of the past live cell imaging applications include:

- Cell tracking and motility
- Cell division
- Wound healing
- Fura-2 imaging
- FRET
- Photoactivation

The Microscopy SRF has recently started collaborations for intravital imaging projects using our newly acquired Olympus FV1000 Multiphoton microscope. Small animals such as mice and rats are ideal for imaging on this system. (Figure 2)

Conclusion: The Microscopy SRF has more than 200 users and is funded and administered through the Associate Dean for Research Resources with guidance from a school-wide Advisory Committee. In the past year, the facility provided training, guidance, and over 7000 hours of instrument time to investigators from more than 100 Mount Sinai laboratories.

Clinical Relevance: As the innovation of small, minimally invasive imaging devices continues to develop, microscopic examination of cells and tissues may provide a possible diagnostic tool for clinical applications.

Figures and tables:

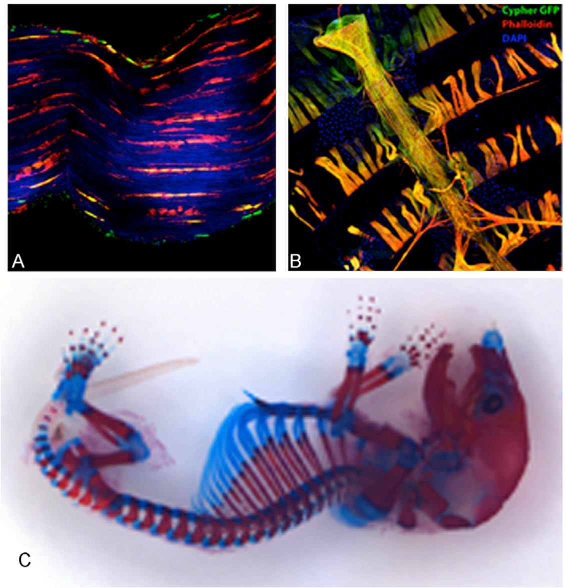

Figure 1. (A) Mouse Tendon with actin cytoskeleton labeled with TR-phalloidin (red), nuclei stained with Hoechst (green), and collagen by SHG (blue). Imaged using Olympus FV1000 multiphoton microscope. Courtesy of Stephen Ros, Evan Flatow Lab. (B) Drosophila heart imaged using Leica SP5 DM confocal microscope. Image courtesy of Jianbo Na, Ross Cagan Lab. (C) Skeletal prep from wt mice(E16.5) stained with Alizarin Red (bone) and Alcian Blue (cartilage). Imaged using Olympus MVX10 stereoscope. Courtesy of Jianyun Yan, Chengleng Cai Lab.

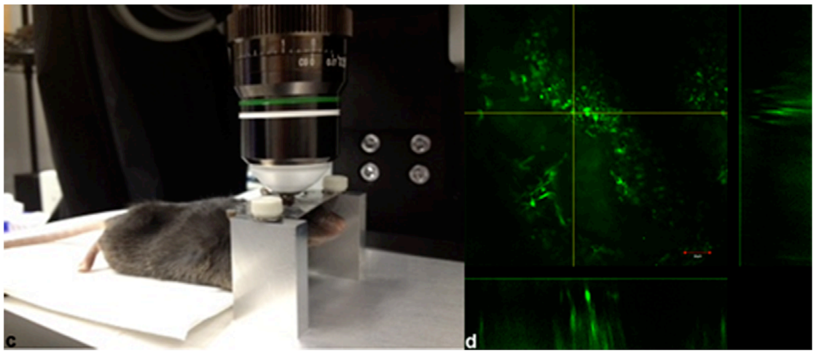

Figure 2. FV1000 Multiphoton microscope stage setup with mouse cranium holder and 25x/1.05NA dipping lens. Image of the same transgenic CX3CR1 GFP mouse that has its microglia stably expressing GFP. Images courtesy of Susana Bardina.

ENOTRIA
WINE IMPORTS

SOFIEBIOSCIENCES